

Utah State University

DigitalCommons@USU

All Graduate Theses and Dissertations

Graduate Studies

5-1996

An Instrument for Experimental Secondary Electron Emission Investigations, with Application to the Spacecraft Charging Problem

Robert Davies
Utah State University

Follow this and additional works at: <https://digitalcommons.usu.edu/etd>



Part of the [Physics Commons](#)

Recommended Citation

Davies, Robert, "An Instrument for Experimental Secondary Electron Emission Investigations, with Application to the Spacecraft Charging Problem" (1996). *All Graduate Theses and Dissertations*. 1697.
<https://digitalcommons.usu.edu/etd/1697>

This Thesis is brought to you for free and open access by the Graduate Studies at DigitalCommons@USU. It has been accepted for inclusion in All Graduate Theses and Dissertations by an authorized administrator of DigitalCommons@USU. For more information, please contact digitalcommons@usu.edu.



AN INSTRUMENT FOR EXPERIMENTAL SECONDARY ELECTRON EMISSION
INVESTIGATIONS, WITH APPLICATION TO THE
SPACECRAFT CHARGING PROBLEM

by

Robert E. Davies

A thesis submitted in partial fulfillment
of the requirements for the degree

of

MASTER OF SCIENCE

in

Physics

Approved:

John R. Dennison
Major Professor

W. John Raitt
Committee Member

Jan J. Sojka
Committee Member

James P. Shaver
Dean of Graduate Studies

UTAH STATE UNIVERSITY
Logan, Utah

1996

UMI Number: 1381713

UMI Microform 1381713
Copyright 1996, by UMI Company. All rights reserved.

**This microform edition is protected against unauthorized
copying under Title 17, United States Code.**

UMI
300 North Zeeb Road
Ann Arbor, MI 48103

Copyright © Robert Edward Davies 1996

All Rights Reserved

ABSTRACT

**An Instrument for Experimental Secondary Electron Emission Investigations,
with Application to the Spacecraft Charging Problem**

by

Robert E. Davies, Master of Science

Utah State University, 1996

**Major Professor: Dr. John R. Dennison
Department: Physics**

Secondary electron emission (SEE) and incident-particle backscattering are important processes accompanying the impact of energetic electrons and ions on surfaces. The phenomena play a key role in the buildup of electrical charge on spacecraft surfaces, and are therefore of particular interest to scientists attempting to model spacecraft charging. In response to a demonstrated need for data, techniques for determining total secondary electron (SE) and backscatter (BS) yields δ and η , and associated scattering-angle-resolved, scattering-energy-resolved, and simultaneous angle-energy-resolved yields have been developed. Further, an apparatus capable of making the necessary measurements for experimental determination of these quantities—for conducting materials in an ultra-high vacuum environment—has been designed, constructed, and partially tested. The apparatus is found to be in working order, though in need of fine-tuning, and the measurement technique successful.

Investigations using a 1-3 keV beam of monoenergetic electrons normally incident on bulk Al have been undertaken with the new apparatus. Electron-stimulated desorption of surface contaminants has been observed, as has been beam-induced carbon deposition, and an empirical model describing the resulting dynamic evolution of δ is presented. Total

δ and η values obtained in the present investigation are found to be in qualitative agreement with the results of previously reported investigations, though quantitative disagreement of δ -values is substantial. Specifically, evidence is presented suggesting that previously reported SE yields for clean Al under electron bombardment (in the 1-3 keV energy range) are in error by as much as 30 %.

(221 pages)

ACKNOWLEDGMENTS

I am pleased to acknowledge the efforts of my advisor, Dr. J.R. Dennison, who has been an unwavering voice of encouragement throughout this project. His unrestrained enthusiasm for all of physics—in both laboratory and classroom—is a constant source of motivation, and I am profoundly grateful for his continuing guidance and (thus far inexhaustible) patience. I look forward to our continued association, both professional and personal.

I am also pleased to recognize the faculty and staff of the Department of Physics, whose enduring efforts have created an intensely supportive work and study environment in which I have been able to develop both as a physicist and personally. In particular, for continuing enthusiasm and patience in the classroom, and for always answering their doors when I knock, my sincere thanks to Professors Farrell Edwards, Charles Torre, and James Wheeler. They have made themselves available for what must seem at times an unending task of explanation. My association with Professor Gordon Lind has also been particularly enjoyable—our impromptu hallway physics has been delightful and thought-provoking. On all matters administrative, Barbara Phillips, Donna Eckberg, Marilyn Griggs, and Renee Tuke take the sting out of even the most crimson red tape.

My studies have been made possible financially by a number of U.S. Government-sponsored programs. I gratefully acknowledge the support of NASA's Rocky Mountain Space Grant Consortium—and in particular my contact with this organization, Professor Jan Sojka, without whose efforts I would not have come to USU—the U.S. Air Force Office of Scientific Research Summer Researcher's Program (under the sponsorship of Dr. Charles Stein and the men and women of Phillips Laboratory's Space Environmental Effects Branch), and NASA's Graduate Student Researcher's Program (under the sponsorship of Dr. Dale Fergusson and NASA's Lewis Research Center). I am honored to have been a part of these programs, and deeply indebted to the people of the United

States for their support of my education, through our government.

For their diligent review of this work and thoughtful inputs, I gratefully acknowledge the efforts of my committee, Drs. John Raitt and Jan Sojka. For their invaluable technical assistance, I would like to acknowledge the contributions of machinists extraordinaire Robert Lowe and Kent Miles, Mr. Peter Mace for his precision magnetic field measurements, Mr. Gordon May for his mechanical design contributions, Pat Espy for his tireless tutorials on electron optics, and Keithely Corporation's Rose Lockhart for her electronic prowess—and more importantly her willingness to share it.

For invaluable personal assistance, I reserve my deepest gratitude (in order of appearance) for: Janice, Raghu, Paul and Patti, Teresa, Marc, Tim and Balraj—your friendship has been the truest source of my education. And especially for Mom, whose love and encouragement are always felt.

Robert E. Davies

CONTENTS

	Page
ABSTRACT	ii
ACKNOWLEDGEMENTS	iv
LIST OF TABLES	v
LIST OF FIGURES	ix
ABBREVIATIONS, SYMBOLS, AND NOTATION	xiii
CHAPTER	
1. PURPOSE AND PLAN	1
1.1 Introduction	1
1.2 Purpose	2
1.3 Plan	2
2. THE SPACECRAFT CHARGING PROBLEM	4
2.1 Definitions	4
2.2 Spacecraft Charging Observations	5
2.3 Charging Effects	6
2.4 Charging Theory and the Current Balance Equation	8
2.5 Importance of Secondary and Backscattered Terms	14
2.6 Modeling Secondary and Backscattered Currents	20
2.7 Conclusions	22
3. SPECIFICATION OF PARAMETERS, MEASUREMENTS, AND METHOD	24
3.1 General Description	24
3.2 Experimental Parameters	24
3.3 Quantities to be Determined, Measurements, and Method	33
4. APPARATUS AND TECHNIQUE	61
4.1 Overview and Definitions	61
4.2 Design Philosophy	64
4.3 Environmental Components	65
4.4 Source-Related Components	77
4.5 Sample-Related Components	79
4.6 Detection-Related Components	83
4.7 Chamber Apparatus	98
4.8 Measurement Technique	107

5. SUPPORT EQUIPMENT TESTING	110
5.1 Vacuum System	110
5.2 Electron Gun	113
5.3 Detection Electronics	117
5.4 Motion Feedthroughs	118
6. PRELIMINARY MEASUREMENTS— ELECTRON BOMBARDMENT OF ALUMINUM	120
6.1 The Sample	120
6.2 Total SE and BSE Yields, δ and η	121
6.3 Angle- and Energy-Resolved Yields	152
7. ANALYSIS AND DISCUSSION	155
7.1 Previous Investigations	155
7.2 Comparison of Results	159
7.3 Possible Sources of Error	161
7.4 Discussion	166
7.5 Proposed Physical Model for $\delta(t)$	167
8. RESULTS, RECOMMENDATIONS, AND CONCLUSION	171
8.1 Results	171
8.2 Immediate Recommendations	172
8.3 Research Possibilities	174
8.4 Extensions of this Research	175
8.5 Initial Program of Study—A Proposal	176
REFERENCES	179
APPENDICES	187
Appendix A: Calculations	188
Appendix B: Scattering Angle as a Function of Detector Position	204

LIST OF TABLES

Table		Page
2.1	Environmental parameters of orbital regimes within Earth's magnetosphere	10
3.1	Experimental parameters	32
3.2	Summary of equations for quantities to be determined	59
4.1	Summary of environment-related components	66
4.2	UHV vacuum chamber design, operating parameters, and support equipment	70
4.3	Electron path deflection due to ambient magnetic field perpendicular to v ($d_t=6.35$ cm)	75
4.4	Summary of source-related components	78
4.5	Electron and ion gun specifications	78
4.6	Summary of sample-related components	80
4.7	Summary of detection system components	84
4.8	Rotatable detector (RD) specifications	94
4.9	Major constituents of various subassemblies	100
4.10	Summary of sample-detector assembly parameters.....	106
4.11	Chamber-assembly specifications	106
5.1	Vacuum chamber performance	111
5.2	Typical beam-current magnitudes and spot sizes for various beam energies	114
5.3	Magnitude and sources of background currents (noise)	118
6.1	Measured δ and η for aluminum	122
6.2	Changes in partial pressures resulting from electron bombardment of sample of ($E_b = 2.0, 2.5$ keV)	134
6.3	Effect of beam energy reduction on vacuum chamber CO_2 levels	134
6.4	Ratios of peak heights for prominent EDX features	147

7.1	Comparison of experimentally determined SE yields for normally incident electrons on bulk Al	156
7.2	Comparison of experimentally determined BSE yields for normally incident electrons on bulk Al	157
7.3	Errors in the measured currents and their effects on SE and BSE yield determination	167
7.4	Estimated values for parameters appearing in Eq. (69)	169
B.1	Scattering angle α as a function of detector position	205

LIST OF FIGURES

Figure		Page
2-1	Orbital regimes within Earth's magnetosphere and associated spacecraft charging levels	7
2-2	Earth's magnetosphere	10
2-3	Schematic depicting source currents to and from a spacecraft operating within the Earth's magnetosphere	12
2-4	Physical processes resulting from energetic electron bombardment of a surface	15
2-5	Typical secondary electron energy spectrum	17
2-6	Dependence of SE yield on primary energy	18
2-7	Energy spectrum for backscattered electrons	18
3-1	Geometry of the incident and scattered beams	25
3-2	Photograph of LDEF tray H-06 after nearly six years in low-Earth orbit	28
3-3	Effect of departure (scattering) angle on the ability of a secondary or backscattered electron to escape the surface of a spacecraft subject to the Earth's magnetic field (B)	31
3-4	Schematic depicting currents to and from (a) a neutrally biased and (b) a positively biased (+50 V) sample for an incident beam of (monoenergetic) electrons	36
3-5	Schematic depicting currents to and from (a) a neutrally biased and (b) a positively biased (+50 V) sample for an incident beam of (monoenergetic) ions	39
3-6	Schematic depicting angle-resolved SE and BSE detection	41
3-7	Schematic depicting angle-resolved detection of SE's and BSE's	44
3-8	Determination of angle-resolved SE yield via negative detector biasing for the cases of (a) incident electrons and (b) incident ions	46
3-9	Concept of energy-resolved SE yield determination via a dome detector that senses only electrons of a certain energy	48

3-10	Schematic illustrating major currents to and from a sample (a) neutrally biased and (b) <i>positively</i> biased to some potential ϕ , where $0 < \phi \leq 50$ V	50
3-11	Schematic depicting angle-energy-resolved yield determination scheme for (a) SE's and (b) BSE's	58
4-1	Photograph of the experimental apparatus, depicting (A) vacuum chamber, (B) chamber apparatus (minus magnetic shielding), (C) electron gun, (D) ion gun, and (E) residual gas analyzer	62
4-2	Schematic depicting the general scenario to be investigated	63
4-3	Vacuum chamber schematics	67
4-4	Magnetic shield	76
4-5	Sample block assembly	81
4-6	Primary sample design	82
4-7	Large Faraday cup in primary sample and holder	82
4-8	Wiring schematic depicting beam current, sample current, and return current detection schemes	85
4-9	Wiring schematic for the rotatable detector	86
4-10	Basic Faraday cup design	89
4-11	(a) Initial and (b) present rotatable detector designs	91
4-12	Diagram tracing the potential (left vertical axis) and energy (right vertical axis) of an electron as it is accelerated from the electron gun cathode to the sample, is backscattered through the 1st and 2nd RD apertures, and enters the negatively biased FC	93
4-13	Sample-detector assembly	99
4-14	Rotatable detector (G) and mounting collar (H) as mounted on 59° arm (I) and additional support arm (J)	101
4-15	Rotatable detector rotation mechanism	101
4-16	Rotatable detector mounted on 59° support arm	102
4-17	Minimum scattering angle available to RD mounted on (a) 45° arm (limited by detector housing radius) and (b) 59° arm (limited by support arm width)	103

4-18	Limits on RD motion about the sample and regions of overlapping angle-resolved measurements	104
5-1	RGA spectra for quiet chamber (no equipment operating)	112
5-2	Electron gun beam current stability	114
5-3	Typical electron gun beamspot profile	116
6-1	Measured δ and η for aluminum	123
6-2	Baseline partial pressures of O, H ₂ O, CO/N ₂ , and O ₂ in the chamber with the electron beam turned off	127
6-3	Effect on baseline partial pressures (of the four species listed) of turning on the electron beam, directing it into the sample FC (t=100 s), and directing it onto the sample surface (t=150 s)	128
6-4	Effect on partial pressures (of species listed) of relocating the electron beam on the sample surface	129
6-5	Effect on partial pressures (of listed species) of relocating electron beamspot on sample surface (at t=100 s, t=125 s, and t=325 s)	130
6-6	Effect of electron beamspot relocation (on sample surface) on partial pressures of listed species	131
6-7	Effect of changing both incident electron beam energy and beamspot location on partial pressures of listed species	132
6-8	Effect of reducing incident electron beam energy on partial pressures of listed species, while beamspot location on the sample remains constant	133
6-9	Relative change in partial pressures as a function of incident electron beam energy	135
6-10	(a) Early dynamic evolution of SE coefficient and (b) extended dynamic evolution of SE and BSE coefficients for electron bombardment of aluminum	137
6-11	(a) Early and (b) extended dynamic evolution of BSE coefficient for electron bombardment of aluminum	138
6-12	Photograph of aluminum sample following long-term electron bombardment	140

6-13	SEM micrographs of the aluminum sample depicting (a) the background aluminum surface, (b) the electron-beam-induced dark region, (c) inclusions in the sample surface, and (d) a ten-fold magnified view of the sample inclusions	143
6-14	EDX spectra for Al sample, off the dark region, taken with probe beam energies of (a) 20 keV and (b) 10 keV	144
6-15	EDX spectra for Al sample, on the dark region, taken with probe beam energies of (a) 20 keV and (b) 10 keV	145
6-16	EDX spectra for surface inclusion on Al sample, taken with a probe beam energy of 10 keV	146
6-17	XPS analysis for the Al sample (a) off and (b) on the dark area	149
6-18	Comparison of (a) XPS carbon peaks and (b) XPS oxygen peaks on and off of the Al sample dark area	150
6-19	(a) View of the sample illustrating misalignment of the RD, when positioned as shown in (b)	154
7-1	Fit of data for dynamic evolution of δ	170
8-1	Possibilities for future work	178
A-1	Percent error in η due to non-normal exit angles of BSE's, for incident energies of (a) 100 eV to 500 eV and (b) 500 eV to 3000 eV	196
A-2	Percent error in δ due to non-normal exit angles of BSE's as a function of beam energy (500 eV to 1500 eV) and BSE yield [(a) $\eta = 0.1$, (b) $\eta = 0.2$, and (c) $\eta = 0.3$	197
A-3	Percent error in δ due to non-normal exit angles of BSE's as a function of beam energy (1500 eV to 3000 eV) and BSE yield [(a) $\eta = 0.1$, (b) $\eta = 0.2$, and (c) $\eta = 0.3$	198
A-4	Percent error in $\delta(E_s)$ as function of sample potential Φ , for Φ ranging from (a) 0 V to 10 V, (b) 10 V to 50 V, and (c) 0 V to 50 V	201
A-5	Expected RD signal as a function of scattering angle ($I_b = 10 \mu A$, $\delta = 0.3$, $\eta = 0.2$)	203
B-1	Scattering angle intercepted by the rotatable detector as a function of detector position	206

ABBREVIATIONS, SYMBOLS, AND NOTATION

AE	auger electron	SE	secondary electron
AES	auger electron spectroscopy	SEE	secondary electron emission
ATS	advanced technology satellite	SEM	scanning electron microscopy
BE	binding energy	SI	secondary ion
BS	backscattered	TS	tertiary sample
BSE	backscattered electron	TSH	tertiary sample holder
BSI	backscattered ion	UHV	ultra-high vacuum
CCD	charge-coupled device	XPS	x-ray photoelectron spectroscopy
DMSP	defense meteorological satellite program	α	polar scattering angle
EDX	energy-dispersive x-ray	B	magnetic field vector
ESD	electron stimulated desorption	δ	total SE yield
EVA	extra-vehicular activity	$\delta(\alpha)$	angle-resolved SE yield
FC	faraday cup	$\delta(E_s)$	energy-resolved SE yield
FOV	field-of-view	$\delta(\alpha, E_s)$	angle-energy-resolved SE yield
FWHM	full-width at half-maximum	$d\Omega$	field-of-view of rotatable detector
GEO	geostationary orbit	E_b	incident beam energy
KCPS	kilo-counts per second	E_s	scattering energy
LDEF	long duration exposure facility	Φ	sample potential
LEED	low-energy electron diffraction	γ	angle of incidence (of incident beam)
LEO	low-Earth orbit	η	total BSE yield
PE	primary electron	$\eta(\alpha)$	angle-resolved BSE yield
PS	primary sample	$\eta(E_s)$	energy-resolved yield
PSH	primary sample holder	$\eta(\alpha, E_s)$	angle-energy-resolved BSE yield
RD	rotatable detector	I_b	beam current
RGA	residual gas analyzer	I_{bse}	BSE current

$I_{d(-50)}$	RD current at –50 V bias
$I_{d(0)}$	RD current at neutral bias
$I_{r(0)}$	return current at neutral bias
$I_{r(50)}$	return current at +50 V bias
$I_{s(0)}$	sample current at neutral bias
$I_{s(50)}$	sample current at +50 V bias
I_{se}	SE current
j	incident species
ϕ_s	azimuthal scattering angle
m	sample material
m_e	electron mass
N	total number of particles
n_{bse}	number of BSE's
n_{bsi}	number of BSI's
n_{se}	number of SE's
Q	total electric charge
q	electric charge of particle
sfc	surface condition
t	time
Z	atomic number

CHAPTER 1

PURPOSE AND PLAN

1.1 Introduction

Scientific observation occurs on many levels. Generally, it can be qualitative (there are two kinds of electric charge—*Benjamin Franklin, 1747*) or quantitative (charged objects exert forces on each other according to Coulomb's law—*Charles Coulomb, 1785*). Also, the observer may be investigating the specifics of a well-known phenomenon or object (e.g., the charge of a single electron—*Robert Millikan, 1913*), or feeling around the edges of little-understood events (Benjamin Franklin flying his kite). If the purpose of an investigation is to better understand fundamental physical processes, and if the observer actively alters (or creates) the events being observed, he or she has entered the realm of experimental physics.

Of prime importance in experimental physics is the method of observation. Once the experimenter has determined what to observe, there is the question of how to observe. For example, the temperature of a piece of metal may be investigated qualitatively by touch (it feels hot or cold) or by sight (it appears red hot or white hot). Quantitatively, the metal's temperature might be determined with a mercury thermometer (employing the principle of thermal expansion), or perhaps a pyrometer (utilizing the temperature dependence of optical spectra).

In short, the challenge of experimental physics is the application of *known* physics toward the discovery of *unknown* physics. This thesis deals primarily with this challenge—that is, the design, construction, and testing of an instrument capable of making a particular (quantitative) observation—and is therefore predominantly an instrumentation thesis. Nevertheless, significant physical discovery is present as well.

1.2 Purpose

This thesis describes an instrument that has been designed, constructed, and partially tested for the purpose of addressing a number of general inquiries. Specifically, given a flux of energetic charged particles (e.g., electrons or ions) incident on a conducting surface,

- (i) what fraction of the incident particles are reflected (backscattered) from the surface, at what angles, and with what energies?,
- (ii) how many electrons per incident particle are ejected (secondary emitted) from the surface, at what angles, and with what energies?, and
- (iii) what material properties and surface conditions affect these results?

1.3 Plan

Material in this thesis is organized in the following format: (i) motivation, (ii) instrumentation, and (iii) observation. As a guide to the reader, a brief overview in the form of a tour through this thesis is now presented. The notation (3.2.4) is used to indicate Section 3.2.4 (i.e., Chap. 3, Sec. 2.4).

Knowledge of motives underlying the questions stated in (1.2) is not prerequisite to an ability to answer them, or to understand their answers. Aesthetically, however, unmotivated science is at best unsatisfying, and usually incomplete. Chapter 2 is therefore presented as motivation for the science that follows. Secondary electron emission (SEE) and incident-particle backscattering are addressed from the perspective of the spacecraft charging problem and attempts to model charging phenomena. It is found that backscattering and SEE characteristics of a great many spacecraft materials are unknown—as are the effects of surface contamination on these processes—and that this lack of information is a serious handicap to spacecraft charging modeling efforts.

Once motivated, the quantities for which experimental values are to be determined, important experimental parameters, and a general measurement scheme are presented in Chapter 3. Specifically, eight quantities are identified for determination and a measurement scheme for each is given. Chapter 4 then describes the experimental apparatus that has been designed and constructed to perform the necessary measurements, as well as specific measurement technique. [Note: It is important at this point to distinguish between the terms *determined quantity* and *measurement*. A measurement involves an actual physical observable, such as electric charge (or current). Determined quantities, such as numbers of charged particles, are not actually measured, but inferred (calculated) from measured quantities.]

Once conceived and built, an apparatus and technique must be tested before confidence in results can be achieved. Chapters 5, 6, and 7 address this point. Performance characteristics of the various pieces of support equipment (e.g., the vacuum system, electrometers, and electron guns) are reviewed in Chapter 5, along with some characteristics of the detection equipment. Chapter 6 gives the results of measurements performed for energetic electrons incident on bulk aluminum, and Chapter 7 compares these results with analogous measurements found in the literature. From this comparison, conclusions are drawn regarding experimental design.

Finally, a summary of results is presented in Chapter 8. Strengths and weaknesses of the apparatus are discussed, including the need for equipment modifications and further testing, and a proposed plan of study incorporating this apparatus is presented. The thesis concludes with a list of extended research topics that may be addressed with the apparatus and techniques described.

CHAPTER 2

THE SPACECRAFT CHARGING PROBLEM

Emerging as a subfield of the study of electric potentials on *all* surfaces in space, ranging from dust grains to planets,¹ spacecraft charging has matured in its own right over the past four decades. This chapter summarizes results and ongoing research in this field insofar as to motivate experimental work presented in later chapters. The phenomenon is defined (2.1), a summary of observations is presented (2.2), and the importance of charging in the context of spacecraft operations is reviewed (2.3). Theoretical formulation of the spacecraft charging problem in the near-Earth environment is then overviewed (2.4), followed by a more detailed discussion regarding the role of SEE and backscattering (2.5), and attempts to model these phenomena (2.6).

For the interested reader, more exhaustive accounts of the spacecraft charging phenomenon can be found in a number of excellent review articles, chief among them “Potentials on Surfaces in Space” by E.C. Whipple¹ and “The Charging of Spacecraft Surfaces” by H.B. Garrett.² Also, Frooninckx³ gives an excellent summary of passive spacecraft charging in the low-Earth orbit (LEO) polar environment.

2.1 Definitions

Spacecraft charging occurs when positively or negatively charged particles accumulate on or are removed from a space vehicle’s surface such that a net charge imbalance induces an electric potential difference between the spacecraft and surrounding neutral plasma.³ *Passive charging* refers to a charge imbalance resulting from natural interactions (i.e. exchanges of charged particles) between the spacecraft and its environment, while *active charging* is achieved by artificial means (e.g. the controlled ejection of charged particles from the vehicle by ion or electron guns). *Differential charging* refers to an uneven charge distribution over the spacecraft surface, creating a

potential difference not only between the vehicle as a whole and the surrounding plasma, but between different portions of the vehicle itself. (Such charging occurs because most spacecraft surfaces are not electrically uniform; rather, they comprise a checkerboard of alternately conducting and insulating surfaces. The resulting inability of a given surface element to equitably distribute any accumulated charge to the rest of the spacecraft, coupled with anisotropic source currents, leads to differential charging of the vehicle.)

2.2 Spacecraft Charging Observations

In situ observations of spacecraft-to-plasma potentials were almost immediate with the advent of routine rocket investigations of the lower ionosphere in the mid-1950's.^{1,2} In the 40 years since, the phenomenon of spacecraft charging has been well documented in every environmental regime investigated. A detailed review of these observations through 1981 can be found in Garrett,² and Frooninckx³ summarizes additional important observations through 1991. Observed charging levels span a considerable spectrum; potentials of a few tenths of a volt are the norm in the lower ionosphere (~70-200 km), undisturbed magnetosphere and interplanetary space, while multi-kilovolt charging events are not uncommon at geosynchronous (~36,000 km) altitudes⁴⁻⁷ (see Fig. 2-1). Indeed, the most severe potential to date, -19 kV, was reported aboard the Advanced Technology Satellite (ATS) in the geosynchronous regime.⁵ Moreover, recent studies have shown that charging levels of several hundred volts^{8,9} to greater-than-kilovolt charging¹⁰ can occur even in the LEO polar environment (~300-1000 km), where previously it had been thought that relatively high ambient plasma densities would suppress the development of severe spacecraft-to-plasma potentials.

The discovery of kilovolt charging at LEO altitudes has lead to NASA concerns over Space Shuttle charging in this environment. Underscoring these concerns is a study by Hall *et al.*,¹¹ which suggests that a several-kilovolt potential difference could arise

between the Shuttle and an extra-vehicular-activity (EVA) astronaut in polar orbit in the upper ionosphere. Such a life-threatening possibility emphasizes the importance of the phenomenon, though is something of a special case. Of more immediate concern to the community of space scientists and spacecraft designers is the broad range of day-to-day operational impacts.

2.3 Charging Effects

The importance of spacecraft charging as a discipline stems from its effects on space operations—i.e., on spacecraft systems and *in situ* observations of the space environment. Documentation of such effects is widespread;^{1,2,12,13} Grard *et al.*¹² gives a detailed review of the subject, and Frooninckx³ points out that over 80 references on spacecraft charging effects are cited by Balmain.¹³ Charging effects arise from both overall and differential vehicle charging. Development of an overall electric potential between a spacecraft and its plasma environment is not generally damaging to spacecraft systems;³ of concern to the space-science community, however, are pronounced effects on *in situ* environmental observations such as charged particle counts and electric and magnetic field measurements.^{1,12} Indeed, in perhaps the first paper on the subject of spacecraft charging, Johnson and Meadows¹⁴ theorized that certain RF mass spectrometer readings above 124 km of altitude were the result of a negative vehicle potential.

Differential charging poses many of the same difficulties to space-environmental investigations as does an overall vehicle potential,¹⁵⁻¹⁷ though it has attracted considerably more attention as a result of deleterious effects on spacecraft systems. Garrett² has summarized the strong evidence linking the occurrence of operational spacecraft anomalies with vehicle potential. Buildup of electric potentials between components can lead to electrostatic discharge, or arcing, which can lead to operational anomalies either by

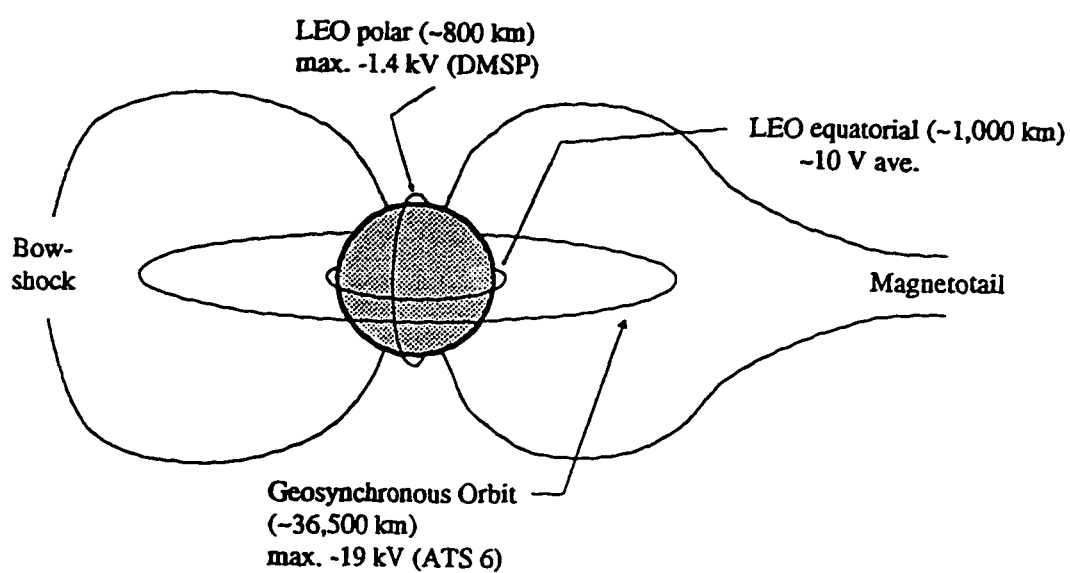


FIG. 2-1. Orbital regimes within Earth's magnetosphere and associated spacecraft charging levels.

direct current injection into onboard electronics, or by means of an electromagnetic pulse created by the arc.^{13,18} Component failure as a result of dielectric breakdown through charge deposition has been the subject of several investigations.^{13,19,20} Resulting anomalies range in severity from negligible to extreme; Wadham²¹ has reported the temporary loss of control of a satellite and subsequent fuel loss as the result of an electrostatic discharge, while Shaw *et al.*²² believe this effect responsible for the loss of an entire spacecraft!

Attempts at preventing or minimizing adverse effects of spacecraft charging have met with some success, and have generally followed one of two tracks: (i) hardening onboard systems to better deal with electrostatic discharging, and (ii) reducing charging levels. One method of reducing charging levels has been the development of electrostatically clean surfaces^{18,23,24} (i.e., surfaces not prone to charging, due in part to material properties). Another approach has been the use of active charging control through charged particle emission²⁵ or neutral plasma emission.²⁶ In conjunction with attempts to design spacecraft that are less susceptible to charging has been an intense effort to accurately model this phenomenon (an effort that includes the work presented in this thesis), allowing the realistic evaluation of new designs before they are constructed and launched. The focus of this review now turns to ongoing modeling efforts.

2.4 Charging Theory and the Current Balance Equation

The fundamental task facing spacecraft modelers is the solution of Poisson's equation

$$\nabla^2\phi = -4\pi\rho \tag{1}$$

for the spacecraft-to-plasma potential ϕ , where ρ is the (surface) charge density of the spacecraft. Among many complexities associated with solving this equation (for the highly dynamic and nonlinear case of a charged object moving in a time varying plasma) is the

need to accurately determine ρ . This requirement, in turn, necessitates the identification and accurate representation of all sources of charge transfer to and from the spacecraft surface—i.e., all sources contributing to ρ . Such a task leads to the notion of *source currents* and the *current balance equation*.

Charging of a spacecraft surface (implying a dynamic process in which the spacecraft transitions from one equilibrium potential to another) occurs when the sources of charge to and from the spacecraft, J_k (source currents), are unbalanced, resulting in a net flux of positive or negative charge. The net flux can be written

$$J_{net} = \sum_k J_k. \quad (2)$$

Charging continues until the various positive and negative J_k —which are themselves functions of ϕ —are balanced and an equilibrium potential is attained; that is, until $J_{net} = 0$. Specific identification of individual source currents, then, is the first task facing modelers.

Theorizing about the nature and magnitude of natural source currents to and from surfaces in space began well before *in situ* measurements were possible,²⁷⁻²⁹ in a time when popular opinion held that the space environment was a single, relatively homogenous region. *In situ* observations over the past 40 years, however, have revealed a vast spectrum of space environmental regimes whose physical characteristics—e.g., magnetic fields, illumination, and particle species, energies, and densities—can and do vary dramatically.^{30,31} Source currents to a spacecraft, therefore, are characteristic of its operating environment. Most often of interest is that region within Earth's magnetosphere, itself composed of widely varying environmental regimes, (see Fig. 2-2 and Table 2.1) where the vast majority of spacecraft operate.

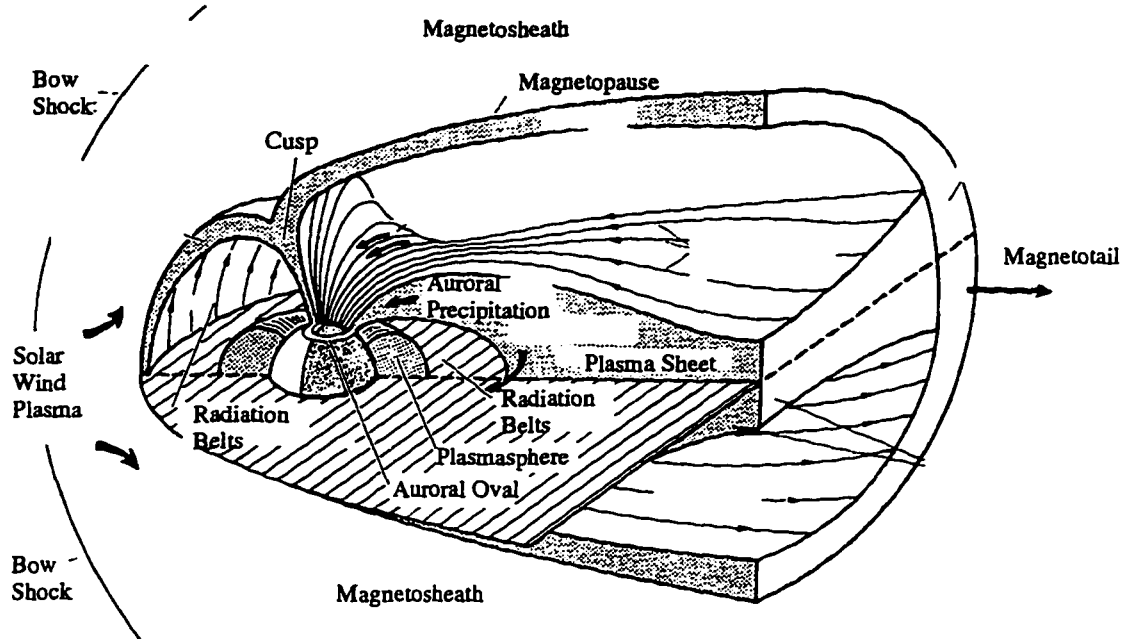


FIG. 2-2. Earth's magnetosphere (adapted from Ref. 30)

TABLE 2.1. Environmental parameters of orbital regimes within Earth's magnetosphere.

Region	Altitude	Plasma Density (# cm ⁻³)	Characteristic Energy (eV)	
			<u>ions</u>	<u>electrons</u>
LEO	150 km	10 ³ - 10 ⁵	0.05 - 0.1	0.1 - 0.2
	1000 km	10 ⁴	0.2 - 0.3	0.2 - 0.4
Plasmasphere	1000 km - 5 R _E	10 ⁴ - 10	< 1	< 1
Geosynchronous	5.62 R _E	2	5000	2500
Magnetospheric Cusp	high latitudes above 1000 km	0.1	200	200

In this regime, with artificial sources neglected (passive charging), Eq. (2) takes the form

$$J_{net} = J_i - J_e + J_{im} - J_{em} + J_{ph} + J_{2ee} + J_{2ei} - J_{2ie} - J_{2ii} + J_{bse} - J_{bsi} = 0 \quad (3)$$

for a spacecraft at equilibrium potential.³ The individual J_k represent current fluxes due to

ambient ions (J_i)

ambient electrons (J_e)

energetic (precipitating) ions of magnetospheric origin (J_{im})

energetic (precipitating) electrons of magnetospheric origin (J_{em})

photoemitted electrons (J_{ph})

secondary electrons due to impacting energetic electrons (J_{2ee})

secondary electrons due to impacting energetic ions (J_{2ei})

secondary ions due to impacting energetic electrons (J_{2ie})

secondary ions due to impacting energetic ions (J_{2ii})

backscattered electrons (J_{bse})

backscattered ions (J_{bsi})

This situation is depicted schematically in Fig. 2-3. Equation (3) is referred to as a current balance equation, and is the most general form of this equation for a spacecraft within Earth's magnetosphere.³ The success of spacecraft charging models, such as NASA's NASCAP, NASCAP LEO, and POLAR codes, begins with accurate modeling of each of the J_k . A summary of each of the terms is therefore presented next.

2.4.1 Ambient Particle Flux

The ambient plasma environment for spacecraft within the Earth's magnetosphere varies significantly. Particle densities vary with altitude by up to six orders of magnitude from the upper ionospheric to geosynchronous regimes, and average ambient plasma temperatures vary from a few electron volts in the plasmasphere to more than 10 keV in the plasmasheet³² (see Table 2.1). In addition, particle densities can vary by several orders of magnitude within the same altitude regime depending on latitude, solar cycle, and local time, and ambient temperatures can vary with species.³ While such variations clearly affect the magnitudes of J_i and J_e , these fluxes are approximately self-balancing (i.e., $J_i \approx -J_e$)

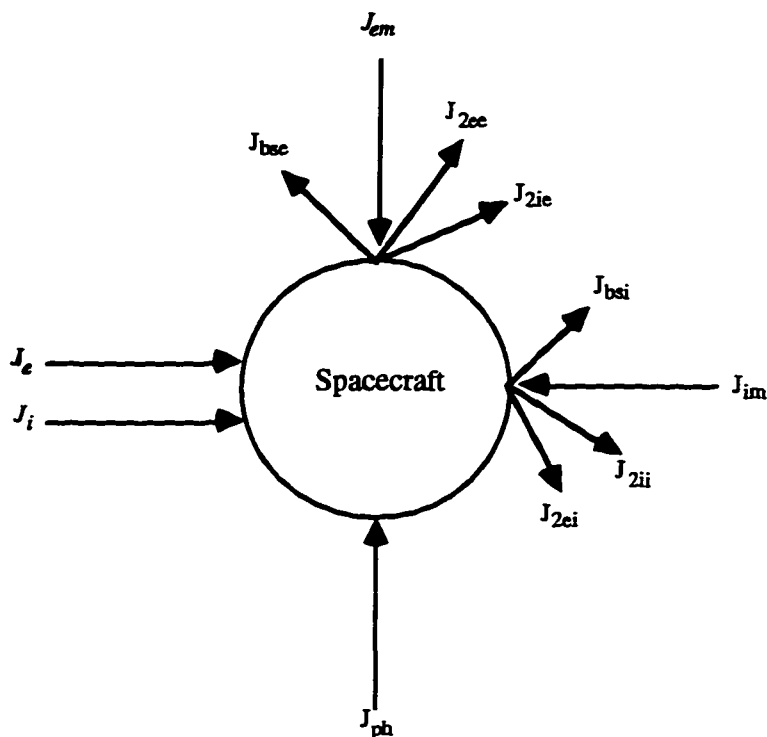


FIG. 2-3. Schematic depicting source currents to and from a spacecraft operating within Earth's magnetosphere.

for an uncharged spacecraft and therefore do not contribute appreciably to net charge accumulation. [NOTE: An exception to this can be found in low-earth orbit, where a disparity between thermal velocities allows ambient electrons access to the rear surface of an orbiting spacecraft, and denies such access to the ambient ions. In this case, J_e and J_i clearly are not self-balancing.] For a charged spacecraft, however, J_e and J_i must be modeled. The nature of Earth's ambient plasma environment has been well-characterized both observationally^{33,34} and from a modeling standpoint,^{35,36} enabling the formulation of ambient current flux terms such as those given by Garrett.²

2.4.2 Precipitating Particle Fluxes

Generally believed to originate from deep within the Earth's magnetotail, highly energized streams of charged particles—mostly electrons and protons—are periodically

injected into the plasmasphere, tracking along Earth's magnetic field lines into the auroral region of the upper ionosphere. These precipitating particles comprise highly anisotropic currents to which orbiting spacecraft are periodically subjected, and their importance as driving terms of vehicle potential in the LEO polar regions, as well as in near-geosynchronous regimes, is well established.⁴⁻¹⁰ Charge deposition by energetic electrons and ions does not generally occur simultaneously, nor at equal levels, and therefore J_{em} and J_{im} do not represent self-balancing terms. Extensive *in situ* energy-resolved observations of these particle populations³⁷⁻³⁹ have enabled accurate modeling of these terms.⁸ The finding by Hardy *et al.*^{37,38} that fluxes of energetic electrons in the energy range 3-30 keV are typically 1-2 orders of magnitude greater than for ions of similar energy has lead some researchers to discard the J_{im} term altogether as unimportant (see, for example, Ref. 8), though such an action may be premature [see (2.5.2)].

2.4.3 Photoemission

Jung (1937) theorized that photoemission would play a dominant role in the electric charging of dust grains in interstellar space. Cosmic dust grains notwithstanding, *in situ* observation has shown photoemission is indeed one of the dominant processes in the charging of spacecraft surfaces.⁴⁰ Photoemission is a function of both the incident electromagnetic spectrum and surface material, as well as vehicle geometry. The solar spectrum and intensity for spacecraft in the near-Earth environment is well-characterized, and considerable experimental work has been done to obtain photoelectron yields for various spacecraft materials,¹ (though Garrett² points out that photoemission properties of many materials are still unknown). Typical expressions used to model the photoelectron flux can be found in a number of references.^{1,2,41}

2.4.4 Backscattered and Secondary Fluxes

Energetic charged particles impacting on solid surfaces effect a number of interesting and important phenomena. Referring to Fig. 2-4, incident particles may be absorbed, scattered, cause the ejection (secondary emission) of particles originally residing within the surface (e.g., electrons or ions), or stimulate the emission of photons.

Absorption of impacting particles represents a contribution to the J_i , J_e , J_{em} , or J_{in} terms, depending on charge and origin. *Backscattering* refers to elastic or inelastic scattering of incident (primary) particles, and its role in overall current balance is accounted for by the J_{bse} and J_{bsi} terms (for electrons and ions, respectively). *Secondary emission* refers to the ejection of surface particles as a result of primary particle impacts, and is described by the J_{2ee} , J_{2ei} , J_{2ie} , and J_{2ii} terms. Backscattered and secondary currents are functions of the fluxes of incident particle species and energies, and therefore do not contribute equally to current balance. In particular, because incident energetic electron fluxes are much greater than those for ions, and because incident electrons produce relatively few secondary ions⁴² (as a result of the tremendous mass differential between electrons and ions), J_{2ei} , J_{2ie} , J_{2ii} , and J_{bsi} are often regarded as small in the current balance equation and neglected.^{2,8,41} The remaining backscattered and secondary terms, J_{2ee} and J_{bse} , have been flagged by researchers as highly relevant to the charging process⁴⁰ and, together with J_{2ei} and J_{bsi} , are the focus of this thesis. An expanded discussion on the nature of these terms, their importance, and how they are modeled is therefore warranted.

2.5 Importance of Secondary and Backscattered Terms

Studies conducted over the past 25 years have revealed a correlation between the spectra of incident energetic *electron* populations, and the severity of charging experienced by spacecraft at a variety of altitudes.^{3,5,7,10,43} Most recently, Frooninckx and Sojka¹⁰

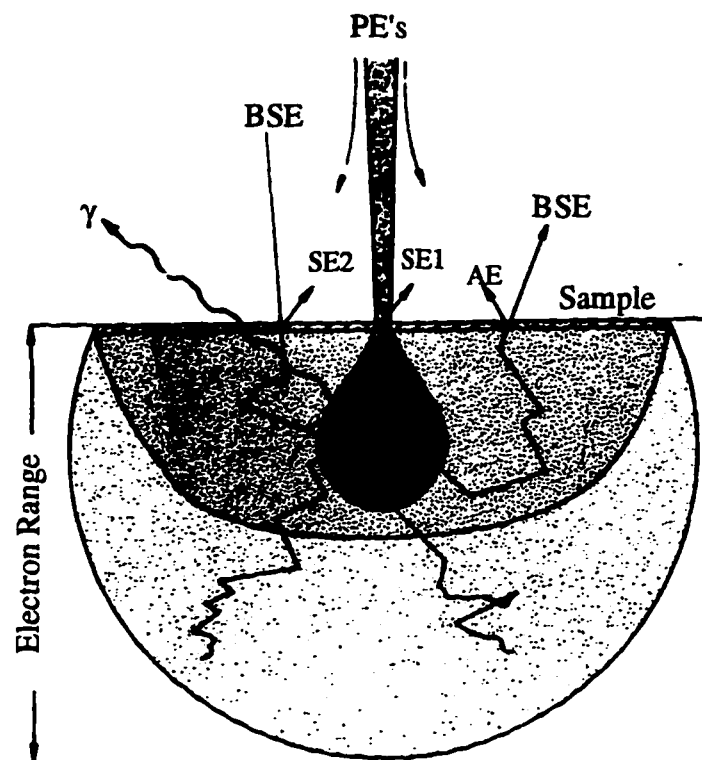


FIG. 2-4. Physical processes resulting from energetic electron bombardment of a surface. Primary electrons (PE's) can be backscattered (BSE), produce secondary electrons (SE₁), or result in the emission of photons (γ). Also, backscattered electrons can produce secondary electrons (SE₂) and Auger electrons (AE). Shaded regions represent volumes of electron trajectories, with trajectory densities increasing with darkness (adapted from Ref. 45).

were able to correlate severe charging of Defense Meteorological Satellite Program (DMSP) spacecraft in the LEO polar environment with enhanced electron fluxes of energies $\geq \sim 10$ keV. Additionally, Gussenhoven and Mullen⁷ were able to demonstrate a similar effect for the P78-2 SCATHA spacecraft—operating at geosynchronous altitudes—for enhanced fluxes of electrons with energies $\geq \sim 54$ keV, coupled with simultaneous reductions in fluxes of electrons with energies $\leq \sim 4$ keV. Such observations are easily understood from the point of view of secondary electron emission (SEE). While the details of modern SEE theory can be quite complex (see, for example, Ref. 66), a brief overview of SEE fundamentals will be more than adequate to illustrate the connection between J_{em} and spacecraft charging levels.

2.5.1 SEE Theory

A portion of the energy deposited in a material by impacting incident particles may be available for absorption by electrons residing within the material. Electrons that absorb enough of this energy to (i) free themselves from the potentials binding them to their location within the material, (ii) migrate to the surface via elastic and inelastic collisions, and (iii) escape the potential at the surface, are emitted as secondary electrons (SE's). While it is impossible to precisely distinguish (experimentally) which electrons have been secondary-emitted and which have been backscattered, previous studies^{44,45} have demonstrated that most SE's ($\sim 90\%$) have energies $< \sim 15$ eV, regardless of the circumstances surrounding their production (see Fig. 2-5). *This has lead to the somewhat arbitrary (though necessary) definition of SE's as those scattered electrons whose energies are ≤ 50 eV.*^{46,47} It has also been determined that SE's originate from a thin emission layer near the surface, typically on the order of tens of angstroms thick (for metals).^{42,48} This is contrasted with the much greater penetration depth of hundreds of angstroms for primary electrons (PE's) with energies $\geq \sim 1$ keV. Primary electrons with 2 keV of energy incident

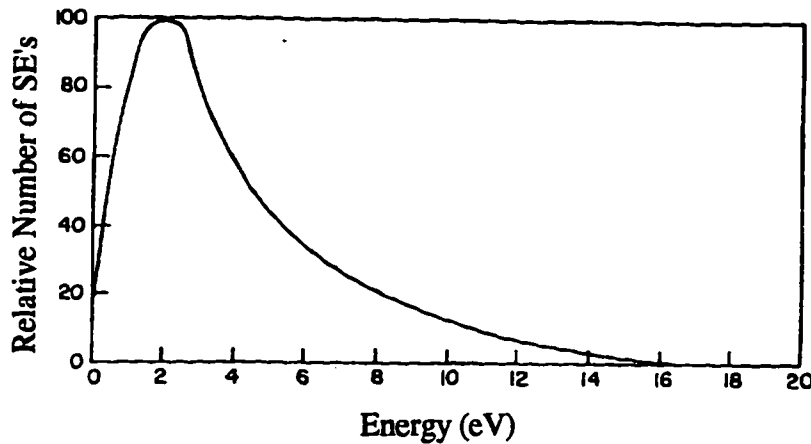


FIG. 2-5. Typical secondary electron energy spectrum (adapted from Ref. 41)

on aluminum, for example, have a penetration depth of 700 \AA ,⁴⁹ while the depth of the SE emission layer is only $50\text{-}80 \text{ \AA}$.⁵⁰

The number of SE's produced for every primary electron, then, will depend on—among other things—the energy of the PE's and the material being bombarded. The nature of the material (e.g., conductivity, work function, and atomic number) will determine how much energy an electron must absorb to escape. The energy of the PE will determine the amount of energy deposited in the emission layer; that is, higher-energy PE's (which deposit most of their energy deeper within the material) will not liberate as many SE's as will lower-energy PE's (which deposit a higher fraction of their energy within the emission layer). Illustrating this point, Fig. 2-6 is a typical SEE curve, showing the number of SE's emitted per incident PE—termed the *SE yield*—as a function of incident energy.

Also, it is important to note the role of backscattered electrons (BSE's) in SE production. Recall that BSE's are primary electrons that have impacted the material, undergone elastic and/or inelastic scattering within the material, and re-emerged from the material. Figure 2-7 is a typical BSE spectra, and shows that a majority of BSE's emerge

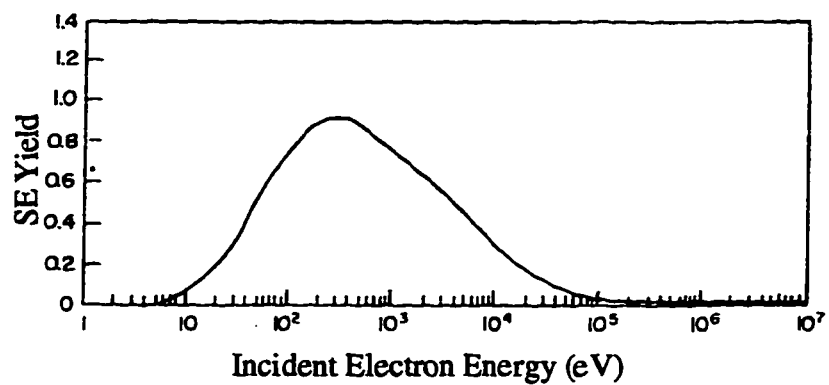


FIG. 2-6. Dependence of SE yield on primary energy (data is for electrons incident on aluminum—adapted from Ref. 41)

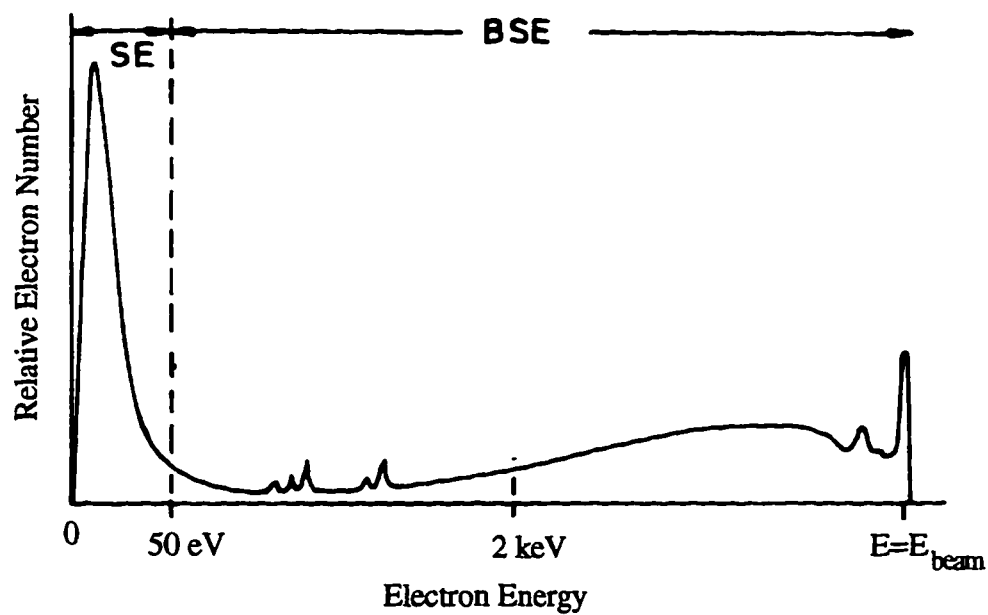


FIG. 2-7. Energy spectrum for backscattered electrons (adapted from Ref. 45)

having lost very little of the energy they possessed as PE's. Just as PE's deposit energy in the SE emission layer as they enter a material, BSE's deposit energy in that same layer as they leave the material—energy available for the production of SE's. And not only do BSE's contribute to the production of SE's, a number of investigations^{49,50,51,52} have demonstrated that BSE's are considerably more efficient producers of SE's than are primary electrons. This result is almost intuitive when one considers that BSE's possess time-averaged momentum vectors directed toward the surface (from beneath it), while PE's possess momentum vectors directed deeper into the material. As an example, Kanter⁴⁹ found that for incident electrons in 2-20 keV energy range, BSE's were nearly five times more effective producers of secondaries than were the PE's.

2.5.2 Discussion

Given the above (albeit qualitative) physical picture, it is not difficult to make sense of the observed correlation between J_{em} and spacecraft charging levels. Large fluxes of low-energy ($\leq \sim 2$ keV) electrons do not lead to significant charging because the resulting SE yield is near unity (meaning the J_{zee} , J_{bse} , and J_{em} currents are essentially self-balancing). The SE yield for higher-energy electrons, however, is considerably lower than unity and increased fluxes of these electrons therefore produce a J_{em} term which dominates the J_{zee} and J_{bse} terms (resulting in overall negative charging of the vehicle). This analysis has led to the long-standing position of the spacecraft charging community that *SEE is one of the two dominating phenomena of spacecraft charging (the other being photoemission), determining the level to which an orbiting spacecraft will charge.*⁴⁰ It is precisely this demonstrated importance of SEE to a spacecraft's potential, coupled with the material dependence of SE yields, has led to the strategy of reducing charging levels via judicious selection of construction materials.^{2,53} Pertaining to the suggestion put forward in (2.4.2) regarding the dismissal of J_{im} (based on its magnitude relative to J_{em}) is challenged when one considers the fact that SE yields due to incident *ions* with energies $\geq \sim 10$ keV can be

considerably greater than unity.^{1,6} Even though J_{em} may be orders of magnitude below J_{im} , the SE yield (J_{2ei}) due to the impacting ions may actually be orders of magnitude above the SE yield (J_{2ee}) due to impacting electrons.

2.6 Modeling Secondary and Backscattered Currents

As important as J_{2ee} and J_{bse} have shown themselves to be, these terms—particularly J_{2ee} —have proven notoriously difficult to accurately model. Examination of typical secondary and backscattering expressions currently used in the modeling community will aid in illustrating where the difficulties lie.

2.6.1 Expressions for J_{2ee} and J_{bse}

Garrett² presents the following as typical expressions for the current density due to secondary and backscattered electrons:

$$J_{2ee} = \frac{2\pi e}{m_e^2} \int_0^\infty dE' \int_0^\infty g(E', E) \delta(E) f(E) E dE \quad (4)$$

where

- e electron charge
- m_e electron mass
- g emission spectrum of SE's due to incident electrons of energy E
- δ SE yield due to incident electrons of energy E
- E' SE energy
- f distribution function of incident electrons at the surface,

and

$$J_{bse} = \frac{2\pi e}{m_e^2} \int_0^\infty dE' \int_0^\infty B(E', E) f(E) E dE \quad (5)$$

where

$$B(E', E) = G\left(\frac{E'}{E}\right) \frac{1}{E}$$

and G is the BSE yield at the fraction $\left(\frac{E'}{E}\right)$ of the incident energy E . Of interest in these expressions are the quantities g , δ , and B (or G)—input parameters which must themselves be modeled. Specific expressions for these terms have been developed,^{6,40,54} though their presentation here is not necessary. What is important is the fact that *each of these terms is dependent on a number of parameters (some known and some unknown)—the most basic of which is material—and expressions used to model them are derived empirically, based on data gathered by experiment.* (Note: f must also be modeled, though it differs from the others in that it is an environmental, rather than material-dependent, parameter.)

2.6.2 Limitations

The absence of experimental SEE data for a wide range of materials has been identified by the spacecraft charging community as a major deficiency in the ongoing effort to accurately model spacecraft potentials. While the *backscattering* characteristics of a host of basic materials (e.g., Al, Ag, Au, Be, C, Cu, and Ni) have been reasonably well investigated over a considerable range of incident-electron energies (~100 eV - ~1.3 MeV), a continuing literature review confirms considerably less work regarding *SEE*. Furthermore, secondary-emission and backscattering properties for a wide range of spacecraft materials—often unique due to special coatings, paints, and surface contaminants—have not been investigated experimentally, leaving modelers to rely on data that is at best incomplete, and often near guesswork.^{2,54,55}

Further complicating the issue is the fact that most of the data currently available and in use was obtained prior to the advent of ultra-high vacuum (UHV) technology,^{6,42} a significant factor considering the extreme sensitivity of SE yields to surface condition^{50,58,59} and the level of contamination generally associated with diffusion pumps of the pre-UHV era. Garrett² (p. 589) has addressed this issue specifically, stating that “...the secondary and backscatter properties of actual satellite surfaces, which are

invariably oxidized or contaminated, are not well known...lack of knowledge in this area is one of the major deficiencies in spacecraft charging theory..." (my italics). Even those measurements that have been made under UHV conditions have not found wide use among the spacecraft charging community, owing largely to insufficiently large data sets. Prokopenko and Laframboise⁶ (p. 4127), for example, specifically state that "*though there exist more recent measurements of [BSE yield]...we have found these results to be too fragmentary for our purposes, and we have therefore used [the older] results throughout...*" (my italics).

Other omissions in the SEE data base impact spacecraft charging issues as well. SE and BSE energy spectrums as functions of *emitted* angle—so-called simultaneous angle- and energy-resolved (differential) SE yields—are an important aspect of SEE that remains largely uninvestigated. Angle-energy-resolved information may prove crucial in understanding phenomena involving the transport of SE's across surfaces, such as "snapover"⁵⁵, the breakdown of surface dielectrics,^{55,56} and the transport of SE's within the plasma sheath surrounding a charged spacecraft.^{54,55} The importance of such angle-energy resolved information has been addressed, though is not considered in current modeling codes.^{8,9,57}

2.7 Conclusions

Spacecraft charging is a problem of ongoing concern in the spacecraft operations community. Its effects include almost-daily operational anomalies, and the complete failure of at least one entire spacecraft has been attributed to this phenomenon. Secondary electron emission, as evidenced by four decades of *in situ* observation and experimentation, plays an important role in the overall charge balance of operating spacecraft. Moreover, strong evidence suggests that this process actually drives spacecraft-to-plasma potentials in particularly severe charging environments at a variety of altitudes. The accuracy of

complex spacecraft charging models (e.g., NASA's NASCAP and NASCAP LEO codes), designed to predict charging levels, has been directly linked to accurate modeling of SE currents. The success of SE models, in turn, relies extensively upon experimentally determined SE yields and associated empirically derived SEE theoretical formulations. SEE is a complex process and SE yields vary considerably with a number of parameters, chief among them material, surface condition, and incident species, angle, and energy. In addition, backscattering characteristics of a given material have been shown to affect SEE.

Based on the above demonstrated need for data, the remainder of this thesis addresses the design, construction, and testing of an apparatus capable of performing secondary-emission and backscattering measurements on conducting materials.

CHAPTER 3

SPECIFICATION OF PARAMETERS, MEASUREMENTS, AND METHOD

Before the specifics of apparatus and technique can be addressed, there yet remains the task of detailing the experimental work in which the apparatus is to play a role. This chapter precisely defines experimental goals, reformulating in a rigorous fashion the broad questions originally posed in Chapter 1. Following a brief review of the physical scenario to be investigated (3.1) and description of experimental parameters (3.2), the quantities to be determined are specifically defined, a mathematical framework for each quantity is developed, and a measurement scheme for determining these quantities experimentally is presented (3.3).

3.1 General Description

This investigation seeks to characterize the populations of secondary electrons (SE's) and backscattered (BS) particles (electrons and ions) resulting from a beam of energetic particles incident on a surface—a scenario depicted schematically in Fig. 3-1. Specifically, total and differential secondary and backscattered yields are to be determined as functions of selected parameters. These parameters and their significance are now discussed in detail.

3.2 Experimental Parameters

An experimental parameter is defined as *a constant or variable term in a function that determines the specific form of the function, but not its general nature*. Parameters addressed in this investigation are associated with one of three principal entities: (i) the sample, (ii) the incident beam, or (iii) the scattered beam (SE and BS particle populations).

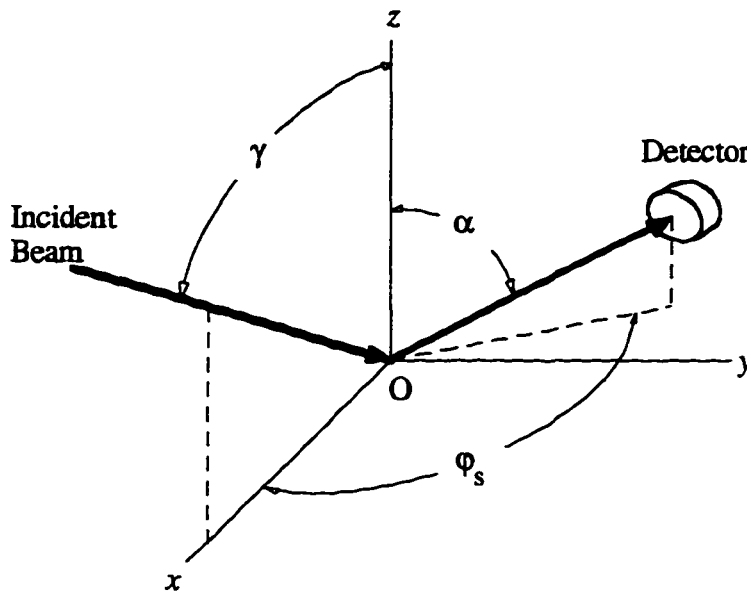


FIG. 3-1. Geometry of the incident and scattered beams.

These parameters are

- (a) material [m]
- (b) surface condition [sfc]
- (c) incident species [j]
- (d) incident particle (beam) energy [E_b]
- (e) incident angle [$\theta_i \equiv \gamma$]
- (f) scattering angle [$\theta_s \equiv \alpha$]
- (g) scattering energy [E_s]

The sample-related parameters m and sfc , as well as incident species, j , serve as fixed parameters for all measurements to be performed; i.e., total *and* differential yields (3.3). The incident beam parameters γ , and E_b act as additional fixed parameters for the various differential yields to be measured, but are varied as free parameters for total yield determinations. Finally, the scattered-beam parameters α and E_s are the variables parameterizing the assorted *differential* yields. Choices of the above parameters and their associated constraints were based on relevance to both spacecraft-charging and solid-state (surface

science) aspects of this research, as well as practical concerns such as cost and complexity of the required experimental apparatus. Discussions of each parameter and its relevance are now presented, and a summary of parameters is given in Table 3.1 at the end of this section.

3.2.1 *Sample-Related Parameters*

Experimentally, measurements will be performed *for a given sample*. Hidden within these measurements and results, then, will be the physical characteristics of the sample. Some of these characteristics, such as size, are more than likely irrelevant to the experimental results. Others of these characteristics, however, will prove highly relevant. Material and surface condition are two physical characteristics of the samples that will be actively ascertained and varied in this investigation.

(a) *Material*

Materials in the present investigation are currently restricted to conductors—a result of experimental technique limitations. Specifically, electrostatic charging of insulators under charged particle bombardment inhibits uniform SE and BS particle production and severely complicates the electric current measurements (3.3) required for accurate yield determination. Though a number of methods have been suggested that may enable future SE and BS particle characterization of insulators [see (8.3)], their increased complexity has kept this initial work focused on conductors.

Given the myriad number of as yet uncharacterized conducting materials employed in spacecraft construction (e.g., various types of coated aluminum),^{53,54} an apparatus and technique capable of determining SE and BS yield characteristics of conductors is of considerable value to the spacecraft charging community. In addition to the qualitative classifications *conductor* and *insulator*, *m* is in some sense quantified with the introduction of atomic number, *Z* (as has been done in a number of previous SE and BSE

investigations^{44,45,59,60-62}).

(b) Surface Condition

Surface condition in the context of this research refers to *contamination*; i.e., the presence and extent of contaminating surface films, such as oxide layers or hydrocarbons, on the bulk material. It remains a largely qualitative parameter, though may be quantified via the introduction of coverage ratios and film thicknesses. Surface *smoothness* is considered in this investigation only to the extent that all samples are given an initially smooth surface [see (6.1.2)], though it is quite likely an important surface characteristic with respect to SE and BS yields.

Surface contamination is particularly relevant to spacecraft charging studies in that operating spacecraft are clearly not maintained in a pristine environment.² “Clean” surfaces, therefore, are not generally accurate representations of spacecraft surfaces (though clean may be a valid condition for surfaces on the ram side of a spacecraft, where impacting ions may remove most contaminants). Illustrating this point, Fig. 3-2 is a photograph depicting the severe contamination of a surface which has spent nearly six years in low-earth orbit as part of NASA's Long duration Exposure Facility (LDEF). By the same token, samples used in SEM studies also undergo a certain level of contamination during preparation.⁶³ For these reasons, the instrument described in this thesis has been designed with the capability of determining SE and BS yields for surfaces in a clean state, as well as under (semi-) controlled levels of contamination.

3.2.2 Incident-Beam Parameters

(c-d) Incident Species and Energy

Incident particles in the present investigation are monoenergetic electrons and ions in the 0-50 keV energy range. Particular ion species to be employed have not been finally determined, but are likely to include H^+ , N_2^+ , and O_2^+ . Practical considerations such as

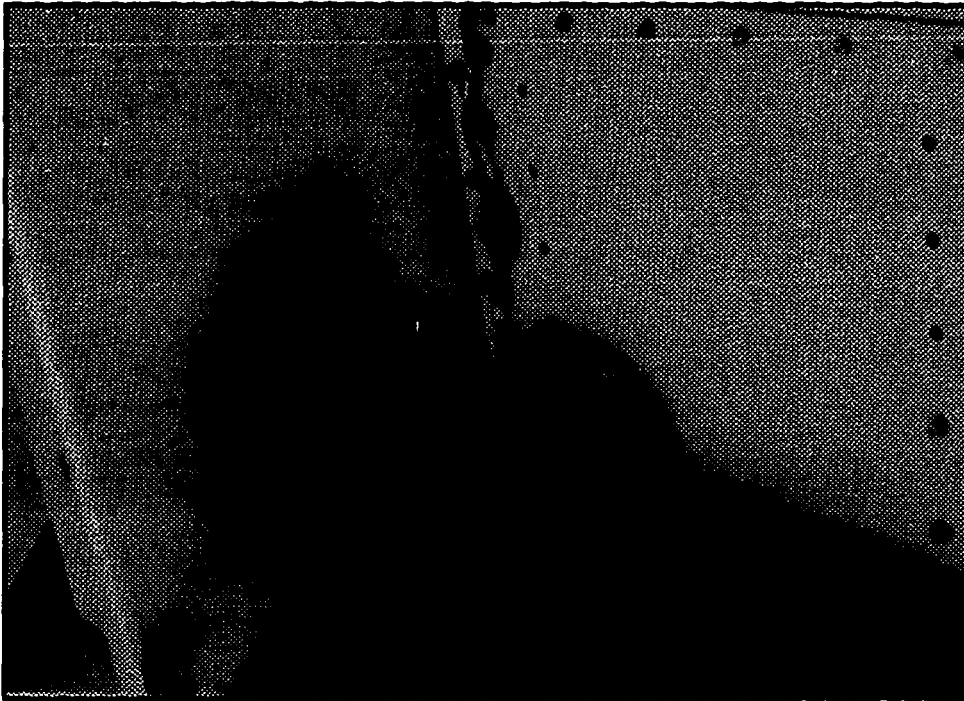


FIG. 3-2. Photograph of LDEF tray H-06 after nearly six years in low-Earth orbit. Dark regions are areas of extreme surface contamination, due primarily to the outgassing of nearby insulators.

availability and cost of electron and ion sources, and safety concerns involving increased x-ray production, preclude this research from pursuing higher energy domains (though SEE investigations at higher energies are certainly warranted).

Pertaining to the spacecraft charging problem, environmental work by Hardy *et al.* has demonstrated that a significant portion of the precipitating particle energy spectrum lies at or below 50 keV.^{37,38} Complementing this work, and perhaps more compelling, is work by Frooninckx indicating that incident electrons with energies 2-5 keV and ≥ 9.6 keV may actually drive severe spacecraft charging in a number of orbital environments.¹⁰ Moving away from spacecraft-charging applications, the 0-50 keV energy range is also relevant to low-energy SEM work,⁴⁵ ion scattering microscopy,⁶⁴ ion sputtering,⁶⁵ and other related surface science techniques.

(e) Incident Angle

Referring to Fig. 3-1, the incident angle γ refers to the angle formed by the velocity vector of the incident particles and the outward normal to the surface. The apparatus designed for this investigation does not permit arbitrary γ , but rather provides for a discontinuous variation in γ from 90° to $\sim 10^\circ$ [as a result of magnetic shielding design, discussed in (4.3.2)].

Previous investigations have clearly demonstrated SE and BS yields to be functions of γ .^{60,62,64} This fact has important implications for the spacecraft charging problem, in that orbiting spacecraft are subject to particle bombardment from all directions (though the presence of ambient and spacecraft-induced electric and magnetic fields often imposes preferred directions). Knowledge of SE and BS yield γ -dependence is therefore necessary to effectively model these terms.² Additionally, the γ -dependence of SE yield is what makes depth-of-field and topography information possible in SEM.⁴⁵ Even more fundamentally, SE and BS yield γ -dependences provide important clues as to underlying

physical processes involved in backscattering and SEE,⁶⁶ and empirical and analytic expressions for this dependence exist for a number of materials.^{50,58,67-72}

3.2.3 *Scattered-Beam parameters*

(f-g) Scattering Angle and Energy

Referring once again to Fig. 3-1, the scattering angle α is seen to be that angle formed by the scattered beam (or, more precisely, that portion of the scattered beam being investigated) and the local normal to the sample surface. Knowledge of the energy spectrum of secondary-emitted and backscattered electrons as a function of emitted angle α is an important aspect of SEE that remains largely uninvestigated. Though a number of angle-resolved and energy-resolved SE and BSE investigations have been accomplished separately,^{58,64,68,70-77} a continuing review of the literature has revealed that combination angle- *and* energy-resolved data is almost nonexistent.^{78,79} The addition of angle-energy-resolved measurements to this investigation therefore represents a unique capability and, upon completion, will constitute a significant contribution to the field. The apparatus described in Chapter 4 permits α -resolved measurements over the range $14^\circ < \alpha < 90^\circ$, with simultaneous energy-resolved measurements over the range $0 \text{ eV} < E_s < 3 \text{ keV}$.

The presence of ambient and spacecraft-induced electric and magnetic fields within the space environment make α and E_s relevant to a spacecraft's overall current balance. Figure 3-3 illustrates how the orientation of Earth's magnetic field relative to a spacecraft surface may cause escaping particles to return to the spacecraft; of real importance is not only the fact that the particle has left the surface, but with what velocity vector relative to the ambient magnetic field. Clearly, a departing particle must have some minimum velocity component perpendicular to \mathbf{B} in order to escape the spacecraft. Modelers must therefore be cognizant not only of overall numbers of charged particles leaving a spacecraft's surface, but also their direction and energy of departure. Additionally, such information

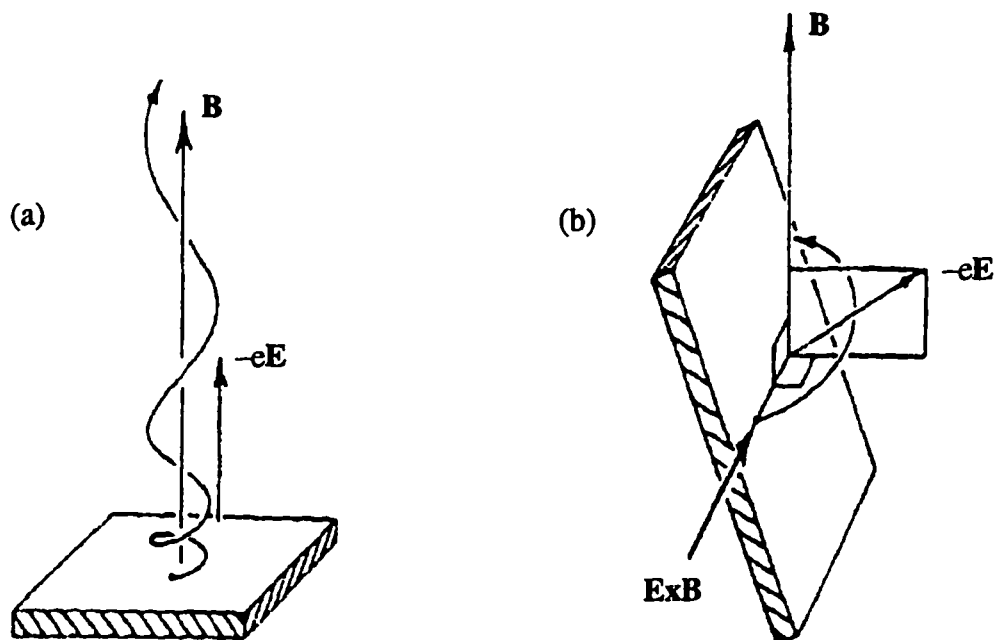


FIG. 3-3. Effect of departure (scattering) angle on the ability of a secondary or backscattered electron to escape the surface of a spacecraft subject to Earth's magnetic field (\mathbf{B}). In (a) the electron escapes the surface as the result of an electric force $-\mathbf{eE}$ parallel to \mathbf{B} . In (b) the electron returns to the surface as the result of a $\mathbf{v} \times \mathbf{B}$ force, and also is transported along the surface as the result of an $\mathbf{E} \times \mathbf{B}$ force (adapted from Ref. 56).

may prove crucial in understanding phenomena involving the transport of SE's across surfaces, such as snapover⁵⁴ and the breakdown of surface dielectrics,⁵⁵ or the transport of SE's within the plasma sheath.⁵³ The importance of such angle-energy-resolved information has been addressed elsewhere,² though is not considered in current modeling codes—due primarily to the lack of experimental values.^{2,54}

3.2.4 Summary

The experimental parameters discussed above are summarized in Table 3.1. For emphasis, it is once again noted that these parameters are by no means all-inclusive of those which could be relevant to SE and BSE investigations.

Having now discussed the quantities which will parameterize this investigation, attention is now turned to the various SE and BSE yields and a strategy for determining them experimentally.

Table 3.1. Experimental parameters.

Sample Parameters	Incident-Beam Parameters	Scattered-Beam Parameters
material [m] (conductors, classified by atomic number)	species [j] (electrons and ions)	energy [E_s] (0-50 keV)
surface condition [sfc] (smooth surface, clean or contaminated)	energy [E_b] (0-50 keV)	angle [α] (14°-90°, continuous)
	angle [γ] (0-90°, discontinuous)	

3.3 Quantities to be Determined, Measurements, and Method

Subject to the parameters and constraints discussed above, the purpose of this work has been to design, construct, and test an experimental apparatus and technique capable of determining four distinct types of quantities:

- (i) total SE and BS yields (3.3.1)
- (ii) angle-resolved (differential) SE and BS yields (3.3.2)
- (iii) energy resolved (differential) SE and BS yields (3.3.3), and
- (iv) simultaneous angle-energy-resolved (differential) SE and BS yields (3.3.4)

Each of these quantities is now precisely defined, and a general plan of attack for the experimental determination of each is presented.

3.3.1 Total SE and BS Yields, δ and η

(a) Definition

The total SE yield δ represents the total number of secondary electrons produced *per incident particle*

$$\delta \equiv \frac{\# \text{ secondary electrons}}{\# \text{ incident particles}} = \frac{n_{se}}{N} \quad (6)$$

Similarly, the total BS yield η represents the total number of backscattered particles (electrons in the case of incident electrons, and ions in the case of incident ions) per incident particle

$$\eta = \frac{n_{bs(e),(i)}}{N} \quad (7)$$

Note from Eqs. (6) and (7) that δ and η are truly dimensionless quantities, and are therefore often termed SE and BS *coefficients*. This work seeks to determine δ and η for a given material, surface condition, incident species, incident energy, and incident angle.

Hence, it is understood that these parameters are implicit within the nomenclature:

$$\begin{aligned}\delta &\equiv \delta(m, sfc, j, E_b, \gamma) \\ \eta &\equiv \eta(m, sfc, j, E_b, \gamma)\end{aligned}\tag{8}$$

[NOTE: To be excruciatingly pedantic, the terms *SE yield* and *BS yield* refer to a measurement of the *functions* $\delta(m, sfc, j, E_b, \gamma)$ and $\eta(m, sfc, j, E_b, \gamma)$ evaluated at particular values (or states) of the above parameters; i.e., $\delta \equiv \delta(m, sfc, j, E_b, \gamma) |_{m=m', sfc=sfc', j=j', E_b=E_b', \gamma=\gamma'}$ and $\eta \equiv \eta(m, sfc, j, E_b, \gamma) |_{m=m', sfc=sfc', j=j', E_b=E_b', \gamma=\gamma'}$]

Attention is now turned to a specific method for determining δ and η . Note that until now the discussion has remained general with respect to incident species. For the remainder of the chapter, however, it will prove convenient to address separately the cases of incident electrons and incident ions when discussing measurement schemes.

(b) Experimental Determination for an Incident Beam of Monoenergetic Electrons

Equations (6) and (7) make it clear that ultimately, the task of any apparatus built to determine δ and η is to *count* charged particles. This investigation, as with most previous SE and backscatter investigations, will measure electric current as a means of counting electrons and ions. Average electric current, I , is given by

$$I \equiv \frac{\Delta Q}{\Delta t} = \frac{Nq}{\Delta t}$$

for total charge Q , time t , number of particles N , and electric charge, q (of each particle). δ and η , then, may be determined by electric current measurements via

$$\begin{aligned}\delta &\equiv \frac{I_{se}}{I_b} = \frac{n_{se}}{N_b} \\ \eta_{(e)} &\equiv \frac{I_{bse}}{I_b} = \frac{n_{bse}}{N_b}\end{aligned}\tag{9}$$

for current due to secondary electrons (I_{se}), current due to backscattered electrons (I_{bse}), and current due to incident (beam) electrons (I_b) [where $\eta_{(e)}$ refers to the yield for back-scattered *electrons*]. The task of determining δ and η , then, becomes one of determining these three currents.

Figure 3-4(a) depicts the various currents to and from an electrically unbiased sample (i.e., a sample with an electric potential of 0 V relative to ground), resulting from an incident beam of energetic electrons. The incident primary electrons comprising I_b are assumed to be monoenergetic, supplied by an electron gun. The presence of the return current $I_{r(0)}$ reflects the fact that the sample is being bombarded with electrons within the confined volume of a vacuum chamber—a volume further reduced by the presence of magnetic shielding (4.3.2). Consequently, $I_{r(0)}$ represents the current due to SE's and BSE's that have left the sample, scattered off of the chamber's interior (creating additional SE's), and *returned* to the sample. Bombardment of the sample by these electrons (no longer monoenergetic) will clearly produce additional SE's and BSE's, accounted for in I_{ser} and I_{bser} , respectively. [NOTE: the subscript (0) on the $I_{r(0)}$ term denotes the sample potential, in volts, relative to ground.] Current due to secondary ions (SI's) is omitted in the figure due to the extreme unlikelihood of secondary ion production (a result of the enormous mass differential between the incident electrons and the atoms comprising the sample, the resulting inefficiency of momentum exchange between these two species, and the large binding energies of the sample atoms to the sample lattice).

Inspection of the figure yields an expression for the net current reaching the sample, $I_{s(0)}$, in the form of a current balance equation

$$I_{s(0)} = I_b - I_{se} - I_{bse} + I_{r(0)} - I_{ser} - I_{bser}$$

The assumption that I_{ser} and I_{bser} are small relative to the other quantities (a good assumption, addressed quantitatively in Appendix A) allows us to neglect these terms

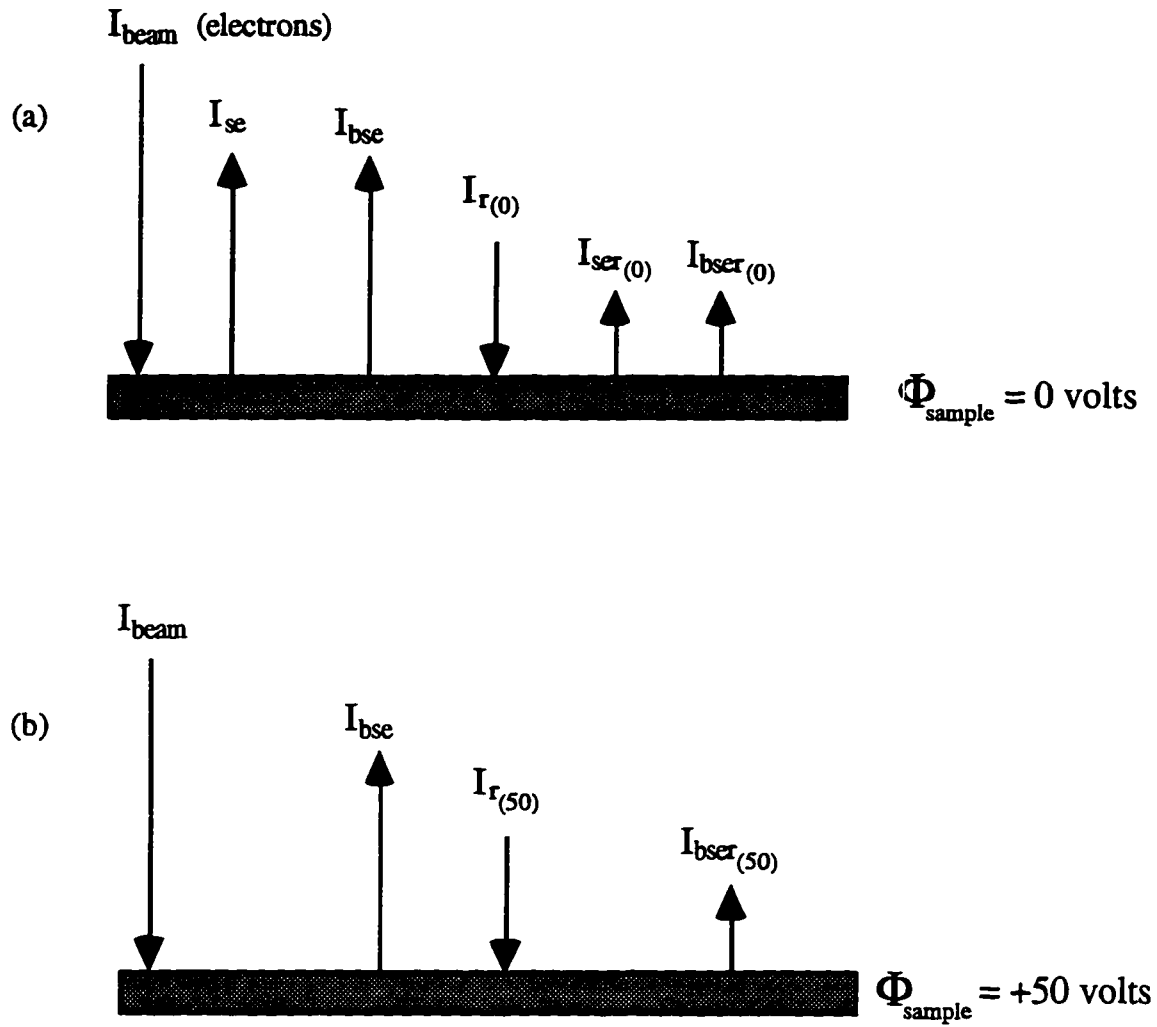


FIG. 3-4. Schematic depicting currents to and from (a) a neutrally biased and (b) a positively biased (+50 V) sample for an incident beam of (monoenergetic) electrons. Currents are due to the incident beam (I_{beam}), secondary electrons (I_{se}), backscattered electrons (I_{bse}), the return current ($I_{\text{r}(0)}$ and $I_{\text{r}(50)}$), secondary electrons produced by the return current (I_{ser}), and backscattered electrons produced by the return current ($I_{\text{bser}(0)}$ and $I_{\text{bser}(50)}$).

to obtain

$$I_{s(0)} = I_b - I_{se} - I_{bse} + I_{r(0)} \quad (10)$$

Recall that Eq. (9) has made determination of the currents I_{se} , I_{bse} , and I_b the goal. The technique used in this work calls for direct measurement of I_b , while I_{se} and I_{bse} are determined indirectly via measurements of other currents. Inspection of Eq. (10), however, reveals insufficient information to determine I_{se} and I_{bse} , even if $I_{r(0)}$ and $I_{s(0)}$ are known. Another relation between these quantities is obtained by biasing the sample to +50 V while leaving I_b unchanged. Figure 3-4(b) depicts the resulting currents to and from such a positively biased sample. Two significant changes should be noted. First, SEE is suppressed in that the SE's—whose energies *by definition* are less than 50 eV—are prevented from escaping the sample. Secondly, the return current to the sample is significantly increased, as all stray electrons within the chamber are now being *attracted* to the sample, giving $|I_{r(50)}| \gg |I_{r(0)}|$. (By contrast, the return current with the sample neutrally biased had been due to stray electrons striking the sample at random.)

The current balance equation

$$I_{s(50)} = I_b - I_{bse} + I_{r(50)} - I_{bser(50)}$$

is obtained from the figure, which becomes

$$I_{s(50)} = I_b - I_{bse} + I_{r(50)} \quad (11)$$

with the assumption $I_{bser(50)}$ small (again, a good assumption addressed quantitatively in Appendix A).

For directly measured quantities $I_{s(0)}$, $I_{s(50)}$, I_b , $I_{r(0)}$, and $I_{r(50)}$ (as described in Chapter 4), Eqs. (10) and (11) are solved for I_{se} and I_{bse} :

$$I_{se} = I_{s(50)} - I_{r(50)} - I_{s(0)} + I_{r(0)} \quad (12)$$

$$I_{bse} = I_b - I_{s(50)} + I_{r(50)} \quad (13)$$

which imply

$$\delta = \frac{I_{s(50)} - I_{r(50)} - I_{s(0)} + I_{r(0)}}{I_b} \quad (14)$$

and

$$\eta_{(e)} = \frac{I_b - I_{s(50)} + I_{r(50)}}{I_b} \quad (15)$$

Equations (14) and (15) represent the measurement scheme employed in this investigation for determination of the total SE and BSE yields δ and $\eta_{(e)}$.

[NOTE: The astute reader has no doubt recognized a flaw in the above scheme; specifically, the fact that electrons with energies less than 50 eV are not the only electrons prevented from leaving the sample when it is biased to +50 V. Electrons with energies *higher* than 50 eV, but with non-normal exit angles are also prevented from escaping—a fact easily understood when one realizes that the *normal component* (to the sample surface) of an electron's momentum vector is the pertinent quantity, rather than its *total* energy. Resulting errors introduced into the calculation of δ and η are addressed quantitatively in Appendix A.]

(c) *Experimental Determination for an Incident Beam of Monoenergetic Ions*

The case for incident ions is completely analogous to that for incident electrons. Figures 3-5 (a) and (b) depict the various significant currents to and from a sample at 0 V and +50 V, respectively, *under ion bombardment*. Note that a backscattered ion current, I_{bsi} , has replaced the I_{bse} term from Figs. 3-3. Also note that once again, any secondary ion current has been neglected. Even though the incident particles are now ions and should therefore transfer their momentum more efficiently to atoms than to electrons, the difference between the binding energies of the atoms locked within the sample lattice, and the work functions of the conduction band and valence electrons, conspires to produce considerably more SE's than SI's.

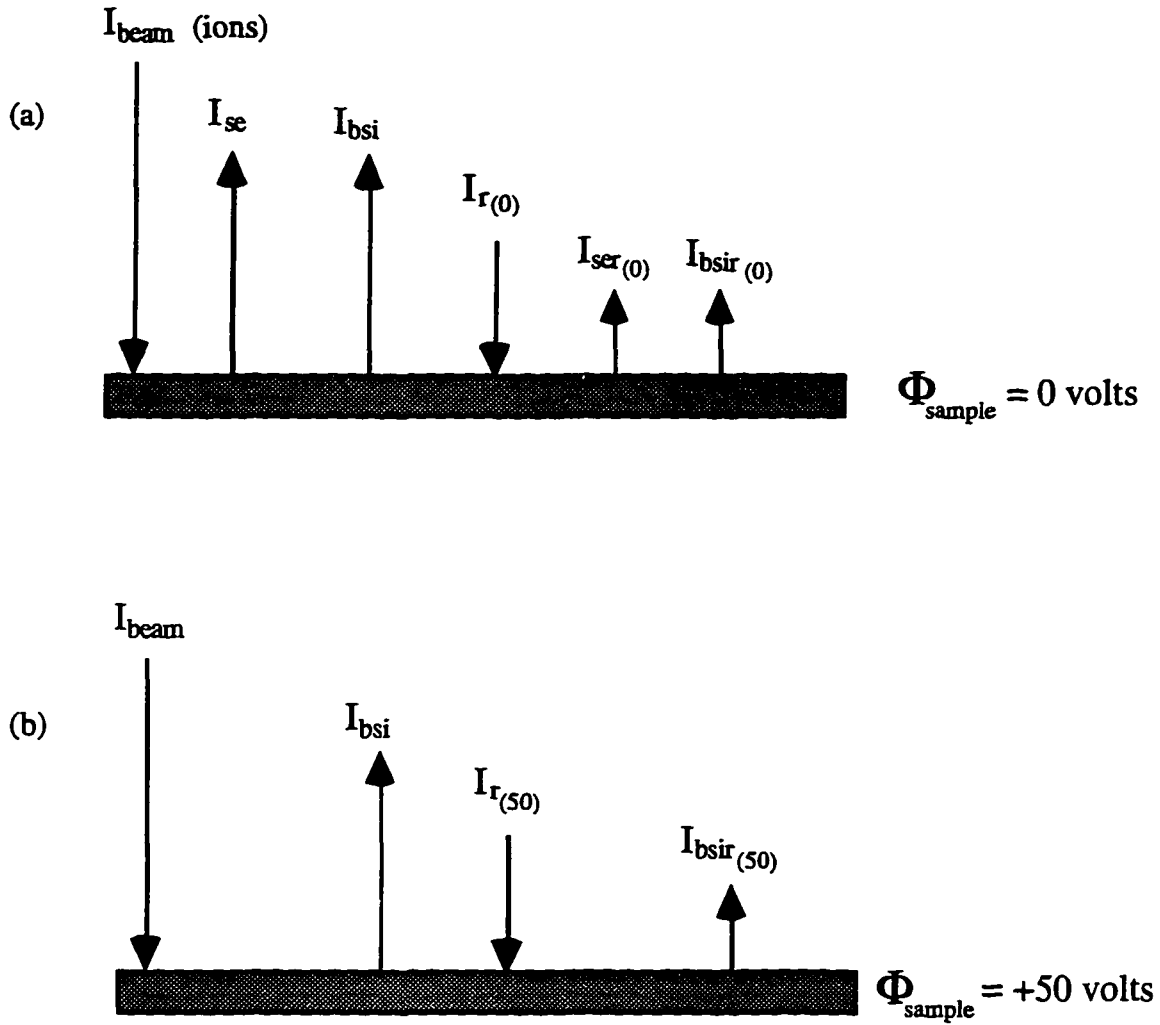


FIG. 3-5. Schematic depicting currents to and from (a) a neutrally biased and (b) a positively biased (+50 V) sample for an incident beam of (monoenergetic) ions. Currents are due to the incident beam (I_{beam}), secondary electrons (I_{se}), backscattered ions (I_{bsi}), the return current ($I_{\text{r(0)}}$ and $I_{\text{r(50)}}$), secondary electrons produced by the return current (I_{ser}), and backscattered ions produced by the return current ($I_{\text{bsir(0)}}$ and $I_{\text{bsir(50)}}$).

The current balance equations

$$I_{s(0)} = I_b + I_{se} - I_{bsi} + I_{r(0)} \quad (16)$$

$$I_{s(50)} = I_b - I_{bsi} + I_{r(50)} \quad (17)$$

are written from the figures, which lead to the relations

$$\delta = \frac{I_{se}}{I_b} = \frac{I_{s(0)} - I_{s(50)} + I_{r(50)} - I_{r(0)}}{I_b} \quad (18)$$

and

$$\eta_{(i)} = \frac{I_{bsi}}{I_b} = \frac{I_b - I_{s(50)} + I_{r(50)}}{I_b} \quad (19)$$

These relations are nearly identical to Eqs. (14) and (15); the differences in relative signs between some of the terms are, of course, due to the sign change of the charges on the incident particles. Also note that the signs of $I_{r(0)}$ and $I_{r(50)}$ relative to I_b may be positive or negative in the case of incident ions, since these currents are composed of both returning electrons and returning ions, and it is not immediately clear which of these terms will dominate.

3.3.2 Angle-Resolved (Differential) SE and BS

Yields, $\delta(\alpha)$ and $\eta(\alpha)$

(a) *Definition.*

Properly defining and understanding the angle-resolved yields $\delta(\alpha)$ and $\eta(\alpha)$ demands a bit more effort than that required for δ and η . Referring to Fig. 3-6 and restricting the discussion to SE's for the moment, it is seen that the total number of SE's, n_{se} , produced at the origin O must pass through the depicted hemispherical surface. The number of SE's emitted at a given α and φ_s is obtained by counting the fraction of SE's, dn_{se} , passing through the area element dA , subtending the solid angle $d\Omega_s$. Defining $\rho_{se}(\alpha, \varphi_s)$ to be the number of SE's emitted per unit solid angle, measured in steradians, and for a given α and φ_s , we have

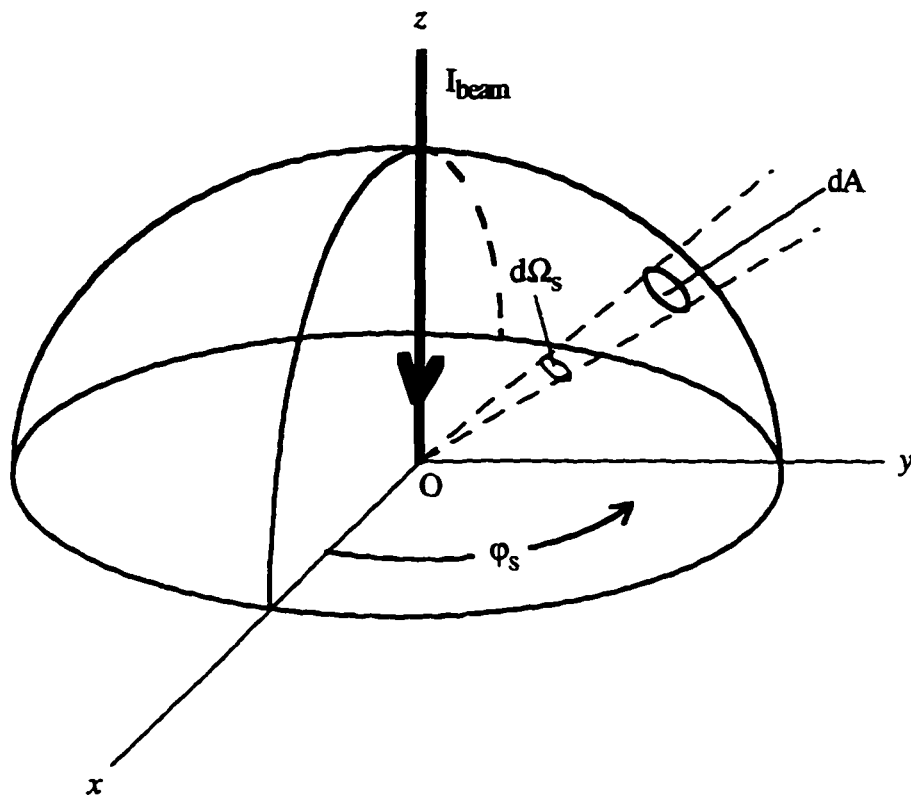


FIG. 3-6. Schematic depicting angle-resolved SE and BSE detection: SE's and BSE's leave the sample within the small solid angle $d\Omega_s$ pass through the area element dA in the dome and are counted.

$$dn_{se}(\alpha, \varphi_s) = \rho_{se}(\alpha, \varphi_s) d\Omega_s \quad (20)$$

Clearly $\rho_{se}(\alpha, \varphi_s)$ will be proportional to the total number of particles incident at O. That is, $\rho_{se}(\alpha, \varphi_s) = N\delta(\alpha, \varphi_s)$, where $\delta(\alpha, \varphi_s)$ represents the constant of proportionality for a given α and φ_s . This implies

$$\delta(\alpha, \varphi_s) = \frac{\rho_{se}(\alpha, \varphi_s)}{N}$$

If the angular distribution of SE's is now assumed to be azimuthally symmetric—i.e., if n_{se} is independent of φ_s —then

$$\delta(\alpha) = \frac{\rho_{se}(\alpha)}{N}$$

and $\delta(\alpha)$ is seen to be the number of SE's emitted per incident particle per unit solid angle, at a given scattering angle α . Clearly then, $\delta(\alpha)$ represents some sort of SE yield (hence the suggestive notation). Replacing $\rho_{se}(\alpha)$ with $N\delta(\alpha)$ in Eq. (20) gives

$$dn_{se}(\alpha) = N\delta(\alpha) d\Omega_s \quad (21)$$

or

$$\delta(\alpha) \equiv \frac{1}{N} \frac{dn_{se}(\alpha)}{d\Omega_s} \quad (22)$$

where (22) is the defining equation for the standard differential scattering cross section.⁸⁰ The units of $\delta(\alpha)$ [sr^{-1}], however, are not those of a differential cross section (because N is not a flux, but a pure number). Rather, $\delta(\alpha)$ has the dimensions of a *differential yield*. Hence, the function $\delta(\alpha)$, evaluated about a particular scattering angle, represents a *differential SE yield (coefficient)*.

The preceding argument can be repeated for BS particles produced at O, leading to the relations

$$dn_{bs}(\alpha) = N\eta(\alpha) d\Omega_s \quad (23)$$

and

$$\eta(\alpha) \equiv \frac{1}{N} \frac{dn_{bs}(\alpha)}{d\Omega_s} \quad (24)$$

for the *differential BS yield*, $\eta(\alpha)$.

Referring to Eqs. (21) and (23), note that the *total* SE and BS yields δ and η can be calculated, via sum rules, if one has knowledge of the differential yields $\delta(\alpha)$ and $\eta(\alpha)$ over a full range of angles:

$$\delta = \frac{n_{se}}{N} = \int_{\text{half-sphere}} \delta(\alpha) d\Omega_s = \int_0^{2\pi} \int_0^{\pi/2} \delta(\alpha) \sin \alpha d\alpha d\varphi_s = 2\pi \int_0^{\pi/2} \delta(\alpha) \sin \alpha d\alpha \quad (25)$$

$$\eta = \frac{n_{bse}}{N} = \int_{\text{half-sphere}} \eta(\alpha) d\Omega_s = \int_0^{2\pi} \int_0^{\pi/2} \eta(\alpha) \sin \alpha d\alpha d\varphi_s = 2\pi \int_0^{\pi/2} \eta(\alpha) \sin \alpha d\alpha \quad (26)$$

The apparatus and technique described in this thesis provide a means of determining the functional forms of $\delta(\alpha)$ and $\eta(\alpha)$ by determining experimentally their values for a sufficient number of scattering angles. That is, given $\delta(\alpha) |_{\alpha'}$ (read “ $\delta(\alpha)$ evaluated at α' ”) and $\eta(\alpha) |_{\alpha'}$ for a sufficient number of scattering angles, it should be possible to construct the functions $\delta(\alpha)$ and $\eta(\alpha)$ empirically. Done correctly, the resulting total yields calculated in Eqs. (25) and (26) should agree with those determined directly, as described in (3.3.1). Conversely, given the total yields δ and η , it should be possible to infer the numbers of SE's and BS particles being emitted in various angular ranges inaccessible to measurement [see (4.7)].

(b) Experimental Determination for an Incident Beam of Monoenergetic Electrons

Analogous to total δ and η determination, various electric current measurements are used to determine $\delta(\alpha) |_{\alpha'}$ and $\eta(\alpha) |_{\alpha'}$. Figure 3-7 is a schematic representing a detector placed to intercept SE's and BSE's passing through the differential area element dA of Fig. 3-6; $d\Omega_s$ therefore represents the *field-of-view of the detector*. Restricting the discussion to

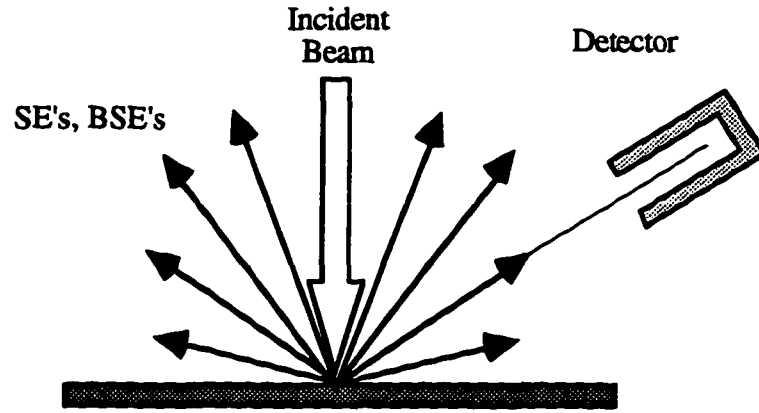


FIG. 3-7. Schematic depicting angle-resolved detection of SE's and BSE's.

SE's for the moment, the current dI_{se} registered by the detector due to SE's emitted at a particular scattering angle α is given by

$$dI_{se}(\alpha) = \frac{dn_{se}(\alpha) \cdot q}{dt} = \frac{Nq\delta(\alpha)d\Omega_s}{dt}$$

which implies

$$\frac{dI_{se}(\alpha)}{I_b} = \delta(\alpha)d\Omega_s$$

or

$$\delta(\alpha) = \frac{1}{I_b} \frac{dI_{se}(\alpha)}{d\Omega_s}. \quad (27)$$

For the detector placed at a *specific* scattering angle, α' , the differential yield $\delta(\alpha)$ at α' is then determined via

$$\delta(\alpha)|_{\alpha'} = \frac{1}{I_b} \left. \frac{dI_{se}(\alpha)}{d\Omega_s} \right|_{\alpha'} \quad (28)$$

and the task becomes one of measuring $dI_{se}(\alpha)|_{\alpha'}$ —the SE current about the scattering angle α' .

Referring to Figure 3-8(a), note that the detector current $I_{d(0)}$ for an electrically unbiased detector is given by

$$I_{d(0)}(\alpha) = dI_{se}(\alpha) + dI_{bse}(\alpha) \quad (29)$$

Biasing the detector to -50 V, however, prevents the SE's from being collected and the detector current $I_{d(-50)}$ is then

$$I_{d(-50)}(\alpha) = dI_{bse}(\alpha) \quad (30)$$

Equations (29) and (30) can be combined to yield

$$dI_{se}(\alpha) = I_{d(0)}(\alpha) - I_{d(-50)}(\alpha) \quad (31)$$

and finally obtain, from (28),

$$\delta(\alpha) \Big|_{\alpha'} = \frac{1}{I_b} \left[\frac{I_{d(0)}(\alpha) \Big|_{\alpha'} - I_{d(-50)}(\alpha) \Big|_{\alpha'}}{d\Omega_s} \right] \quad (32)$$

Following a similar development for $\eta(\alpha)$, one is lead to the relation

$$\eta_{(e)}(\alpha) \Big|_{\alpha'} = \frac{1}{I_b} \frac{I_{d(-50)}(\alpha) \Big|_{\alpha'}}{d\Omega_s} \quad (33)$$

For the directly measured currents $I_{d(0)}$, $I_{d(-50)}$, and I_b , and for the known detector field-of-view (FOV) $d\Omega_s$, Eqs. (32) and (33) illustrate how the differential yields $\delta(\alpha)$ and $\eta_{(e)}(\alpha)$ will be experimentally determined in this investigation.

(c) Experimental Determination for an Incident Beam of Monoenergetic Ions

Figure 3-8(b) is a schematic representing the current reaching the detector in the case of an ion beam incident on the sample. In this case, it is seen that

$$I_{d(0)} = dI_{bsi} - dI_{se} \quad (34)$$

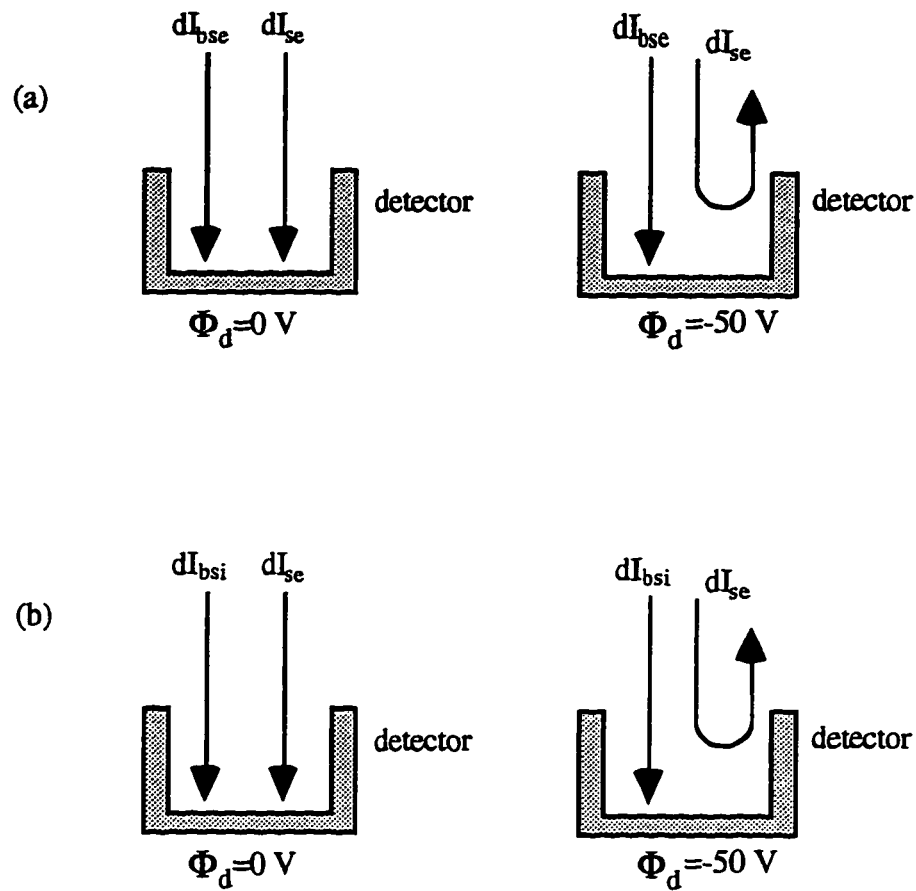


FIG. 3-8. Determination of angle-resolved SE yield via negative detector biasing for the cases of (a) incident electrons and (b) incident ions.

where the minus sign is a result of the opposite charge carried by ions and electrons.

Biasing the detector to -50 V will once again eliminate the SE current and leave the BSI current unaffected *assuming the detector is properly shielded from the BSI population at large*. One is then led to the relations

$$\delta(\alpha)|_{\alpha'} = \frac{1}{I_b} \left[\frac{I_{d(-50)}(\alpha)|_{\alpha'} - I_{d(0)}(\alpha)|_{\alpha'}}{d\Omega_s} \right] \quad (35)$$

$$\eta_{(i)}(\alpha)|_{\alpha'} = \frac{1}{I_b} \frac{I_{d(-50)}(\alpha)|_{\alpha'}}{d\Omega_s} \quad (36)$$

in the same fashion that produced Eqs. (32) and (33).

3.3.3 *Energy-Resolved (Differential) SE and BS Yields, $\delta(E_s)$ and $\eta(E_s)$*

(a) *Definition*

The energy-resolved coefficients $\delta(E_s)$ and $\eta(E_s)$ are completely analogous to the angle-resolved differential coefficients $\delta(\alpha)$ and $\eta(\alpha)$; consequently, the development presented in this section will closely parallel that of (3.3.2).

The quantities $\delta(E_s)$ and $\eta(E_s)$ represent, respectively, the total numbers of SE's and BS particles per incident particle, *per unit energy*, measured in eV. These quantities, then, characterize the energy spectrums of the SE and BS particle populations (or, more accurately, the spectrums of δ and η). Referring to Fig. 3-9 and once again restricting the discussion to SE's for the time being, one can imagine a dome placed over the sample which counts n_{se} , the total number of SE's emitted at all angles from the origin O. One can further imagine a dome which counts only that fraction of SE's, $dn_{se}(E_s)$, whose energy falls within a certain small energy range dE_s , where dE_s lies between 0 eV and 50 eV. Analogous to Eq. (21), we postulate dn_{se} to be proportional to the number of incident

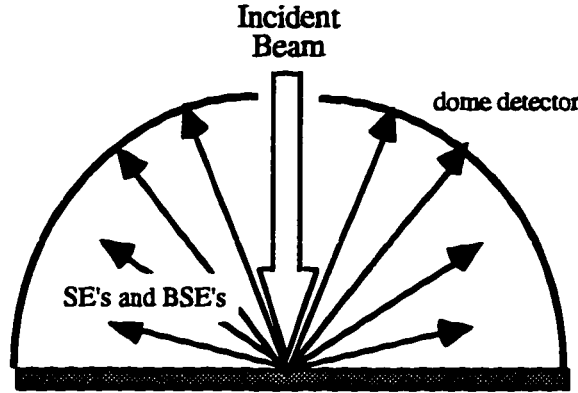


FIG. 3-9. Concept of energy-resolved SE yield determination via a dome detector that senses only electrons of a certain energy.

particles N , and the constant of proportionality (for a given E_s) to be the object $\delta(E_s)$:

$$dn_{se}(E_s) = N\delta(E_s)dE_s$$

or

$$\delta(E_s) = \frac{1}{N} \frac{dn_{se}(E_s)}{dE_s} \quad (0 < dE_s \leq 50 \text{ eV}) \quad (37)$$

Hence it is seen that the function $\delta(E_s)$, evaluated about a particular scattering energy, represents a differential SE yield, this time energy resolved, analogous to $\delta(\alpha)$.

Expanding the discussion now to include BS particles, we have

$$dn_{bs}(E_s) = N\eta(E_s)dE_s$$

or

$$\eta(E_s) = \frac{1}{N} \frac{dn_{bs}(E_s)}{dE_s} \quad (50 \text{ eV} < dE_s \leq E_b) \quad (38)$$

where $50 \text{ eV} < dE_s \leq E_b$.

As an energy analog to Eqs. (25) and (26), calculation of the total SE and BS yields δ and η is possible given knowledge of the energy-resolved yields $\delta(E_s)$ and $\eta(E_s)$ over a full range of energies:

$$\delta = \frac{n_{se}}{N} = \int_0^{50\text{eV}} \delta(E_s) dE_s \quad (39)$$

$$\eta = \frac{n_{bse}}{N} = \int_{50\text{eV}}^{E_b} \eta(E_s) dE_s \quad (40)$$

The apparatus described in Chapter 4 does not allow for direct determination of $\eta(E_s)$, though indirect characterization of the BS spectrum should be possible [see (3.3.4)]. Measurements allowing for the direct determination of $\delta(E_s)$, however, are possible. Completely analogous to the case for $\delta(\alpha)$, this apparatus will enable determination of the functional form of $\delta(E_s)$ by empirical construction, based on experimental determination of its value about a sufficient number of scattering energies. Done correctly, the resulting total yield calculated in Eq. (39) should agree with δ as determined by the method described in (3.3.1).

(b) Experimental Determination for an Incident Beam of Monoenergetic Electrons

Determination of $\delta(E_s)$ is achieved via measurement (once again) of various electric currents to and from the sample. In effect, the sample itself is treated as the imaginary dome detector of Fig. 3-9. The same general measurement technique is employed as was used for the determination of the total SE yield δ [see (3.3.1b)]. In the case of $\delta(E_s)$, however, measurements are not taken for the sample biased only to 0 V and +50 V; rather, a series of current measurements are taken as the sample is biased from 0 V to +50 V *incrementally*.

Figure 3-10 illustrates the significant currents to and from (a) an unbiased sample, and (b) the same sample biased to some *positive* potential ϕ , where $0 < \phi \leq 50$ V. As expected, SE's of all energies (0-50 eV) produced on the surface are uninhibited by the unbiased sample in their departure, and the current due to these SE's is represented by

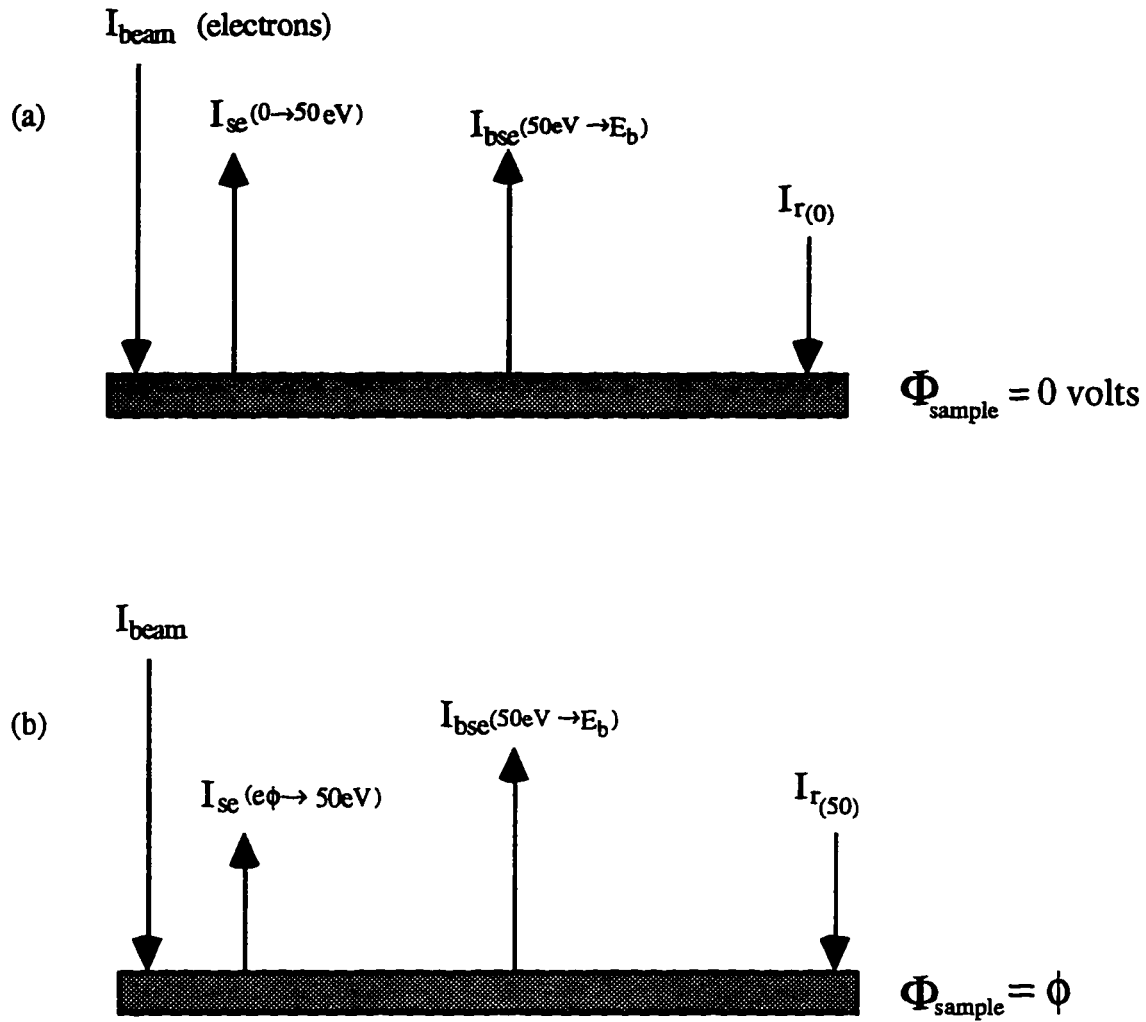


FIG. 3-10. Schematic illustrating major currents to and from a sample (a) neutrally biased and (b) *positively* biased to some potential ϕ , where $0 < \phi \leq 50$ V.

$I_{se}(E=0 \rightarrow 50\text{eV})$. Recalling the defining equation for electric potential energy, $U = q\Phi$, it is seen that an electron ($q = -e$) successfully departing a surface held at constant (positive) potential $\Phi_s = \phi$ must have a kinetic (scattering) energy E_s of at least $E_s = e\phi$. The current due to these SE's is therefore represented by $I_{se}(E_s=E \rightarrow 50\text{eV})$. If it is now assumed that ϕ is only slightly higher than zero (ground) potential, i.e., $\phi \rightarrow d\phi$, then the current dI_{se} due to SE's with energies $0 < E_s \leq 50\text{ eV}$ is given by

$$dI_{se}(E_s) = \frac{dn_{se}(E_s) \cdot q}{dt} = \frac{Nq\delta(E_s)dE_s}{dt},$$

where dE_s is viewed as the energy resolution of the detector. This implies

$$\frac{dI_{se}(E_s)}{I_b} = \delta(E_s)dE_s$$

or

$$\delta(E_s) = \frac{1}{I_b} \frac{dI_{se}(E_s)}{dE_s}. \quad (41)$$

Recognizing that in the laboratory the energy resolution is indeed finite, i.e., $dE_s \rightarrow \Delta E_s$, define

$$E'_s \equiv \frac{1}{2}(E_s + \Delta E_s) \quad (42)$$

to be the energy about which a measurement is made. Hence, the differential yield $\delta(E_s)$ evaluated for a particular scattering energy E'_s is given by

$$\delta(E_s) \Big|_{E'_s} = \frac{1}{I_b} \frac{dI_{se}(E_s) \Big|_{E'_s}}{dE_s} \quad (43)$$

and the task becomes one of measuring $dI_{se}(E_s) \Big|_{E'_s}$ —the SE current about the scattering energy E'_s .

Referring once again to Fig. 3-10 and defining I_d as the sum of the SE and BSE

currents (i.e., the current due to all electrons leaving the surface),

$$I_d \equiv I_{se} + I_{bse} \quad (44)$$

the following relations are obtained for the net sample currents for sample biases of 0 and ϕ , respectively, where $|\phi| \leq 50V$:

$$\begin{aligned} I_{s(0)} &= I_b - I_{se}(E_s=0 \rightarrow 50eV) - I_{bse}(E_s=50eV \rightarrow E_b) + I_{r(0)} \\ &\approx I_b - I_d(E_s=0 \rightarrow E_b) + I_{r(0)} \end{aligned} \quad (45)$$

$$\begin{aligned} I_{s(\phi)} &= I_b - I_{se}(E_s=E \rightarrow 50eV) - I_{bse}(E_s=50eV \rightarrow E_b) + I_{r(\phi)} \\ &\approx I_b - I_d(E_s=E \rightarrow E_b) + I_{r(\phi)} \end{aligned} \quad (46)$$

The various I_d (due to various sample potentials Φ_s) are termed *integrated currents*, in that they represent the current due to all electrons leaving the surface *at and above* a specified energy (determined by Φ_s). Clearly, the current due to SE's with energies between zero and E is given by the difference of the two SE currents of Eqs. (45) and (46):

$$I_{se}(E_s=0 \rightarrow E) = I_{s(\phi)} - I_{s(0)} + I_{r(\phi)} - I_{r(0)} \quad (47)$$

Note that the BSE current has been eliminated, determining $I_{se}(E_s=0 \rightarrow E)$ in terms of the sample and return currents, which are measured directly (4.6). More generally, for measured sample currents $I_{s(\phi_1)}$ and $I_{s(\phi_2)}$, where $0 < \phi_1 < \phi_2 \leq 50 V$ and $\Delta E_s \equiv e(\phi_2 - \phi_1)$, it is seen that

$$\begin{aligned} I_{se}(E_s=E_1 \rightarrow E_2) &= I_{s(\phi_2)} - I_{s(\phi_1)} + I_{r(\phi_1)} - I_{r(\phi_2)} \\ &\equiv I_{se}(\Delta E_s) \end{aligned} \quad (48)$$

In the limit ΔE_s becomes small, it is seen that $I_{se}(\Delta E_s) \rightarrow dI_{se}(E_s) \big|_{E_s'}$, for E_s' given by Eq. (42). Hence, from (43),

$$\delta(E_s) \bigg|_{E_s'} = \frac{1}{I_b} \frac{I_{s(\phi_2)} - I_{s(\phi_1)} + I_{r(\phi_1)} - I_{r(\phi_2)}}{dE_s} \quad (49)$$

The difficulty in obtaining $\eta(E_s)$ via the above measurement scheme is now clear;

increasing the sample potential affects the effective impacting energy of the incident particles (decreasing E_b in the case of incident electrons, and increasing E_b in the case of incident ions). This is not a significant effect for $\delta(E_s)$ determination in that the sample need only be biased to a maximum of +50 V; since the minimum beam energy being considered in this study is 1.0 keV, 50 V amounts to a 5% change in E_b at worst, and should have little effect on $\delta(E_s)$. Characterizing the energy spectrum of BS particles in this manner, however, would require the sample to be biased up to E_b —significantly altering the impacting energy of the incident particles and negating E_b as a controlled parameter.

(c) *Experimental Determination for an Incident Beam of Monoenergetic Ions*

Gratefully, the only changes for the case of impacting ions are the relative signs of the sample currents. Consequently, one is lead to the expression

$$\delta(E_s) \Big|_{E_s} = \frac{1}{I_b} \frac{I_{s(\phi_2)} - I_{s(\phi_1)} + I_{r(\phi_1)} - I_{r(\phi_2)}}{dE_s} \quad (50)$$

via precisely the same path that produced (49).

3.3.4 *Combination Angle-Energy-Resolved (Differential) SE and BS Yields, $\delta(\alpha, E_s)$ and $\eta(\alpha, E_s)$*

(a) *Definition*

Combining the discussions of (3.3.2) and (3.3.3), it should be readily accepted that the angle-energy-resolved SE coefficients $\delta(\alpha, E_s)$ and $\eta(\alpha, E_s)$ represent, respectively, the number of SE's and BSE's emitted per incident particle, at a given scattering angle, and with a given scattering energy. That is, these coefficients serve to characterize the angular dependence of the SE and BS energy spectrums.

Following the development of Eqs. (22) and (37), and (24) and (38), the

expressions

$$\delta(\alpha, E_s) \equiv \frac{1}{N} \frac{d^2 n_{se}(\alpha, E_s)}{d\Omega_s dE_s} = \frac{1}{N} \frac{d^2 n_{se}(\alpha, E_s)}{dE_s d\Omega_s} \quad (51)$$

$$\eta(\alpha, E_s) \equiv \frac{1}{N} \frac{d^2 n_{bse}(\alpha, E_s)}{d\Omega_s dE_s} = \frac{1}{N} \frac{d^2 n_{bse}(\alpha, E_s)}{dE_s d\Omega_s} \quad (52)$$

are obtained, which readily yield the following relations (sum rules):

$$\delta(\alpha) = \int_0^{50\text{eV}} \delta(\alpha, E_s) dE_s \quad (53)$$

$$\delta(E_s) = \int_{\text{half-sphere}} \delta(\alpha, E_s) d\Omega_s = 2\pi \int_0^{\pi/2} \delta(\alpha, E_s) \sin \alpha d\alpha \quad (54)$$

$$\delta = \int_0^{50\text{eV}} \int_{\text{half-sphere}} \delta(\alpha, E_s) d\Omega_s dE_s = 2\pi \int_0^{50\text{eV}} \int_0^{\pi/2} \delta(\alpha, E_s) \sin \alpha d\alpha dE_s \quad (55)$$

$$\eta(\alpha) = \int_{50\text{eV}}^{E_b} \delta(\alpha, E_s) dE_s \quad (56)$$

$$\eta(E_s) = \int_{\text{half-sphere}} \eta(\alpha, E_s) d\Omega_s = 2\pi \int_0^{\pi/2} \eta(\alpha, E_s) \sin \alpha d\alpha \quad (57)$$

$$\eta = \int_{50\text{eV}}^{E_b} \int_{\text{half-sphere}} \eta(\alpha, E_s) d\Omega_s dE_s = 2\pi \int_{50\text{eV}}^{E_b} \int_0^{\pi/2} \eta(\alpha, E_s) \sin \alpha d\alpha dE_s \quad (58)$$

Paralleling the development of the angle- and energy-resolved yields, the apparatus described in Chapter 4 enables determination of the functional forms of $\delta(\alpha, E_s)$ and $\eta(\alpha, E_s)$ by measuring their values experimentally about a sufficient number of scattering angles and energies. That is, given $\delta(\alpha, E_s) \big|_{\alpha, E_s}$ and $\eta(\alpha, E_s) \big|_{\alpha, E_s}$ over full range of angles and energies, it should be possible to construct the *functions* $\delta(\alpha, E_s)$ and $\eta(\alpha, E_s)$

empirically such that the relations above are satisfied. The calculated quantities δ , η , $\delta(\alpha)$, $\eta(\alpha)$, and $\delta(E_s)$ from Eqs. (53)-(58) can be compared with those determined experimentally *a la* (3.3.1)-(3.3.3). Such comparisons will serve to verify some measurements, as well as provide a means to infer other quantities precluded from measurement due to limitations of the apparatus and technique. An extreme example is presented by $\eta(E_s)$; unable to determine $\eta(E_s)$ experimentally as the result of an ill-suited measurement scheme, Eq. (57) provides an alternate means of characterizing the BS spectrum.

(b) Experimental Determination for an Incident Beam of Monoenergetic Electrons

Just as $\delta(E_s)$ characterizes the spectrum of the total SE yield δ , $\delta(\alpha, E_s)$ characterizes the spectrum of the angle-resolved yield $\delta(\alpha)$. Hence, just as the measurement scheme for $\delta(E_s)$ presented in (3.3.3b) was a variant on that used for δ , so to is the scheme for $\delta(\alpha, E_s)$ an analogous variant on that used for $\delta(\alpha)$, presented in (3.3.2b).

Returning to Fig. 3-7, recall that the detector collects only those electrons emitted within a given solid angle, $d\Omega_s$. Once again restricting the discussion to SE's for convenience, one can now imagine that in addition, the detector collects only those electrons within a given energy range dE_s ($0 < E_s \leq 50\text{eV}$). Then the current $d^2I_{se}(\alpha, E_s)$ registered by the detector is due to SE's leaving the sample at a given angle, and with a given energy:

$$d^2I_{se}(\alpha, E_s) = \frac{d^2n_{se}(\alpha, E_s) \cdot q}{dt} = \frac{qN\delta(\alpha, E_s)d\Omega_s dE_s}{dt}$$

Introduction of the beam current leads to

$$\delta(\alpha, E_s) = \frac{1}{I_b} \frac{d^2I_{se}(\alpha, E_s)}{d\Omega_s dE_s}$$

or, for specific values of α and E_s ,

$$\delta(\alpha, E_s) \Big|_{\alpha', E_i} = \frac{1}{I_b} \frac{d^2 I_{se}(\alpha, E_s) \Big|_{\alpha', E_i}}{d\Omega_s dE_s} \quad (E_s \leq 50V) \quad (59)$$

A similar development can be accomplished for BSE's by adjusting E_s such that $50eV < E_s \leq E_b$. One is then lead to the relation

$$\eta_{(e)}(\alpha, E_s) \Big|_{\alpha', E_i} = \frac{1}{I_b} \frac{d^2 I_{bse}(\alpha, E_s) \Big|_{\alpha', E_i}}{d\Omega_s dE_s} \quad (E_s > 50V) \quad (60)$$

The task, then, is the experimental determination of $d^2 I_{se}(\alpha, E_s) \Big|_{\alpha', E_i}$ and $d^2 I_{bse}(\alpha, E_s) \Big|_{\alpha', E_i}$.

Returning to the detector of (3.3.2a) and Fig. 3-7, Fig. 3-11 depicts the currents to (a) a *negatively* biased detector, and (b) a *more negatively* biased detector, where $0 < |\phi_1| < |\phi_2| \leq E_b$. The negative detector bias accomplishes the same objective as did the positive sample bias in Fig. 3-10; in this case, however, the detector is not the sample, and the electrons therefore are not leaving the detector, but being collected by it. Following Eq. (29), the current reaching the detector in each case is seen from the figure to be

$$I_{d(\phi_1)}(\alpha) = dI_{se}(\alpha, E_s=E_1 \rightarrow 50eV) + dI_{bse}(\alpha, E_s=50eV \rightarrow E_b) \quad (|\phi| \leq 50V) \\ = dI_d(\alpha, E_s=E_1 \rightarrow E_b)$$

$$I_{d(\phi_2)}(\alpha) = dI_{se}(\alpha, E_s=E_2 \rightarrow 50eV) + dI_{bse}(\alpha, E_s=50eV \rightarrow E_b) \quad (|\phi| \leq 50V) \\ = dI_d(\alpha, E_s=E_2 \rightarrow E_b)$$

or

$$I_{d(\phi_1)}(\alpha) = I_{bse}(\alpha, E_s=E_1 \rightarrow E_b) \quad (|\phi| > 50V) \\ = dI_d(\alpha, E_s=E_1 \rightarrow E_b)$$

$$I_{d(\phi_2)}(\alpha) = I_{bse}(\alpha, E_s=E_2 \rightarrow E_b) \quad (|\phi| > 50V) \\ = dI_d(\alpha, E_s=E_2 \rightarrow E_b)$$

where these are, as the notation suggests, already angle-resolved currents. It is also seen that the *detector* current is identically the *integrated* current introduced in the previous section. The addition of energy resolution is achieved by differencing $I_{d(\phi_1)}$ and $I_{d(\phi_2)}$, to

obtain

$$\begin{aligned}
 I_{d(\phi_1)} - I_{d(\phi_2)} &= dI_d(E_s=E_1 \rightarrow E_b) - dI_d(E_s=E_2 \rightarrow E_b) \\
 &= dI_{se}(E_s=E_1 \rightarrow 50\text{eV}) - dI_{se}(E_s=E_2 \rightarrow 50\text{eV}) \\
 &\equiv dI_{se}(E_s=E_1 \rightarrow E_2) \quad (|\phi| \leq 50\text{V}) \\
 &= dI_{bse}(E_s=E_1 \rightarrow E_b) - dI_{bse}(E_s=E_2 \rightarrow E_b) \\
 &\equiv dI_{bse}(E_s=E_1 \rightarrow E_2) \quad (|\phi| > 50\text{V})
 \end{aligned}$$

In the limit where $\Delta\phi=\phi_1-\phi_2$ becomes small, $dI_{se}(E_s=E_1 \rightarrow E_2) \rightarrow d^2I_{se}(\alpha, E_s)$, and $dI_{bse}(E_s=E_1 \rightarrow E_2) \rightarrow d^2I_{bse}(\alpha, E_s)$, yielding

$$d^2I_{se}(\alpha, E_s) = I_{d(\phi_1)} - I_{d(\phi_2)} \quad (|\phi| \leq 50\text{V}) \quad (61)$$

$$d^2I_{bse}(\alpha, E_s) = I_{d(\phi_1)} - I_{d(\phi_2)} \quad (|\phi| > 50\text{V}) \quad (62)$$

The (doubly) differential currents $d^2I_{se}(\alpha, E_s)$ and $d^2I_{bse}(\alpha, E_s)$ are now determined in terms of the measured currents $I_{d(\phi_1)}$ and $I_{d(\phi_2)}$, and from Eqs. (59) and (60),

$$\delta(\alpha, E_s) \Big|_{\alpha', E_s'} = \frac{1}{I_b} \frac{I_{d(\phi_1)} - I_{d(\phi_2)}}{d\Omega_s dE_s} \quad |\phi| \leq 50\text{V} \quad (63)$$

$$\eta_{(e)}(\alpha, E_s) \Big|_{\alpha', E_s'} = \frac{1}{I_b} \frac{I_{d(\phi_1)} - I_{d(\phi_2)}}{d\Omega_s dE_s} \quad |\phi| > 50\text{V} \quad (64)$$

where E_s' is once again given by Eq. (42), dE_s represents the energy resolution $\Delta E=e\Delta\phi$, and $d\Omega_s$ represents the detector's FOV. Note that the difficulty arising with direct determination of $\eta(E_s)$ does not arise for $\eta(\alpha, E_s)$. This is because the sample is no longer being electrically biased, but rather a separate detector is biased, leaving E_b unaffected.

(c) *Experimental Determination for an Incident Beam of Monoenergetic Ions*

The measurement scheme used in the case of incident ions is essentially that for incident electrons, with one important distinction: when determining $\eta_{(i)}(\alpha, E_s)$, it is necessary that the detector be positively biased, in order to filter out successively higher

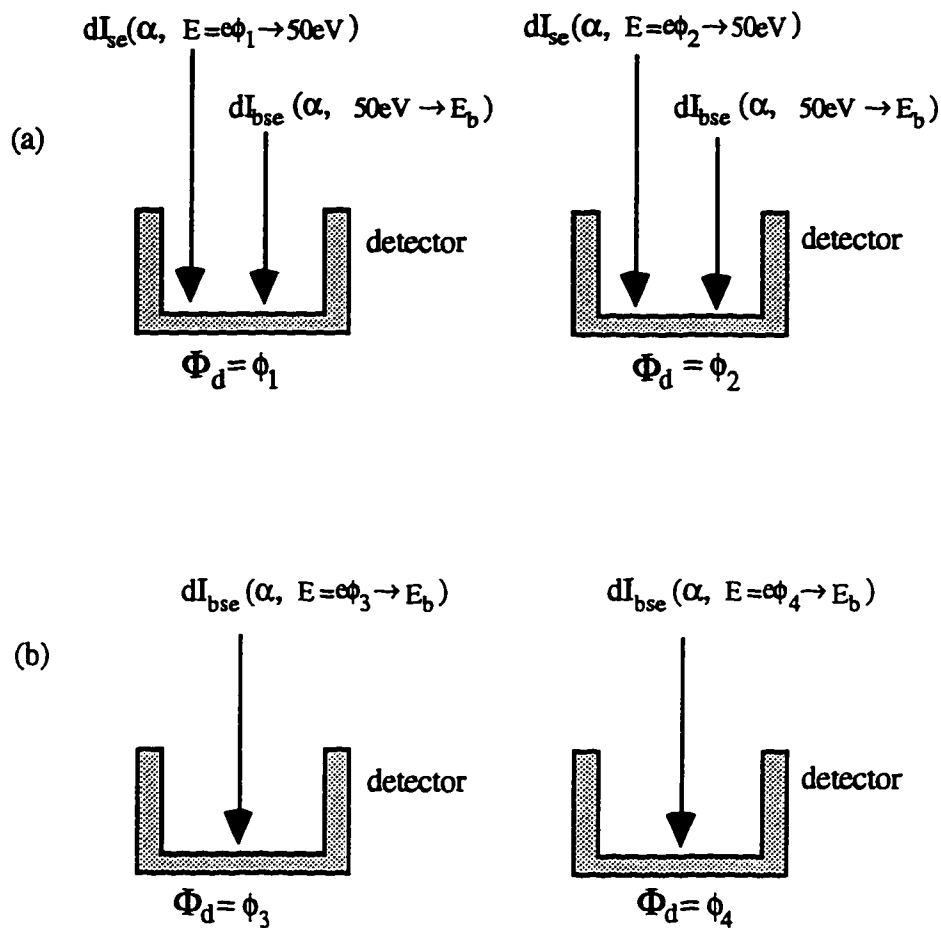


FIG. 3-11. Schematic depicting angle-energy-resolved yield determination scheme for (a) SE's and (b) BSE's. In the figure, $-50 \text{ V} \leq \phi_2 < \phi_1 \leq 0$, and $-E_b < \phi_3 < \phi_4 < -50 \text{ V}$.

energy BSI's. Providing the detector is properly shielded from the SE and BSI populations away from the detector, such a detector bias will not affect the SE current. One is then led to Eq. (63) for $\delta(\alpha, E_s)$, where $\Phi_s < 0$, and Eq. (64) for $\eta_{(i)}(\alpha, E_s)$, where $\Phi_s > 0$.

3.3.5 Summary of Measurements

Results of the mathematical development presented in (3.3.1)-(3.3.4) are summarized in Table 3.2. It is once again emphasized that development of the equations listed in the last two columns of Table 3.2 was based on the following assumptions:

- (i) secondary ion production due to an incident electron or ion beams (in the energy range under consideration) is negligible (all measurements)
- (ii) secondary and backscattered currents resulting from return current to the sample are negligible (all measurements)
- (iii) bombarding species are normally incident on the sample (angle-resolved measurements)
- (iv) the entire beamspot falls within the FOV of the RD (angle- and angle-energy-resolved measurements)

TABLE 3.2. Summary of equations for quantities to be determined.

Quantity	Defining Equation	Scheme for Determination	
		Incident Electrons	Incident Ions
δ	(6)	(14), (25), (39), (55)	(18), (25), (39), (55)
η	(7)	(15), (26), (40), (58)	(19), (26), (40), (58)
$\delta(\alpha)$	(22)	(32), (53)	(35), (53)
$\eta(\alpha)$	(24)	(33), (56)	(36), (56)
$\delta(E_s)$	(37)	(49), (54)	(50), (54)
$\eta(E_s)$	(38)	(57)	(57)
$\delta(\alpha, E_s)$	(51)	(63)	(63)
$\eta(\alpha, E_s)$	(52)	(64)	(64)

Having sufficiently defined the goals of this investigation and outlined a comprehensive scheme for determination of the desired quantities, the focus of this thesis now turns to the apparatus and technique that have been developed to accomplish the necessary measurements.

CHAPTER 4

APPARATUS AND TECHNIQUE

This chapter describes the apparatus that has been designed and constructed to accomplish the measurements detailed in Chapter 3. An overview of the apparatus as a whole is presented first (4.1), followed by a review of major design considerations (4.2). Descriptions of major components are presented next (4.3) - (4.6), important points regarding construction of the sample-detector assembly are discussed (4.7), and a review of measurement technique concludes the chapter (4.8).

4.1 Overview and Definitions

Figure 4-1 depicts the apparatus, excluding electronics, discussed in this chapter. Components of the apparatus are grouped into four functional categories:

- (i) environmental (4.3)
- (ii) source-related (4.4)
- (iii) sample-related (4.5)
- (iv) detection-related (4.6)

Major components in each of these categories are summarized in Tables 4.1, 4.3, 4.6, and 4.7. To facilitate clear discussion, the term *support equipment* refers to such items as the vacuum system, particle sources, and various electronic components (e.g., electrometers and power supplies) located outside of the vacuum chamber. The term *chamber apparatus* refers to those components that are inserted into the vacuum chamber—seen at (B) in the figure. The term *apparatus* refers to the instrument as a whole; that is to say, the support equipment and chamber apparatus together.

Figure 4-2 is a representation of the general situation to be investigated by this apparatus. A beam of charged particles is normally incident on a sample, producing a scattered beam—where *scattered beam* refers the combined SE and BSE/BSI populations



FIG. 4-1. Photograph of the experimental apparatus, depicting (A) vacuum chamber, (B) chamber apparatus (minus magnetic shielding), (C) electron gun, (D) ion gun, and (E) residual gas analyzer.

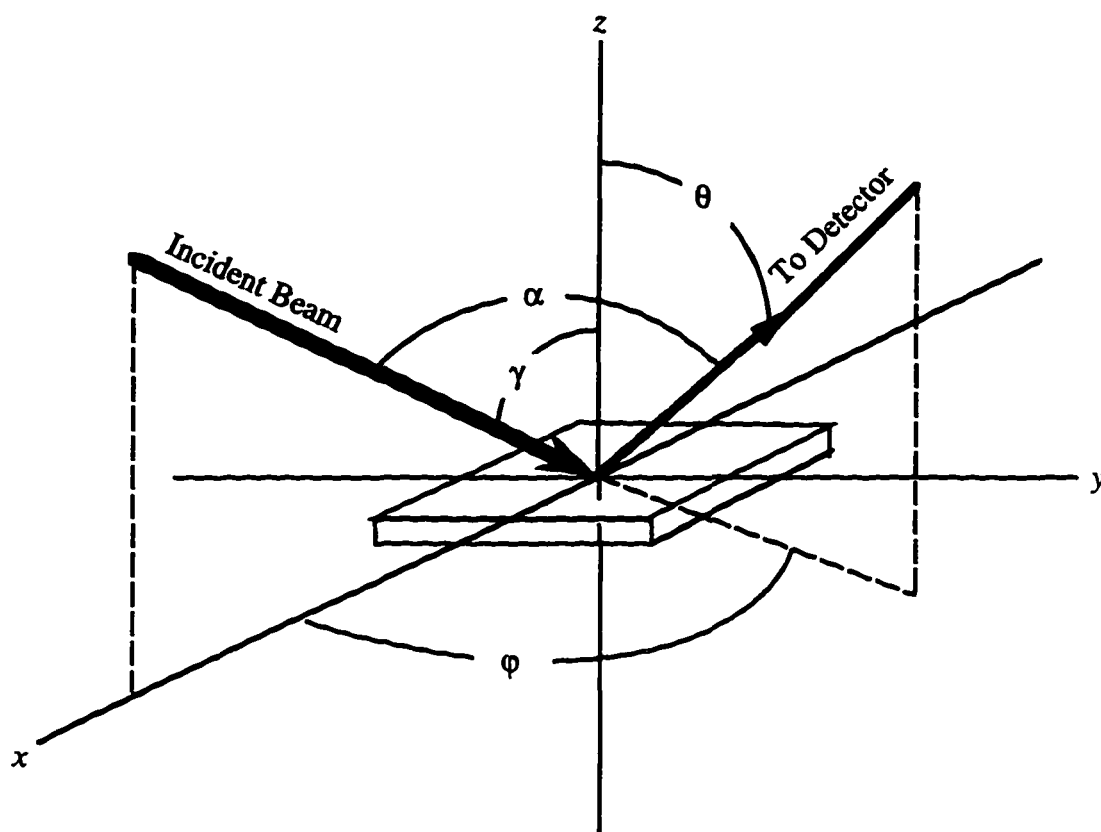


FIG. 4-2. Schematic depicting the general scenario to be investigated.

emanating from the sample in all directions. In the figure, γ is seen to be the angle between the z -axis and the incident beam, θ the angle between the z -axis and the scattered beam (the polar angle), ϕ the angle between the x -axis—defined by the projection of the beam onto the horizontal plane—and the projection of the scattered beam into the x - y plane (the azimuthal angle), and α the angle between the incident and scattered beams (the scattered angle).

4.2 Design Philosophy

Support equipment was chosen primarily based on cost and availability. Specifically, a conscious effort was made to use as many components as possible already in the possession of the USU Department of Physics. These include such items as the vacuum system, electron and ion sources, electrometers, motion feedthroughs, and power supplies.

Design of the chamber apparatus was influenced primarily by three considerations: (i) the design of the detector charged with making angle-energy-resolved measurements; (ii) space constraints within the vacuum chamber; and (iii) the desire to accomplish both total and angle-resolved δ and η measurements simultaneously, and with independent detection systems. The roles of (i) and (ii) are discussed further in (4.7.1). Regarding (iii), simultaneous total and angle-resolved measurements allow for meaningful comparison between SE and BS yields measured directly, and those obtained via integration of angle-resolved yields (since they represent measurements taken under (nearly) identical beam and sample-surface conditions). Overall, design, construction, and testing were accomplished relatively quickly, and for a minimal investment in new equipment.

Having reviewed the apparatus as a whole, attention is now turned to the details of individual subsystems and components.

4.3 Environmental Components

Achieving, maintaining, and monitoring a suitable environment in which the desired measurements can be performed is a principal concern. Three aspects of the sample environment—vacuum quality (pressure and contaminants), magnetic fields, and temperature—are addressed by the environmental subsystems. Each of these subsystems and their major components are now described, and a summary of environmental-related components is presented in Table 4.1.

4.3.1 *Vacuum System*

The vacuum system is responsible for maintaining the sample environment at the desired pressure, as well as controlling its composition. The vacuum system employed in this research is designed to maintain the sample in an ultra-high vacuum (UHV) environment, and is capable of base pressures of $\sim 2 \times 10^{-11}$ Torr⁸² (see Ref. 81 for a description of the standard levels of vacuum quality, and for a definition of units). Its primary components are a chamber, two roughing pumps, two high-vacuum pumps, three absolute pressure gauges, one partial pressure gauge, two leak valves, and a bakeout oven. Each of these components is described below.

(a) *Vacuum Chamber*

Figure 4-3 is a schematic of the vacuum chamber used in this investigation, while Table 4.3 summarizes major design parameters. Configured for this investigation, two ports are used for diagnostic instrumentation, three for electrical access, two for motion feedthroughs, two for charged particle sources, two for pumps, two for leak valves, and one for illumination. In addition, four quartz windows afford excellent visibility into the chamber. All ports use standard conflat flange knife-edge seals with copper gaskets.

TABLE 4.1. Summary of environment-related components.

Vacuum System	Magnetic Shielding	Thermal Control
Chamber (custom built, stainless steel, .025 m ³)	Canister (.014" CO-NETIC)	Sample Heater (resistive)
Roughing Pumps (cryosorption, turbomolecular)	Baseplate Shield (.030" NETIC)	Power Supply
High-Vacuum Pumps (ion, Ti sublimation)	Top Plate Shield (.030" NETIC)	Thermocouple
Absolute Pressure Gauges (pirani, thermocouple, ion, quadrupole mass spectrometer)		
Partial Pressure Gauge (residual gas analyzer)		
Leak Valves		
Bakeout Oven (custom built)		

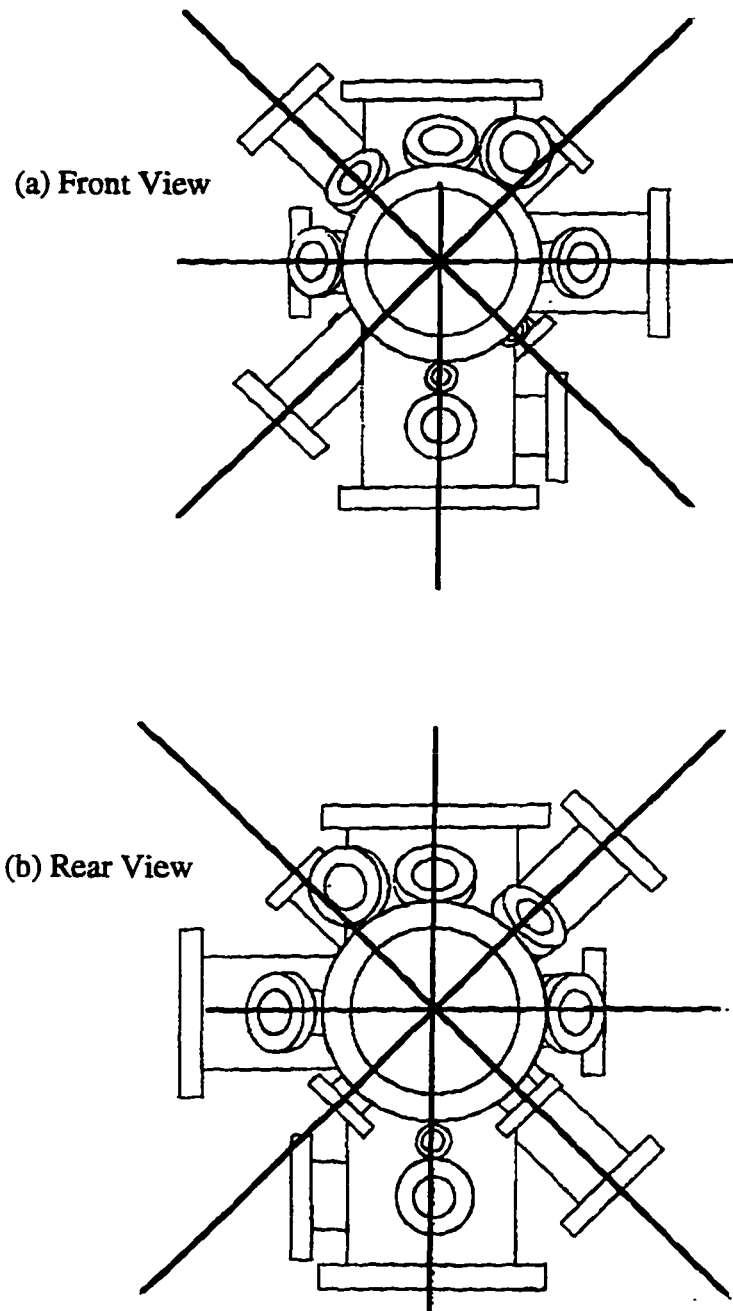
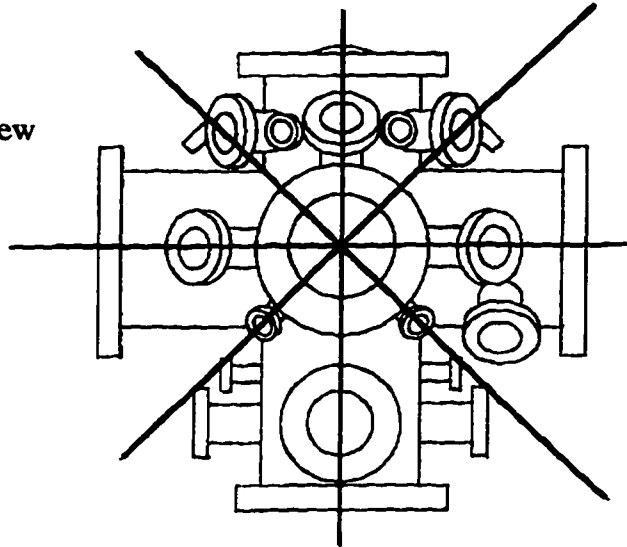


Figure 4-3. Vacuum chamber schematics.

(c) Left View



(d) Right View

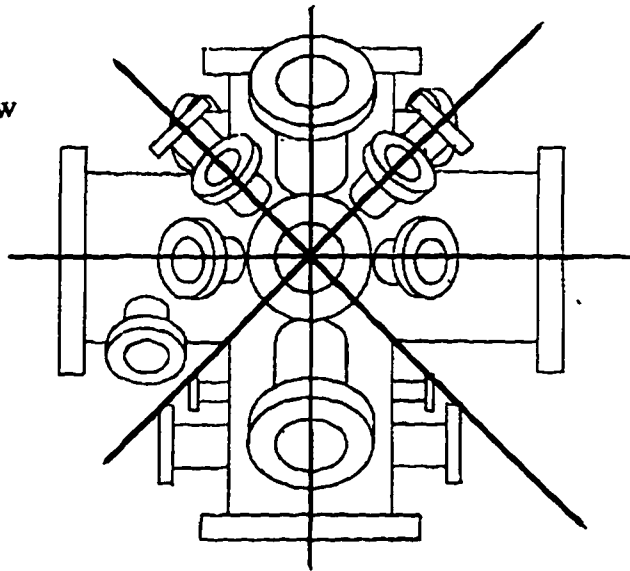
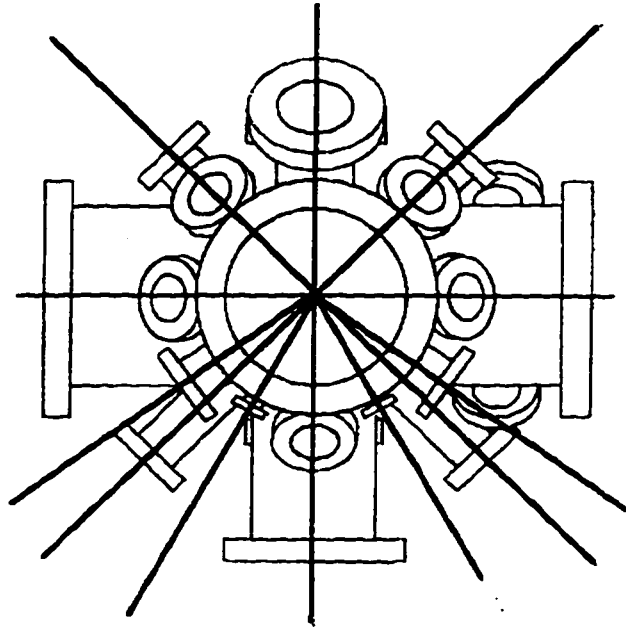


Figure 4-3. Continued.

(e) Top View



(f) Bottom View

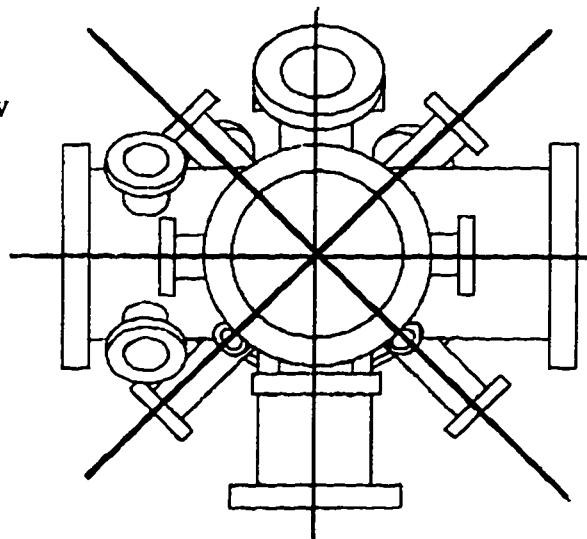


Figure 4-3. Continued.

TABLE 4.2. UHV vacuum chamber design, operating parameters, and support equipment.

Parameter	Description
Materials:	304 and 316 stainless steel flanges and walls
Volume:	~1500 in ³ (.025 m ³)
Access Ports:	4 - 6" CFF ports 1 - 4" CFF port 4 - 2 1/2" CFF ports 15 - 1 1/2" CFF ports 10 - 3/4" (10)
Base Pressure:	~2x10 ⁻¹¹ Torr
Magnetic Field in Sample Region:	≤ 1 mG
Vacuum Pumps:	Cryosorption Ti Sublimation Magnetic Ion
Vacuum Gauges:	Vacuum Thermocouple Pirani Ion Quadrupole Mass Spectrometer

(b) Roughing Pumps

Pump-down of the chamber is accomplished in two phases; the initial, or roughing, phase reduces the chamber pressure from atmospheric pressure (~ 1 atm) to $\sim 10^{-3}$ Torr, while the second, or high-vacuum, phase then reduces the chamber pressure into the UHV realm. A cryosorption roughing pump, as well as a mechanical-pump-backed turbomolecular pump, are both available for the roughing phase, though only the cryosorption pump is normally used. [Operating on the principle of adsorption, high surface-area activated alumino silicates (zeolites), cooled by liquid nitrogen reduce the chamber pressure from 1 atm to $\sim 10^{-3}$ Torr.] In addition to small size and ease of operation, the cryo-pump has the highly desirable advantage of not introducing organic contaminants into the rarefied chamber atmosphere.

(c) High Vacuum Pumps

The combination of a magnetic ion pump and a Ti sublimation pump takes over for the roughing pump at a chamber pressure of $\sim 10^{-3}$ Torr, and is capable of reducing the base chamber pressure to $\sim 2 \times 10^{-11}$ Torr (with a bakeout). The sublimation pump is typically operated intermittently, and with decreasing frequency as the pressure drops, while the magnetic ion pump is operated continuously. (It is interesting to note that the magnetic ion pump relies heavily on SEE for its operation.⁸¹) Neither of these pumps contributes organic contamination to the chamber.

(d) Absolute Pressure Gauges

The vacuum system employs two independent means of measuring total chamber pressure in both roughing and UHV phases of operation. For pressures above 10^{-4} Torr, pirani [VG Instruments ARGAs Plus] and thermocouple [Varian Model 801] gauges are used (operating on the principles of pressure-dependent thermal conductivity and the thermoelectric effect, respectively).⁸¹ Pressure determination at pressures above 10^{-3} Torr

serves primarily to indicate when high-vacuum pumping can begin; since this process can begin within a sizable pressure range, extreme accuracy is neither required nor afforded by the gauges employed. For pressures below $\sim 10^{-8}$ Torr, pressure measurements are accomplished independently with a nude UHV ion gauge and gauge controller [Granville-Phillips Model 307], and a quadrupole mass spectrometer configured for total pressure measurement [VG Instruments ARGAs Plus]. These gauges offer absolute pressure determination to within a factor of two of their displayed readouts, down to minimum absolute pressures of 10^{-12} Torr and 10^{-11} Torr, respectively.^{83,84}

(e) Partial Pressure Gauge (Residual Gas Analyzer)

The quadrupole mass spectrometer portion of the ARGAs Plus instrument (discussed above) can also be used as a residual gas analyzer (RGA), measuring *partial* pressures in the chamber (to 10^{-12} Torr)⁸⁴ due to individual species. This is an exceptionally useful capability, affording knowledge of the species and quantity of contaminants in the vacuum. Moreover, linking the RGA to a personal computer, continuous monitoring of chamber atmosphere is possible while samples are being characterized, providing information regarding contaminants present on the sample surface [discussed further in (6.2.1)].

(f) Leak Valves

The ability to actively control levels of certain contaminant gases is achieved via two variable leak valves [Granville-Phillips Series 203]. These devices allow for the introduction of specific quantities (fluxes) of desired gases, while maintaining an overall UHV pressure environment. Used in conjunction with the RGA, the leak valves afford the added capability of maintaining a controlled, rarefied atmosphere within the chamber.⁸⁵

(g) Bakeout Oven

Achieving base pressures $\sim 10^{-11}$ Torr in a timely fashion requires a bakeout of the

chamber,⁸⁶ and is accomplished with an oven custom-designed for this vacuum system. The bakeout oven is a large, insulated sheet-metal box placed over the entire vacuum chamber. Heating elements mounted to the interior walls of the oven are used to bake the chamber at temperatures typically $>150\text{ }^{\circ}\text{C}$ [though bakeout temperatures are currently limited to $\sim 100\text{ }^{\circ}\text{C}$ by the rotary feedthrough, described in (4.7.2), and Teflon insulators employed in the rotatable detector (4.6.5)]. The effectiveness of such bakeouts is discussed in Chapter 5.

4.3.2 Magnetic Shielding

Experiments involving the trajectories of charged particles, such as our measurements of the angles at which SE's and BS particles leave the sample, dictate a concern for magnetic environment. The effect of ambient magnetic fields is to alter particle trajectories, the significance of which depends upon the magnitude and direction of the total magnetic field \mathbf{B} , the energy of the electron E_s , and the target distance (the distance from the sample to the detector) d_t . Specifically, the magnetic force on the electron, given by

$$\mathbf{F} = e\mathbf{v} \times \mathbf{B} = evB \sin\theta$$

(for electron velocity \mathbf{v} and the angle θ between \mathbf{v} and \mathbf{B}), produces a constant transverse acceleration with magnitude

$$a = \frac{F}{m_e} = \frac{evB \sin\theta}{m_e} \quad (65)$$

(for electron mass m_e) over the time required to travel the distance d_t ,

$$t = \frac{d_t}{v}. \quad (66)$$

The electron's velocity can be expressed in terms of its energy

$$v = \sqrt{\frac{2E}{m_e}} \quad (67)$$

yielding, via Eqs. (65)-(67), an expression for the deflected distance Δd in terms of B , d_t , and E_s

$$\Delta d = \frac{1}{2}at^2 = \frac{1}{2}eB\sin\theta d_t^2 \sqrt{\frac{1}{2Em_e}} \quad (68)$$

Note that for fixed B and d_t , Δd increases for decreasing E_s , making directional measurements of low-energy electrons (e.g., SE's) particularly vexing.

(a) *Ambient Magnetic Fields*

Sources of B inside the vacuum chamber include the geomagnetic field, the ion pump's magnet (located in the bottom of the chamber, approximately one-half meter below the sample), and magnetic materials used in construction of the chamber and chamber apparatus. Measurements of the composite magnetic field within the chamber prior to shielding revealed a maximum magnetic field magnitude of 0.5 Gauss in the region occupied by the sample and detector. Assuming B perpendicular to the electron path—the worst case scenario—and using a target distance of 6.35 cm, the second column of Table 4.3 summarizes the resulting Δd for variety of electron energies. The deflection is considered significant if Δd is comparable to the size of the detector aperture. For a detector aperture of 1.6 mm, $|B| = 0.5$ G clearly precludes accurate angular determinations for all but the highest energy electrons considered in this work. Consequently, it is necessary to regulate the magnetic environment in the region surrounding the sample and detector.

(b) *Shield Design*

Reduction of B near the sample and detector is accomplished by shielding the ambient chamber B , and by using nonmagnetic materials for all apparatus components within the shielded region. Figure 4-4 depicts the magnetic shield constructed to enclose

TABLE 4.3. Electron path deflection due to ambient magnetic field perpendicular to v ($d_t=6.35$ cm).

Energy (eV)	Δd	
	(mm)	(μm)
	<u>$B = 0.5$ G</u>	<u>$B = 1.26$ mG</u>
1	30.0	75.6
2	21.1	53.2
10	9.5	23.8
3000	0.5	1.38
10,000	0.3	0.76
50,000	0.1	0.34

the sample-detector assembly. Holes in the side of the shield are for incident beam and visual access, while holes in the top and bottom are for electrical connections.

Construction material is .014" CO-NETIC [Perfection Mica] shielding, commonly referred to as μ -metal. An additional layer of .030" NETIC shielding is added to both top and bottom plates.

An expression for the theoretical effectiveness of this shield design is given by⁸⁷

$$B_I = \frac{B_0 D}{\mu t}$$

for magnetic field B_I inside the shielded volume, ambient magnetic field B_0 , cylinder diameter D , and shield thickness t . For $D = 13.5$ cm, $B_0 = 0.5$ G, $\mu = 150,000$ (given in Ref. 87), and $t = 0.36$ mm (0.014"), an interior field $B_I \cong 1.3$ mG is calculated. Design of the shield, coupled with the size of the available magnetometer probes, prevents confirmation of this value via direct measurement. It is therefore assumed, for the time being, that this is a realistic estimate for the magnitude of B in the sample/detector region.

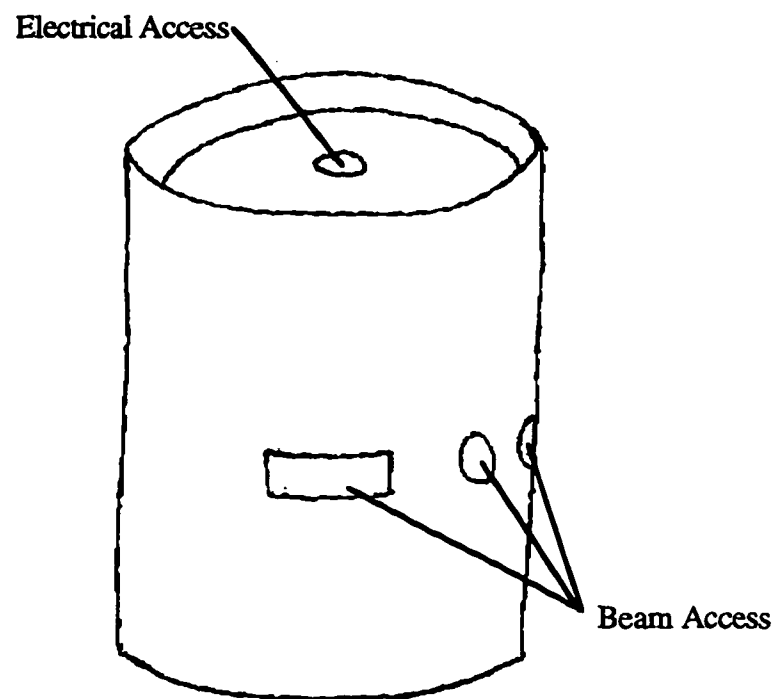


FIG. 4-4. Magnetic shield. A μ -metal cylindrical shell and top plate welded into one piece, and bottom plate attached separately.

The third column of Table 4.3 summarizes the resulting path deflection (for $\mathbf{B} \perp \mathbf{v}$) for a variety of electron energies for such a magnetic field strength. These deflections represent a worst-case scenario, and the errors they introduce into angular measurements fall well below the angular resolution of the detector (4.6.5).

4.3.3 Thermal Control System

Provisions for heating the sample are present in the apparatus, though not for cooling. A resistive heater is located within the sample holder [see (4.5.2) and (4.5.4)], controlled by power supply located outside the chamber. Sample temperature is to be monitored via a thermocouple.

4.4 Source-Related Components

4.4.1 Electron Sources

An Auger electron gun [Varian model 981-2455] and its associated power supply / controller [Varian model 981-0246] together comprise the electron source currently in use. Specifications for this instrument are given in Table 4.5.⁸⁸ Further information regarding the gun can be found in Refs. 88 and 89. Beam-spot characterization was accomplished during initial testing, revealing typical spot sizes of ~ 1 mm (see Chapter 5). Mounting of the gun to the vacuum chamber is illustrated in Fig. 4-1. Limited space within the chamber dictated that the gun be mounted at a 45° angle and not extend into the main chamber volume [keeping it clear of the magnetic shield described in (4.3.2)], the latter being accomplished via the construction of an extension tube, visible in the figure.

In addition to the Auger electron gun, a LEED/Auger electron gun [Varian model 981-2125] is also available. With beam energies of 3 eV - 3 keV, a tungsten filament, and beam currents $\sim 10^{-8}$ - 10^{-4} A, this gun is similar to the other, though allows for lower beam energies.⁹⁰

TABLE 4.4. Summary of source-related components.

Electron-Source Components	Ion-Source Components
Auger Electron Gun / Controller (tungsten filament, 0-3 keV)	Ion Gun / Controller (two-tungsten wire filament, 140-590 eV)
LEED Electron Gun / Controller (tungsten filament, 3 eV - 3 keV)	Leak Valves

TABLE 4.5. Electron and ion gun specifications.

Parameter	Electron Gun (Auger)	Ion Gun
Beam Energy:	20 eV - 3000 eV	140 eV - 590 eV
Beam Current:	maximum 200 μA at 3 kV	Maximum 4.6 $\mu\text{A}/\text{cm}^2$
Filament:	tungsten ribbon - replaceable	two tungsten wire - replaceable
Beam Deflection:	X- and Y-deflection plates for positioning beam on sample	mechanical
Beam Spot Size:	~ 1.5 mm—see (5.2.2)	—
Bakability:	maximum $\sim 150^\circ\text{C}$	maximum 250°C
Operating Pressure:	10^{-4} Torr to UHV	$\sim 10^{-3}$ - 10^{-6} Torr

Lastly, a 0.5 - 50 keV electron gun has been funded, extending the available energy range, and will soon be on hand for use with this apparatus.⁹¹

4.4.2 *Ion Sources*

The system currently in place for ion production consists of a ion gun [Varian model 981-0043] and its associated power supply [Varian model 981-2046] and control unit [Varian model 981-0046]. This system may be used for sputtering (cleaning the sample via ion bombardment) or as a source for incident ion investigations. Notable operating parameters are given in Table 4.5.⁹² Further technical information may be found in Refs. 92, 93, and 94. Reference 92 gives the ion beam diameter as ~1.5 cm at 6 cm gun-to-target distance, 8×10^{-5} Torr Argon chamber pressure, and 600 eV beam energy. This large beam spot is desirable for sputtering, less so for SEE investigations. Since the gun-to-target distance for this apparatus is ~12 cm, and SEE studies will be carried out at pressures below 10^{-8} Torr, the spot size and beam currents will need to be characterized experimentally (in the same manner as that used for the electron beam), though as yet this has not been accomplished.

4.5 Sample-Related Components

Sample-related components include the primary sample, its associated sample holder, two tertiary samples and their holders, and a sample block. Together, these components constitute the sample-block assembly depicted in Fig. 4-5. Additional related components are a power supply enabling positive and negative biasing of the primary and tertiary samples (4.6.2), the sample heater and associated power supply (4.5.4), and the ion sputtering gun (4.4.2).

TABLE 4.6. Summary of sample-related components.

Samples	Holders
Primary Sample - 1 (20x20x3.2 mm)	Primary Sample Holder
Tertiary Samples - 2 (20x10x3.2 mm)	Tertiary Sample Holders
Sample Block	

4.5.1 *Samples*

The primary sample is that sample directly bombarded by the electron and ion beams. It is a conductor measuring 20 mm by 20 mm by 3.2 mm. Machined into the sample are four Faraday cups of varying sizes (depicted in Fig. 4-6) for use in beam characterization and location, and various required current measurements [discussed further in (4.6.2)]. The two tertiary samples are composed of the same material as the primary sample, and are each half the size of the primary sample. The function of these samples is to serve as the return current detector, and as such are discussed further in (4.6.3).

4.5.2 *Sample Holders*

The sample holders, constructed of aluminum, and are used to mount the samples to the sample block. Samples are simply placed into the holders, with no need for additional “fastening.” Since the samples are in direct electrical contact with the holders, electrical connections to the samples can be accomplished via wires attached to the holders. The primary sample holder is considerably larger than the tertiary sample holders (Fig. 4-5), since it must house the sample heater (described below), and a continuation of the large Faraday cup machined into the primary sample.

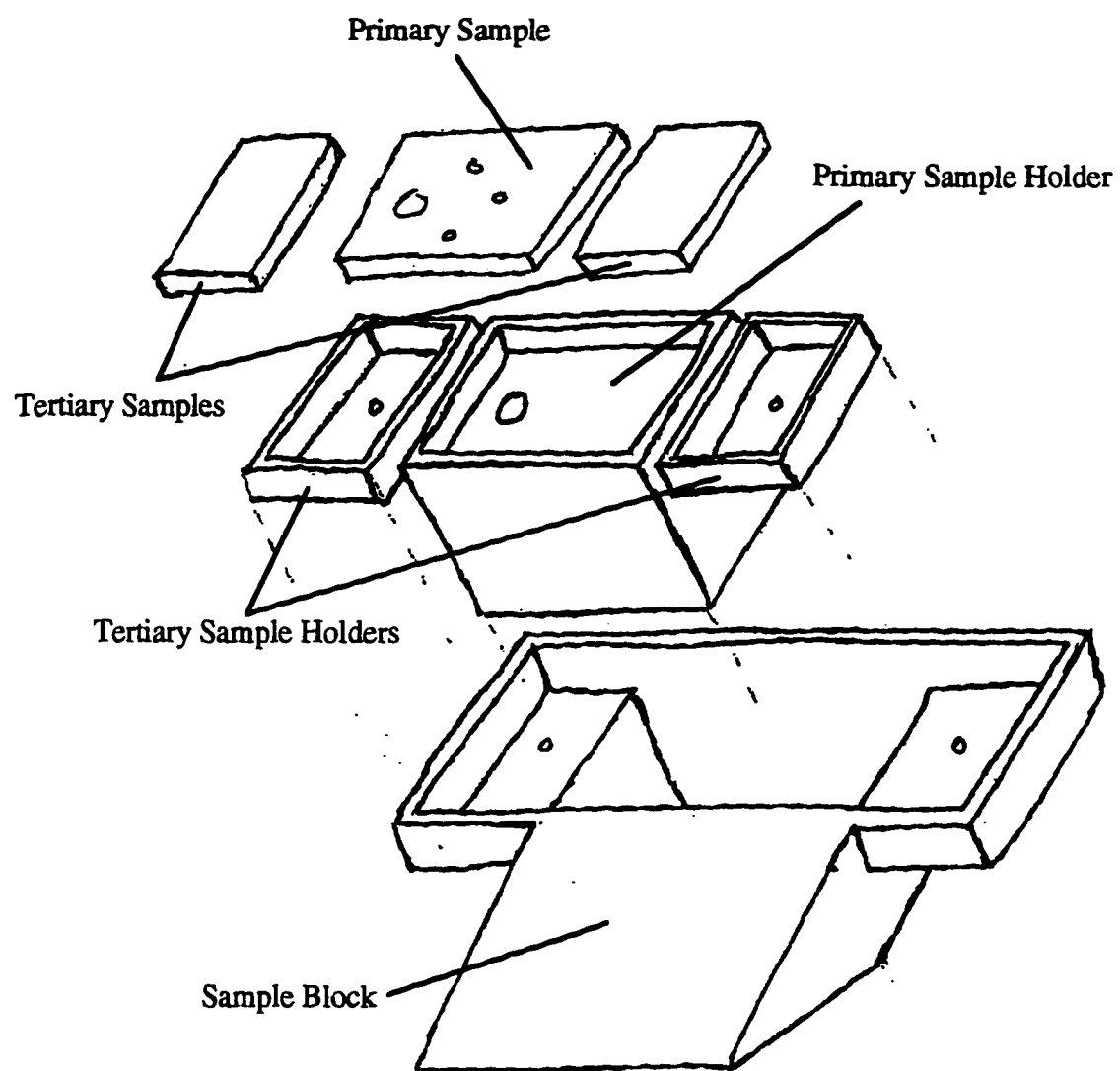


FIG. 4-5. Sample block assembly.

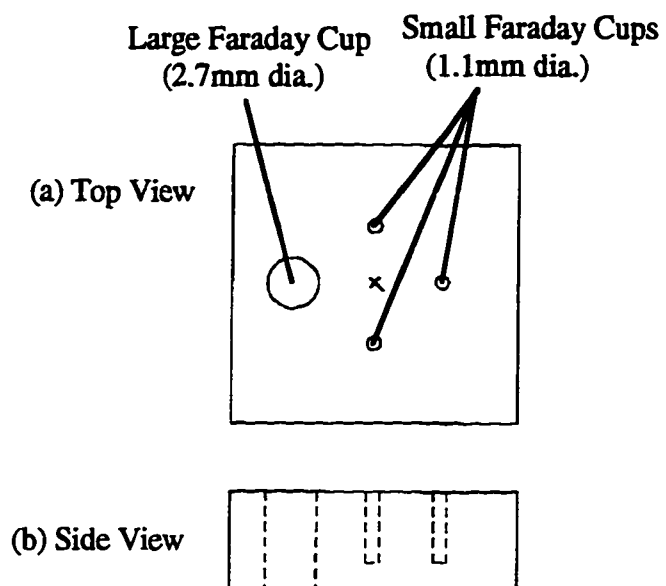


FIG. 4-6. Primary sample design.

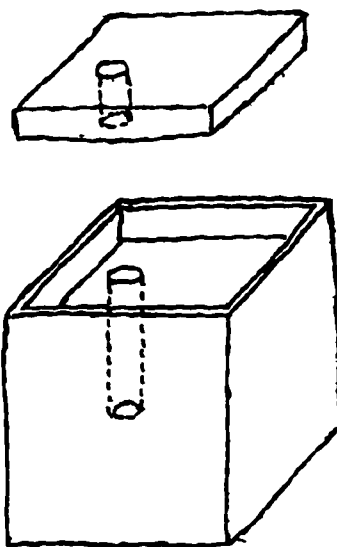


FIG. 4-7. Large Faraday cup in primary sample and holder.

4.5.3 *Sample Block*

The sample block, precision machined from a single piece of aluminum, serves to mount the samples rigidly to the entire sample-detector assembly. The sample holders are mounted to the sample block with non-magnetic stainless-steel screws, which are isolated electrically from the block via ceramic standoffs. Electrical connections to the holders (and therefore the samples) are accomplished via these screws. The 45° incline of the sample block serves to orient the sample surfaces normally to the incident beam, itself entering the chamber at a 45° angle [see (4.6.1)].

4.5.4 *Sample Heater*

The heater currently installed in the sample block is a 14W, 120V [Hotwatt, model SC121] cylindrical resistive heater, 3 mm dia. x 2.5 cm long. Difficulties with insulation on the electrical leads (6.2.5) make it likely that this heater will be replaced with a similar model.

4.6 Detection-Related Components

Recall from Chapter 3 that determination of the various SE and BS coefficients is based on measurement—under varying conditions of electrical biasing—of four currents: the sample current (I_s), return current (I_r), beam current (I_b), and an angle-resolved detector current (I_d). Measurement of each of these currents requires a detection system, consisting of a detector, an electrometer, a power supply (for sample and detector biasing), and associated wiring, connectors, and shielding. Components of each detection system are summarized in Table 4.7, and schematic representations are given in Figs. 4-8 and 4-9. Detectors and electrometers for each system, as well as rationale for their selection, are described below; power supplies are addressed where relevant. Also presented are descriptions of wiring, connections, and shielding.

TABLE 4.7. Summary of detection system components.

Meas.	Detector	Electrometer	Power Supply	Wire
I_s	Sample	Keithley 616	0-350 V variable	Interior: KAP4 Exterior: Belden 8254 RG-62/U
I_r	Tertiary Samples	Keithley 616 Keithley 160	0-350 V variable	Interior: KAP4 Exterior: Belden 8262 RG-58 C/U
I_b	Faraday cup in sample	Keithley 616	none	Interior: KAP4 Exterior: Belden 8254 RG-62/U
I_d	Rotatable Faraday cup	Keithley 616	0-3000 V variable	Interior: KAP4 Exterior: Belden 8254 RG-62/U

4.6.1 Sample Current Detection

Since the sample current represents the net current reaching the sample from all sources (e.g., primary particles, secondary and backscattered particles, return current, etc.), determination of this current is achieved by isolating the sample from ground and connecting it directly to an electrometer. In this sense, the sample itself plays the role of detector. The electrometer used in this measurement is the Keithley Model 616, capable of reliable current measurements of $\sim \pm 10^{-15}$ amperes.⁹⁵ Readings are accurate to $\pm(0.5\%$ of reading plus 0.1% of the range). Though absolute sample currents in this work are on the order of microamperes (μA)—not particularly small—it is the ability to measure small *changes* in the sample current (as the sample is incrementally biased) which establishes the energy resolution of the $\delta(E_s)$ determination; hence the need for the Model 616's level of sensitivity.

Required biasing of the sample is achieved by connecting a 0-350 V DC power

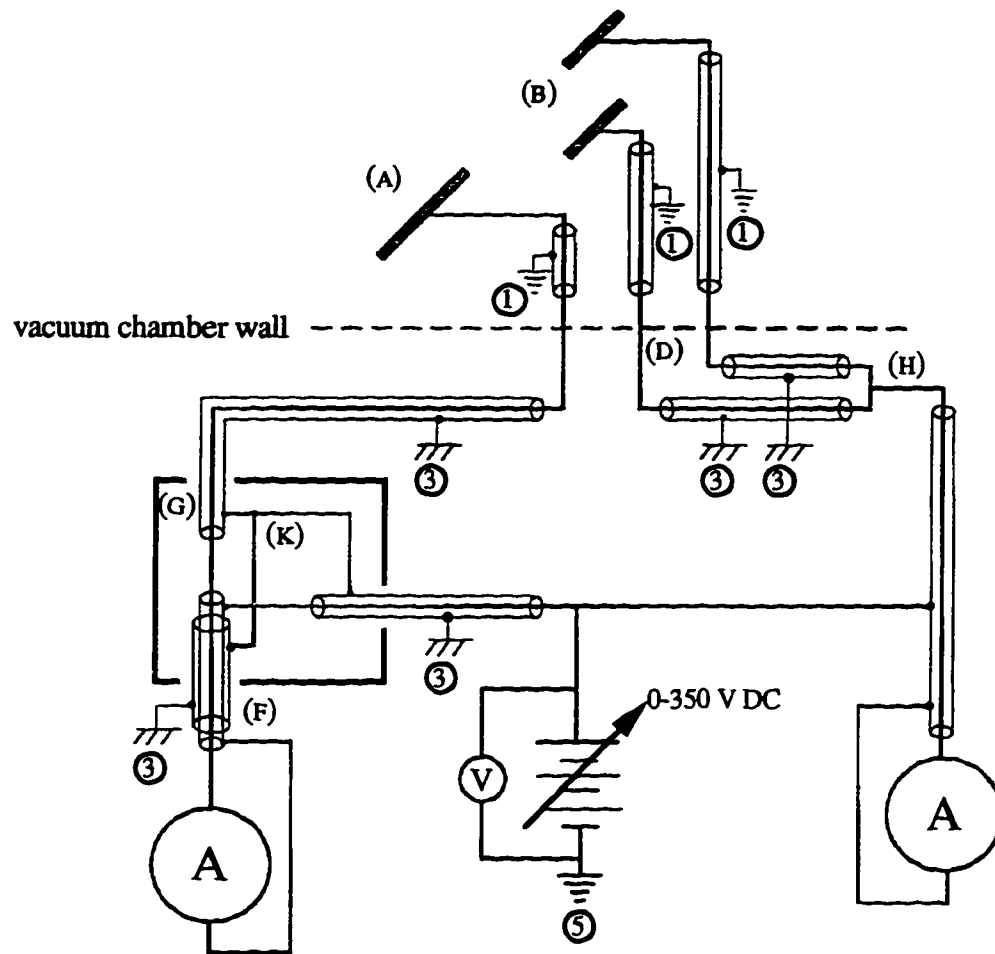


FIG. 4-8. Wiring schematic depicting beam current, sample current, and return current detection schemes.

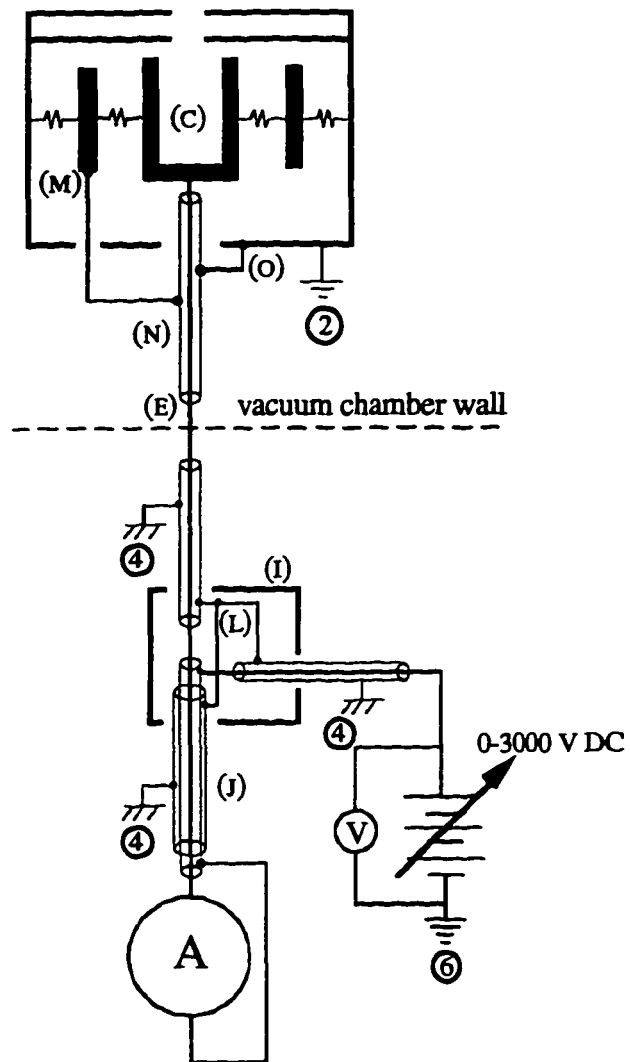


FIG. 4-9. Wiring schematic for the rotatable detector.

supply [Kikusui Model PAB] in series with the electrometer (Fig. 4-8), which floats both the electrometer and the sample to the desired potential.

4.6.2 *Return Current Detection*

The return-current detection scheme is identical to that used for sample current detection, employing the two tertiary samples as the return-current detector. Recall that the return current is that current reaching the sample from sources other than the incident beam. The disappearance of measurable return current when the incident beam is turned off (or directed into the FC) indicates >99% of this current is due to charged particles (SE's, SI's, BSE's, and BSI's) that have left the sample as a result of incident-beam impacts, scattered off of the interior of the chamber, and returned to the sample. (The magnitude of the return current ranges from 10^{-9} A to 10^{-6} A, depending on bias—see Chapter 6). The number of charged particles reaching the sample in this manner is clearly proportional to its exposed surface area. The two tertiary samples placed on either side of the primary sample, together with their holders, present a surface area to the incident return current nearly identical to that of the primary sample and its holder. Additionally, these are samples of the same material as the primary sample, and should therefore have identical secondary-emission and backscattering characteristics. Grounding them through an electrometer [Keithley Model 160], then, is a simple and effective means of measuring the return current. Biasing of the tertiary samples occurs in parallel with biasing of the primary sample, using the same power supply (Fig. 4-8).

4.6.3 *Beam Current Detection*

Measurement of the beam current is accomplished by directing the incident beam into a Faraday cup built into the primary sample and sample holder (Fig. 4-7). The detection system described for sample current measurement (4.6.1) is then used to measure the beam current.

The Faraday cup (FC) is a stalwart of charged particle detection. For a thorough and concise history and a summary of numerous practical variations, the reader is referred to Ref. 96. Figure 4-10 is a schematic of a basic Faraday cup design. Though variations on this design are nearly unlimited, all center around the same theme: electrons (or ions) are collected in a conducting “cup” connected to an ammeter, where they are registered as current. Clearly (and interestingly, considering the nature of this investigation), SEE and backscattering play an important role in the design of the cup; in order that the current registered by the electrometer be an accurate measure of the number of electrons (ions) collected, few of these electrons (ions), and their secondaries, must be allowed to escape. Methods for achieving this goal include: (i) coating the cup's interior with a low SE yield material; (ii) roughening its interior surfaces; (iii) increasing the ratio of the cup's depth to its aperture diameter (the so-called *aspect ratio*); and/or (iv) adjusting the shape of the collecting cavity. The Faraday cup in this case uses a combination of options (i), (iii), and (iv); its interior is coated with colloidal graphite [which has a (relatively) low SE yield], it has an aspect ratio of 10:1 (which has been shown to prevent 95% of SE's and BSE's from escaping⁹⁶), and the aperture in the sample is smaller than that in the sample holder—resulting in a geometry which further decreases the likelihood of SE and BSE escape. A 2.7 mm dia. outer aperture ensures that the entire incident beam [~1.3 mm dia.—see (5.2.2)] can be accommodated within the FC.

4.6.4 *Angle-Resolved Scattered-Beam Current Detection*

The detector chosen for angle- and angle-energy-resolved current measurements has played a large role in overall apparatus design [see (4.7.1)]. Among the most prominent candidates for the role were electron multiplying devices (e.g., the channeltron), a variety of solid-state devices [e.g., charge-coupled devices (CCD's)], and the Faraday cup. The specific parameters and objectives of this investigation made a Faraday cup design the

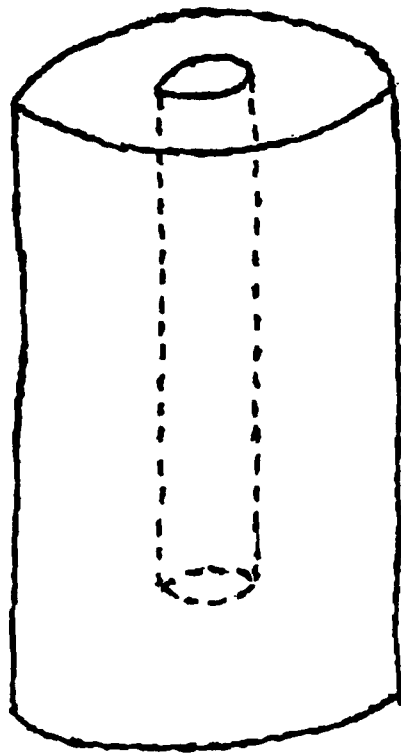


FIG. 4-10. Basic Faraday cup design.

most logical choice. First, electron multipliers are not efficient collectors of low-energy (<300 eV) electrons⁹⁷—the primary target group of this work; second, solid-state detectors are not generally suitable for energies < ~30 keV,⁹⁷ a range outside our present scope. The Faraday cup, by contrast, can be used over the full spectrum of particle energies.⁹⁶ Additional considerations which make the FC a good choice for this apparatus are (i) low cost and relative ease of fabrication; (ii) small size, enabling its motion about a sample (required for angle-resolved measurements) within the confines of a vacuum chamber; and (iii) its ability to achieve energy resolution via differential biasing. Because of the importance of this detector [referred to as the *rotatable detector* (RD)] to the chamber apparatus design, a summary of not only the present version of this detector, but also its design history is appropriate.

(a) *Initial Detector Design*

Figure 4-11(a) is a schematic of the detector design originally employed. It consists of an aluminum FC (A in the figure) mounted in a stainless steel housing (B) and preceded by an electrostatic filter (C), itself mounted in a stainless steel housing (D). This detector was originally designed for use inside a scanning electron microscope; its dimensions were chosen as a trade-off between maximum current collection (large FC desired) and minimizing interference with the incident beam at low scattering angles (small FC desired). Biasing of the filter, a precision machined stainless steel disc with a small aperture, was to accomplish desired energy selection. For example, biasing the filter to -50 V should, within a certain margin of error, allow only those electrons with kinetic energies greater than 50 eV to pass through and be collected by the FC. (Design of the filter was accomplished with the aid of sophisticated computer modeling⁹⁸ and painstaking machining.) The filter housing serves to shield the scattered beam from the electric field created by the biased filter, while the FC housing serves to shield the FC from stray

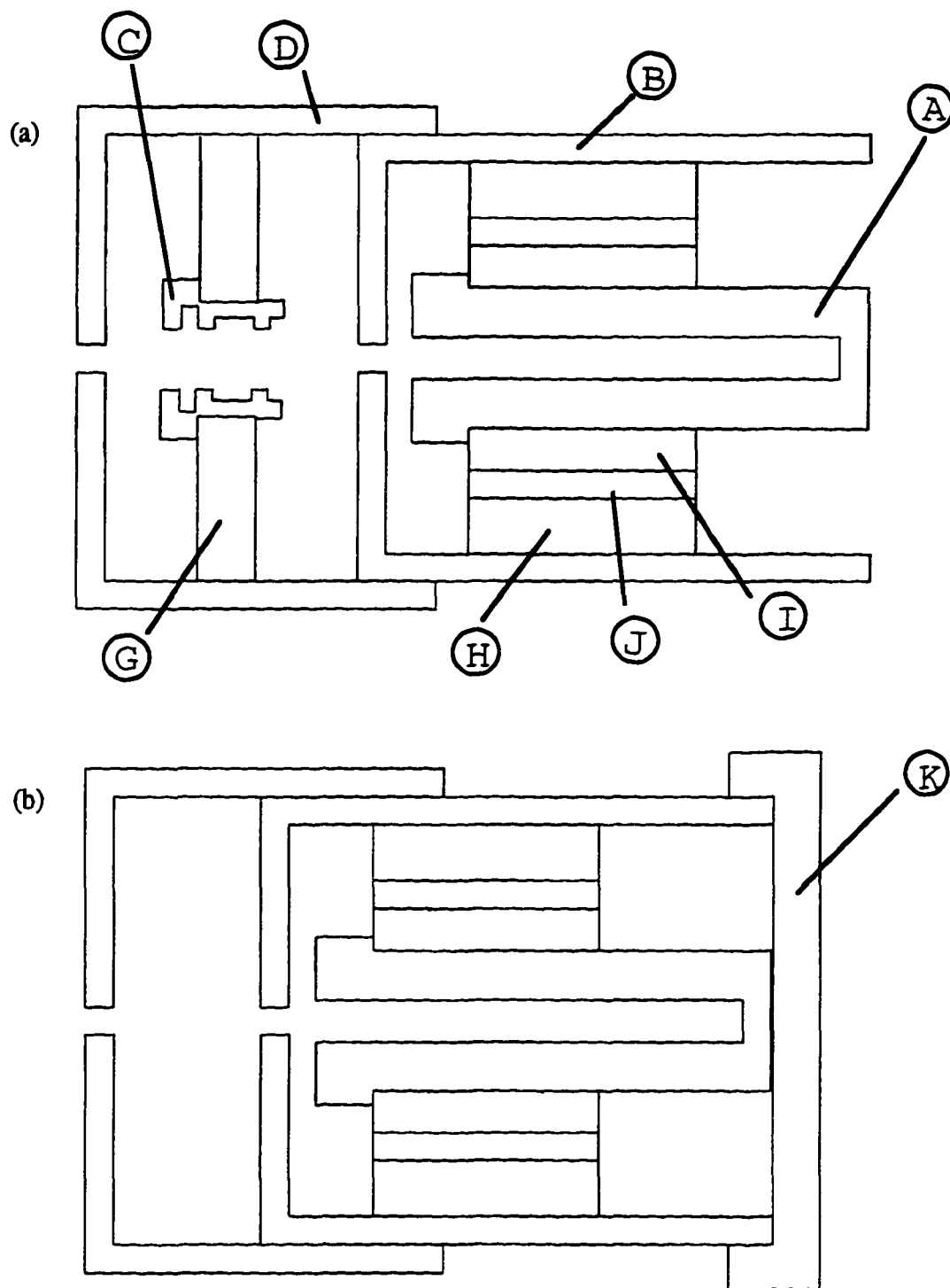


FIG. 4-11. (a) Initial and (b) present rotatable detector design.

electrons in the chamber. Apertures in the housings served to collimate the incoming (scattered) beam, and to determine the spot size observed on the sample and the detector's angular resolution. Teflon sleeves (G, H, and I) are used to mount both the filter and the FC in their respective housings. A grounded aluminum plate (J) is mounted between the FC and the housing in order to absorb any leakage current to the FC from the charged filter. (A zeroth-order calculation of the leakage current is given in Appendix A, which estimates it to be $\sim 10^{-13}$ A.)

(b) Present Detector Design

Figure 4-11(b) is a schematic of the detector design presently in use, and Table 4.8 summarizes major design parameters. Extensive testing of the original detector revealed that SE's produced on the filter's inner aperture surface were contaminating the signal to the FC to such an extent as to render the current measurement useless.⁹⁹ Specifically, the filter and rear housing wall together behaved as an electrostatic lens, focusing all SE's produced within the filter, along with the electrons comprising the desired signal, into the FC. Clearly a redesign was necessary. The decision was made to remove the filter altogether and accomplish energy-resolved measurements by biasing the FC itself. [NOTE: This was not done initially for fear that a negatively biased FC would eject all SE's and BSE's produced within it. A reasonable assumption at first glance, the energy diagram depicted in Fig. 4-12 clearly shows it to be false; the geometry of the FC is such that a SE or BSE produced within the cup sees no significant potential gradient inside the cup.] In addition to removing the filter, biasing of the FC dictated that the grounding plate located between the FC and housing no longer be grounded, but biased to approximately the same potential as the FC in order to minimize leakage current. The old filter housing remains a part of the detector only because the detector mounting collar, already built, requires its presence. It should not be detrimental to the signal. Both housing apertures, as well as the interior of the FC, are coated with colloidal graphite to reduce SE production. One further

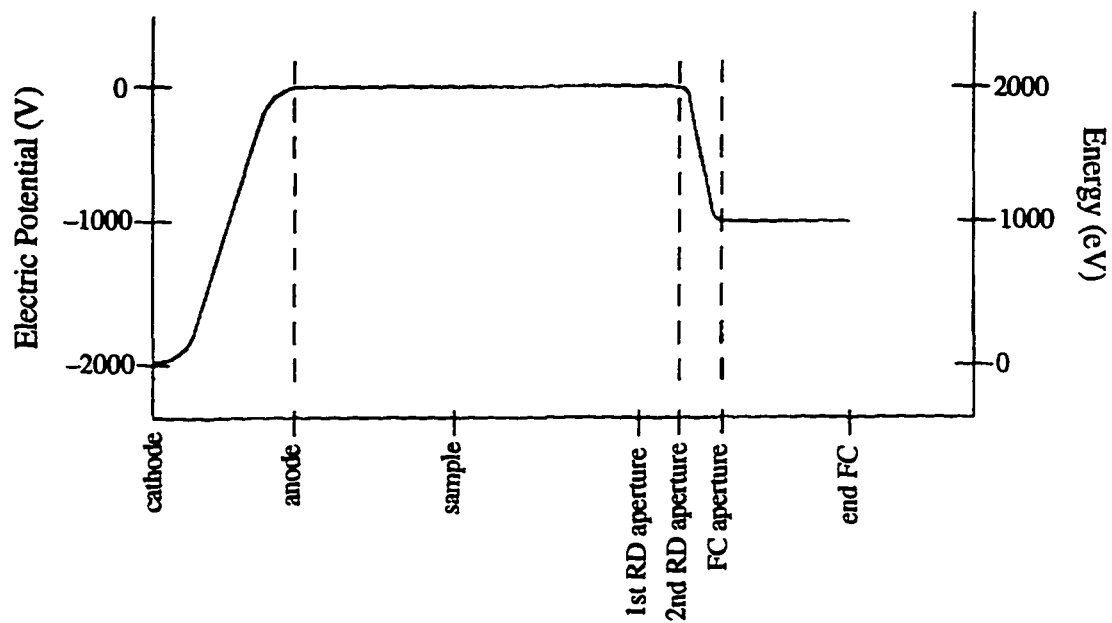


FIG. 4-12. Diagram tracing the potential (left vertical axis) and energy (right vertical axis) of an electron as it is accelerated from the electron gun cathode to the sample, is backscattered through the 1st and 2nd RD apertures, and enters the negatively biased FC.

TABLE 4.8. Rotatable detector (RD) specifications.

Parameter	Dimension
Length:	44.5 mm
Diameter:	3.2 mm
1st Aperture: (Filter Housing)	1.6 mm dia. by 1.6 mm deep
2nd Aperture: (FC Housing)	1.6 mm dia. by 1.6 mm deep
Faraday Cup	
Aperture:	2.4 mm
Depth:	123.8 mm
Aspect Ratio:	10:1
Energy Resolution:	~1% —see (6.3.2)

modification to the original design was the addition of an end cap (K), shielding the rear of the FC from stray electrons.

(c) Electrometer and Power Supply

Unlike typical sample currents, which are on the order of microamps, scattered beam angle- and angle-energy-resolved currents reaching the rotatable detector will have maximum values on the order of nanoamps (nA), to below our detection limit (see Appendix A for order-of-magnitude calculations). Consequently, our most accurate available electrometer, the Keithley Model 616 [described in (4.6.1) above], is used for all current measurements involving the rotatable detector. The power supply used to bias the RD must be capable of producing an electric potential commensurate with the incident beam energy, since a full backscattered energy spectrum is desired. A 0-3 kV DC power supply [Hewlett-Packard Model 6516A] is used in this role, in conjunction with a digital multimeter [BK Precision Model 388HD] for accurate measurement of detector potential.

4.6.5 Wiring, Connections, and Shielding

Low-level current measurements—such as those being attempted here—are notoriously susceptible to signal noise. Some important sources of noise currents include:¹⁰⁰ (i) frictional (triboelectric) effects within the wires ($\sim 10^{-15}$ - 10^{-8} A); (ii) electrochemical effects resulting from the presence of contaminants on both wires and insulators (10^{-13} - 10^{-8} A); (iii) induced currents due to time-varying ambient electric fields (electrostatic coupling); and (iv) currents arising between different grounding points (ground loops). Proper selection of wires and preparation of connections, thorough shielding, and careful grounding are effective means of minimizing these effects. A thorough discussion of these topics is therefore necessary to any meaningful evaluation of the experimental arrangement.

(a) Wires

Referring to Fig. 4-8, two kilovolt, 4.5 A coaxial Kapton wire [MDC KAP4] is used inside the chamber to connect the primary sample (A), tertiary samples (B), and RD Faraday cup (C) to their respective feedthroughs (D,E). This wire was selected for its UHV compatibility, small size (1.43 mm O.D.), and relatively high-voltage rating (originally listed by the manufacturer as 8 kV, and later amended to 2 kV). The wires are shielded by a conducting braid (85% min. coverage¹⁰¹). In an effort to minimize exposed insulators within the chamber, the outer Kapton insulating layer has been removed from the wire, exposing the shielding. The RD has been biased to 3 kV using this wire, with no ill effects noted.

Outside the chamber, 50-Ohm coaxial cable is presently used for all three signals: [Belden 8254 RG-62/U] for the sample and detector currents, and [Belden 8262 RG-58C/U] for the return current. These cables were selected for no other reason than they are shielded (96% coverage). Plans have been made to replace these cables with more suitable

selected varieties [either triaxial (Belden 922) or low-noise coaxial (Belden 9223)].

(b) Connections and Feedthroughs

Inside the chamber, primary and tertiary sample wires are attached to their respective sample holders via (non-magnetic) stainless-steel screws, and to the vacuum feedthrough via Be-Cu connectors crimped to the wires. All three wires connect to the same feedthrough—a ten-pin Type K thermocouple instrumentation feedthrough [ISI Model 9342012]. Fiberglass insulating braid covers each connector to prevent electrical contact with each other or the chamber wall. Connections to the sample holders are shielded by a copper foil which wraps around the back of the sample block, and connections to the feedthrough are shielded by a 1" dia. metal sleeve (an extension of the chamber wall, surrounding the feedthrough pins and connectors). Be-Cu push-on connectors are also used to attach the RD Faraday cup wire to the Faraday cup (via a mating pin pressed into the FC), as well as to its own single-pin, HV instrumentation feedthrough. The connection to the FC is shielded by the RD end cap (see Fig. 4-11), and the feedthrough connection is shielded by a copper sleeve (completely enclosing the connector and feedthrough pin).

Outside the chamber, Be-Cu connectors attach the three coaxial sample cables to the feedthrough. This arrangement is shielded by a 1" dia., 3" sleeve attached to the chamber. The primary sample signal is taken into the Model 616 electrometer via a triaxial input cable and connector [Keithley Model 6011], located at (F) in Fig. 4-8. This connection is made via a junction box (G). The two tertiary cables are joined via a 3-way BNC connector (H), and their combined signal is taken into the Model 160 electrometer via a standard banana plug. The coaxial cable carrying the RD signal attaches to the HV feedthrough with an MHV connector, and the signal delivered to the Model 616 electrometer via a junction box [(I) in Fig. 4-9], triaxial cable (J), and connector identical to those used for the sample current.

(c) Grounding

The following grounding scheme is employed in an effort to prevent ground loops:

1. Sample wires inside the chamber are bundled together with copper wire, their respective braided shields in solid electrical contact with each other. These shields are grounded to the chamber via a single copper wire running from the bundle to a bolt on the bottom of the chamber apparatus [ground (1) in Figs. 4-8 and 4-9]. The bundle has no other points of contact with the chamber.
2. Outer shields on the exterior sample-current and detector-current cables are connected to each other at a single point, (K) and (L), respectively, and to the electrometer case grounds via the triaxial input connectors [grounds (3) and (4)].
3. Inner shields on the sample- and detector-current triaxial cables are grounded through their respective power supplies, as are the shields on the exterior coaxial return-current cables [grounds (5) and (6)].
4. The grounding plate (M) surrounding the RD Faraday cup is grounded to the FC signal wire shielding (N), which is itself grounded to the chamber via a copper wire to a screw on the RD housing at (O) [ground (2)]. The cable shielding does make contact with the chamber (via the chamber apparatus) at several other locations, though these contacts are intermittent and should not be considered solid grounding points.

[Note: Grounds (1) and (2) are regarded as separate grounds, since they attach to the chamber at different locations. Grounds (3-6) are all “third-prong” grounds, where the third-prong ground of the power strip is connected by a single grounding line to the master ground terminal strip of the chamber. The terminal strip itself is connected to the third prong of a single 110 V wall socket.]

It is noted that replacement of the exterior coaxial cables in favor of (low-noise) triaxial cables will allow all inner shields (outside of the chamber) to be biased (floated) along with the signal-carrying conductors. Such an arrangement will aid in the reduction of leakage current (resulting from the biasing of the samples and RD Faraday cup with the

signal-carrying conductors within the cables).

4.7 Chamber Apparatus

The Sample-Detector Assembly (depicted in Fig. 4-13) consists of the RD (Fig. 4-14), the Sample-Block Assembly (Fig. 4-5), and a support structure [described in (4.7.2) and (4.7.3)]. This structure, enclosed by the magnetic shield described in (4.3.2), forms the Chamber Apparatus. (Major constituents of the various subassemblies are summarized in Table 4.9.) This “soup can” assembly is attached to a combination linear/rotary motion feedthrough via an adapter (A in Fig. 4-13) and inserted into the vacuum chamber from the top, as depicted in Fig. 4-1. Important Sample-Detector Assembly and Chamber-Apparatus design parameters are summarized in Tables 4.10 and 4.11.

Almost every piece of the Chamber Assembly was custom designed and fabricated. As the heart of this experimental design, it will be helpful to discuss its components in some detail. First however, a summary of major design decisions is presented.

4.7.1 Design History

Once again recall the desire for simultaneous angle- and energy-resolved characterization of the scattered beam. The decision to use a single, rotatable detector to obtain angle-energy-resolved measurements was first. A *single* detector was selected (as opposed to an array of detectors situated at various scattering angles about the sample) because a suitable model had already been designed and built (4.6.4). This choice then dictated that the detector be *rotatable* about the sample. The apparatus resulting from these initial design decisions is depicted in Figure 4-13. Referring to Fig. 4-16, the sample is tilted 45° to allow the detector to be placed farther from the target within the confines of the vacuum chamber. Positioning the detector as far from the sample as possible, along with elevating the detector above the incident beam and angling it 59° down (in order to aim it at

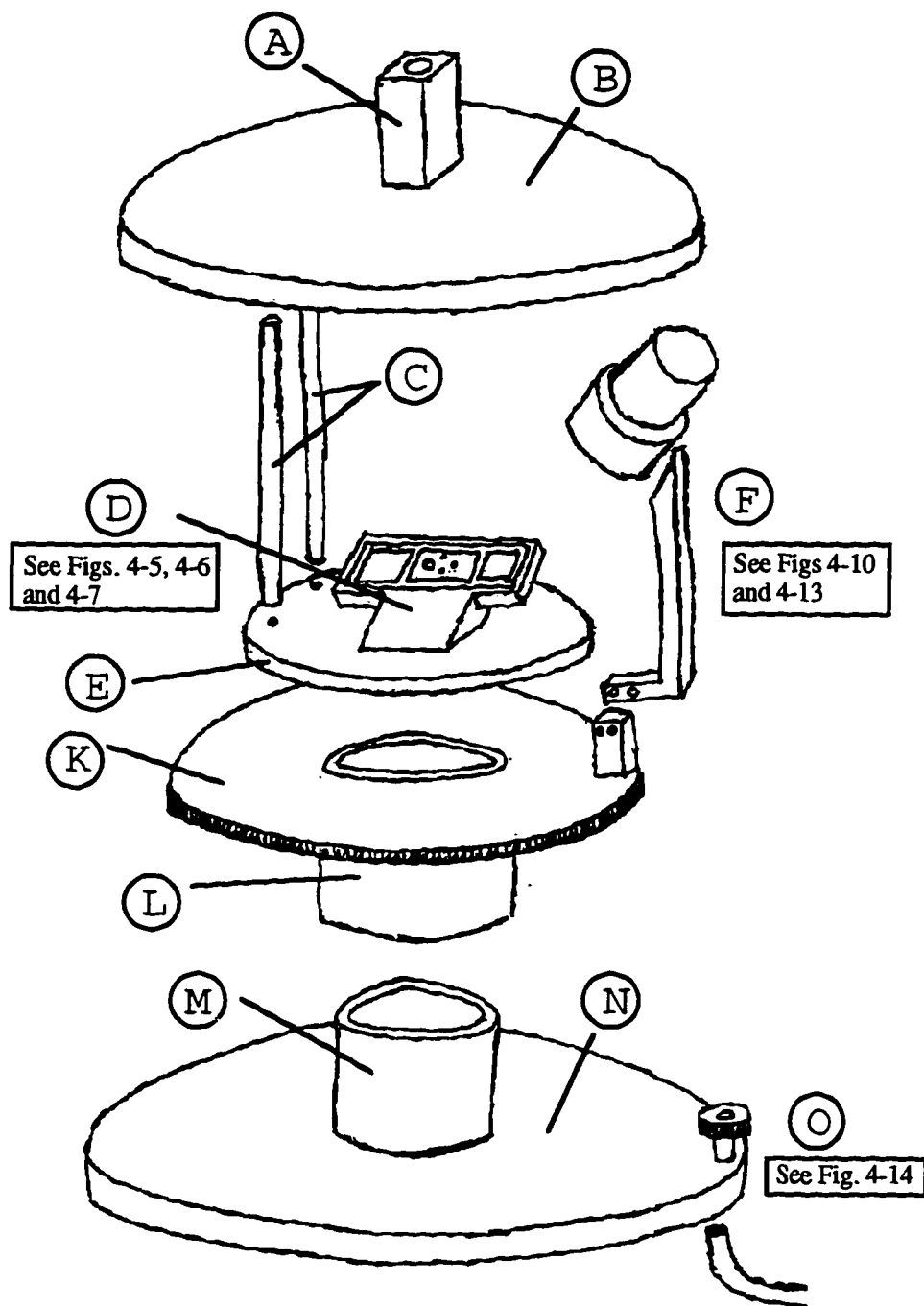


FIG. 4-13. Sample-detector assembly.

TABLE 4.9. Major constituents of various subassemblies.

Assembly	Consists of:
Chamber Apparatus	sample-detector assembly, magnetic shield
Sample-Detector Assembly	sample block assembly, rotatable detector, spur gear, rotary cable, support structure
Sample Block Assembly	sample block, sample holders, samples, heater, mounting plate, copper shield
Rotatable Detector (RD)	detector housing, ground plate, Teflon insulating sleeves, Faraday cup
Support Structure	Base plate, axle, rotating sleeve, rotating plate, RD arms, support rods, top plate, feedthrough adapter

the center of the sample), minimizes the range of scattering angles over which the detector housing blocks the incident beam (Fig. 4-17). With the detector placed at low α 's, the limiting factor becomes the width of support arm [(I) in Fig. 4-14] rather than the width of the RD (G). This arrangement allows for characterization of the scattered beam for $14^\circ \leq \alpha \leq 76^\circ$ (see Fig. 4-16). To enable measurements at α 's $> 76^\circ$, a second support arm—one that angles the RD at 45° rather than 59° —is also available.

Two important operational points regarding the above arrangement should be mentioned, both stemming from the fact that as the RD rotates about the sample, the *azimuthal* angle of the scattered beam, ϕ_s (see Fig. 4-2), is continually changing. First, from Fig. 4-2, it is clear that the ratio of the change in α to the change in ϕ_s is nonlinear as the detector moves about the sample. The specific relationship between these two angles is given in Appendix B. Secondly, *this arrangement does not allow for meaningful angular crosssections of the scattered beam in the case of a non-normal incident beam*. This is because, unlike normally incident beams, non-normal incident beams produce scattered beams which are not azimuthally symmetric⁷⁷—i.e., the scattered beam becomes a function

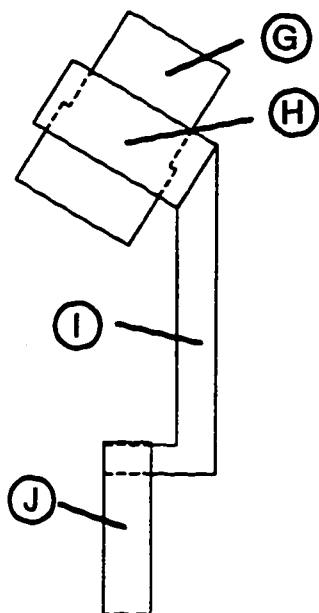


FIG. 4-14. Rotatable detector (G) and mounting collar (H) as mounted on 59° arm (I) and additional support arm (J).

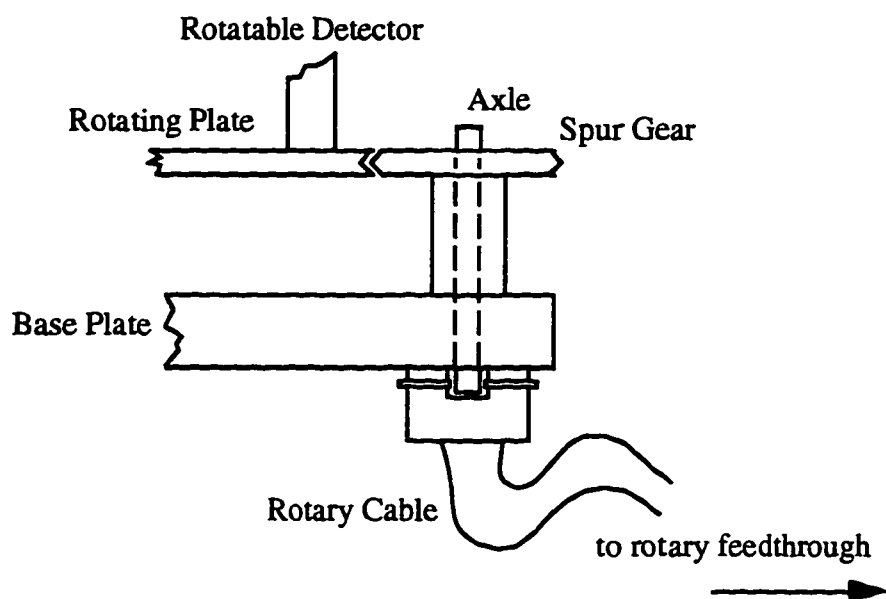


FIG. 4-15. Rotatable detector rotation mechanism.

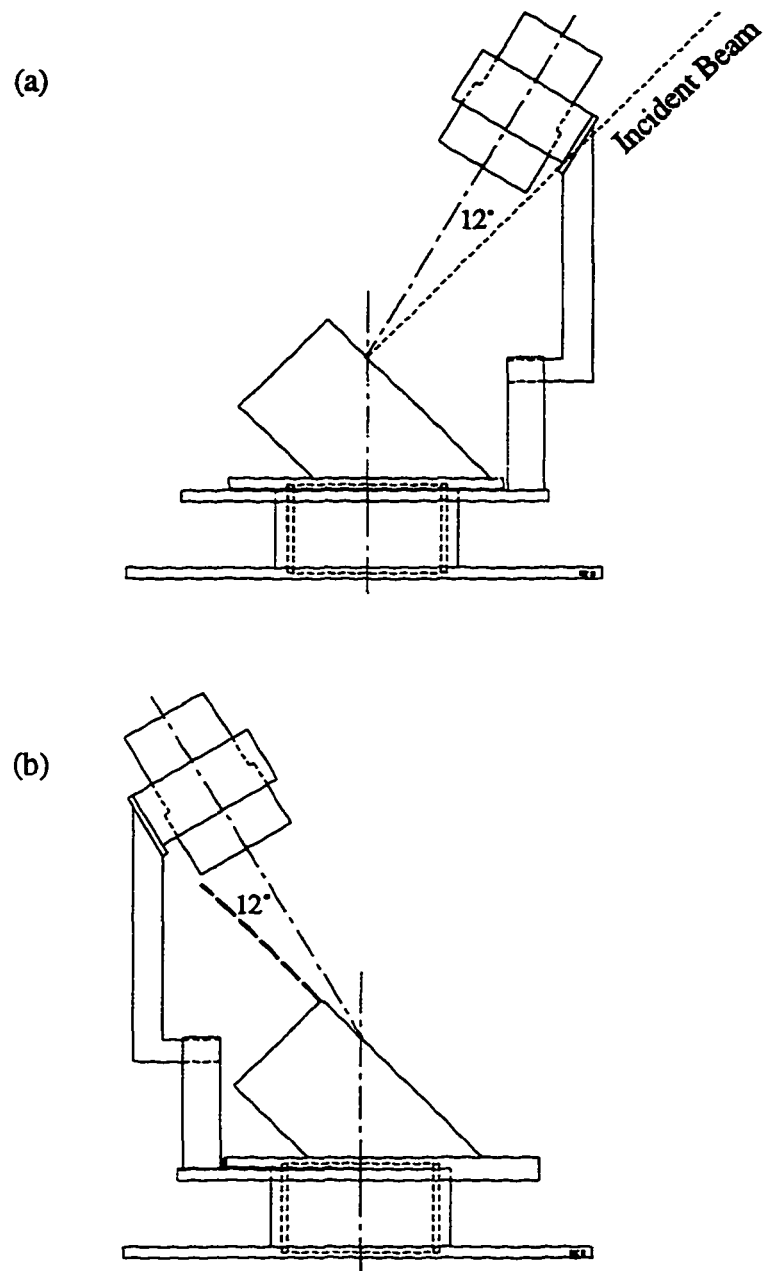


FIG. 4-16. Rotatable detector mounted on 59° support arm.

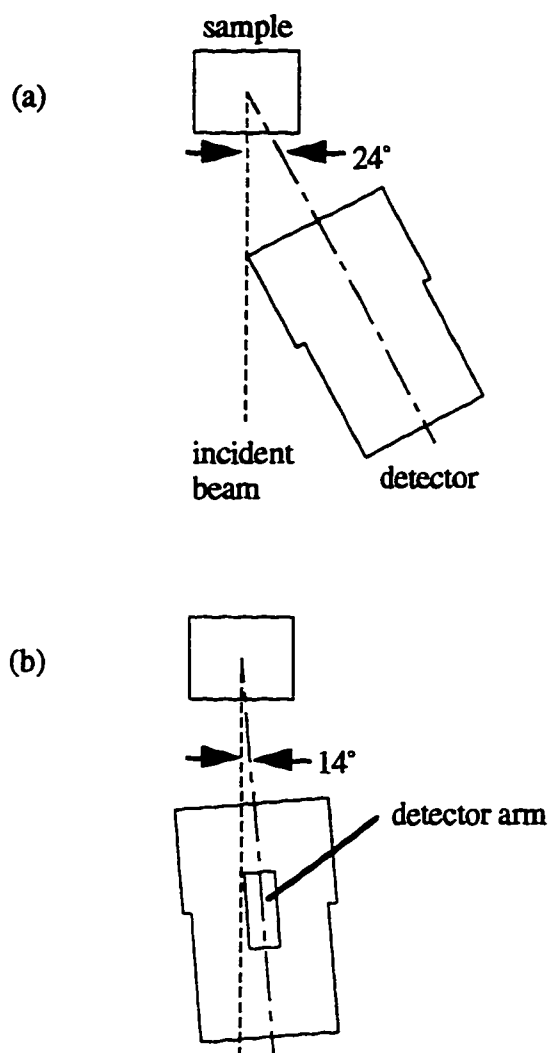


FIG. 4-17. Minimum scattering angle available to RD mounted on (a) 45° arm (limited by detector housing radius) and (b) 59° arm (limited by detector arm width).

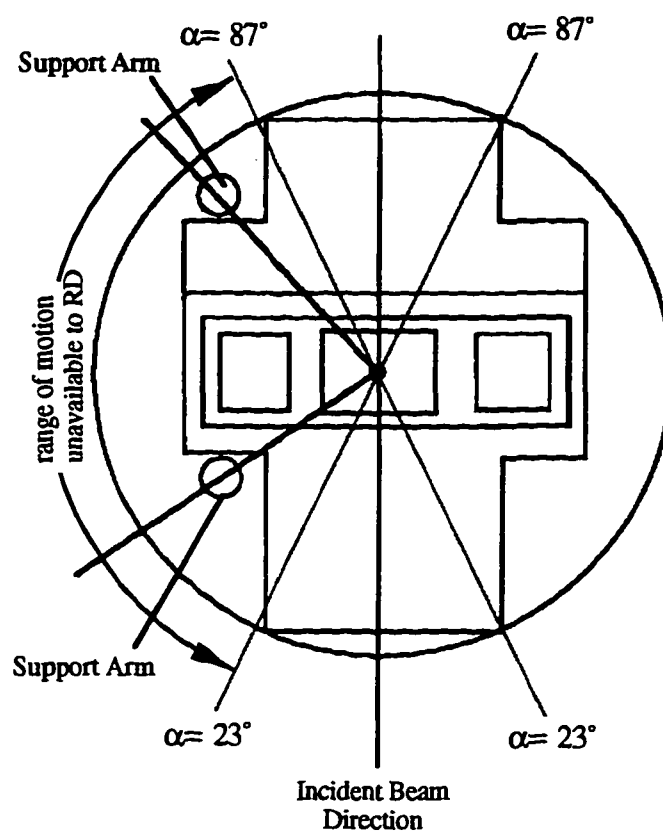


FIG. 4-18. Limits on RD motion about the sample and regions of overlapping angle-resolved measurements.

of φ_s , for $\varphi_s \neq 90^\circ$. Since the apparatus described above cannot measure a range of α 's for a *single* φ_s , angle-resolved measurements are only meaningful for a scattered beam which does not depend on φ_s —as should be the case for a normally incident beam.

4.7.2 Rotatable Detector Mounting and Rotary Feedthrough

The RD (G in Fig. 4-14) can be mounted at either 45° or 59° relative to horizontal, and rotated about the sample on a vertical axis (see Figs. 4-13 and 4-16). It is mounted in an aluminum collar (H), which is subsequently mounted to either the 45° or 59° arm (I). This arm is then mounted to the rotating plate (K) via the plate arm (J). Both the detector-detector arm mounting and the detector arm-plate arm mounting have sufficient play to allow for aiming of the detector during assembly. The rotating plate consists of a gear (K) pressed onto a sleeve (L), and slipped over the support shaft (M)—itself pressed into the base plate (N); thus the support shaft acts as an axle about which the gear can rotate. The arrangement is lubricated with a small amount of colloidal graphite. Rotation is achieved with a matching gear attached to a rotary feedthrough [MDC Model BRM-133] via a cable arrangement (see Figs. 4-13 and 4-15). The rotary feedthrough is graduated in 5° increments, and bakable to 100°C . Construction materials are almost exclusively aluminum, and all materials (with the exception of the rotary cable), including screws, are non-magnetic. In deference to their importance, the following points concerning construction of the Sample-Detector Assembly are emphasized:

1. All materials *within the can* are nonmagnetic, in an attempt to eliminate all ambient magnetic fields and their associated effects on charged particle trajectories.
2. There are no exposed insulators within the can, as electric fields associated with electrostatic charging of insulators under charged-particle bombardment will also influence charged-particle trajectories.
3. Tolerances on most machined parts were to .001" in an attempt to keep the RD always looking at the center of the sample as it rotates about the sample.

TABLE 4.10. Summary of sample-detector assembly parameters.

Parameter	59° Arm	45° Arm
Target Distance, d_t : (dist. from sample to front of 2nd aperture)	7.9 cm	3.8 cm
Field of View	3.34×10^{-2} sr (1.5 cm spot on sample)	3.34×10^{-2} sr (0.6 cm spot on sample)
Angular Resolution		
point source:	1.2° (3.2×10^{-4} sr)	2.4° (1.4×10^{-3} sr)
1.5 mm beam spot:	2.3° (1.3×10^{-3} sr)	4.8° (5.5×10^{-3} sr)
Range of Scattering Angles	$14^\circ - 76^\circ$	$35^\circ - 90^\circ$

TABLE 4.11. Chamber-assembly specifications.

Diameter:	5.3"
Height:	9.25"
Range of Motion	
Linear:	± 0.25 " from center in x ± 0.25 " from center in y ± 0.50 " from center in z
Rotational:	full 360° about the z-axis

4.7.3 Support Structure

The support structure is that portion of the chamber apparatus which facilitates mounting of the Sample-Detector Assembly in the vacuum chamber. It consists of a mounting arm (A in Fig. 4-13), a top plate (B), and two support rods (C). The design provides for a rigid, stable structure as mounted to the combination linear/rotary feedthrough shaft. The presence of the two support rods precludes full rotation of the RD about the sample (Fig. 4-18), though the RD's range of motion is more than adequate to cover the full range of scattering angles. Note from the figure that this arrangement allows for angle-resolved measurements to be taken symmetrically about the x -axis over a moderate range of scattering angles (0° to 23° , and 87° to 90°). For example, a measurement at $\alpha=23^\circ$ may be taken with the RD positioned at $\phi_s = \pm 30^\circ$ (from the conversion table in Appendix B), and a measurement at $\alpha=87^\circ$ may be taken at $\phi_s=154^\circ$ or at $\phi_s=206^\circ$. Such a capability will prove useful when verifying the RD's alignment (6.3.2).

4.7.4 Cleaning and Assembly of Chamber Apparatus

One hundred and twenty-five parts together comprise the chamber apparatus.¹⁰² All parts were cleaned and assembled using standard UHV procedures. The assembly sequence is important, involving a number of critical steps that can easily be overlooked. Consequently, a checklist detailing the assembly procedure has been prepared.¹⁰³

4.8 Measurement Technique

Assessing the reliability of any set of physical measurements requires a detailed knowledge of how the measurements were made—that is to say the measurement technique. As an example, the checklist detailing measurement procedures for total δ and η determination is given below. Similar procedures for $\delta(E)$, $\delta(\alpha)$, $\eta(\alpha)$, $\delta(\alpha, E)$, and

$\eta(\alpha, E)$ have been prepared and are compiled in a handbook kept with the apparatus.

Total δ and η Measurement Checklist

Preliminary Configuration / Preparation

1. Chamber apparatus - centered in chamber ($x=0''$, $y=0''$, $z=4.75''$)
2. Rotate chamber apparatus to $\phi=20^\circ$ (to block incident beam from sample during beam warm-up)
3. Sample current electrometer (Keithley 616)
 - a. Range - 10^{-6} A
 - b. Mode - fast
 - c. Sensitivity - auto
 - d. Power - on (30 min. warm-up)
4. Return current electrometer (Keithley 160)
 - a. Range - 100 nA
 - b. Power - on (30 min. warm-up)
5. Record base chamber pressure
6. Electron gun
 - a. Beam energy - set to desired value
 - b. Power - on (60 min. warm-up)
 - c. Focus - appropriate for beam energy

Measurements

1. Sample power supply - check set to 0 V.
2. Sample power supply - on.
3. Zero electrometers
4. Rotate chamber apparatus to $\phi=0^\circ$
5. RD - check out of beam line

6. Visually center beam on sample
7. Adjust focus for smallest beam spot
8. Record operating chamber pressure
9. Record unbiased sample current ($I_{s(0)}$)
10. Record unbiased return current ($I_{r(0)}$)
11. Deflect beam into large FC
12. Record beam current (I_b)
13. Return beam to center of sample
14. Sample power supply - set to +50 V
15. Record biased sample current ($I_{s(50)}$)
16. Record biased return current ($I_{r(50)}$)
17. Calculate δ via

$$\delta = \frac{I_{s(50)} - I_{r(50)} - I_{s(0)} + I_{r(0)}}{I_b}$$

18. Calculate η via

$$\eta_{(e)} = \frac{I_b - I_{s(50)} + I_{r(50)}}{I_b}$$

19. Repeat steps (6) - (18) for all desired beam energies.

Having detailed the measurements to be performed, as well as the apparatus and technique for performing them, attention is now turned to verification of the apparatus and technique.

CHAPTER 5

SUPPORT EQUIPMENT TESTING

Testing of the apparatus to date has consisted of (i) operational characterization of the support equipment and (ii) overall evaluation of experimental design and technique. This chapter summarizes results of the former, detailing operating characteristics of the vacuum system (5.1), electron gun (5.2), detection systems (5.3), and motion feedthroughs (5.4). Evaluation of the experimental design as a whole—i.e., chamber apparatus performance and measurement technique—is addressed in Chapters 6 and 7.

5.1 Vacuum System

The vacuum system described in Chapter 4 has been characterized previously with respect to total chamber pressure, levels and types of contaminants, and pump-down times,⁸² though not as configured for the present investigation (i.e., with the chamber apparatus installed, and with an operating electron source incident on a sample). In a bare configuration, the system has been shown capable of attaining base pressures of $\sim 2 \times 10^{-11}$ Torr, with negligible carbon contamination (generally regarded as the most obnoxious). Results of testing in the chamber's present operational configuration are given below.

5.1.1 Total Chamber Pressure and Pump-Down Time

Total chamber pressures are distinguished as either *base* pressures or *operating* pressures. A system's *base pressure* is the lowest attainable pressure with only the pumps—and no other equipment—in operation, and it is this parameter that is generally cited when characterizing the quality of the vacuum. A system's *operating pressure* is that pressure typically present within the chamber under operating conditions—e.g., with an operating electron beam incident on a sample (in the case of the present investigation). Table 5.1 summarizes the results of four chamber pumpdowns performed over a four-

TABLE 5.1. Vacuum chamber performance.

Pumpdown	Bakeout	Base Pressure Range (Torr)
1	none	High 10^{-8} after 1 day, low 10^{-8} after 10 days, mid- 10^{-9} after 15 days
2	75°C (12 hrs)	Low 10^{-9} immediately
3	100°C (24 hrs)	Low 10^{-9} immediately, high 10^{-10} after 1 day
4	97°C (20 hrs)	Low 10^{-9} immediately, high 10^{-10} after 1 wk

month period during system testing.^{104,105} Note that the pressures listed are base pressures (typical operating pressures are 2-5 times greater, in the mid- 10^{-9} Torr range). These data show that the vacuum system, as configured for this investigation, reaches UHV pressures with only modest bakeouts. (The rotary feedthrough and Teflon insulating sleeves in the RD presently limit bakeout temperatures to below 100°C.)

5.1.2 Contaminants

As mentioned earlier, UHV work is not only a question of total pressure, but also of the partial pressures of contaminants. The RGA allows for the identification of contaminant species within the chamber.⁸⁴ Certain limitations in species identification arise from the fact that the RGA uses mass-to-charge ratios as the means of distinction; different species with the same mass and charge, therefore, cannot be distinguished directly (e.g., N_2^+ and CO^+). Figure 5-1 is a representative plot of partial pressure vs. atomic weight for residual gas in the chamber with no equipment running, at a base pressure of 1.4×10^{-9} Torr. Atomic and molecular hydrogen, carbon, oxygen, OH, water, CO/ N_2 , and CO_2 are shown to be the major contaminants. The relatively large water presence is the result of only a modest bakeout having been performed. The reason for the presence of CO and CO_2 remains unclear, though may have to do with carbon contamination introduced with

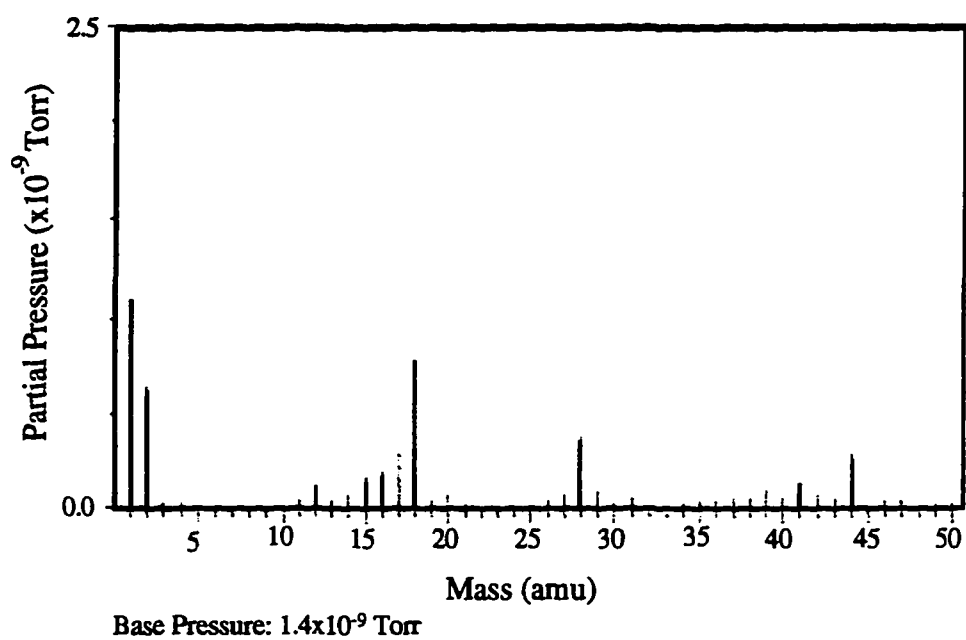


FIG. 5-1. RGA spectra for quiet chamber (no equipment operating).

the chamber apparatus (discussed further in Chapters 6 and 8). The peak at 28 amu could be attributed to molecular nitrogen (N_2) and/or CO, though the relative abundance of carbon (mass 12) and atomic oxygen (mass 16), and absence of atomic nitrogen (mass 14), suggests that most of this peak can be attributed to CO. The absence of fluorine (mass 19) takes on significance in Chapter 6.

5.2 Electron Gun

5.2.1 Beam Current

Beam current characteristics of primary concern are *magnitude* and *stability*, where stability refers to the dynamical behavior of the magnitude. Specifically, it is important that the magnitude of the beam current not vary significantly over time periods on the order of those required to perform individual measurements. Tests regarding these parameters were performed by directing the beam into the large FC in the sample and measuring overall beam current, as well as its behavior over time. Data for magnitude are presented in Table 5.2, and show typical beam currents to be $\sim 10 \mu A$. Note that the values presented represent the range of beam currents measured for various beam energies over several months of operations; *they do not represent the variation in beam current for a given trial.*

Beam-current stability observations have been somewhat informal to date; a quantitative assessment of beam stability is therefore unjustified for most beam energies. The exception is a 32-hour investigation for $E_b = 2.0 \text{ keV}$. Results of this test are depicted in Fig. 5-2. These data show worst-case variations $\sim 4\%$ over periods of several hours, and $< \sim 0.3\%$ over periods of several minutes. These results represent exceptional stability. As a qualitative observation, similar behavior has been observed for energies greater than approximately 1.0 keV. Below 1 keV the beam current appears considerably more unstable, though this has not yet been quantified. Stability over time periods on the order of minutes is particularly important in that this is the time period required to perform a full set

TABLE 5.2. Typical beam-current magnitudes and spot sizes for various beam energies.

Beam Energy (keV)	Beam Current (μ A)	Spot Size (mm) (FWHM from beam profiles)	Focus (spot size only)
1.0	8.6 - 14.9	1.3	0
1.5	9.5 - 15.0	1.4	0
2.0	9.1 - 16.5	1.35	15
2.5	6.5 - 15.8	1.35	30
3.0	5.7 - 16.3	1.2	20

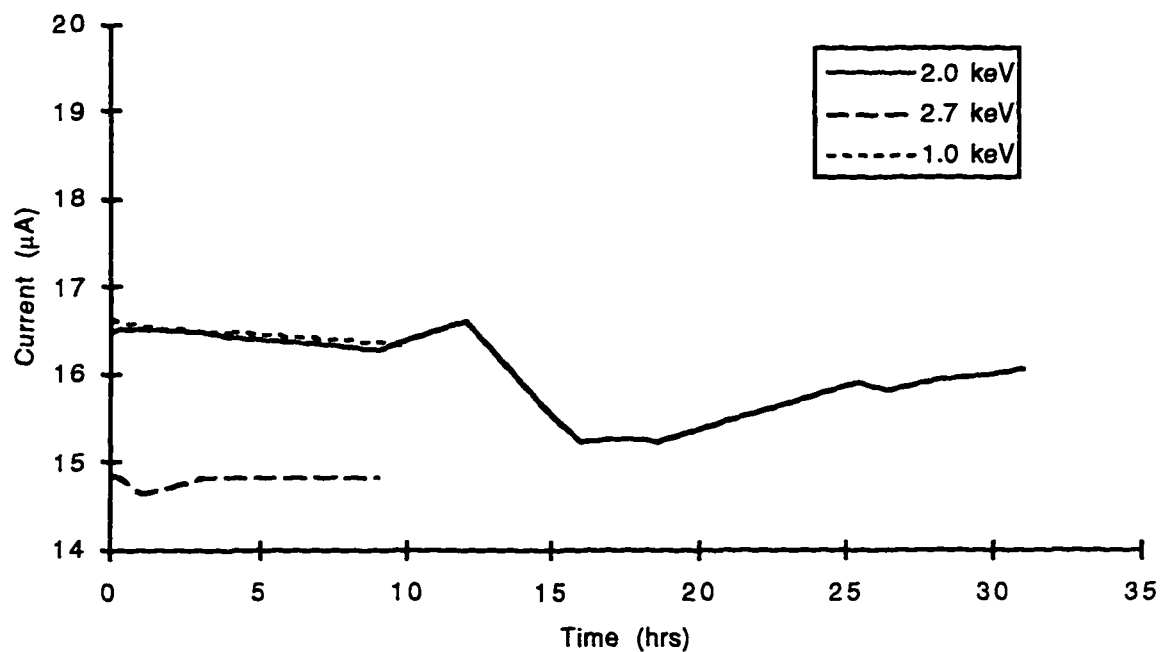


FIG. 5-2. Electron gun beam current stability.

of measurements. [NOTE: significant changes in beam current can occur rapidly as a result of filament wear or insufficient warm-up time, though this is not the normal state of affairs and such an event would be immediately noticeable should it occur during a measurement.]

5.2.2 *Beamspace*

Beamspace characteristics of primary concern are *visibility*, *mobility*, and *size*.

Visibility and mobility relate to one's ability to place the spot at the desired location on the sample, while size of the beam spot will determine the angular resolution of the rotatable detector (see, for example, Table 4.10).

Initial visibility and mobility tests were conducted with a small phosphorous screen in the sample holder. The beam spot was easily visible as a blue spot on the screen at all energies above a few hundred eV. Moving the spot is achieved without difficulty via the *x*- and *y*- deflector plate controls on the electron gun controller, and the range of motion extends beyond the primary sample in all directions. Subsequent testing involving an aluminum sample (discussed in Chapter 6) revealed that the beam was also visible (once again as a blue spot) on aluminum at all beam energies above 900 eV. [NOTE: If the spot is not visible, the four Faraday cups machined into the sample can be used to center the beam on the sample by simply noting the settings on the horizontal and vertical deflectors when the spot is in each Faraday cup, and using this information to calculate the proper settings for the point midway between the four cups.]

Characterization of the beamspace size is accomplished by directing the spot onto the sample and, using the linear motion feedthrough, tracking one of the small FC's built into the sample across the spot in the *y*-direction. Size determination is then accomplished by plotting sample-current vs. sample position. This was accomplished for a range of energies, and the results are presented in Table 5.2. Note that adjusting the electron gun focus will change the spot size for a given target distance. The data given in the table

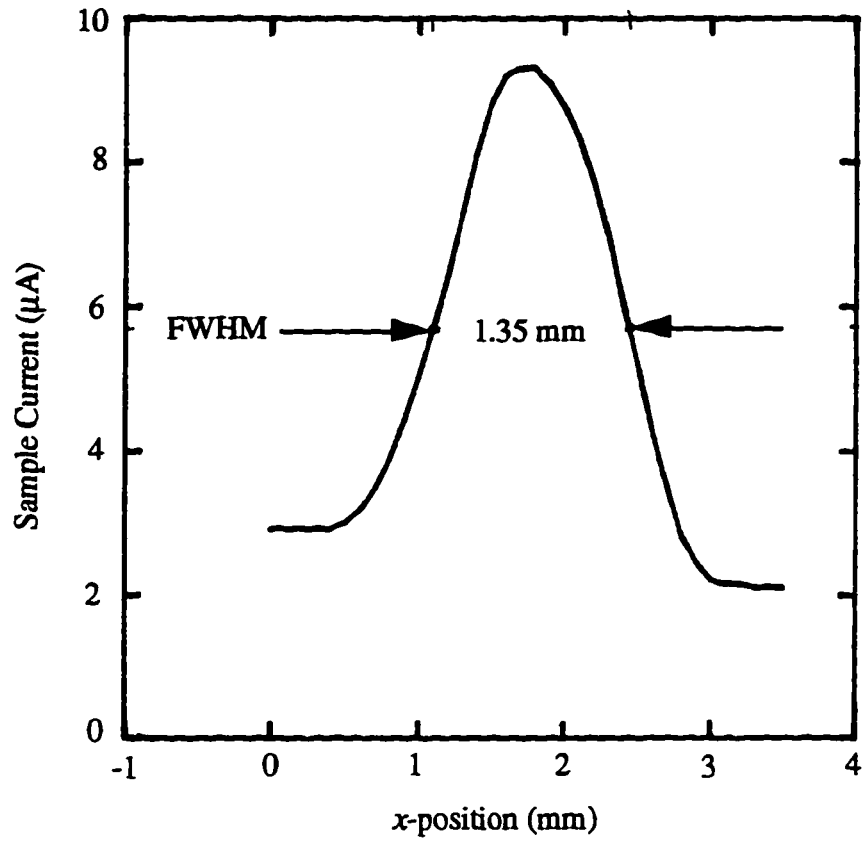


FIG. 5-3. Typical electron gun beamspot profile. The spot size is seen to be 1.35 mm at FWHM. $E_b=2.0$ keV, focus=15 (units arbitrary).

represent the smallest spot size attainable. A typical current vs. position beam profile is illustrated in Fig. 5-3. Similar testing must be accomplished with the ion gun, though this has not yet been done.

5.3 Detection Electronics

Characterization of the detection systems consisted of stability testing of the electrometers, and determination of various background currents, or noise.

5.3.1 *Electrometer Stability*

Performance testing indicates that the Keithley Model 616 electrometers require a minimum 30-minute warm-up before they will maintain a current zero; 1-2 hours, however, is preferable. Once warmed up, both electrometers hold their zeroes to within $\sim 1 \times 10^{-14}$ A over periods of several hours.

5.3.2 *Background Currents*

Shielding of connections has evolved through several generations, where changes leading to the present scheme have been based primarily on noise testing. Table 5.3 summarizes the background currents registered by the apparatus as presently configured. Referring to the table, noise due to ion gauge operation does not pose a problem in that the ion gauge need not be operating while measurements are being performed. Similarly, noise due to the ion pump can be eliminated by turning it off while making measurements, though this is only necessary when accuracy in the sample current measurements on the order of 10^{-14} A is required (e.g., for energy-resolved SE determinations). Noise in the electrometers with all equipment turned off was found to be $\sim 1.7 \times 10^{-15}$ A,¹⁰⁶ in agreement with the manufacturer's claims for the sensitivity of the instruments.⁹⁵ Finally, detector currents induced by moving the RD ($\sim 10^{-11}$ A) pose no difficulties as measurements are not taken while the RD is in motion.

TABLE 5.3. Magnitude and sources of background currents (noise).

Measurement	Noise	Source
Sample Current	$\sim 10^{-14}$ A	ion pump
	$\sim 10^{-13}$ A	ion gauge
Rotatable-Detector Current	$\sim 10^{-14}$ A	ion gauge
	$\sim 10^{-11}$ A	detector motion
	$\sim 10^{-12}$ A	leakage current (FC bias -50 V)
Noise Detection Limit	10^{-15} A	

5.3.3 Rotatable-Detector Leakage Current

Leakage current in the RD, resulting from negative biasing of the RD Faraday cup, currently poses a significant problem for energy-resolved angular measurements. *Leakage current* refers to the migration of charge from the Faraday cup [A in Fig. 4-11(a)] to the ground plate (J), via the Teflon sleeve (I) that separates the two. Calculations in App. A reveal that for a leakage current $\sim 10^{-12}$ A, induced by a potential of -50 V on the Faraday cup, the resistance for the Teflon is on the order of $10^{13} \Omega$ —a reasonable value. Biasing the ground plate to approximately the same potential as the FC, and replacing the Teflon with a better insulator should all but eliminate this difficulty [see (8.1.2)].

5.4 Motion Feedthroughs

5.4.1 Rotary Feedthrough

Rotary tests of the RD about the sample revealed the length of the rotary cable (connecting the rotary feedthrough to the RD gear) to be important. Specifically, the cable must be long enough to allow for rotation and translation of the entire chamber apparatus, but short enough to minimize play, or “sloppiness” in the motion of the RD.

Experimenting with cable lengths showed 28 cm to be sufficiently long to allow for all desired motion of the can, while providing for smooth motion of the RD. Nevertheless, some backlash ($\sim 9^\circ$) exists when reversing the direction of motion of the RD.

5.4.2 *Linear/Rotary Feedthrough*

No difficulties have been experienced in moving the can through its full range of motion, however one must be careful not to rotate the can more than one full revolution — either clockwise or counterclockwise — in order to avoid tangling the RD rotary cable with some of the interior wiring. The sample is aligned in the chamber for normally incident electrons for the following settings on the linear/rotary feedthrough: $\phi=0^\circ$, $x=0$, $y=0$, and $z=4.75$ ".

CHAPTER 6

PRELIMINARY MEASUREMENTS—ELECTRON BOMBARDMENT OF ALUMINUM

Reproduction of previously reported, widely accepted results is perhaps the surest way to validate new equipment and methods. This chapter describes efforts to reproduce previously reported SE and BSE yields for bulk aluminum under electron bombardment at normal incidence, using the apparatus and technique described in Chapters 3 and 4. Aluminum was chosen for its status as an oft-characterized material in the literature,² as well as an ubiquitous material found in spacecraft construction. In hindsight, the choice of aluminum as the material for initial verification testing has proven less than ideal, though highly educational—an observation addressed further in Chapter 8.

Preceded by a brief description of the sample and its preparation (6.1), total δ and η values obtained in this investigation are presented, followed by the results of four additional diagnostic investigations (6.2). A brief discussion of preliminary energy-, angle-, and angle-energy measurements (6.3) concludes the chapter. Comparison of δ and η values presented here with values found in the literature is deferred until Chapter 8.

6.1 The Sample

Given the objective of this work—to characterize a pure, smooth Al surface—and given aluminum's strong penchant for oxidation, careful sample preparation is clearly important. The aluminum sample used in this investigation is a commercial sample of 99.99% (4N) purity.¹⁰⁷ Major bulk contaminants are Ca (13 ppm), Cu (12 ppm), Fe (<77 ppm), Si (<72 ppm), and Mg (17 ppm). Prior to its characterization, the sample underwent three phases of preparation: machining, polishing, and cleaning. *Machining* entailed cutting the aluminum to the proper size and drilling the various Faraday cups into the

sample (see Fig. 4-6) . *Polishing*, required to effect a smooth surface and to remove the bulk of any surface oxidation, was accomplished in several stages. After machining, the sample was hand-polished in successive steps with fine-grit sandpaper, and 20 μm , 3 μm , and 0.3 μm Al_2O_3 powder. Mechanical polishing completed the process. It is significant to note that the cloth used in the mechanical polishing was not clean, but replete with by-products of previously polished materials (this fact likely accounts for some of the data to be presented later). *Cleaning* of the sample, intended to remove contaminants such as dust and fingerprints, was accomplished ultrasonically in baths of methanol and methylene chloride just prior to its insertion into the vacuum chamber. Nevertheless, the sample was exposed to the ambient atmosphere for approximately one hour prior to evacuation of the chamber—more than enough time to permit significant oxidation.

6.2 Total SE and BSE Yields, δ and η

Results of total δ and η determinations are listed in Table 6.1, and depicted in Fig. 6-1. The exact procedure used to obtain these values is that presented in (4.8). Immediately during the course of the measurements the sample current was observed to be highly dynamic, while the beam current remained stable. With the beam continuously bombarding the same location on the sample's surface, the general trend was for the sample current to start low and then increase. Upon moving the beam spot to a fresh location on the sample, the sample current would initially increase very quickly, become quasi-stable after ~20 minutes—i.e., become stable over time periods on the order of minutes—but continue to increase over longer periods. Hence, two sets of measurements were performed—one immediately upon moving the beam to a new location, and one after a period of approximately 20 minutes, when the dynamics had slowed.

Noting that the initially fast changing sample current had a pronounced effect on δ —as evidenced by the large spread in initial δ 's—but an almost negligible effect on the

TABLE 6.1. Measured δ and η for aluminum.

Beam Energy (keV)	δ		η	
	Initial	After ~20 min.	Initial	After ~20 min.
1.0	.73 \pm .68 \pm 1%	.43 \pm 2%	.237 \pm 3%	.200 \pm 3%
1.5	.72 \pm .57 \pm 1%	.33 \pm 2%	.223 \pm 3%	.196 \pm 4%
2.0	.64 \pm .56 \pm 1%	.29 \pm 3%	.208 \pm 3%	.193 \pm 4%
2.5	.57 \pm .50 \pm 2%	.25 \pm 3%	.206 \pm 4%	.195 \pm 4%
3.0	.54 \pm .46 \pm 3%	.22 \pm 5%	.200 \pm 6%	.199 \pm 6%

Note: Listed uncertainties indicate uncertainty due to instrumental resolution, but exclude possible systematic errors.

Base Pressure: 1×10^{-9} Torr

Operating Pressure: 5×10^{-9} Torr

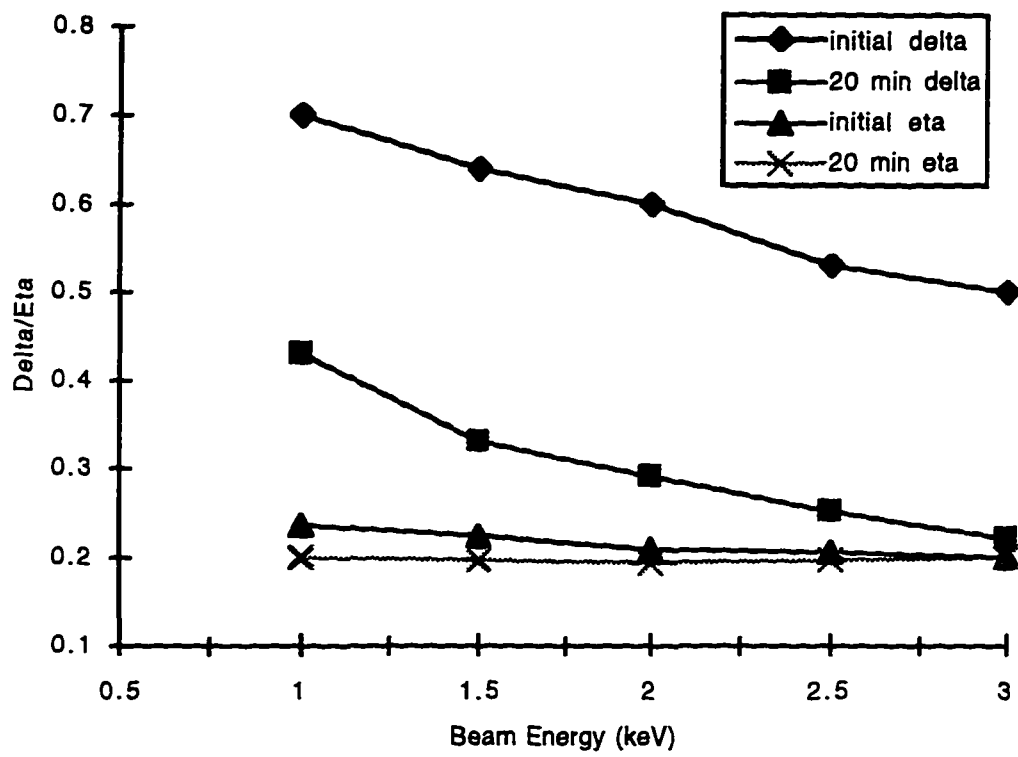


FIG. 6-1. Measured δ and η for aluminum (after Table 6.1).

η 's, it was decided that a likely cause for this behavior was a dynamical evolution of the surface condition, to which δ would be extremely sensitive, and η less so. Specifically, one could argue that something was either being deposited *on* or removed *from* the surface by the beam. This conjecture led to a series of investigations designed to determine the nature of the surface modification. Foregoing the suspense, the conclusion resulting from these investigations (described below) is that *surface layers are being both removed from and deposited on the surface as a result of the incident electron beam*, and in a manner that is at least partially understood. In particular, we contend that weakly bound surface contaminants are being evolved on a rapid times scale, an oxide layer is being removed on an intermediate time scale, and disordered carbon is being deposited on a longer time scale. Evidence supporting this conclusion is summarized below.

6.2.1 *Characterization of the Chamber Atmosphere with Beam on Sample—RGA Spectra*

Given aluminum's well-known proclivity to oxidize, the search for surface modifications began with a search for evidence of electron-beam-induced dissociation of an oxide layer. Dynamic monitoring of the chamber atmosphere with the RGA proved an ideal tool for this search.

Removal of contaminants from a bulk surface via energetic particle bombardment is a well-documented phenomenon.^{108,109} Ion sputtering—i.e., bombardment of a surface with energetic (~ 500 eV) ions—is in fact a technique often used by surface scientists to remove surface contaminants. In the case of surface layer removal by incident *electrons*, the effect is known as Electron Stimulated Desorption (ESD). ESD occurs when electrons incident on a surface deposit sufficient energy into the surface layer to break the bonds of physisorbed or chemisorbed species residing there, liberating them into the ambient atmosphere as a gas. This effect should be observable in RGA measurements via

- (i) elevated partial pressures of the desorbed species, and
- (ii) *increased* elevations of partial pressures with decreasing incident-beam energy (i.e., assuming the incident electrons possess energies greater than those binding the contaminants to the surface—energies ~meV for physisorbed species, and ~1-10 eV for chemisorbed species—the ESD efficiency should increase with decreasing incident energy, as more energy is deposited near the surface).

And indeed this behavior is observed in RGA measurements taken during electron bombardment of the aluminum sample.

(a) *Description of data*

Figures 6-2 through 6-8 are plots of partial pressure vs. time for a variety of contaminant species within the chamber atmosphere. The species are atomic oxygen (O), water (H₂O), carbon monoxide (CO), and molecular oxygen (O₂), with atomic masses of 16, 18, 28, and 32 amu, respectively. [NOTE: In addition to CO, N₂ also has an atomic mass of 28 amu.] Inspection of these figures reveals that the data were taken for a variety of conditions (with the electron beam “off,” the electron beam “on” and directed into the large FC built into the sample, and with the beam “on” and located on the sample surface), at a variety of beam energies, and while the beam spot was being moved about on the sample surface. The time between successive data points is 15 seconds.

Thorough, quantitative analysis of these data would likely lead to a number of interesting suppositions regarding the nature and sources of some of the contaminating species present within the vacuum chamber and on the sample itself. For the purposes of this thesis, however, such an analysis is not necessary; the following general observations, readily gleaned from the RGA measurements, contain abundant clues regarding the nature of the interactions occurring on the sample surface:

1. In the absence of an operating electron beam, partial pressures of the monitored species remain steady (at least over periods of ~5-10 minutes) [Fig. 6-2].

2. With the electron beam turned on but directed into the sample FC, a steady state is quickly achieved, with baseline pressures only slightly elevated (10% - 20%) over their corresponding beam-off values (Figs. 6-3 and 6-4).
3. With the electron beam turned on, directed onto the sample surface, and held in a fixed location, a steady state is quickly achieved (~15 seconds), but with baseline pressures elevated four- to ten-fold over their corresponding beam-off values (Figs. 6-5 and 6-6).
4. Relocations of the beamspot on the sample surface are immediately accompanied by measurable elevations (above the beam-on-surface baseline values) of the partial pressures of some species—most notably CO and CO₂—which then quickly decay back to their beam-on-surface baselines [Figs. 6-4, 6-5, 6-6, and 6-7(a), and Table 6.2]. Furthermore, the magnitude of the pressure elevation exhibits a dependence on the distance between the old beamspot location and the new beamspot location (increasing for distances greater than ~2mm) [Figs. 6-5 and 6-7(a), Table 6.2].
5. Reductions in the incident beam energy coincident with beamspot relocations result in successively higher partial pressure elevations for all monitored species (Fig 6-7, Table 6.3).
6. Reductions in the incident beam energy with the beamspot remaining at a fixed location result in differing partial pressure elevations (above beam-on-surface baseline values) for different species at different energies (Figs. 6-8 and 6-9). That is, the magnitude of a pressure elevation for a particular species exhibits a dependence on the incident beam energy.

(b) Analysis

Comparison of the above observations with the expected impact of ESD on concurrent RGA measurements [points (i) and (ii) above] yields strong indirect evidence for the presence of surface contaminants on the sample, and the (at least partial) removal of this layer by the incident electron beam. Pertaining to (i) above, observed CO and CO₂ partial pressure elevations above baseline with beamspot relocation suggests that these two species are being desorbed by the electron beam. The subsequent rapid decay of their partial pressures back to baseline values indicates these contaminants are quickly depleted

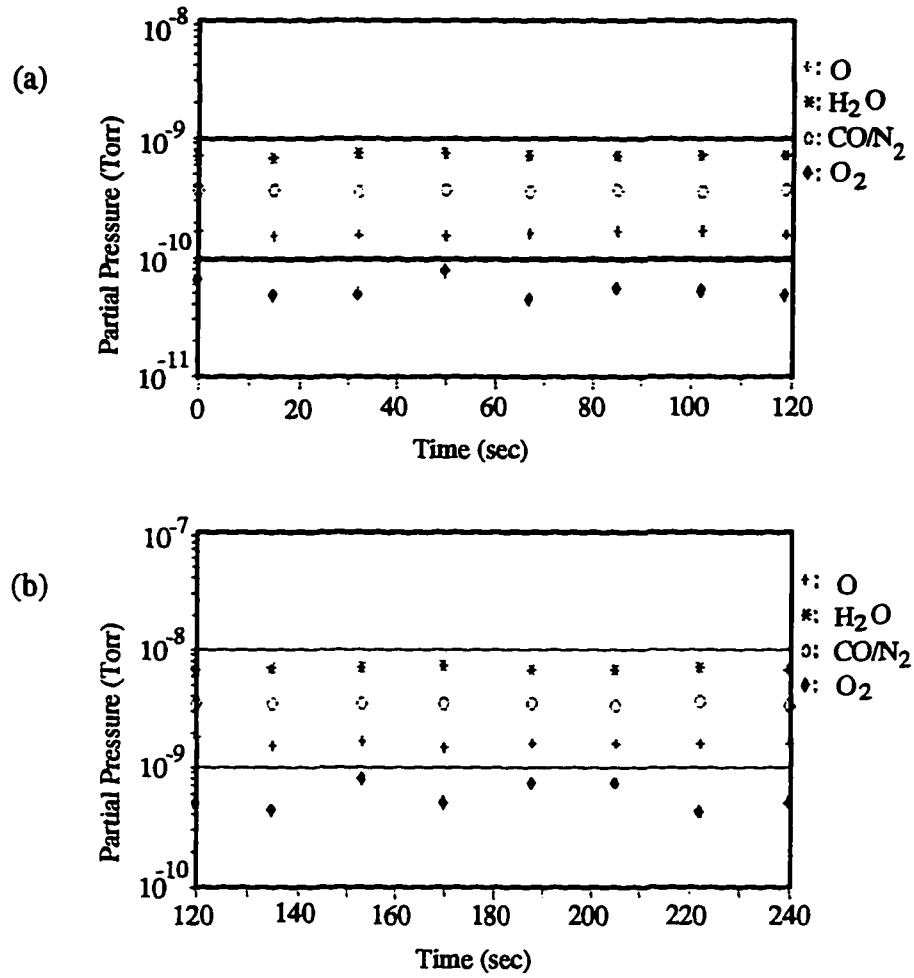


FIG. 6-2. Baseline partial pressures of O, H₂O, CO/N₂, and O₂ in the chamber with the electron beam turned off. Base Pressure: 1.9×10^{-9} Torr.

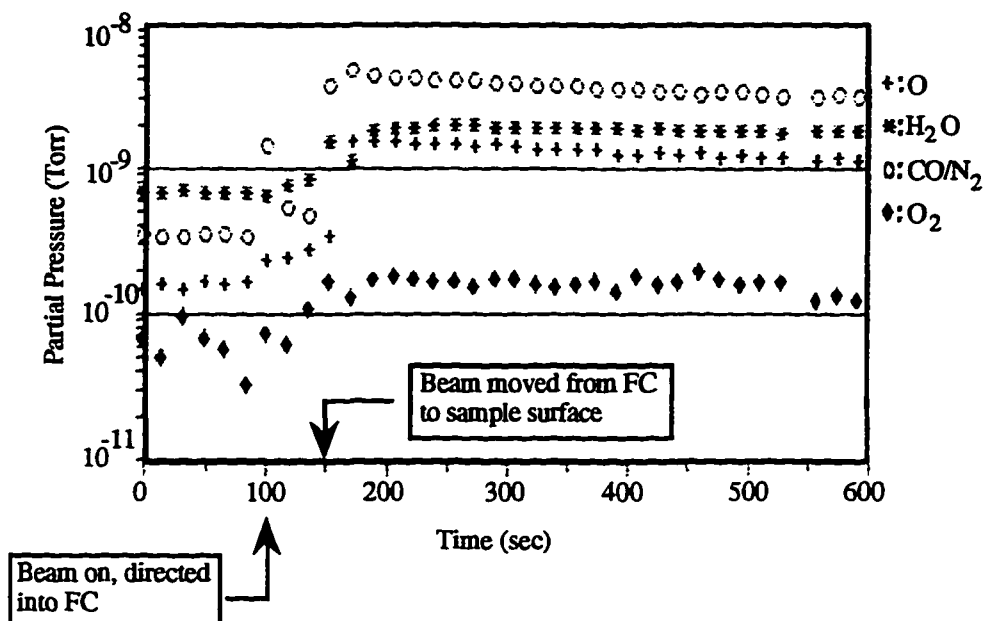


FIG. 6-3. Effect on baseline partial pressures (of the four species listed) of turning on the electron beam, directing it into the sample FC ($t=100$ s), and directing it onto the sample surface ($t=150$ s). Base Pressure: 1.2×10^{-9} Torr. Operating Pressure: 3×10^{-9} Torr (beam in cup), 1.4×10^{-8} Torr (beam on surface). Beam Energy: 2.0 keV.

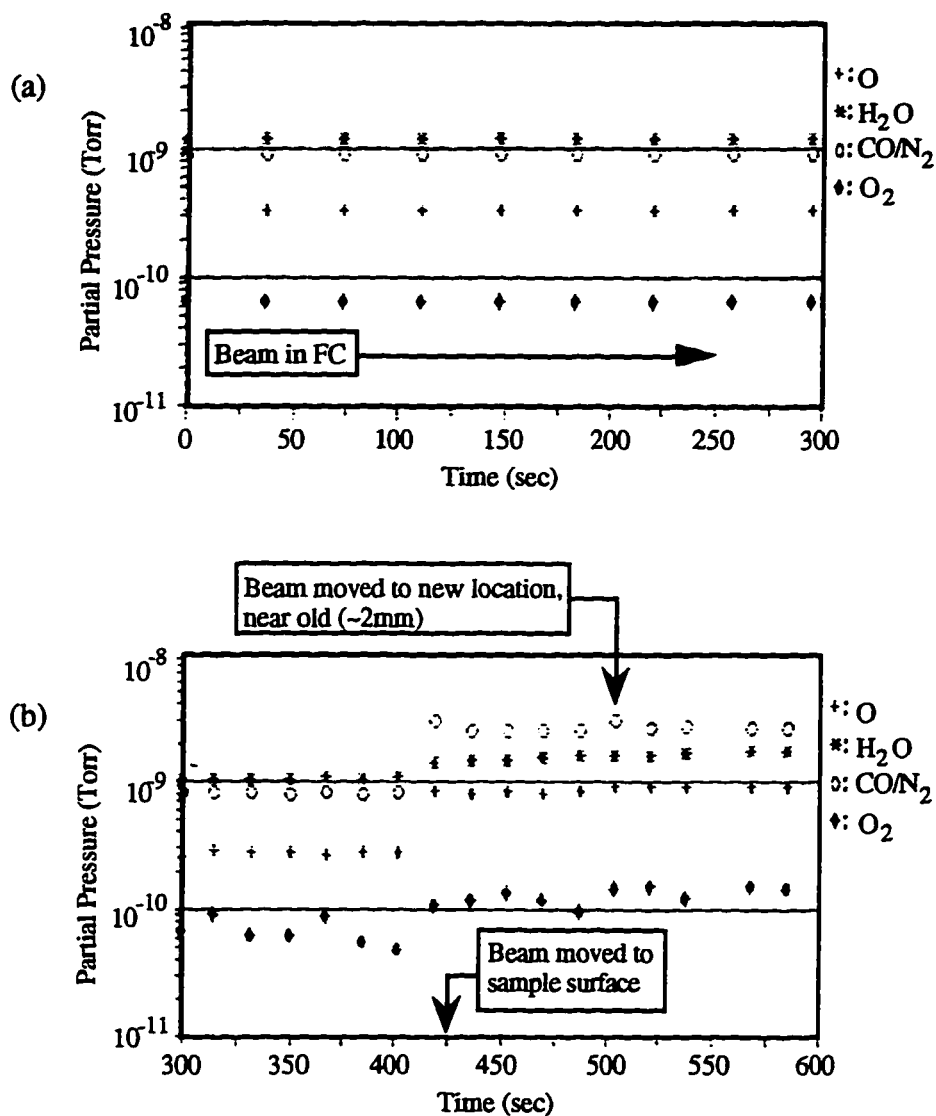


FIG. 6-4. Effect on partial pressures (of species listed) of relocating the electron beam on the sample surface. The beam spot is first moved out of the FC and onto the surface ($t=425$ s), and then moved to a fresh location on the surface, very near the old ($t=500$ s). Base and operating pressures are as given in Fig. 6-3. Beam Energy: 2.0 keV.

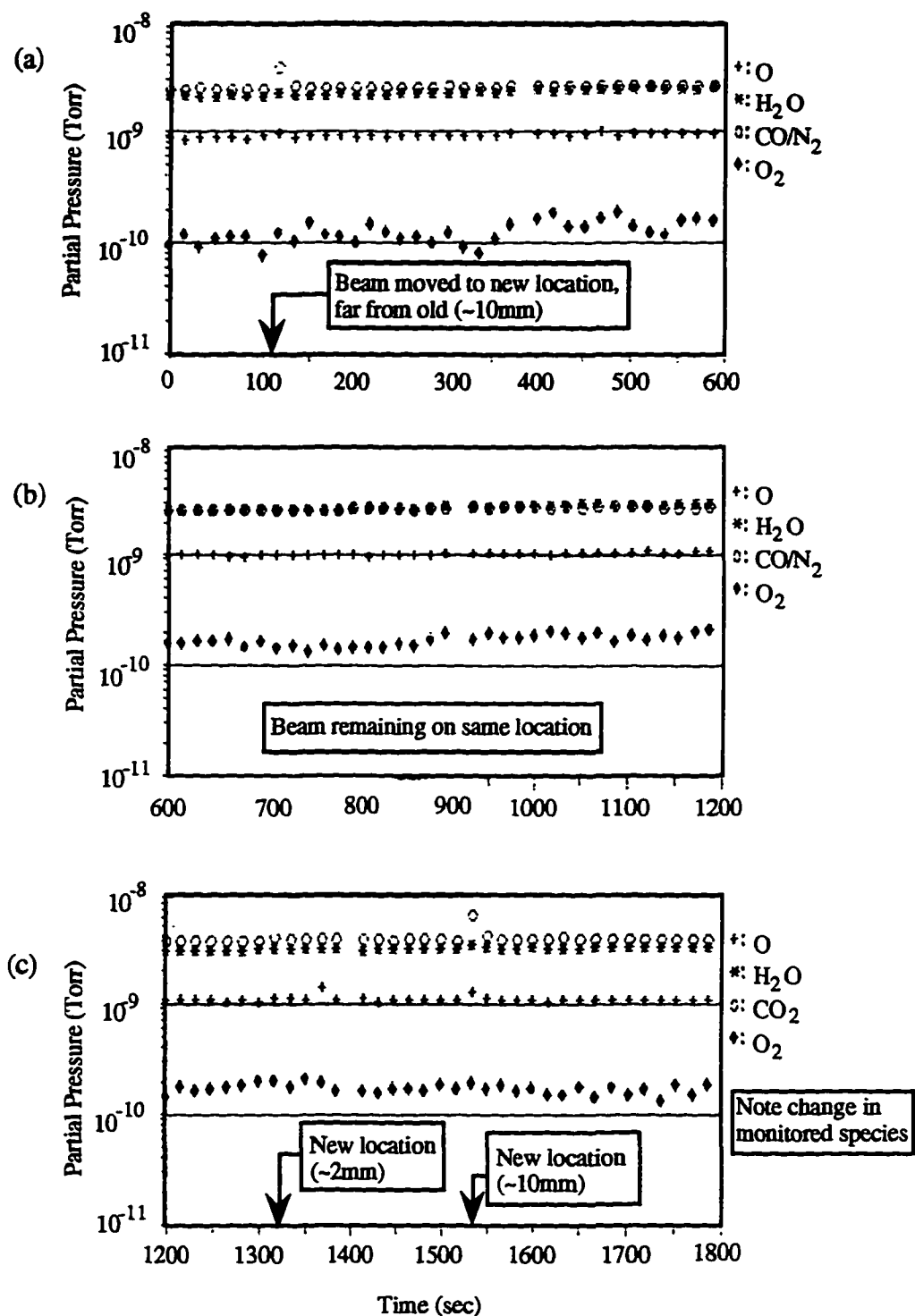


FIG. 6-5. Effect on partial pressures (of listed species) of relocating electron beamspot on sample surface (at $t=100$ s, $t=125$ s. and $t=325$ s). Base and operating pressures are as given in Fig. 6-3. Beam Energy: 2.5 keV.

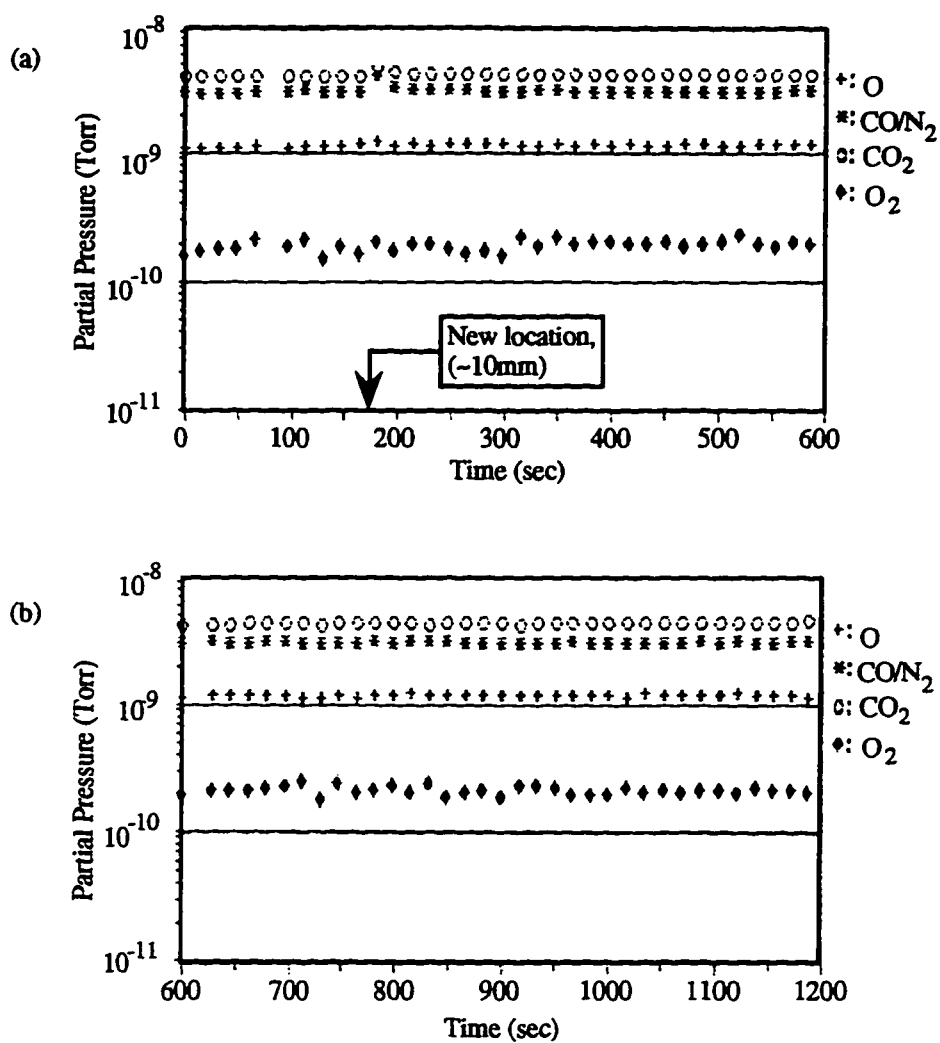


FIG. 6-6. Effect of electron beamspot relocation (on sample surface) on partial pressures of listed species. (Note the change in species from previous figures.) Base and operating pressures are as given in Fig. 6-3. Beam Energy: 2.5 keV.

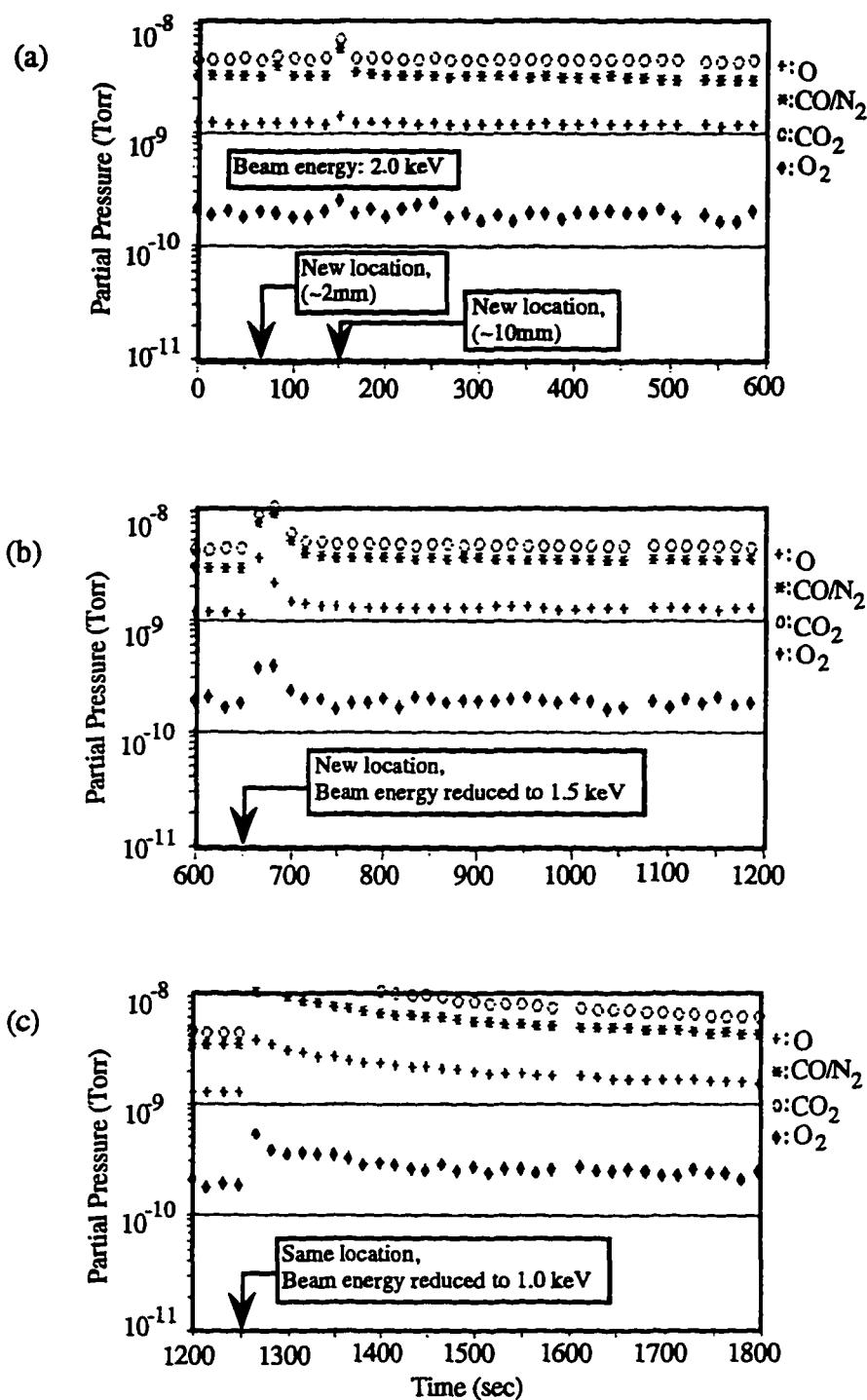


FIG. 6-7. Effect of changing both incident electron beam energy and beamspot location on partial pressures of listed species. The beam energy is reduced from 2.0 keV to 1.5 keV ($t=675$ s), and then further reduced to 1.0 keV ($t=1275$ s). Base Pressure: 1.4×10^{-9} Torr. Operating pressures vary in low- 10^{-8} Torr range.

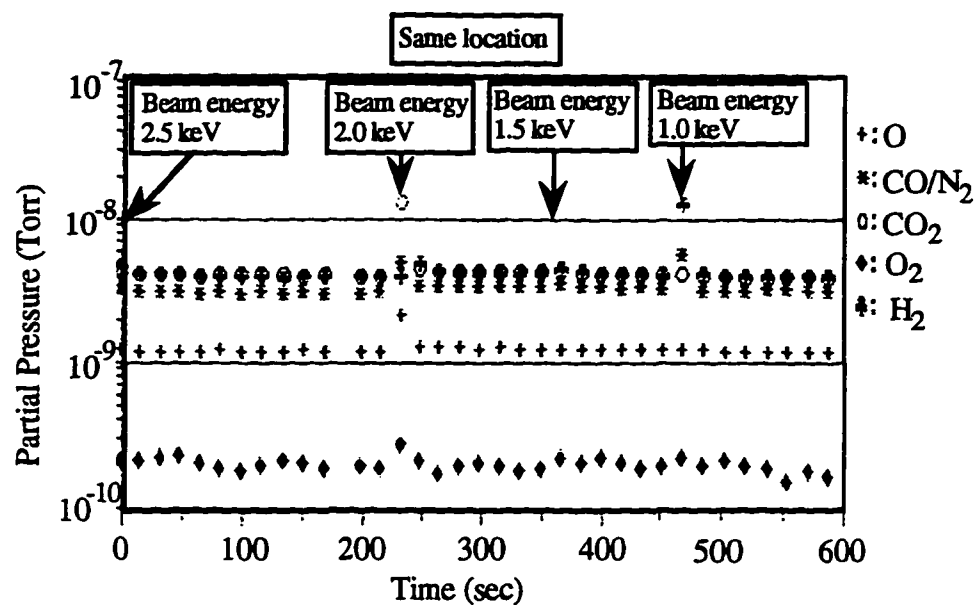


FIG. 6-8. Effect of reducing incident electron beam energy on partial pressures of listed species, while beamspot location on the sample remains constant. Base and operating pressures are as given in Fig. 6-7.

TABLE 6.2. Changes in partial pressures resulting from electron bombardment of sample of ($E_b = 2.0, 2.5$ keV).

Species (atomic mass)	Relative increase in partial pressure due to moving beam...		
	out of FC	from initial spot to new spot (2 mm away)	from initial spot to new spot (10 mm away)
O (16)	10	—	1.2
H ₂ O (18)	3	—	1.25
CO/N ₂ (28)	10	1.2	2
O ₂ (32)	4	—	—
CO ₂ (44)	*	1.2	2

Base Pressure: $\sim 1 \times 10^{-9}$ Torr

Operating Pressure: $\sim 1 \times 10^{-8}$ Torr

— indicates no detectable change

* indicates not investigated

TABLE 6.3. Effect of beam energy reduction on vacuum chamber CO₂ levels.

Beam Energy (keV)	% partial pressure increase above baseline for new spot (CO ₂)
2.0	200
1.5	350
1.0	600-700 (est.)

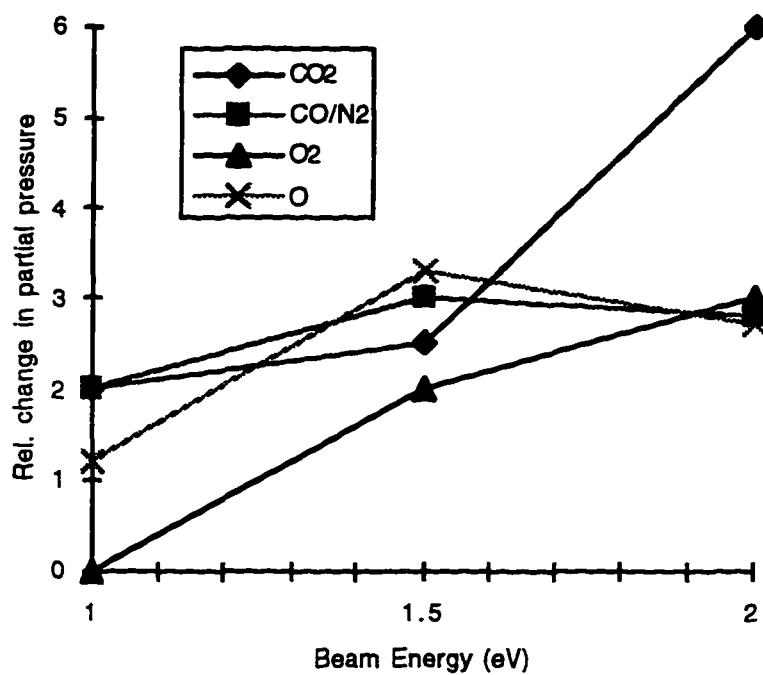


FIG. 6-9. Relative change in partial pressures as a function of incident electron beam energy (after Table 6.2).

(via ESD) from the sample location under bombardment. Pertaining to (ii) above, an incident-beam energy dependence of partial pressure elevations is also observed, reinforcing the ESD hypothesis. One further point of interest is the considerable disparity between beam-off and beam-on-surface baseline partial pressures. The significant increase in baseline partial pressures of *all* species when moving from beam-off conditions (Fig. 6-2) to the beam on the sample surface (Figs. 6-3 to 6-8), is plausibly explained by assuming the presence of each of the monitored species on secondary surfaces within the chamber—such as the chamber walls—whose supply of these contaminants is not readily depleted by the impacting scattered beam.

The preceding data strongly point to the *removal* of material from the sample surface by the electron beam. Attention is now turned to studies revealing beam-induced *deposition*.

6.2.2 *Extended-Term Dynamic Studies of δ , η*

Given strong evidence for the removal of contaminants from the surface, several extended-term dynamic studies of δ and η (~10-30 hrs) were performed with the expectation that, at some point, all surface layers would be desorbed, the surface current would become completely stable, and the SE and BSE coefficients would then be those for clean Al (and therefore appropriate for comparison with the literature). For a given beam energy ($1.0 \text{ keV} \leq E_b \leq 3.0 \text{ keV}$), the beam was directed to a “fresh” location on the sample, which it continuously bombarded for the duration of the trial. Data from these trials are presented below.

(a) Description of data

The most complete set of data taken during these trials was that for the 2.0 keV beam; Figs. 6-10 and 6-11 are plots of δ and η vs. time for this case. Data (i.e., the electric current measurements with which δ and η were calculated) were taken at

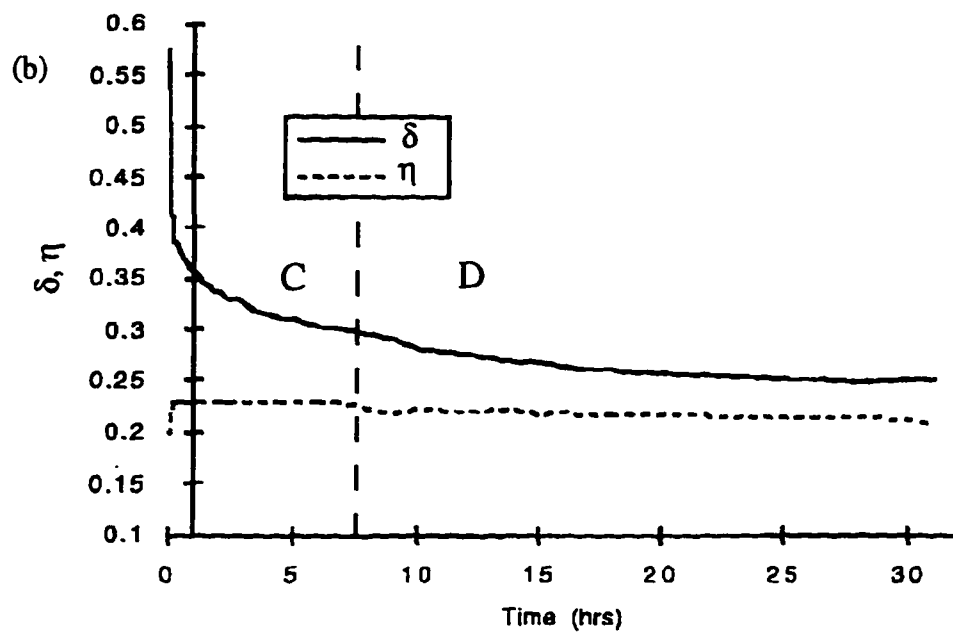
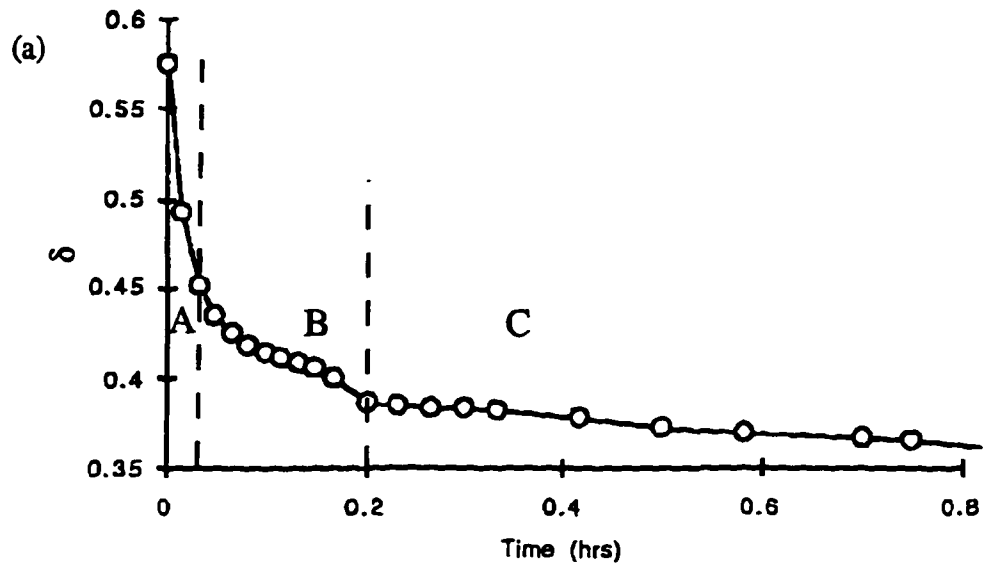


FIG. 6-10. (a) Early dynamic evolution of SE coefficient and (b) extended dynamic evolution of SE and BSE coefficients for electron bombardment of aluminum. Beam Energy: 2.0 keV.

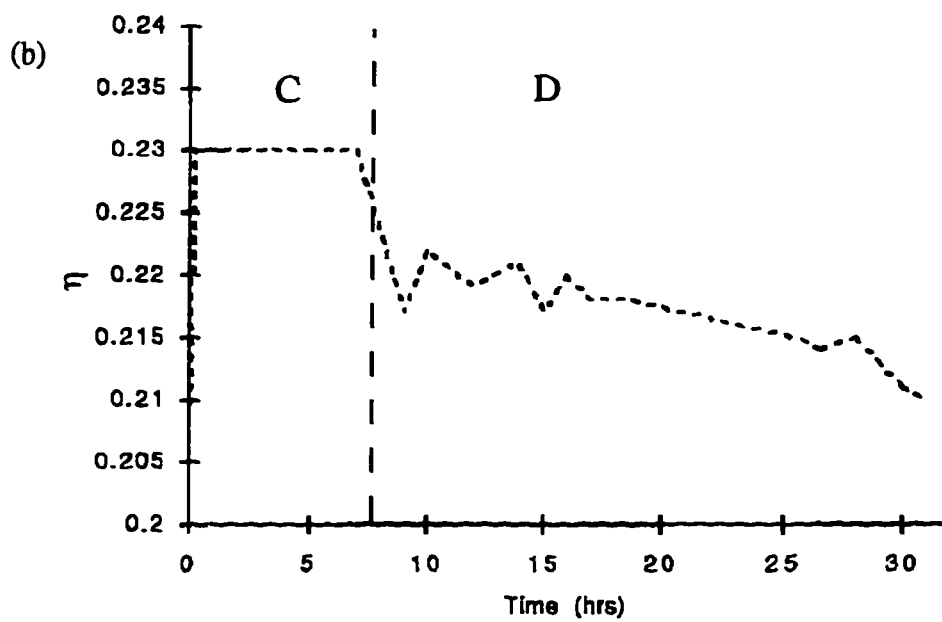
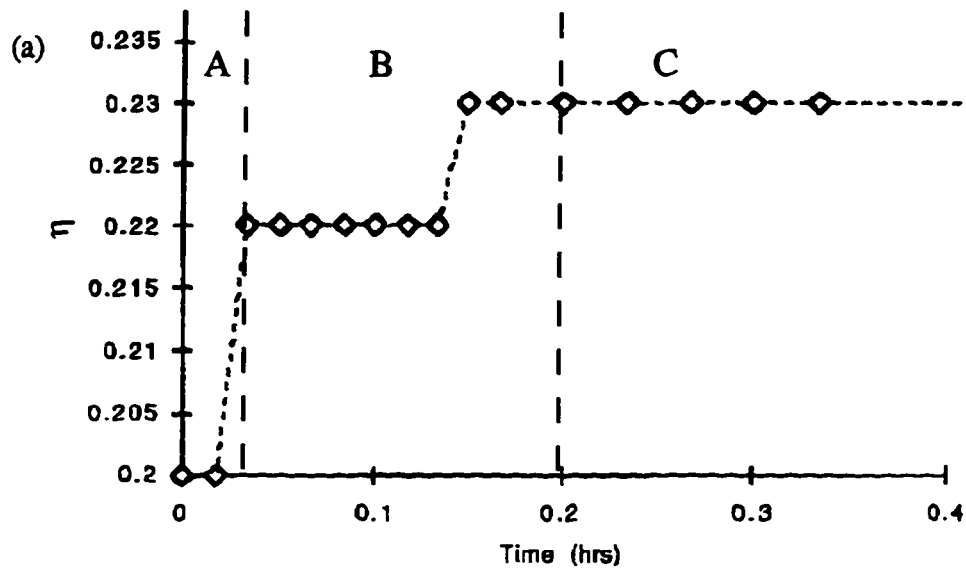


FIG. 6-11. (a) Early and (b) extended dynamic evolution of BSE coefficient for electron bombardment of aluminum. Beam Energy: 2.0 keV.

successively longer intervals as the trial progressed, reflecting the slowing of the dynamics over time. Measurements were recorded every 10 seconds for the first 3 minutes, then every minute for the next 7 minutes, and then at progressively longer intervals through the first 5 hours, at which point measurements were recorded approximately every hour through the end of the trial. Fig. 6-10(a) depicts δ over the first hour, while Fig. 6-10(b) illustrates both δ and η over the entire trial. Note that these two plots are not to the same scale, and that the dynamics over the first hour are considerably different than those later on. Similarly, Fig. 6-11(a) depicts the behavior of η over the first half-hour, and Fig. 6-11(b) depicts η over the entire trial.

One further observation during these long-term dynamic studies was the development of a dark brown spot on the sample at the beam location. Fig. 6-12 is a photograph of the sample, taken after it was removed from the chamber, clearly depicting the spot. In a 1954 paper, Sternglass⁴⁴ describes concern over a similar phenomena occurring under similar circumstances. He determined the blemish to be a thin film of carbon, deposited on the sample by the electron beam, and whose sources were diffusion pump oil and his electron gun cathode (filament). Sternglass' solution to the problem was to use a mercury- rather than oil-diffusion pump, and to angle his gun such that the sample could not “see” the cathode, guiding the beam to the sample via magnetic deflectors. Following this example, the 2.0 keV data described above was taken with the beam-spot location on the sample out of view of the cathode (where the FOV of the cathode is clearly discernible on the sample as a white “spotlight” approximately 1 cm in diameter). Given that the blemish again developed, the effect does not appear to be (at least entirely) due to the deposition of cathode material onto the sample. Likely sources of contamination are discussed in (6.2.5).

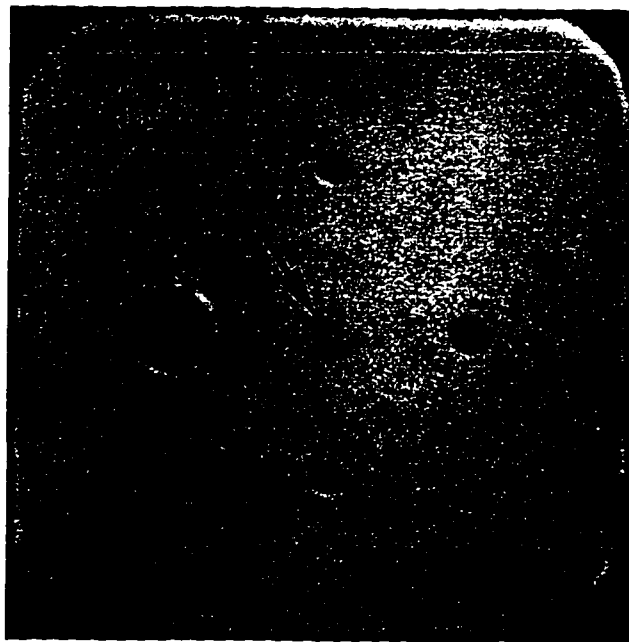


FIG. 6-12. Photograph of aluminum sample following long-term electron bombardment. The electron-beam-induced deposition is visible as a dark region at the center of the sample.

(b) Analysis

Though the mechanism remains uncertain, the information presented above, both visual and quantitative, quickly leads one to the supposition that something is being deposited on the sample surface by the beam. Aspects of the data consistent with this hypothesis are:

1. *The appearance of some sort of deposit*—i.e., the brown spot.
2. *The behavior of δ* . As time progresses and the thickness of the deposit approaches the maximum depth at which SE's are produced ($\sim 50\text{-}80 \text{ \AA}$)⁵⁰, one would expect the SE yield to approach that for the bulk material for whatever is being deposited. Indeed this is just the behavior depicted in Figs. 6-10(a) and (b); as time progresses and the deposit becomes (ostensibly) thicker, δ appears to be leveling off asymptotically—decreasing by $\sim 50\%$ over 30 hours.
3. *The behavior of η* . One would expect that any surface-film deposition would initially have little effect on η , which is not particularly sensitive to surface condition. However, as the thickness of the film increases, its influence on η should increase. Though not as compelling as the data for δ , one can see such a trend in η in Fig 6-11(a), beginning at time $t=0.15$ hours (9 min); η remains constant over the first 7 hours, and then decreases $\sim 9\%$ over the next 25 hours.

Two further points regarding the data should be mentioned. First, the behavior of η over the first 9 minutes appears at odds with the deposition theory. No explanation for this behavior is offered at this time. Second, the issue of charging has not been addressed. If material is being deposited on the surface (and indeed it is, as the following sections will confirm) and its conductivity is poor, charging of this material under electron bombardment is quite possibly skewing the data with which δ and η are determined.

Now that the likelihood of a beam-induced deposition has been established, characterization of this deposition, to include composition and depth, is the subject of the final two sets of data.

6.2.3 EDX / SEM analysis

Following the SE and BSE characterizations, the sample was removed from the chamber and delivered to the USU Electron Microscopy Facility, where an energy-dispersive x-ray (EDX) analysis was performed with an Hitachi S-4000 field-emission scanning electron microscope (SEM). This instrument is capable of detecting Be and all heavier elements.¹¹⁰ Unfortunately, the lowest available probe energy with the SEM in the EDX mode is 10 keV, which is not particularly surface sensitive. Nevertheless, some evidence was obtained concerning the nature of the surface film deposited on the Al sample.

(a) Description of data

“Visual” images of the sample were taken by the SEM in the scanning microscopy mode and are shown in Fig. 6-13. The deposit is clearly visible on the sample surface as a darker gray area. This implies a drastic change in SE yield in this area, since this is what contrast in a SEM is based on (confirming, at least in a relative sense, the δ measurements presented above). These images also show the sample to have a relatively smooth surface, with occasional small inclusions (~a few microns) embedded in the Al.

EDX spectra for both the Al background and the deposited film are given in Figs. 6-14 and 6-15. These figures depict total number of counts on the vertical axis vs. emitted (x-ray photon) energy on the horizontal axis, with elements corresponding to given electron transition energies labeling the various peaks. Finally, an EDX spectrum for one of the surface inclusions is presented in Fig. 6-16.

(b) Analysis

EDX spectra of both the background aluminum and the deposited layer reveal the presence of all major contaminants listed by the manufacturer of the sample (6.1), with the exception of Mg. Direct comparison of Figs. 6-14 and 6-15, looking for clues as to the

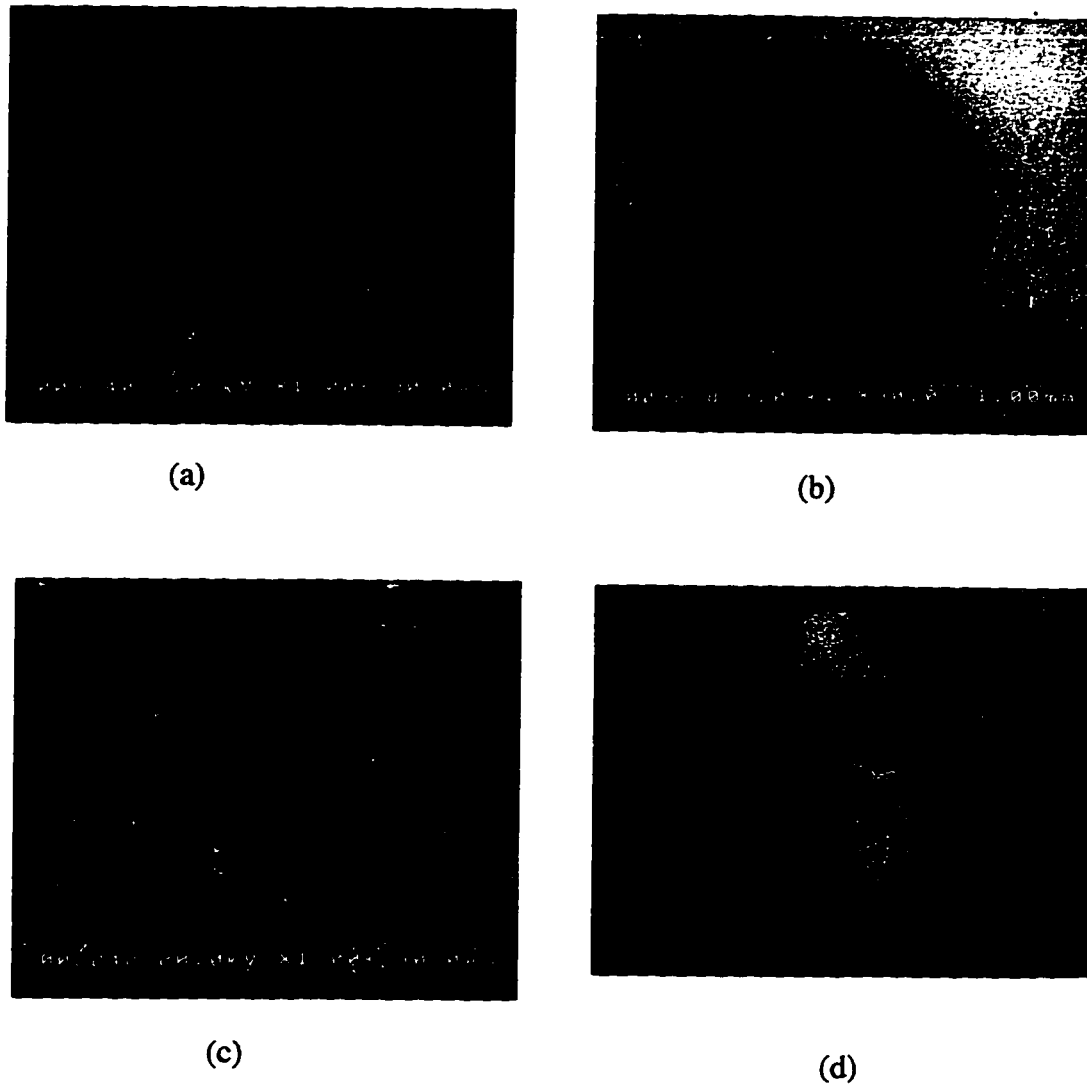


FIG. 6-13. SEM micrographs of the aluminum sample depicting (a) the background aluminum surface, (b) the electron-beam-induced dark region, (c) an inclusion in the sample surface, and (d) a ten-fold magnified view of the sample inclusion.

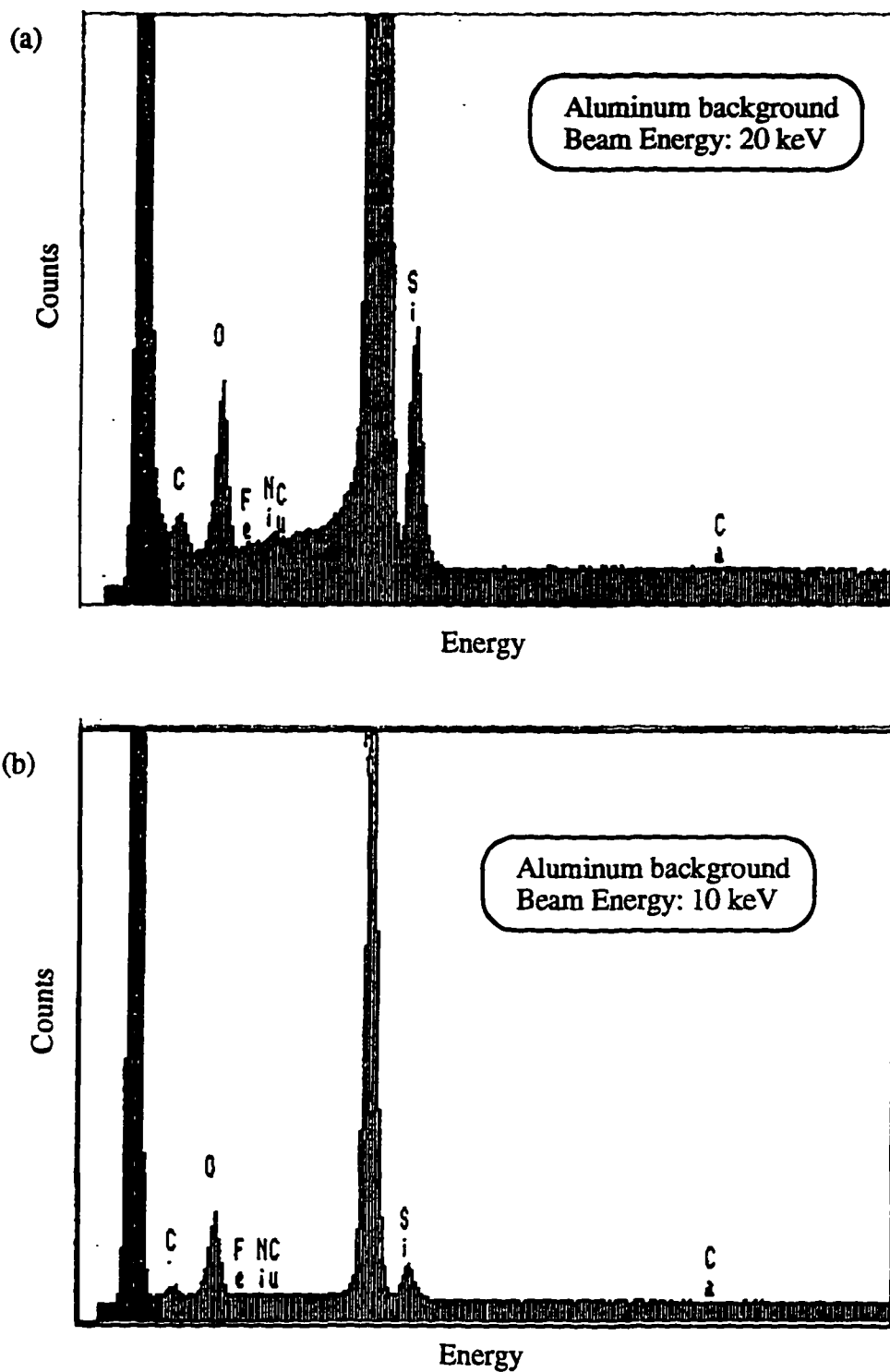


FIG. 6-14. EDX spectra for Al sample, off the dark region, taken with probe beam energies of (a) 20 keV and (b) 10 keV.

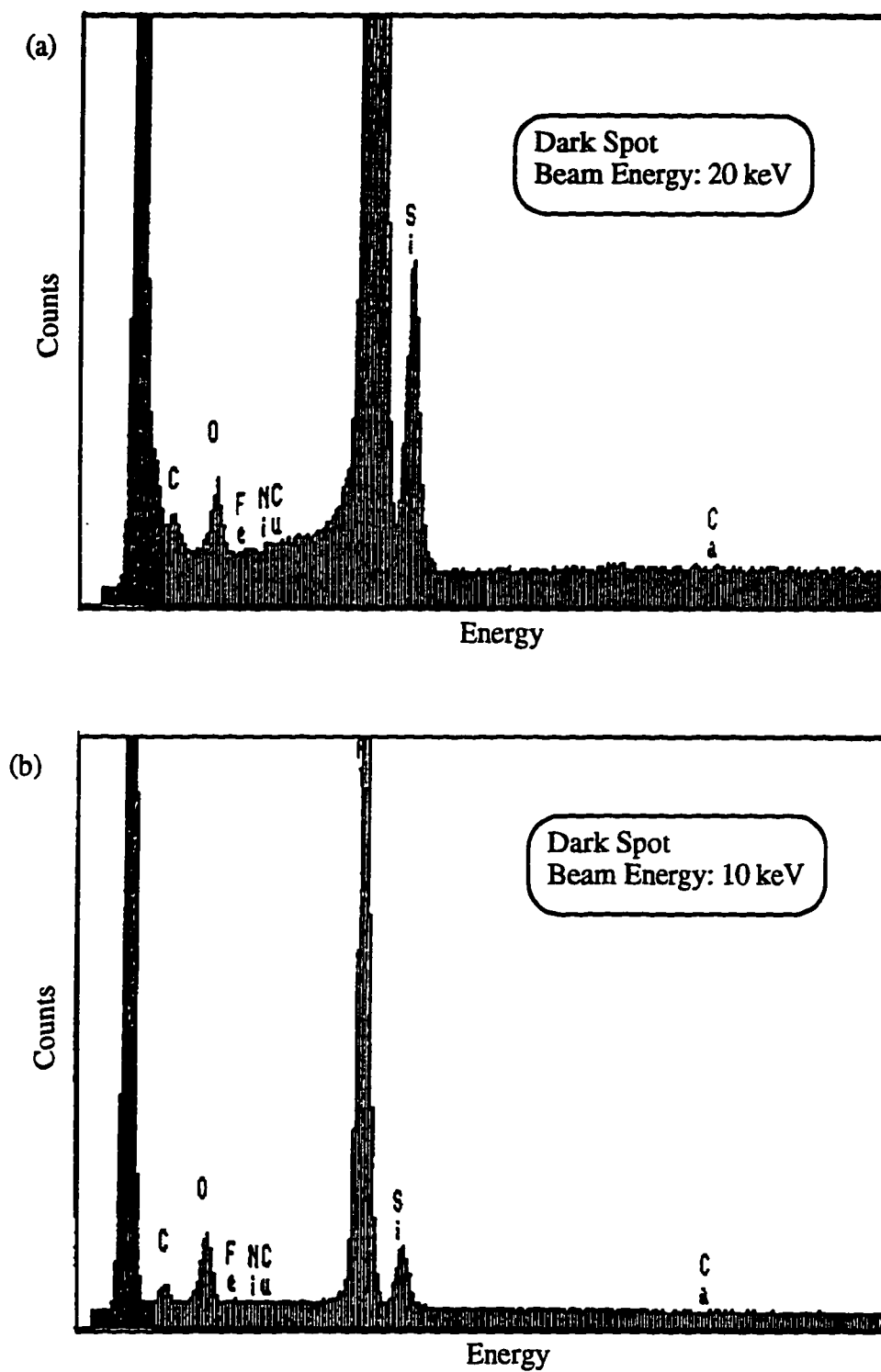


FIG. 6-15. EDX spectra for Al sample, on the dark region, taken with probe beam energies of (a) 20 keV and (b) 10 keV.

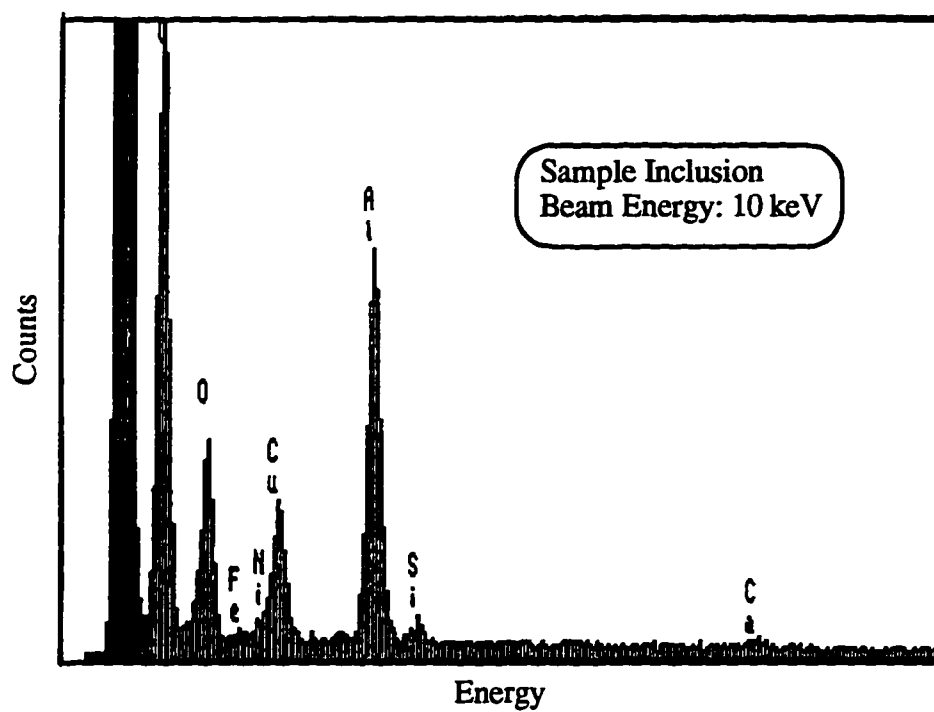


FIG. 6-16. EDX spectra for surface inclusion on Al sample. Taken with a probe beam energy of 10 keV.

TABLE 6.4. Ratios of peak heights for prominent EDX features.

Beam Energy (keV)	Sample Area	Intensity: O to Si	Intensity: C to O	Intensity: C to Si
10	background Al	2.67	0.13	0.67
10	deposit	1.20	0.25	0.30
10	inclusion	6.40	4.04	20.20
20	background Al	0.74	0.19	0.14
20	deposit	0.28	0.29	0.08
30	deposit	—	—	—
30	inclusion	2.00	0.79	1.58

composition of the surface deposit, is difficult. More telling is a comparison of relative amounts of oxygen, silicon, and carbon, presented in Table 6.4. An increase in the relative amount of carbon in moving from the background Al to the dark spot for the 10 keV spectra (the most surface sensitive) is particularly apparent. Uncertainty in this result is attributable to instrument sensitivity. The penetration depth of the 10 keV beam into the sample is on the order of micrometers, and assuming the deposited film to be ~1 nm thick (3-4 atomic layers), it will show up at roughly a 0.1% concentration level. Unfortunately, this is also the listed sensitivity of the instrument,¹¹¹ meaning the signal from the surface contamination is likely at or just above detectable limits. Nevertheless, evidence that the surface film is carbon, though not compelling, is present. The presence of surface inclusions (Fig. 6-13) of varying composition is likely the result of polishing the sample with a used polishing cloth [see (6.1)] and not related to the deposition of material on the surface by the beam.

6.2.4 XPS analysis

Subsequent to the SEM/EDX analysis, X-ray Photoelectron Spectroscopy (XPS) analysis of the sample was accomplished at the Vacuum Generators facility (England) using a Fission Instruments XPS spectrometer. Source x-rays were 1489 eV Al K_{α} , with an energy resolution of 1 eV. As a technique, XPS is ideally suited to the characterization of the surface film in that it is highly surface-sensitive; its only weakness being an inability to detect H and He. Data and analysis are given below.

(a) Description of data

Figure 6-17 depicts binding energy (BE) plotted vs. kilo-counts per second (KCPS) for regions off of the dark spot (a) and on the dark spot (b) on the sample. Figure 6-18 depicts comparisons of carbon levels on and off the dark spot (a) and oxygen levels on and off the dark spot (b).

(b) Analysis

Fig. 6-17(a) confirms what one would expect from the composition of an oxidized aluminum surface—the presence of both oxygen and aluminum. Carbon is also seen to be present in significant amounts. Contrasting these data, Fig. 6-17(b) reveals that the surface film is comprised primarily of carbon. The carbon signal is nearly double that of the region off the dark spot, and the Al signal has all but disappeared, suggesting a carbon film thick enough (perhaps a few monolayers) to prevent the 1422 eV electrons [i.e., the 1489 eV photon energy minus the 67 eV Al (2p) binding energy] from escaping from the underlying aluminum. The oxygen signal has decreased by a factor of three, though its continued presence may indicate that the carbon film is deposited on top of an oxide layer—meaning the oxide layer was not entirely desorbed before significant carbon deposition began.

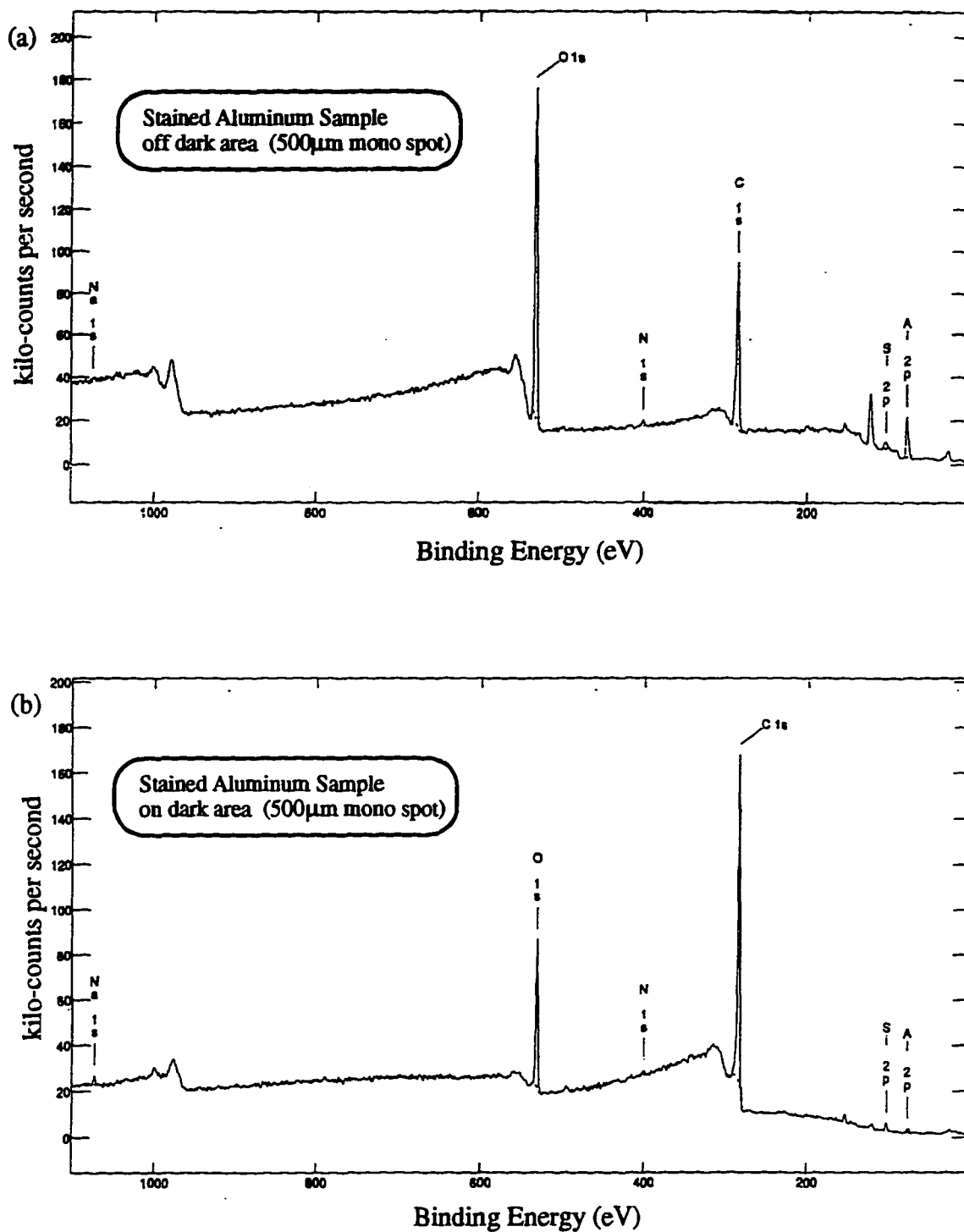


FIG. 6-17. XPS analysis for the Al sample (a) off and (b) on the dark area. The probe beam consisted of 1489 eV Al K_{α} photons.

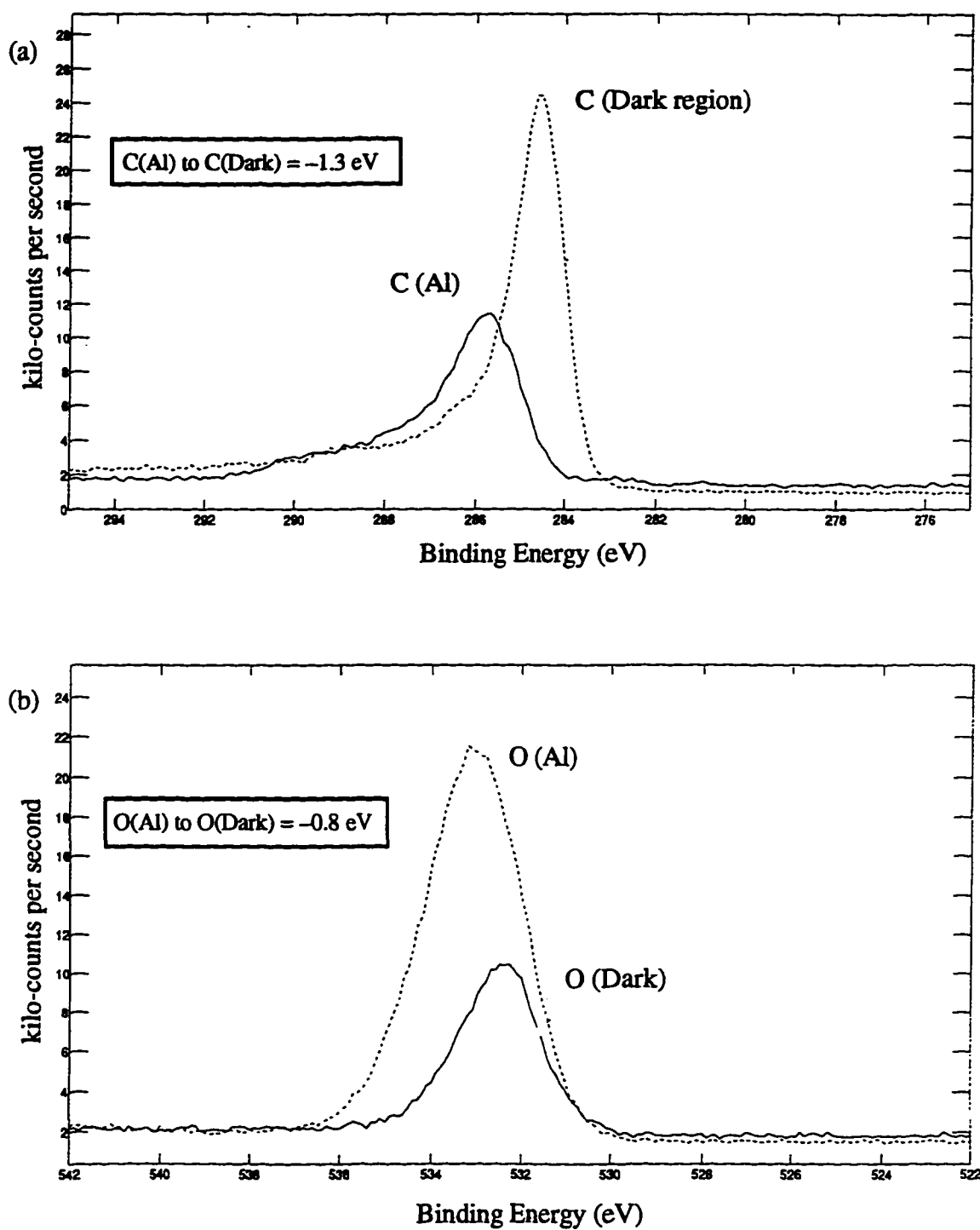


FIG. 6-18. Comparison of (a) XPS carbon peaks and (b) XPS oxygen peaks on and off of the Al sample dark area.

Inspection of Fig. 6-18 offers one further insight—that the chemical nature of the carbon on and off the dark spot is possibly different. In addition to significantly increased amounts of carbon [Fig. 6-18(a)] and significantly decreased amounts of oxygen [Fig. 6-18(b)], the plots reveal a shift in the peak BE of the carbon of -1.3 eV (in moving to the dark spot from off of the dark spot), and a shift in the peak BE of the oxygen to be -0.8 eV. Shifts in BE peaks generally occur in XPS analysis for two reasons: sample charging, and chemical differences.¹¹² In the case of sample charging, one would expect the same shift in both the C and O peaks. Since this is not the case, it is probable that at least some of the differential in the carbon spectra is due to the chemical nature of the film.

6.2.5 Conclusions

The above investigations demonstrate that: (i) contaminant species present on the sample surface were at least partially removed via ESD, (ii) a beam-induced deposition is occurring, and (iii) this deposit is (at least primarily) some form of carbon. The question of where the carbon is coming from, and the exact mechanism for its deposition, remains.

Addressing the first question, there are a number of possible carbon sources in the system:

1. *Wire insulation.* A purple film noted on surfaces adjacent to the heater wires strongly suggests outgasing from the (purple) insulation coating the two interior sample heater wires. Certainly, this is one source of carbon.
2. *Teflon.* A well-known method for producing carbon fluoride (CF) gas is to heat Teflon,¹¹³ which is precisely what was done when the chamber—including the Teflon insulation sleeve inside the RD detector—was baked. Indeed, this sleeve was partially melted during the first bakeout, to 100° C. The absence of CF (atomic mass 31 amu) and F (mass 19 amu) in the RGA scan presented in Fig. 5-1 detracts from the Teflon theory as a carbon source, though does not discount it altogether.
3. *Electron gun filament.* The filament used in the electron gun is made of tungsten, but the process of preparing the filament introduces significant amounts

of carbon into the tungsten. It is possible this carbon is dissociating from the filament and finding its way to the sample.

4. *Colloidal graphite.* Apertures in the RD housing, as well as the entire interior surface of the Faraday cup in the RD, were coated with colloidal graphite in an effort to reduce SE production on these surfaces. Also, the rotating plate bushing was lightly lubricated with colloidal graphite. In a UHV environment, outgasing of these graphite coatings would contribute carbon to the chamber atmosphere.

5. *SiC inclusions.* The inclusions noted by the SEM scans [Fig. 6-13(c)] and shown by EDX analysis to contain carbon are likely SiC from the polishing powder used in preparation of the sample (6.1). These inclusions must be considered as a possible carbon source.

6. *Inadequate cleaning.* A momentary lapse in proper cleaning and handling procedures could easily introduce carbon into the system in the form of fingerprints, grease, grime, etc. Modest bakeout temperatures may have been insufficient to fully remove this source.

Regarding the mechanism of deposition, the formation of insulating carbon polymer films via the charged-particle bombardment of adsorbed hydrocarbons is a well documented phenomenon,^{114,115} and is likely the culprit in this case. Clearly, eliminating the source(s) of carbon in the system is the key to preventing the formation of the unwanted carbon film. Methods for achieving this are addressed in Chapter 9.

Attention is now turned briefly to initial results for energy-, angle-, and angle-energy-resolved δ and η determinations.

6.3 Angle- and Energy-Resolved Yields

6.3.1 Energy-Resolved Measurements

Only cursory testing of SE energy resolution—using both the sample and the RD as detectors, as discussed in Chapter 3—has been accomplished. Results indicate that the procedure for $\delta(E_s)$ determination outlined in (3.3.3) is satisfactory. Specifically, a peak in the SE spectra at ~ 2 eV has been observed, consistent with the literature (see Fig. 2-5).

Characterization of the RD's energy resolution also has not yet been done, primarily due to difficulties with leakage current across the FC's Teflon insulators [see (5.3.3)].

6.3.2 *Angle- and Angle-Energy-Resolved Measurements*

A number of attempts were made to obtain angle-resolved SE and BSE yields, though none were successful. Data sets were not coherent. Further analysis has revealed a likely explanation to be improper alignment of the rotatable detector. Referring to Fig. 6-19, it appears that the RD is looking “high and to the left” (when positioned at near-normal scattering angles) with respect to the center of the sample. This means that as the RD is rotated about the sample, its field-of-view does not remain fixed on the same location on the sample, but rather various portions of the beam spot drift in and out of view. Such a condition would be consistent with the (illogical) data obtained. Given this state of affairs, no attempt has yet been made to obtain angle-energy-resolved data. Further testing of the angle- and angle-energy-resolved techniques will continue once the RD has been properly aligned [see (8.1.2).]

Having discussed in detail the initial δ and η values obtained by this instrument for aluminum—as well as difficulties encountered in obtaining them—a comparison of these results with those given in the literature, and subsequent conclusions regarding the reliability of the apparatus and technique, is presented next.

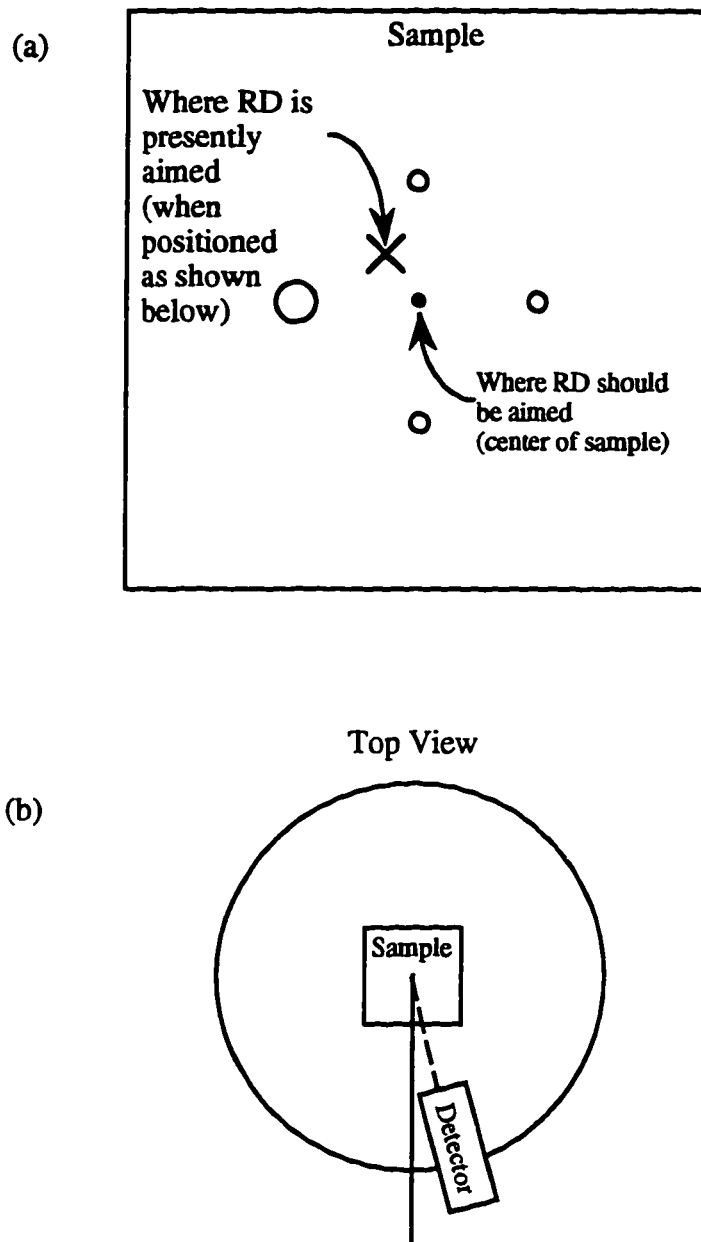


FIG. 6-19. (a) View of the sample illustrating misalignment of the RD, when positioned as shown in (b).

CHAPTER 7

ANALYSIS AND DISCUSSION

The purpose of this chapter is to draw conclusions—from results presented in the previous chapter—regarding the performance and viability of the apparatus and technique described in Chapters 3 and 4. Results of previous SE investigations for normally incident electrons on Al are reviewed (7.1), comparisons of these results with those obtained in the present investigation are made (7.2), possible sources of error are reviewed (7.3), and conclusions regarding the viability of the experimental design are presented (7.4). The chapter concludes with a physical model describing the dynamic evolution of δ presented in (6.2.2) (7.5).

7.1 Previous Investigations

Experimentally determined SE and BSE yields reported in the literature for 1-3 keV electrons normally incident on Al, along with those determined in this investigation, are presented in Tables 7.1 and 7.2. Evident in these tables is considerable disagreement among the several sets of previously reported values. Disparity among δ values ranges from more than a factor of two at $E_b = 1.0$ keV, to 20% at $E_b = 3$ keV. Limited data for η reveals disagreement of up to 40% in this same energy range. It is necessary, therefore, that some understanding be achieved regarding the nature of these discrepancies before meaningful comparisons can be made between the literature and the results of the present investigation. This is perhaps best accomplished via examination of the varying vacuum conditions and methods of sample preparation used in the previous investigations listed.

7.1.1 Vacuum Conditions and Sample Preparations

Measurements in the early 1970's by both Thomas and Pattinson⁵⁰ and Shimizu⁵⁹ were performed under UHV conditions, at operating pressures below 5×10^{-9} Torr. The

TABLE 7.1. Comparison of experimentally determined SE yields for normally incident electrons on bulk Al.

E_b	δ					
	<u>Present Work (initial surface)</u>	<u>Present Work (modified surface)</u>	<u>Kanter* (1961)</u>	<u>Whipple* (1965)</u>	<u>Thomas & Pattinson* (1970)</u>	<u>Shimizu* (1974)</u>
1.0 keV	.73 - .68	.43	—	.70	.61	1.65
1.5	.72 - .57	.33	—	.68	.50	—
2.0	.64 - .56	.29	1.00	.65	.43	.80
2.5	.57 - .50	.25	.82	.60	—	—
3.0	.54 - .46	.22	.74	.57	—	.60

*Values are approximate, taken from graphical data

TABLE 7.2. Comparison of experimentally determined BSE yields for normally incident electrons on bulk Al.

E_b	η					
	<u>Present Work</u> <u>(initial surface)</u>	<u>Present Work</u> <u>(modified</u> <u>surface)</u>	<u>Kanter*</u> <u>(1961)</u>	<u>Thomas &</u> <u>Pattinson*</u> <u>(1970)</u>	<u>Shimizu*</u> <u>(1974)</u>	<u>Reimer*</u> <u>(1993)</u>
1.0 keV	.24	.20	—	.23	.24	.20
1.5	.22	.20	—	.23	—	—
2.0	.21	.19	.14	.23	—	.16
2.5	.21	.20	.14	—	—	—
3.0	.20	.20	.14	—	.22	—

*Values are approximate, taken from graphical data

samples used by Thomas and Pattinson were prepared *in situ* by evaporating thick films of aluminum (i.e., films thick enough to prevent complete penetration by the primary electrons, thereby behaving—ostensibly—as bulk Al) onto gold, silver, and platinum substrates. The samples were then baked at 800° C for repeated six-hour periods in an effort to ‘de-gas’ the surface—i.e., drive off any surface contaminants. The authors claim this procedure produced “*a clean Al surface, relatively free from any contaminants...*”⁵⁰ (p. 350, italics added)—a claim which appears reasonable, though no direct supporting evidence (such as XPS or Auger data) is offered. Shimizu's sample, by contrast, was electrolytically polished prior to its insertion into the vacuum system, and then cleaned *in situ* via argon ion bombardment (sputtering) at a beam current density of 2×10^{-5} A/cm² (duration of the sputtering was not given). According to Shimizu this technique “*does not always guarantee a clean surface free from slight oxidation due to residual gas, even in the present UHV system...*”⁵⁹ (p. 2109, italics added).

Details regarding vacuum quality and sample preparation are not reported by Kanter,⁴⁸ nor by Garrett,² who presents the results of Whipple. However, given the absence of modern UHV technology during the era in which both sets of measurements were taken, these results are almost certainly those for aluminum oxide. Kanter in fact states that “*the influence of the surface condition on yield is not well known, even for clean surfaces, and the surfaces of the films used in these experiments cannot be considered clean...*”⁴⁸ (p. 680, italics added). Finally, the original source of the BSE yields reported by Reimer⁴⁵ has not been discerned, and therefore no information regarding surface condition or sample preparation can be surmised.

7.1.2 Conclusion Regarding Variability of Results

In summary, results from Thomas & Pattinson⁵⁰ likely represent those for relatively clean Al, while those from Kanter,⁴⁸ Whipple (as reported by Garrett²), and

Shimizu⁵⁹ are from samples all exhibiting some level of surface contamination; results from Reimer⁴⁵ are uncertain in this regard. Varying surface conditions likely account for most of the large variability in these results. Proceeding on this assumption, a comparison with δ and η values obtained in the present investigation can now be attempted.

7.2 Comparison of Results

Referring to Tables 7.1 and 7.2, δ and η values determined in this investigation are presented in two categories: initial surface, and modified surface. The SE and BSE yields under the heading *initial surface* are those values obtained immediately after the electron beam was placed on a new sample location [region A in Fig. 6-10(a)], and are taken from the “Initial” column in Table 6.1. Recall that data from the RGA spectra (6.2.1) strongly suggests these values are not those for clean aluminum, but rather for a contaminated sample surface (quite possibly an oxide layer, Al_2O_3 , with an assortment of other adsorbed species). Hence, comparison of *initial surface* values with those of Kanter, Whipple, and Shimizu is reasonable. Yields under the *modified surface* heading are those values for which current measurements had stabilized over periods of minutes [region B in Fig. 6-10(a)], and are taken from the “~20 min.” column in Table 6.1. Though it is not claimed that this surface is clean aluminum, it is reasonable to assume it to be at least cleaner than the initial surface, and likely lies somewhere in between an oxidized, carbonized, and clean aluminum surface. Nevertheless, comparison of the *modified surface* values with those of Thomas and Pattinson would seem warranted. The notion that the initial surface is in fact a (contaminated) oxide layer is further supported by the fact that the initial-surface δ 's are larger than those for the modified surface—where oxide layers in general are known to have larger SE and BSE yields than do clean(er) metallic surfaces.⁴⁸

7.2.1 *Comparison of δ 's*

Inspection of Table 7.1 reveals good agreement between initial-surface δ 's (assumed now to be contaminated Al_2O_3) of the present work, and those found by Whipple (as reported by Garrett²). This agreement is reasonable given the assertion that Whipple's results are indeed those for Al_2O_3 . Troubling is the relatively good agreement of these same results with those of Thomas and Pattinson, whose surface is assumed clean. Further examination of Table 7.1 shows poor agreement between the modified-surface δ 's of the present investigation and any of those in the literature. Specifically, the SE yields found for the modified surface are 40-50% lower at $E_b = 1.0$ keV than anything else previously reported, and 60% lower at $E_b = 3.0$ keV.

7.2.2 *Comparison of η 's*

Inspection of Table 7.2 reveals reasonable agreement between both sets of η 's obtained in this investigation, and those of Thomas and Pattinson, Shimizu, and Reimer. It is significant to note that the initial-surface η values decrease with increasing beam energy—once again consistent with the notion of an oxide layer. That is, at low beam energies the PE's do not penetrate as deep into the sample, and BSE's therefore originate from layers nearer the surface [see (2.5.1)]. Consequently, oxide layers (ostensibly comprising the first few monolayers of the sample surface) should have a greater effect on BSE yields obtained at lower beam energies than those obtained at higher beam energies, whose BSE's originate from deeper within the sample. Assuming η greater for Al_2O_3 than for clean Al (for a given E_b), decreasing η 's with increasing E_b is a logical result.

Contrasting the beam-energy dependence of the initial-surface η 's, the modified-surface η 's remain steady with changes in incident energies (in the 1-3 keV range), consistent with (a) a very thick, uniform contamination layer (an unlikely condition), or (b) a relatively clean surface—either of which would provide a homogeneous emitting layer.

[NOTE: This observation adds support to the notion that ~20 minutes of exposure to the electron beam has removed a considerable fraction of the surface contamination (at the beamspot location), including any oxide layer.]

7.2.3 Discussion

The above comparisons contain *some* well-grounded evidence to the effect that the apparatus and method are performing well. Particularly encouraging are comparisons of the initial-surface δ 's with Whipple's results, and the initial-surface η 's with Shimizu's results. Somewhat troubling, on the other hand, are comparisons of the modified-surface δ 's *and* η 's with the results of Thomas and Pattinson. Specifically, why are the δ 's ~30% low, and the η 's ~13% low? One potential explanation for this result—as well as for the radically differing δ values of Thomas and Pattinson *vs.* Shimizu—is the possible “channeling effects in the relatively large single-crystal grains that occur in high-purity Al...”⁵⁸ (p. 1971). (If this channeling effect is indeed legitimate, then one might expect better agreement among δ 's for oxide layers as opposed to those for clean surfaces of high-purity aluminum.) More conventionally, two additional possibilities also come to mind: (i) systematic errors in the equipment and/or technique, or (ii) the discrepancies are the result of differing surface conditions on the respective samples. An evaluation of possible errors in the various measurements is warranted before a reasonable conclusion can be drawn.

7.3 Possible Sources of Error

It is reasonable to consider the following possible sources of experimental error:

- (i) systematic errors in the electrometers
- (ii) systematic errors in one or more of the current measurements, resulting from apparatus design.

The question of systematic electrometer error is easiest to address. More complicated is the question of systematic errors due to apparatus design. Pertaining to possible electrometer

errors, the roles of the various electrometers were interchanged from time to time throughout the course of this study, and it was found that results were reproducible in this fashion. Hence it is unlikely that any substantial calibration or zeroing problems are present in these instruments. Pertaining to systematic errors introduced via the apparatus, recall from Chapter 3 that δ and η are determined with the measured quantities I_b , $I_{s(0)}$, $I_{r(0)}$, $I_{s(50)}$, and $I_{r(50)}$ via the relations

$$\delta = \frac{I_{s(50)} - I_{s(0)} + I_{r(0)} - I_{r(50)}}{I_b} \quad (14)$$

and

$$\eta = \frac{I_b - I_{s(50)} + I_{r(50)}}{I_b} \quad (15)$$

(where experimentally, all currents are $\sim\mu\text{A}$, with the exception of $I_{r(0)}$, which is $\sim 10\text{ nA}$). Any errors in δ and η , then, must come from measurement errors in the above quantities. What, then, are the possible errors in each of these quantities? This question is now addressed for each current, in turn.

7.3.1 Errors in I_b

Recall that I_b is measured by placing the beam into the large FC in the sample. Errors in I_b therefore will occur if (i) the entire beam spot is not contained within the cup, (ii) significant numbers of SE's and BSE's escape the cup, and/or (iii) there is measurable noise within the circuit. A FC diameter of 2.7 mm (Fig. 4-6), measurements of beamspot sizes of $\sim 1.2\text{-}1.4\text{ mm}$ (Table 5.2), and the observed disappearance of *any* detectable return current when the beam is in the FC eliminate both (i) and (ii) as likely sources of error. [Additionally, note that errors in either of these assumptions would result in a measured I_b that is too low. Correcting for such a case, however (by increasing I_b in Eqs. 14 and 15), would further *decrease* both δ and η (Table 7.3)—a result which does not explain the observed disagreement between the values obtained in this investigation and those in the

literature.] Regarding (iii), the most probable source of noise in the circuit takes the form of stray (tertiary) electrons striking the beam-current feedthrough pin inside the chamber. But once again, a return-current signal ($I_{r(0)}$) of $< 10^{-14}$ A when the beam is in the FC makes this scenario improbable, since the sample-current and return-current feedthrough pins sit adjacent one another and are shielded equally. (That is, both pins should be subject to similar noise levels, and since none is observed in the return current, it is assumed none is present in the sample current as well.) Also, note that the presence of such noise would lead to $I_{b(\text{meas})} > I_{b(\text{true})}$; however, the numerator in the right-hand side of Eqn. (14) above is larger than that of Eq. (15)—meaning any correction lowering I_b would have a greater effect on η than on δ , which is inconsistent with the discrepancies noted in (7.1.3). Confidence in the accuracy of I_b is therefore high.

7.3.2 Errors in $I_{s(0)}$

The most probable source of error in $I_{s(0)}$ is noise in the form of stray electrons at the feedthrough pin. Unlike the case with the beam directed into the FC, placement of the beam on the sample surface produces a considerable number of tertiary electrons in the chamber (i.e., assuming I_b is $\sim 15 \mu\text{A}$ and $I_{s(0)}$ is $\sim 10 \mu\text{A}$, approximately $5 \mu\text{A}$ worth of stray electrons are flying about the chamber!)—some of which may manifest themselves as noise at the feedthrough pin. But regardless of the magnitude of this noise, it should be about the same as that for $I_{r(0)}$, since, as mentioned above, these two feedthrough pins sit next to one another and are similarly shielded. And since the terms $I_{s(0)}$ and $I_{r(0)}$ appear together in Eq. (14) as a difference, the effects of this error are minimized. That is,

$$(I_{r(0)} + \text{noise}_{(0)}) - (I_{r(s0)} + \text{noise}_{(s0)}) \approx I_{r(0)} - I_{r(s0)}$$

assuming $\text{noise}_{(0)} \approx \text{noise}_{(s0)}$. Also note that any error in $I_{s(0)}$ would have no effect on η . Confidence in $I_{s(0)}$, therefore, is also high.

7.3.3 Errors in $I_{r(0)}$

Recall that the return current is the current collected by the tertiary samples, and models the effect of tertiary (stray) electrons in the system reaching the primary sample.

Several possibilities exist here for error:

1. *Sample holder geometry.* Note that $I_{r(0)}$ and $I_{s(0)}$ include not only electrons reaching the tertiary and primary *samples*, respectively, but also those reaching the sample *holders*. The potential for error exists here in that the combined size (total surface area) of the two tertiary sample holders (TSH's) is considerably smaller than that for the primary sample holder (PSH). If many more electrons are reaching the PSH than the TSH's, then $I_{r(0)(\text{meas})}$ is too small. Two points tend to discredit this scenario as a source of significant error:
 - a. correcting for such an error would further *decrease* δ , and
 - b. though *overall* surface areas differ considerably, the TSH and PSH surface areas *directly exposed to the tertiary flux* are identical.

Again note that any error in $I_{r(0)}$ will have no effect on η .

2. *Asymmetric tertiary flux.* If distribution of the tertiary current flux is such that considerably more current is collected by the tertiary samples than the primary samples, then the measured $I_{r(0)}$ is too large and correction for this error would increase δ . While this situation is certainly possible, particularly if there are stray electric or magnetic fields present near the samples, the fact that $I_{r(0)}$ is already small ($I_{r(0)} \approx 10 \text{ nA}$, as compared with $I_{s(50)} - I_{s(0)} + I_{r(50)} \approx 1 \text{ }\mu\text{A}$) would seem to eliminate this situation as a source of significant error.

3. *Noise.* Once again, tertiaries reaching the feedthrough pin are a likely source of noise, though using the argument of (7.3.2), this error can be ignored with respect to its effect on δ .

7.3.4 Errors in $I_{s(50)}$

Recall $I_{s(50)}$ is the sample current when the sample and tertiary samples are biased to +50V, and the difference between $I_{s(50)}$ and $I_{s(0)}$ ostensibly represents the SE current. Two major possibilities present themselves as potential sources of error in this measurement:

1. *Error in the sample bias.* Biasing the sample greater or less than +50 V would result in $I_{s(50)}$ measurements that are too large, or too small, respectively. However, it is important to note that ~50% of the SE current is due to SE's with energies ≤ 4 eV, and ~90% is due to those with energies ≤ 15 eV (Fig. 2-5)—meaning once the sample has been biased to +15 V, further biasing has only second-order effects on $I_{s(50)}$. An error in the sample bias as great as 10 V, therefore, would still have little impact on $I_{s(50)}$ (and therefore δ and η)—and a realistic estimate of the bias-voltage error is only ~0.1 V.)
2. *Noise.* Tertiaries reaching the feedthrough pin remain the only evident source of significant noise and, repeating the arguments of (7.2.2), resulting errors introduced into $I_{s(50)}$ will not contribute to significant errors in δ or η . (Also note that the presence of positively biased samples in the chamber greatly reduces the number of tertiary electrons dashing about the chamber, eligible to manifest themselves as noise at the feedthrough pins.)

7.3.5 Errors in $I_{r(50)}$

Unlike the case for $I_{r(0)}$, $I_{r(50)}$ is on the order of microamps; significant error in this measurement will therefore introduce a significant error in both δ and η . Recall that $I_{r(50)}$ is that current reaching the tertiary samples when both the primary and tertiary samples (and holders) are biased to +50V, modeling the tertiary current reaching the primary sample (and holder) under such conditions of electrical bias. The most likely mechanisms for introducing error into $I_{r(50)}$ measurements are as follows:

1. *Electric field asymmetry.* Though the geometry of the samples and holders is not complicated (Fig. 4-5), and the electric field in the region just above the samples (resulting from the +50V bias) should be fairly uniform, one can imagine asymmetries in the field which could result in a significant disparity in the number of stray electrons collected by the tertiary and primary samples. If the return current collected by the tertiary samples were substantially greater than that of the primary sample, then $I_{r(50)(\text{meas})}$ would be high, and correcting for this would increase δ and decrease η . Conversely, if most of the tertiaries were being collected by the primary sample, then $I_{r(50)(\text{meas})}$ would be low and correction would decrease δ and increase η . Two observations indicate that such is not the case:

- a. trials involving biasing of only the primary sample (as opposed to the primary sample together with the tertiary samples) strongly indicate that the return current is evenly split between the primary and tertiary samples—i.e., that the tertiary samples are an accurate indicator of return current reaching the primary sample
 - b. an error in $I_{r(50)}$ alone, regardless of its sign or magnitude, cannot simultaneously cause both δ and η to be low.
2. *Noise.* Once again, stray electrons at the feedthrough are possible, and once again such a situation will not introduce significant error into the values for δ or η .

7.3.6 Summary

The above review of possible errors in each of the five current measurements shows that a systematic error in the apparatus or measurement method does not appear a likely cause of disagreement between the δ and η values of this investigation and those in the literature. No compelling evidence of measurement errors has been found, and even if any of the above errors are present, none can account for the observed disagreements of the various δ 's and η 's. This last observation is illustrated in Table 7.3. Only when $I_{b(\text{meas})} > I_{b(\text{true})}$ (which is unlikely) can this, by itself, account for an increase in both δ and η , and even then not by the required magnitudes.

7.4 Discussion

Given the comparisons of (7.1) and the error analysis of (7.2), it appears that *the most likely causes of disagreement between the SE and BSE yields of this investigation, and those of previous studies (and between the previous studies themselves), are varying surface conditions of the samples used in each of the assorted investigations.* This is in itself an important result, and while a considerable volume of interesting physics can likely be extracted from a more careful study of these data, such analysis is not warranted until a better surface characterization is performed. *It is enough to state here that the equipment*

TABLE 7.3. Errors in the measured currents and their effects on SE and BSE yield determination.

Quantity (measured)	Error	Effect on δ , η if corrected	
		δ	η
I_b	High	increase	increase
	Low	decrease	decrease
$I_{s(0)}$	High	increase	none
	Low	decrease	none
$I_{r(0)}$	High	decrease	none
	Low	increase	none
$I_{s(50)}$	High	decrease	increase
	Low	increase	decrease
$I_{r(50)}$	High	increase	decrease
	Low	decrease	increase

and technique of this investigation are yielding reasonable results. Nevertheless, it is also clear that further verification is warranted; disagreement within the literature, a proclivity for oxidation, and more exotic complicating factors such as possible channeling effects all contribute to the difficulty of using aluminum for an initial verification of the equipment. A brief discussion of plans for further verification testing is presented in Chapter 8. First however, having ascertained some measure of credibility for our preliminary measurements, a proposed empirical model accounting for the dynamic evolution of δ [described in (6.2.2)] is presented.

7.5 Proposed Physical Model for $\delta(t)$

We wish to develop a physical model to fit the SE yield measurements of (6.2.2).

The expression

$$\delta(t) = Ae^{-\alpha t} + Be^{-\beta t} + Ce^{-\gamma t} + D \quad (69)$$

is proposed, describing δ as a function of electron-beam exposure time, t . The terms and coefficients have the following physical interpretation:

$Ae^{-\alpha t}$	term representing the rapid electron stimulated desorption of weakly bound (physisorbed) species, from the surface. These species may include CO, CO ₂ , N ₂ , and O ₂ .
$Be^{-\beta t}$	term representing the less rapid electron desorption of tightly bound(chemisorbed) species, from the surface. This may include Al ₂ O ₃ , Al ₂ O ₃ ·n(H ₂ O), Al O(OH), Al(OH) ₂ , Al ₄ C ₃ , AlN, and Al ₂ S ₃ .
$Ce^{-\gamma t}$	term representing the decrease in scattering from metallic Al as a thin film of amorphous carbon is deposited on the surface
D	term representing the bulk SE yield for the deposited film material, $\delta_{\text{film}}^{\text{bulk}}$.
C	coefficient representing the difference between $\delta_{\text{film}}^{\text{bulk}}$ and δ for a clean Al surface, $\delta_{\text{Al}}^{\text{bulk}}$.
B	coefficient representing the difference between $\delta_{\text{Al}}^{\text{bulk}}$ and δ for and Al surface coated with chemisorbed layers, $\delta_{\text{Al}}^{\text{chem}}$
A	coefficient representing the difference between δ for an uncleaned Al surface ($\delta_{\text{Al}}^{\text{dirty}}$) and one with the physisorbed (but not chemisorbed) material removed, $\delta_{\text{Al}}^{\text{chem}}$.
γ	the deposition rate of the thin carbon film in hr ⁻¹ .
β	the desorption rate of the chemisorbed material in hr ⁻¹ .
α	the desorption rate of the physisorbed material in hr ⁻¹ .

Values for the above parameters, obtained through nonlinear regression analysis of the curves depicted in Fig. 6-10, are given in Table 7.4. Figure 7-1 is a comparison of the resulting fit [Eq. (69) using the values from Table 7.4] and the actual data points.

Inspection of Fig. 7-1 shows the fit to be good, though in need of some fine-tuning. For our purposes, though, the fit demonstrates a more-than-reasonable grasp of

the physical processes involved in the evolution of δ with time—specifically, a rapid electron-beam induced desorption of some species from the sample surface, a somewhat slower desorption of other species, and a still (much) slower beam-induced carbon deposition.

TABLE 7.4. Estimated values for parameters appearing in Eq. (69).

Parameter	Value	Uncertainty
A	0.181	~10%
B	0.075	~10%
C	0.069	~5%
D	0.251	~1%
α	35.5 hr ⁻¹	~15%
β	0.707 hr ⁻¹	~15%
γ	0.113 hr ⁻¹	~15%

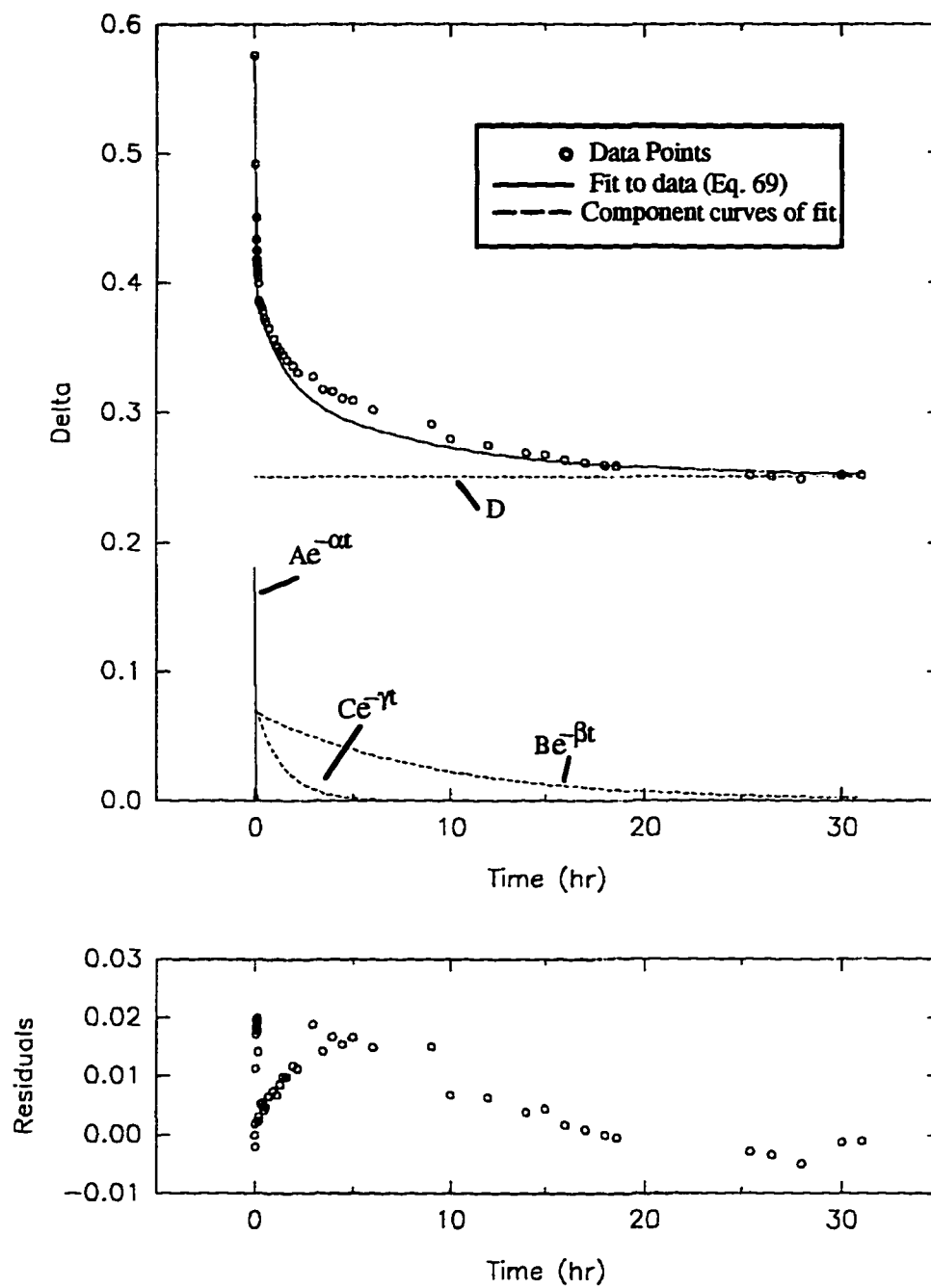


FIG. 7-1. Fit of data for dynamic evolution of δ . The solid curve represents Eq. (69), using the free parameters listed in Table 7.4.

CHAPTER 8

RESULTS, RECOMMENDATIONS, AND CONCLUSION

This chapter summarizes results obtained to date (8.1) and addresses necessary refinements in the apparatus and method (8.2), a proposed course of research once these refinements are accomplished (8.3) and (8.4), and recommendations for extensions of this research (8.5).

8.1 Results

Primary results of the work presented in this thesis are restated below.

- (i) The apparatus and technique developed for total SE and BSE yield determination are working.
- (ii) The absence of adequate (or any) surface characterizations accompanying previously reported experimental SE yield investigations is a key omission in the data. Results of these investigations, consequently, are fundamentally flawed. Specifically, previously reported results for normally incident electrons on Al are almost certainly incorrect.
- (iii) The surface of the Al sample characterized in this investigation was a contaminated oxide layer. The effects of extended exposure of this surface to the electron beam were the (at least partial) removal of the oxide and other contaminants, and the formation of a thin (several monolayers) film of carbon, all occurring on competing time scales.

8.2 Immediate Recommendations

8.2.1 *Further Verification*

In retrospect, aluminum was not a reasonable choice for the verification trials. Major difficulties with this material were (i) a proclivity to oxidize, (ii) possible channeling effects, and (iii) disagreement of δ and η values *within the literature* for the 1-3 keV

incident energy range [where (iii) is likely the consequence of (i) and (ii)]. The obvious solution to this problem is to repeat the trials with a different material—one less susceptible to the above difficulties. Gold is a suitable candidate; it does not form a stable oxide, and previously reported SEE and backscattering characterizations are in much better (though not perfect) agreement in the 1-3 keV energy range.^{44-46,50,116,117} Total δ and η characterizations of gold can be accomplished quickly, with no modifications to equipment or procedure.

Angle-, energy-, and angle-energy-resolved measurements must also be performed and evaluated; of these, energy-resolved SE trials can be performed immediately. Angle- and angle-energy-resolved measurements must wait until the RD can be properly aligned.

8.2.2 *Required Equipment and Procedural Modifications*

In addition to required further verification trials, work thus far has also revealed a number of shortcomings in the apparatus and basic procedures. These are: (i) sample surface preparation, characterization, and prevention of unwanted surface modification, (ii) RD alignment, and (iii) leakage current in the RD. The following steps address these difficulties:

1. *Performing a hotter bakeout.* This will improve vacuum quality, thereby reducing the level of contaminant species in the chamber, and will require:
 - a. replacement of the rotary feedthrough (the present rotary feedthrough is bakeable to only 100°C), and
 - b. replacement of the Teflon insulation sleeves in the RD with sapphire (the Teflon begins to deform at ~95°C).
2. *Mechanically polishing the sample with a clean cloth.* Considerable surface contamination in the form of surface inclusions, as evidenced by the SEM images, were the likely result of using a "dirty" polishing cloth [see (6.1.2)].
3. *Electropolishing the sample.*

4. *Annealing the sample in situ.* Annealing will aid in driving off unwanted contaminants. The installation of a thermocouple or platinum resistance thermometer on the sample block is required.
5. *Reducing carbon sources.* Minimizing carbon film buildup will require significant reduction of carbon sources within the chamber. Thorough baking of the chamber will go a long way toward this end. Other steps to be taken are:
 - a. replacement of heater wires (the hydrocarbon-base insulation on these wires appears to be outgasing),
 - b. replacement of Teflon sleeve in RD with sapphire insulator (Teflon is a source of CF), and
 - c. removing graphite coatings from inside RD Faraday cup (used to reduce SEE within the cup), and from support shaft (used to lubricate rotating plate).
6. *Minimizing beam time on sample,* resulting in a reduction of carbon build-up.
7. *Addition of Auger Electron Spectroscopy (AES) electronics.* AES capability will enable *in situ* analysis of surface species—particularly important for characterizing the state of contamination.
8. *Development of method for RD alignment prior to chamber insertion.*
9. *Redesigning the RD.* The current RD was designed for use with an electrostatic filter (Fig. 4-10). Making the RD smaller and placing it closer to the sample would make it easier to aim, and would expand the angular range over which measurements can be made.
10. *Replacing RD Teflon with sapphire.* The (volume) resistivity of sapphire is considerably higher than that of the Teflon currently being employed (10^{18} Ohm-cm as opposed to 10^{12} Ohm-cm).¹⁰⁰ Leakage current from the Faraday cup in the RD should drop by six orders of magnitude (or more, if a smaller contact area is used) as a result of this modification.
11. *Biasing the ground plate in the RD.* Biasing the ground plate along with the Faraday cup in the RD will also greatly reduce the leakage current. Even without replacing the Teflon, ground-plate biasing should reduce leakage currents to levels below detection limits.

Once testing is completed, there is the question of what new physics can be accomplished with this apparatus. The remainder of the chapter addresses this question.

8.3 Research Possibilities

A considerable volume of original experimental work will be immediately accessible once the apparatus and method have been fully verified. Accompanying the data will be an opportunity for comparison of results with existing SEE theory. Examples of both experimental investigations and theoretical comparisons are given below.

8.3.1 *Experimental Investigations*

Experimental (angle-resolved, energy-resolved, angle-energy-resolved, and total) SE and BSE yield investigations possible with the apparatus described in this thesis, as modified above, include (1-3 keV energy range):

- (i) characterization of clean metals,
- (ii) characterization of never-before-characterized (conducting) spacecraft materials, coatings, and paints,
- (iii) controlled sample contamination studies,
- (iv) studies involving sample temperature as a parameter,
- (v) studies involving surface roughness as a (qualitative) parameter, and
- (vi) studies involving sample conductivity as a parameter.

Total yields for a number of metals (including Ag, Au, Cu, C, Ni, Pt, and others) have been measured previously (though we have not yet completed an exhaustive review of the literature). Moreover, most of these materials are not subject to oxidation difficulties as severe as those for aluminum. Nevertheless, it is impossible to say with certainty that measurements for *clean* metal surfaces have been accomplished, since surface conditions associated with most prior measurements are, in general, poorly documented. Rather, levels of contamination must be inferred from such considerations as vacuum quality and *in*

situ cleaning methods. Systematic SEE characterization of basic metals, therefore, with simultaneous Auger analysis documenting the surface quality, will be of significant value to the field. Studies involving additional parameters, such as temperature, surface roughness, and conductivity, may then be performed with a reasonable degree of confidence.

8.3.2 Comparisons with Theory

There exists within the literature a well-developed fundamental theory of SEE,⁶⁶ as well as a number of empirical mathematical models based on previous experimental investigations.^{45,61,118-120} Data obtained from the investigations listed above may be used to evaluate both theoretical and empirical SEE formulations. Some examples include:

- (i) comparison of total yields with atomic number models,^{44,45,61}
- (ii) comparison of angle-resolved yields with existing angular formulations,^{45,69} and
- (iii) comparison of clean aluminum yields with published fundamental theory specifically for SEE in Al.⁶⁷

8.4 Extensions of This Research

It should be recognized that the basic apparatus and technique developed for the above-proposed research possess considerable potential for significantly expanded SE and BS investigations—some of which would require modifications to the apparatus and the development of new measurement techniques. Some examples are:

- (i) backscattering measurements for insulators,
- (ii) SEE measurements for insulators,
- (iii) measurements for higher or lower incident electron energies,
- (iv) measurements for incident ions,
- (v) work involving simultaneous bombardment by combinations of electrons, ions, and photons,
- (vi) measurements for positively and/or negatively biased samples, and

- (vii) investigations of SE roles in such phenomena as "snapover"—the breakdown of insulators in a plasma—and other little-understood manifestations of electrical breakdown.

Techniques for the determination of BSE yields for insulators have been developed,¹¹⁶ at least partially, and should be readily adaptable to this apparatus. They involve *in situ* deposition of thin conducting films (with known backscatter characteristics) on insulators. It is possible that a similar (though not identical) process may be applied toward SE characterization of insulators as well. SE and BSE studies involving incident electron energies both above and below the present 1-3 keV range are merely a question of appropriate electron sources; likewise, SE and BS studies involving incident ions require only the acquisition of suitable ion sources—a process already underway. Parametric studies involving incident electrons, ions, and photons may be possible in a new UHV scattering chamber, already under construction at USU. Finally, the role of SE's in snapover may be investigated in a low-density plasma chamber available at NASA's Lewis Research Center (LeRC). Initial coordination for such work has already been accomplished and funding secured. The preceding lines of possible research are displayed graphically in Fig. 8-1.

8.5 Initial Program of Study—A Proposal

The prodigious volume of possible research listed in (8.3) suggests the need for an organized plan according to which research can proceed. The following sequence of investigation is suggested, prioritizing SE and BSE Z-dependence and the importance of contamination:

1. *Completion of an exhaustive literature review.* Though a good deal of this work has already been accomplished, more remains to be done. Simply summarizing all SE and BS investigations to date, and their results, will prove invaluable in plotting the course of future research, and will itself represent an important contribution to the field.

2. *Total SE and BSE yield characterization of a series of clean metals, and comparison of results with fundamental and empirical models.* Such an investigation is a logical place to start, and may suggest further avenues of research. Metals characterized in this work might include the Nobel metals Au, Ag, and Cu, and/or the Alkali metals Li, Na, K, Rb, and Cs. Also included here should be a thorough investigation of clean Al, something that may well never before have been accomplished.

3. *Total SE and BSE yield investigations of never-before-characterized spacecraft materials.* This work will represent an immediate contribution to the spacecraft charging community, and should be accomplished based on consultation with NASA's LeRC. Actual samples from two spaceflight projects have already been secured: NASA's LDEF, and a USU rocket (SPEAR III).

4. *Extensive SE and BSE yield characterization of one particular sample, including angle-, energy-, and angle-energy-resolved yields, and comparison with theory.* An investigation of this type will validate apparatus and technique, and results may suggest further research. Gold is a likely candidate for this investigation.

5. *Controlled contamination studies.* Review of the literature thus far, as well as experimental experience, has shown the lack of data regarding the effect of surface contamination on SE yield to be a major deficiency in the field. Oxidation of Al presents itself as an immediate candidate for this work. Other forms of natural contamination, such as fingerprints, or depositions resulting from propellants or from the outgassing of organic materials, may also be of immediate interest to spacecraft charging modelers.

6. *Studies involving additional parameters such as temperature, surface roughness, and conductivity.* To our knowledge such investigations have not been performed and would represent an entirely new direction in the field of SEE.

Clearly, the above plan is intended as a guideline, and should be modified as work progresses. The most productive lines of discovery are rarely scripted.

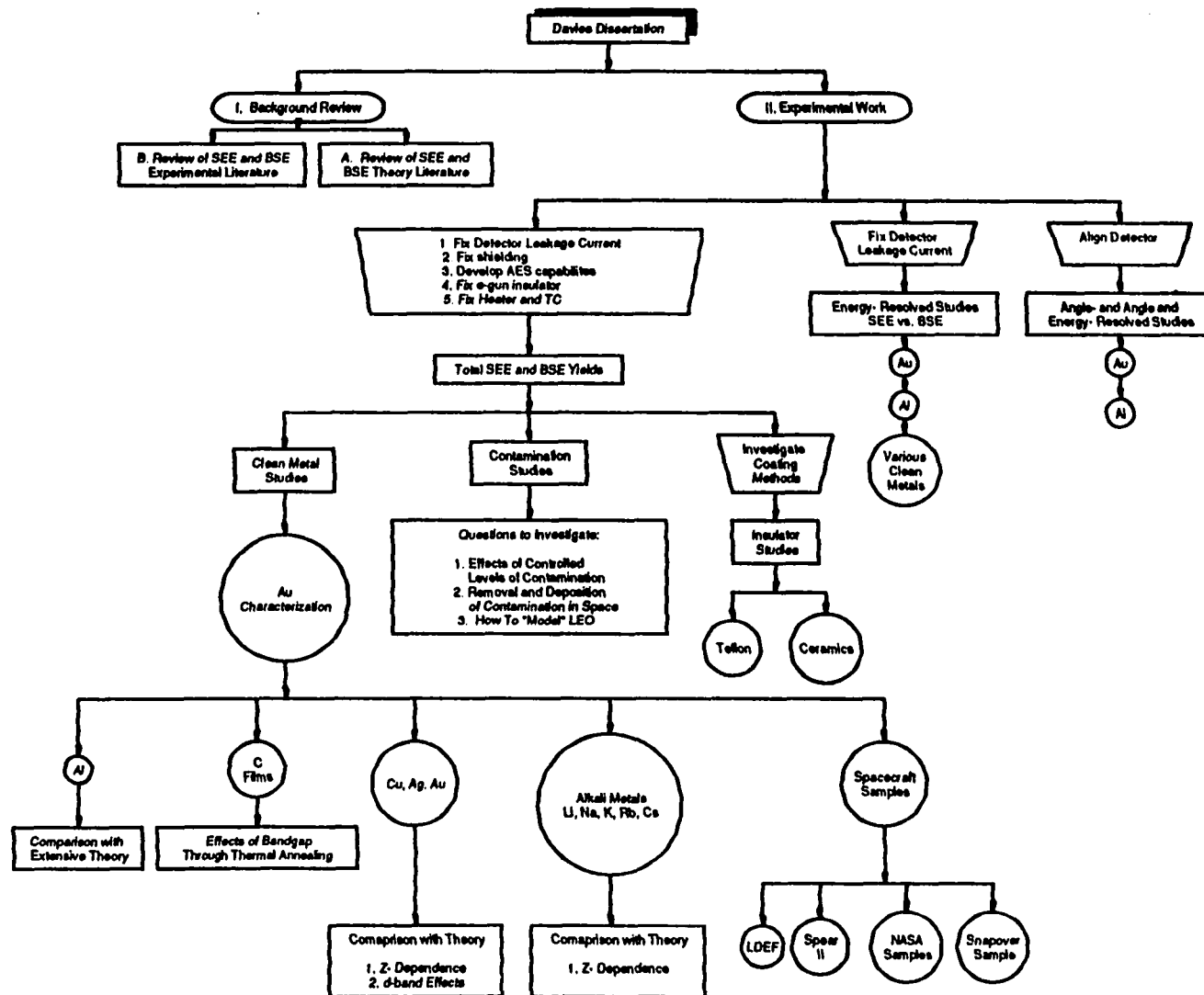


FIG. 8-1. Possibilities for future work.

REFERENCES

1. E.C. Whipple, "Potentials of surfaces in space," Rep. Prog. Phys. **44**, 1197 (1981).
2. H.B. Garrett, "The charging of spacecraft surfaces," Rev. Geophys. Space Phys. **19** (4), 577 (1981).
3. Thomas B. Frooninckx, M.S. thesis, Utah State University, 1991.
4. S.E. DeForest, "Spacecraft charging at synchronous orbit," J. Geophys. Res. **77**, 651 (1972).
5. R.C. Olsen, "Record charging events from Applied Technology Satellite 6," J. Spacecraft Rockets **24**, 362 (1987).
6. S.M.L. Prokopenko and J.G. Laframboise, "High-voltage differential charging of geostationary spacecraft," J. Geophys. Res. **85** (A8), 4125 (1980).
7. M.S. Gussenhoven and E.G. Mullen, "Geosynchronous environment for severe spacecraft charging," J. Spacecraft Rockets **20** (1), 26 (1983).
8. H.-C. Yeh and M.S. Gussenhoven, "The statistical electron environment for defense meteorological satellite program eclipse charging," J. Geophys. Res. **92** (A7), 7705 (1987).
9. M.S. Gussenhoven *et al.*, "High-level spacecraft charging in the low-altitude polar auroral environment," J. Geophys. Res. **90** (A11), 11,009 (1985).
10. T.B. Frooninckx and J.J. Sojka, "Solar cycle dependence of spacecraft charging in low earth orbit," J. Geophys. Res. **97** (A3), 2985 (1992).
11. W.N. Hall *et al.*, "Polar-auroral charging of the Space Shuttle and EVA astronaut," in The Aerospace Environment at High Altitudes and its Implications for Spacecraft Charging and Communications. AGARD-CP-406, (North Atlantic Treaty Organization, Neuilly sur Seine, France, 1987), p. 34-1.
12. R. Grard, K. Knott, and A. Pedersen, "Interactions between a large body and its environment in a low polar orbit," in Proceedings of the Air Force Geophysics Laboratory Workshop on Natural Charging of Large Space Structures in Near Earth Polar Orbit, edited by R.C. Sagalyn, D.E. Donatelli, and I. Michael, Rep. AFGL-TR-83-0046. ADA134894 (Air Force Geophys. Lab., Hanscom Air Force Base, MA, 1983), p. 175.
13. K.G. Balmain, "Arc propagation, emission, and damage on spacecraft dielectrics," in The Aerospace Environment at High Altitudes and its Implications for Spacecraft Charging and Communications. AGARD-CP-406, (North Atlantic Treaty Organization, Neuilly sur Seine, France, 1987), p. 16-1.
14. C.Y. Johnson and E.B. Meadows, "First investigation of ambient positive-ion composition to 219 km by rocket-borne spectrometer," J. Geophys. Res. **60**, 193 (1955).

15. H.B. Garrett and S.E. DeForest, "Time-varying photoelectron flux effects on spacecraft potential at geosynchronous orbit," *J. Geophys. Res.* **84**, 2083 (1979).
16. R.C. Olsen *et al.*, "Observations of differential charging effects on ATS 6," *J. Geophys. Res.* **86**, 6809 (1981).
17. E.C. Whipple and R.C. Olsen, "High spacecraft potentials on ESEE-1 in sunlight," in The Aerospace Environment at High Altitudes and its Implications for Spacecraft Charging and Communications. AGARD-CP-406, (North Atlantic Treaty Organization, Neuilly sur Seine, France, 1987), p. 8-1.
18. L. Broihanne, "Spacecraft protection against electrostatic discharge—Application to the ARABSAT spacecraft," in The Aerospace Environment at High Altitudes and its Implications for Spacecraft Charging and Communications. AGARD-CP-406, (North Atlantic Treaty Organization, Neuilly sur Seine, France, 1987), p. 22-1.
19. D.K. Davies, "Radiation charging and breakdown of insulators," in The Aerospace Environment at High Altitudes and its Implications for Spacecraft Charging and Communications. AGARD-CP-406, (North Atlantic Treaty Organization, Neuilly sur Seine, France, 1987), p. 19-1.
20. A. Rosen, "Spacecraft charging: Environment-induced anomalies," *J. Spacecraft Rockets* **13**, 129 (1976).
21. P.N. Wadham, "The effects of electrostatic discharge phenomena on Telesat's domestic communications satellites," in The Aerospace Environment at High Altitudes and its Implications for Spacecraft Charging and Communications. AGARD-CP-406, (North Atlantic Treaty Organization, Neuilly sur Seine, France, 1987), p. 25-1.
22. R.R. Shaw *et al.*, "Observations of electrical discharges caused by differential satellite charging," in Spacecraft Charging by Magnetospheric Plasmas. Prog. Astronaut. Aeronaut., edited by A. Rosen (AIAA Press, New York, 1976), Vol. 47, p. 61.
23. H. Lechte, "Electrostatic immunity of geostationary satellites," in The Aerospace Environment at High Altitudes and its Implications for Spacecraft Charging and Communications. AGARD-CP-406, (North Atlantic Treaty Organization, Neuilly sur Seine, France, 1987), p. 24-1.
24. D. Verdin and M.J. Duck, "Surface modifications to minimise the electrostatic charging of Kapton in the space environment," in The Aerospace Environment at High Altitudes and its Implications for Spacecraft Charging and Communications. AGARD-CP-406, (North Atlantic Treaty Organization, Neuilly sur Seine, France, 1987), p. 26-1.
25. W.J. Raitt *et al.*, "Active vehicle charging measurements in sounding rocket and Space Shuttle orbiter environments at low-Earth orbit (LEO) altitude," in The Aerospace Environment at High Altitudes and its Implications for Spacecraft Charging and Communications. AGARD-CP-406, (North Atlantic Treaty Organization, Neuilly sur Seine, France, 1987), p. 9-1.

26. B.M. Shuman *et al.*, "Automatic charge control system for geosynchronous satellites," in The Aerospace Environment at High Altitudes and its Implications for Spacecraft Charging and Communications, AGARD-CP-406, (North Atlantic Treaty Organization, Neuilly sur Seine, France, 1987), p. 27-1.
27. B. Jung, "The origin of solid particles in interstellar space," *Astron. Nachr.* **263**, 426 (1937).
28. L. Spitzer, Jr., "The temperature of interstellar material," *Astrophys. J.* **107**, 6 (1948).
29. L. Spitzer, Jr. and M.P. Savedoff, "The temperature of interstellar matter, III," *Astrophys. J.* **111**, 593 (1950).
30. M.C. Kelley, The Earth's Ionosphere, (Academic Press, San Diego, 1989), p. 20.
31. W. Jiang, M.S. report, Utah State University, 1992.
32. E.C. Whipple, Jr., "An overview of charging of large space structures in polar orbit," in Proceedings of the Air Force Geophysics Laboratory Workshop on Natural Charging of Large Space Structures in Near Earth Polar Orbit, edited by R.C. Sagalyn, D.E. Donatelli, and I. Michael, Rep. AFGL-TR-83-0046. ADA134894 (Air Force Geophys. Lab., Hanscom Air Force Base, MA, 1983), p. 11.
33. J. Lemaire, "The quiet and disturbed plasmasphere," in The Aerospace Environment at High Altitudes and its Implications for Spacecraft Charging and Communications, AGARD-CP-406, (North Atlantic Treaty Organization, Neuilly sur Seine, France, 1987), p. 1-1.
34. F.J. Rich, "Ionospheric characteristics: A review," in Proceedings of the Air Force Geophysics Laboratory Workshop on Natural Charging of Large Space Structures in Near Earth Polar Orbit, edited by R.C. Sagalyn, D.E. Donatelli, and I. Michael, Rep. AFGL-TR-83-0046. ADA134894 (Air Force Geophys. Lab., Hanscom Air Force Base, MA, 1983), p. 29.
35. R.W. Shunk, "A mathematical model of the middle and high latitude ionosphere," *Pure Appl. Geophys.* **127**, 255 (1988).
36. J.J. Sojka, "Global scale, physical models of the F region ionosphere," *Rev. Geophys.* **27**, 371 (1989).
37. D.A. Hardy *et al.*, "A statistical model of auroral electron precipitation," *J. Geophys. Res.* **90** (A5), 4229 (1985).
38. D.A. Hardy *et al.*, "A statistical model of auroral ion precipitation," *J. Geophys. Res.* **94** (A1), 370 (1989).
39. E.G. Mullen *et al.*, "SCATHA survey of high-level spacecraft charging in sunlight," *J. Geophys. Res.* **91**, 1474 (1986).

40. I. Katz *et al.*, "Secondary electron generation, emission and transport: Effect on spacecraft charging and NASCAP models," in The Aerospace Environment at High Altitudes and its Implications for Spacecraft Charging and Communications, AGARD-CP-406, (North Atlantic Treaty Organization, Neuilly sur Seine, France, 1987), p. 14-1.
41. H.B. Garrett, Spacecraft Potential Calculations—A Model, AFGL-TR-78-0116, (Air Force Geophysics Laboratory, Hanscom Air Force Base, MA, 1978), pp. 7-19.
42. J.R. Dennison, (private communication).
43. I. Katz *et al.*, "The importance of accurate secondary electron yields in modeling spacecraft charging," J. Geophys. Res. **91**, 13,739 (1986).
44. E.J. Sternglass, "Backscattering of kilovolt electrons from solids," Phys. Rev. **95**, 345 (1954).
45. L. Reimer, Image Formation in Low-Voltage Scanning Electron Microscopy, (SPIE, Bellingham, Wash., 1993), pp. 57-70.
46. L. Reimer and H. Drescher, "Secondary electron emission of 10-100 keV electrons from transparent films of Al and Au," J. Phys. D: Appl. Phys. **10**, 805 (1977)
47. E.J. Sternglass, "Theory of secondary electron emission by high speed ions," Phys. Res. **108**, 1 (1957).
48. H. Kanter, "Energy dissipation and secondary electron emission in solids," Phys. Rev. **121** (3), 677 (1961)
49. H. Kanter, "Contribution of backscattered electrons to secondary electron formation," Phys. Rev. **121** (3), 681 (1961).
50. S. Thomas and E.B. Pattinson, "Range of electrons and contribution of back-scattered electrons in secondary production in aluminum," J. Phys. D: Appl. Phys. **3**, 349 (1970).
51. I.M. Bronshtein and R.B. Segal, Sov. Phys.—Solid-St. **1**, 1365 (1960).
52. I.M. Bronshtein and B.S. Fraiman, Sov. Phys.—Solid-St. **3**, 1188 (1961).
53. A.G. Rubin *et al.*, "Reduction of spacecraft charging using highly emissive surface materials," in Proceedings of the 1978 Symposium on the Effects of the Ionosphere on Space and Terrestrial Systems, (Naval Research Laboratory, Washington, DC, 1978), p. 313.
54. Gary Jongeward (private communication).
55. Dale Fergusson (private communication).
56. L.L. Hatfield (private communication).

57. J.G. Laframboise, "Is there a good way to model spacecraft charging in the presence of space-charge coupling, flow, and magnetic fields?," in Proceedings of the Air Force Geophysics Laboratory Workshop on Natural Charging of Large Space Structures in Near Earth Polar Orbit, edited by R.C. Sagalyn, D.E. Donatelli, and I. Michael, Rep. AFGL-TR-83-0046. ADA134894 (Air Force Geophys. Lab., Hanscom Air Force Base, MA, 1983), p. 57.
58. E.H. Darlington and V.E. Cosslett, "Backscattering of 0.5-10 keV electrons from solid targets," J. Phys. D: Appl. Phys. **5**, 1969 (1972).
59. R. Shimizu, "Secondary electron yield with primary electron beam of kilo-electronvolts," J. Appl. Phys. **45**, 2107 (1974).
60. G. Neubert and S. Rogaschewski, "Backscattering coefficient measurements of 15 to 60 keV electrons for solids at various angles of incidence," Phys. Stat. Sol. (a) **59**, 35 (1980).
61. S. Ono and K. Kanaya, "The energy dependence of secondary emission based on the range-energy retardation formula," J. Phys. D: Appl. Phys. **12**, 619 (1979).
62. E. H. Darlington, "Backscattering of 10-100 keV electrons from thick targets," J. Phys. D: Appl. Phys. **8**, 85 (1975).
63. J.I. Goldstein, D.E. Newbury, P. Echlin, D.C. Joy, A.D. Robig, C.E. Lyman, D. Fiori, and E. Lifshin, Scattering Electron Microscopy and X-Ray Analysis, 2nd. ed. (Plenum Press, New York, 1992), p. 649.
64. H. Niedrig, "Electron backscattering from thin films," J. Appl. Phys. **53**, R15 (1982).
65. H. Drescher *et al.*, "Backscattering and secondary electron emission of 10-100 keV electrons and correlations to scanning electron microscopy," Z. Angew. Phys. **29**, 331 (1970).
66. M. Rosler and W. Brauer, "Theory of secondary electron emission, I," Phys. Stat. Sol. (b) **104**, 161 (1981).
67. M. Rosler and W. Brauer, "Theory of secondary electron emission, II," Phys. Stat. Sol. (b) **104**, 575 (1981).
68. A. Darlinski, "Measurements of angular distribution of the backscattered electrons in the energy range of 5 to 30 keV," Phys. Stat. Sol. (a) **63**, 663 (1981).
69. Tesar and Eckertora, "The dependence of the angular distribution of backscattered electrons on the atomic number of the target," Czech. J. Phys. **B23**, 867 (1973).
70. W. Oppel and H. Hahrreiss, "Angular distribution measurements of secondary electrons from thin selfsupporting Al and Au films," Z. Phys. **252**, 107 (1972).
71. H. Hahrreiss and W. Oppel, "Angular distributions of secondary electrons originating from thin films of different metals in re-emission and transmission," J. Vac. Sci. Technol. **9**, 173 (1971).

72. J.L.H. Jonker, "The angular distribution of the secondary electrons of nickel," Philips Res. Rep. **6**, 372 (1951).
73. H. Kanter, "Zur ruckstreuung von elektronen im energiebereich von 10 bis 100 keV," Ann. Phys **6**, 144 (1957).
74. T. Matsukawa *et al.*, "Measurements of the energy distribution of backscattered kilovolt electrons with a spherical retarding-field energy analyser," J. Phys. D: Appl. Phys. **7**, 695 (1974).
75. D.H. Rester and J.H. Derrickson, "Electron backscatter measurements for perpendicular and non-perpendicular incidence at 1.0 MeV bombarding energy," Nucl. Instrum. Methods **86**, 261 (1970).
76. H.-J. Fitting, "The energy loss of transmitted and backscattered electrons," J. Phys. D: Appl. Phys. **8**, 1480 (1975).
77. L. Reimer, Image Formation in Low-Voltage Scanning Electron Microscopy (SPIE, Bellingham, WA, 1993), pp. 51-70.
78. P. Gerard *et al.*, "Systeme de mesure de l'energie d'electrons retrodiffuses en fonction de l'angle d'emission," J. Phys. III France **2**, 1015 (1992).
79. P.L. Gruzin, "Measuring spectral angular distributions of backscattered electrons," Sov. J. At. Energ. **33**, 779 (1972).
80. C. Cohen-Tannoudji, B. Diu, and F. Laloe, Quantum Mechanics (John Wiley & Sons, New York, 1977), pp. 905-906.
81. T.A. Delchar, Vacuum Physics and Techniques (Chapman & Hall, London, 1993), p. 101.
82. J.R. Dennison, Surface analysis chamber notebook, Jan. 89 - Jan. 91 (unpublished).
83. Veeco Instruments, Operation and maintenance manual for ionization gauge control model RG-84, (unpublished).
84. VG Quadrupoles, User's manual for VG ARGAs partial and total pressure analyzer, 1986 (unpublished).
85. Granville Phillips, Variable leak valve series 203 installation and operating instructions, 1971 (unpublished).
86. L.T. Lamont, Jr., in Methods of Experimental Physics, edited by G.L. Weissler and R.W. Carlson, (Academic Press, New York, 1979), Vol. 14, Chap. 14, pp. 491-503.
87. Magnetic Shield Corporation, Perfection Mica Company, Material and fabrication guide, 1988 (unpublished).

88. Varian, Instruction manual for Auger electron gun models 981-2454 and 981-2455, 1973 (unpublished).
89. Varian, Operating instructions for Auger electron gun power supply model 981-0246, 1970 (unpublished).
90. Varian, LEED/Auger electron gun model 981-2125 instruction manual, 1978 (unpublished).
91. JR Dennison (private communication).
92. Varian, Instruction manual for ion bombardment gun model 981-1045/0043, 1972 (unpublished).
93. Varian, Operating instructions for ion bombardment gun control unit model 981-0046, 1970 (unpublished).
94. Varian, Instruction manual for ion bombardment gun power supply model 981-2046, 1985 (unpublished).
95. Keithley Instruments Inc., Instruction manual for digital electrometer model 616, 1975 (unpublished).
96. C.E. Kuyatt, in Methods of Experimental Physics, edited by B. Bederson and W.L. Fite (Academic Press, New York, 1968) Vol. 7, pp. 19-23.
97. J.H. Moore, C.C. Cavis, and M.A. Coplan, Building Scientific Apparatus (Addison-Wesley, London, 1983), pp. 319-322.
98. R. Davies, "An experiment to determine the angular distribution of backscattered electrons as a function of energy and material," Final report, United States Air Force Office of Scientific Research 1991 Summer Researcher's Program (unpublished).
99. R. Davies, Notebook II pp. 21-25 (unpublished).
100. Keithley Instruments, Low Level Measurements Handbook, 4th ed. (Keithley Instruments, Cleveland, OH 1992), pp. 2-12 to 3-4.
101. MDC corporation (private communication, 1996).
102. R. Davies, Notebook I, p. 23 (unpublished).
103. R. Davies, Procedures checklists (unpublished).
104. R. Davies, Notebook I, pp. 27-49 (unpublished).
105. R. Davies, Notebook II, pp. 1-32 (unpublished).
106. R. Davies, Notebook I, pp. 38 (unpublished).
107. ISI (private communication).

108. R.D. Ramsier and J.T. Yates, Jr., "Electron-stimulated desorption: Principles and applications," *Surf. Sci. Rep.* **12**, 243-378 (1990).
109. T. Smith, "Auger electron spectroscopy and ion sputter profiles of oxides on aluminum," *Surf. Sci.* **55**, 601-624 (1976).
110. William McManus (private communication).
111. Nabil Youssef (private communication).
112. J.E. Goldstein and D.E. Newbury, Scanning Electron Microscopy and X-Ray Microanalysis, 2nd edit. (Plenum, New York, 1992).
113. Patrick Espy (private communication).
114. J. Hillier, "On the investigation of specimen contamination in the electron microscope," *J. Appl. Phys.* **18**, 153 (1947).
115. J.H. Moore, C.C. Cavis, and M.A. Coplan Building Scientific Apparatus (Addison-Wesley, London, 1983), p. 335.
116. J.E. Holliday and E.J. Sternglass, "Backscattering of 5-20 keV electrons from insulators and metals," *J. Appl. Phys.* **28**, 1189 (1957).
117. H.E. Bishop, "Electron scattering in thick targets," *Brit. J. Appl. Phys.* **18**, 703 (1967).
118. G.F. Dionne, "Origin of secondary-electron-emission yield-curve parameters," *J. Appl. Phys.* **46**, 3347 (1975).
119. K. Kanaya and H. Kawakatsu, "Secondary electron emission due to primary and backscattered electrons," *J. Phys. D* **5**, 1727 (1972).
120. R.C. Alig and S. Bloom, "Secondary-electron-escape probabilities," *J. Appl. Phys.* **49**, 3476 (1978).

APPENDICES

APPENDIX A

Calculations

A.1 Importance of I_{ser} , $I_{bser(0)}$, and $I_{bser(50)}$

In addition to demonstrating that the currents I_{ser} , $I_{bser(0)}$, and $I_{bser(50)}$ from Fig. 3-4 are indeed small in comparison to the other currents, one can in fact show that regardless of their magnitudes, these terms can be neglected. For ease of calculation, we introduce the notation

PS(0)	primary sample current at 0 V bias	(measured)
PS(50)	primary sample current at +50 V bias	(measured)
TS(0)	tertiary sample current at 0 V bias	(measured)
TS(50)	tertiary sample current at 50 V bias	(measured)
B	incident beam current	(measured)
SE	secondary electron current	
BSE	backscattered electron current	
R(0)	return current at 0 V bias	
R(50)	return current at +50 V bias	
SER	SE current due to $r(0)$	
BSER(0)	BSE current due to $r(0)$	
BSER(50)	BSE current due to $r(50)$	

where those currents that are actually *measured* by the apparatus have been so marked.

Then with the samples biased to 0 V and +50 V, in turn, we can write

$$PS(0) = B - SE - BSE + R(0) - SER - BSER(0) \quad (A1)$$

$$PS(50) = B - BSE + R(50) - BSER(50) \quad (A2)$$

$$TS(0) = R(0) - SER - BSER(0) \quad (A3)$$

$$TS(50) = R(50) - BSER(50) \quad (A4)$$

Subtracting (A3) from (A1) and (A4) from (A2) gives

$$PS(0) - TS(0) = B - SE - BSE \quad (A5)$$

$$PS(50) - TS(50) = B - BSE \quad (A6)$$

which in turn gives

$$\text{BSE} = B - \text{PS}(50) + \text{TS}(50) \quad (\text{A7})$$

$$\text{SE} = \text{PS}(50) - \text{PS}(0) + \text{TS}(0) - \text{TS}(50) \quad (\text{A8})$$

and we have now solved for the SE and BSE currents [Eqs. (A7) and (A8)]—the goal, in determining δ and η —without making any assumptions whatsoever about the magnitudes of SER, BSER(0), and BSER(50). Dividing the Eqs. (A7) and (A8) by the beam current B and returning to the notation of (3.3.1), we retrieve Eqs. (14) and (15)

$$\delta = \frac{I_{s(50)} - I_{r(50)} - I_{s(0)} + I_{r(0)}}{I_b} \quad (14)$$

$$\eta_{(e)} = \frac{I_b - I_{s(50)} + I_{r(50)}}{I_b} \quad (15)$$

Quantitatively, we can show I_{ser} , $I_{\text{bser}(0)}$, and $I_{\text{bser}(50)}$ are small by looking at some data typical of the δ and η investigations for electrons incident on Al. For a beam energy of 2.0 keV, the following currents were measured:

$$B = 15.20 \mu\text{A}$$

$$\text{PS}(0) = 6.60 \mu\text{A}$$

$$\text{TS}(0) = 0.06 \mu\text{A}$$

$$\text{PS}(50) = 13.35 \mu\text{A}$$

$$\text{TS}(50) = 1.50 \mu\text{A}$$

Then from Eqs. (A7) and (A8) we have

$$\text{BSE} = 3.35 \mu\text{A} \quad \Rightarrow \quad \eta = .22$$

$$\text{SE} = 5.31 \mu\text{A} \quad \Rightarrow \quad \delta = .35$$

Returning to Eqs. (A4) and (A5), and regarding $R(0)$ and $R(50)$ as the incident “beam” currents producing SER, BSER(0), and BSER(50), we can solve for these currents:

$$\begin{aligned} \text{TS}(50) &= R(50) - \text{BSER}(50) \\ &= R(50) - .22R(50) = .78R(50) \end{aligned}$$

$$\Rightarrow R(50) = \frac{\text{TS}(50)}{.78} = 1.92 \mu\text{A}$$

$$\Rightarrow \text{BSER}(50) = .22(1.92 \mu\text{A}) = .42 \mu\text{A}$$

and

$$\begin{aligned}
 TS(0) &= R(0) - SER - BSER(0) \\
 &= R(0) - .35R(0) - .22R(0) = .43R(0) \\
 \Rightarrow R(0) &= \frac{TS(0)}{.43} = .14 \mu A
 \end{aligned}$$

$ \begin{aligned} \Rightarrow SER &= .35(.14 \mu A) = .048 \mu A \\ BSER(0) &= .22(.14 \mu A) = .031 \mu A \end{aligned} $

which are small compared to the other quantities in Eqs. (14) and (15). It is noted that in the above determinations of I_{ser} , $I_{bser(0)}$, and $I_{bser(50)}$ we have assumed that $I_{r(0)}$ and $I_{r(50)}$ represent monoenergetic beams of 2.0 keV electrons. Clearly this is not an accurate assumption, though we contend that its accuracy is sufficient to allow order-of-magnitude calculations.

A.2 Error Introduced into δ , η , and $\delta(E_s)$ Determinations due to Non-Normal Exit Angles

In biasing the primary and tertiary samples we are attempting to measure current to the primary sample due to SE's with energies *at and below* a given energy $e\Phi$, where Φ is the sample bias—see Figs. 3-5 and 3-10 [(3.3.1) and (3.3.3)]. In addition, however, we measure current due to electrons with energies *greater* than $e\Phi$, but which are prevented from escaping the sample due to non-normal exit (scattering) angles; that is, an electron will not escape the sample (and will therefore be counted in any measured sample current), even if its total energy is greater than $e\Phi$, when the perpendicular component (to the sample surface) of its velocity vector (given by $v_{\perp} = \cos \alpha$) is such that $1/2 mv_{\perp}^2 < e\Phi$. This fact introduces error into our determinations of δ and η , as well as $\delta(E_s)$, and we wish to determine the extent of this error.

A.1.1 Errors in δ and η

For δ and η determination, sample-current measurements are made at $\Phi=0$ V and $\Phi=+50$ V. All SE's are clearly held on the sample, regardless of exit angle, when the sample is biased to +50 V. Error introduced into $I_{s(50)}$ is therefore due to BSE's whose exit angles do not permit them to escape the sample even though their energies are greater than 50 eV. For example, a BSE with $E_s = 100$ eV will not escape if its exit angle α is greater than $\alpha_c = \cos^{-1}(50/100) = 60^\circ$, and a 2 keV BSE will not escape if its exit angle is greater than $\alpha_c = \cos^{-1}(50/2000) = 88.6^\circ$. [Clearly then, the distribution of BSE energies—i.e., the BSE spectrum—is important in determining which BSE's are prevented from escaping a positively biased sample.] If we can calculate the magnitude of the current due to BSE's that are held on to, or “captured,” by a sample biased to +50 V, $I_{\text{captured}}^{\text{bse}}$, then we can determine its importance via comparison to the total BSE current $I_{\text{tot}}^{\text{bse}}$.

First, for an unbiased sample, the current due to BSE's leaving at a given α is given by

$$I^{\text{bse}}(\alpha') = 2\pi \int_{50\text{eV}}^{E_b} I^{\text{bse}}(E, \alpha') dE$$

where $I^{\text{bse}}(E, \alpha')$ is the BSE spectrum at $\alpha = \alpha'$. Assuming the α -dependence to follow a Lambert cosine law—i.e., $I^{\text{bse}}(\alpha') = I^{\text{bse}}(\alpha=0) \cos \alpha$ —we have

$$I^{\text{bse}}(\alpha') = 2\pi \cdot I(0) \int_{50\text{eV}}^{E_b} I^{\text{bse}}(E) \cos \alpha' dE$$

and the total BSE current—i.e., the current due to BSE's emitted at all angles—can be written

$$\begin{aligned} I_{\text{tot}}^{\text{bse}} &= 2\pi \cdot I(0) \int_{50\text{eV}}^{E_b} \int_0^{\pi/2} I^{\text{bse}}(E) \cos \alpha \sin \alpha d\alpha dE \\ &= \pi \cdot I(0) \int_{50\text{eV}}^{E_b} I^{\text{bse}}(E) dE \end{aligned} \quad (\text{A9})$$

Next, for a sample biased to +50 V, we calculate the current due to BSE's which do not escape via introduction of the Θ -function, $\Theta(50\text{eV} - E\cos\alpha)$, given by

$$\Theta(e\Phi - E\cos\alpha) = \begin{cases} 1 & \text{if } (50\text{eV} - E\cos\alpha) \geq 0 \\ 0 & \text{otherwise} \end{cases}$$

Following a development similar to the unbiased case, then, the current due to the captured BSE's can be written

$$\begin{aligned} I_{\text{captured}}^{\text{bse}} &= 2\pi \cdot I(0) \int_{50\text{eV}}^{E_b} \int_0^{\pi/2} I^{\text{bse}}(E) \cos\alpha \Theta(50\text{eV} - E\cos\alpha) \sin\alpha \, d\alpha \, dE \\ &= 2\pi \cdot I(0) \int_{50\text{eV}}^{E_b} \int_0^{\cos^{-1}(\frac{50\text{eV}}{E})} I^{\text{bse}}(E) \cos\alpha \sin\alpha \, d\alpha \, dE \end{aligned} \quad (\text{A10})$$

and we see the effect of the Θ -function is to alter the limits of integration over α .

[Alternately, we could have used Θ to alter the limits of integration over E , though we shall see this would not have been as convenient.] Performing the integration over α we obtain

$$I_{\text{captured}}^{\text{bse}} = \pi \cdot I(0) \int_{50\text{eV}}^{E_b} I^{\text{bse}}(E) \cdot \{1 - \sin^2[\cos^{-1}(\frac{50\text{eV}}{E})]\} \, dE \quad (\text{A11})$$

In order to evaluate the integrals in (A9) and (A11), we must know the specific form of $I^{\text{bse}}(E)$. Figure 2-7 illustrates the general shape of the BSE spectrum, though a specific expression for $I^{\text{bse}}(E)$ has thus far not been found in the literature. For our purposes, however, it is sufficient to model the BSE spectrum by assuming all BSE's possess a single, average energy. An expression for the average integrated (i.e., averaged over all α 's) BSE energy E_{ave} is given by⁴⁴

$$E_{\text{ave}} = (.45 + 2 \times 10^{-3}Z)E_b$$

for the atomic number Z of the sample. Though this expression has been found to underestimate E_{ave} somewhat, we will nonetheless use it, as underestimating E_{ave} is a more conservative calculation (i.e., the lower E_{ave} , the larger $I_{\text{captured}}^{\text{bse}}$). Further simplifying, and erring a bit more conservatively, we assume simply $E_{\text{ave}} = .45E_b$. Then $I^{\text{bse}}(E)$ can be expressed in terms of the Dirac δ -function

$$I^{bse}(E) = \delta(E - .45E_b)$$

and we have

$$\begin{aligned} \frac{I_{captured}^{bse}}{I_{true}^{bse}} &= \frac{\pi \cdot I(0) \int_{50eV}^{E_b} \delta(E - .45E_b) \{1 - \sin^2[\cos^{-1}(\frac{50eV}{E})]\} dE}{\pi \cdot I(0) \int_{50eV}^{E_b} \delta(E - .45E_b) dE} \\ &= 1 - \sin^2[\cos^{-1}(\frac{50eV}{.45E_b})] \end{aligned} \quad (A12)$$

Equation (A12) represents the relative error in $I_{s(50)}$. We now wish to determine the effect of this error on our determinations of δ and η , and we begin by showing that Eqn. (A12) also represents the relative error in η :

$$\begin{aligned} \eta_{meas} &= \frac{I_b - I_{s(50)meas} + I_{r(50)}}{I_b} \\ &= \frac{I_b - (I_{s(50)true} + I_{captured}^{bse}) + I_{r(50)}}{I_b} \\ &= \frac{I_b - I_{s(50)true} + I_{r(50)} - \{1 - \sin^2[\cos^{-1}(\frac{50eV}{.45E_b})]\} \eta_{true} I_b}{I_b} \\ &= \eta_{true} - \{1 - \sin^2[\cos^{-1}(\frac{50eV}{.45E_b})]\} \eta_{true} \\ &\Rightarrow \frac{\eta_{meas}}{\eta_{true}} = \sin^2[\cos^{-1}(\frac{50eV}{.45E_b})] \end{aligned}$$

The relative error in η is then given by

$$\boxed{\frac{\Delta\eta}{\eta} = 1 - \frac{\eta_{meas}}{\eta_{true}} = 1 - \sin^2[\cos^{-1}(\frac{50eV}{.45E_b})]} \quad (A13)$$

Results given by Eqn. (A13) are plotted in Fig. A-1, and reveals a worst-case error in η of ~5% for a beam energy of 500 eV, decreasing to less than 1% for beam energies above 1 keV. Errors for beam energies below 500 eV are considerably higher, though measurements at such energies are not being considered in the present investigation.

Calculation of error in δ due to $I_{\text{captured}}^{\text{bse}}$ is a bit more complicated, in that the error in δ becomes a function of η :

$$\begin{aligned}\delta_{\text{meas}} &= \frac{I_{\text{true}}^{\text{se}} + I_{\text{captured}}^{\text{bse}}}{I_b} \\ &= \frac{I_{\text{true}}^{\text{se}} + \{1 - \sin^2[\cos^{-1}(\frac{50\text{eV}}{.45E_b})]\}\eta I_b}{I_b} \\ &= \delta_{\text{true}} + \{1 - \sin^2[\cos^{-1}(\frac{50\text{eV}}{.45E_b})]\}\eta\end{aligned}$$

which gives

$$\boxed{\frac{\Delta\delta}{\delta} = \frac{\delta_{\text{meas}} - \delta_{\text{true}}}{\delta_{\text{true}}} = \frac{\{1 - \sin^2[\cos^{-1}(\frac{50\text{eV}}{.45E_b})]\}}{\delta_{\text{meas}} - \{1 - \sin^2[\cos^{-1}(\frac{50\text{eV}}{.45E_b})]\}} \quad (\text{A14})}$$

Results given by Eqn. (A14) are plotted in Figs. A-2 and A-3 for selected values of η and δ_{meas} . *It is emphasized that Eqs. (A13) and (A14) represent worst-case errors, and are intended to demonstrate that for incident energies of concern to this thesis ($> \sim 500$ eV), errors in δ and η due to non-normal exit angles are negligible for all but the lowest beam energies.*

A.1.2 Error in $\delta(E_s)$

Calculating the effect of non-normal exit angles on $\delta(E_s)$ determinations proceeds in a similar manner as that for δ and η . In this case, however, the sample is not biased to +50 V only, but to +50 V *incrementally*. Having already shown the effect of “captured” BSE's to be small, we will concentrate on the effect of SE's with non-normal exit angles. Then, after Eqn. (A9),

$$I_{\text{tot}}^{\text{se}} = \pi \cdot I(0) \int_0^{50\text{V}} I^{\text{se}}(E) dE$$

or we can write the true current due to SE's at and below a given energy, $e\Phi$,

$$I_{\text{true}}^{\text{se}}(\Phi) = \pi \cdot I(0) \int_0^{e\Phi} I^{\text{se}}(E) dE$$

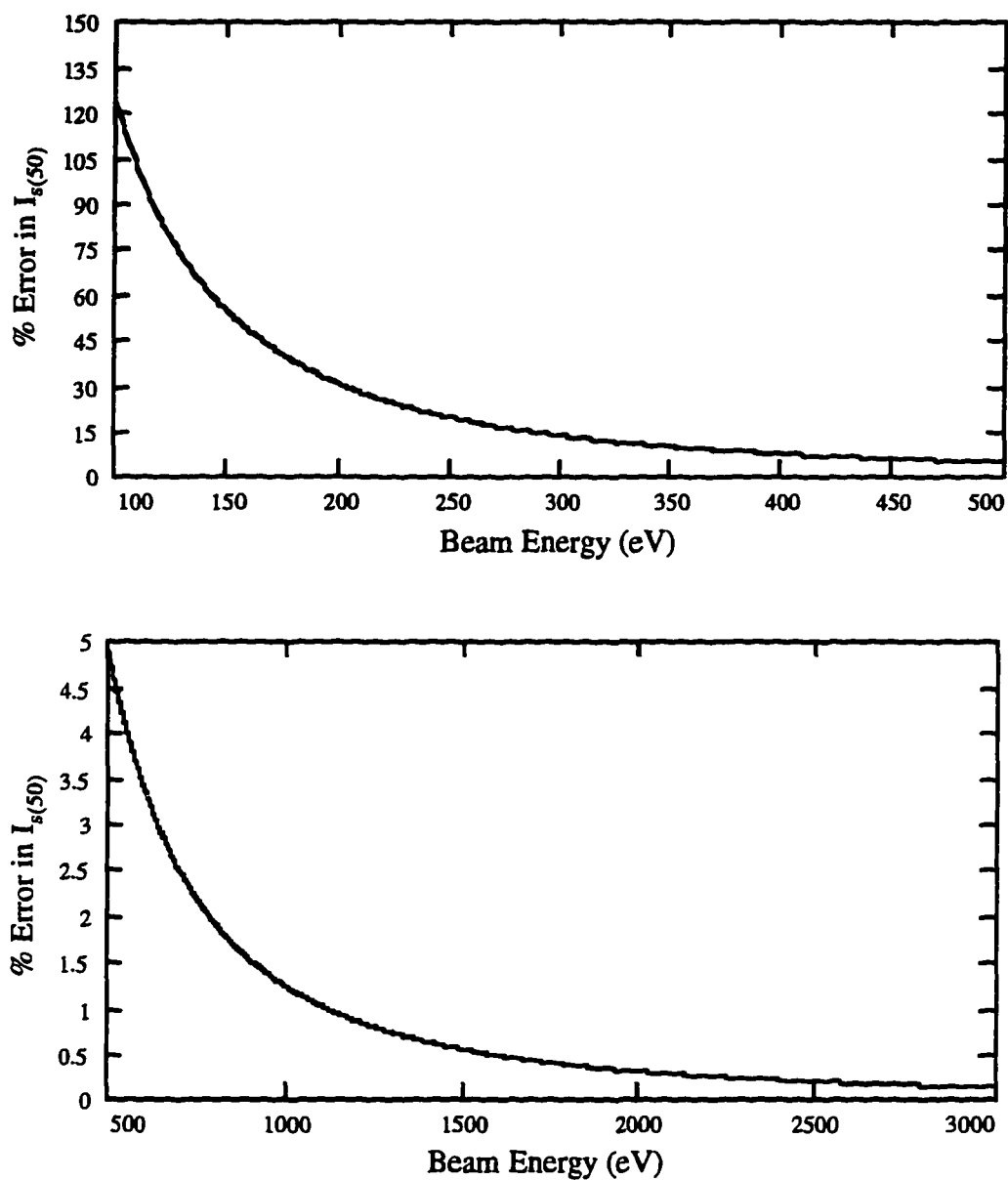


FIG. A-1. Percent error in η due to non-normal exit angles of BSE's, for incident energies of (a) 100 eV to 500 eV and (b) 500 eV to 3000 eV.

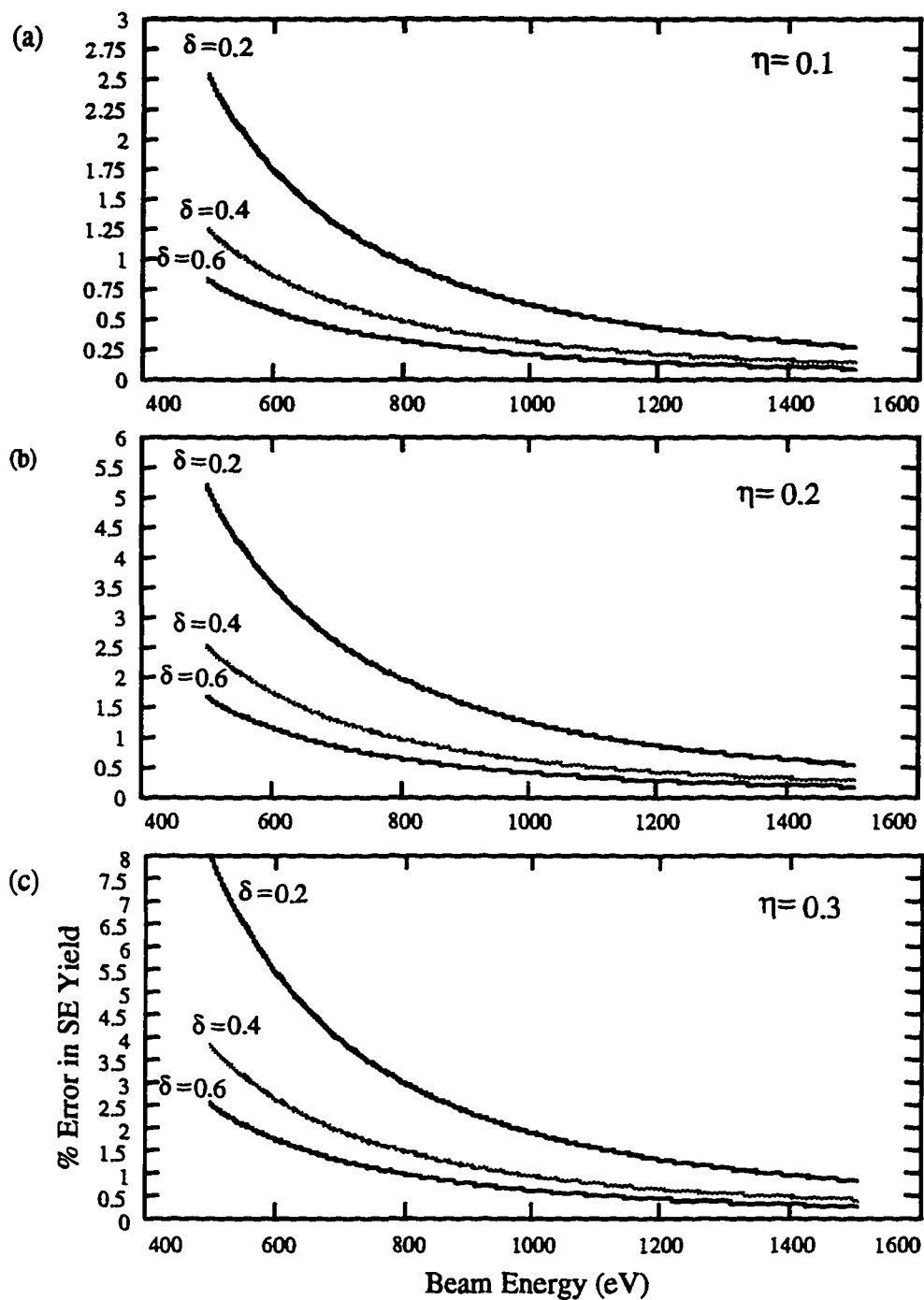


FIG. A-2. Percent error in δ due to non-normal exit angles of BSE's as a function of beam energy (500 eV to 1500 eV) and BSE yield [(a) $\eta = 0.1$, (b) $\eta = 0.2$, and (c) $\eta = 0.3$].

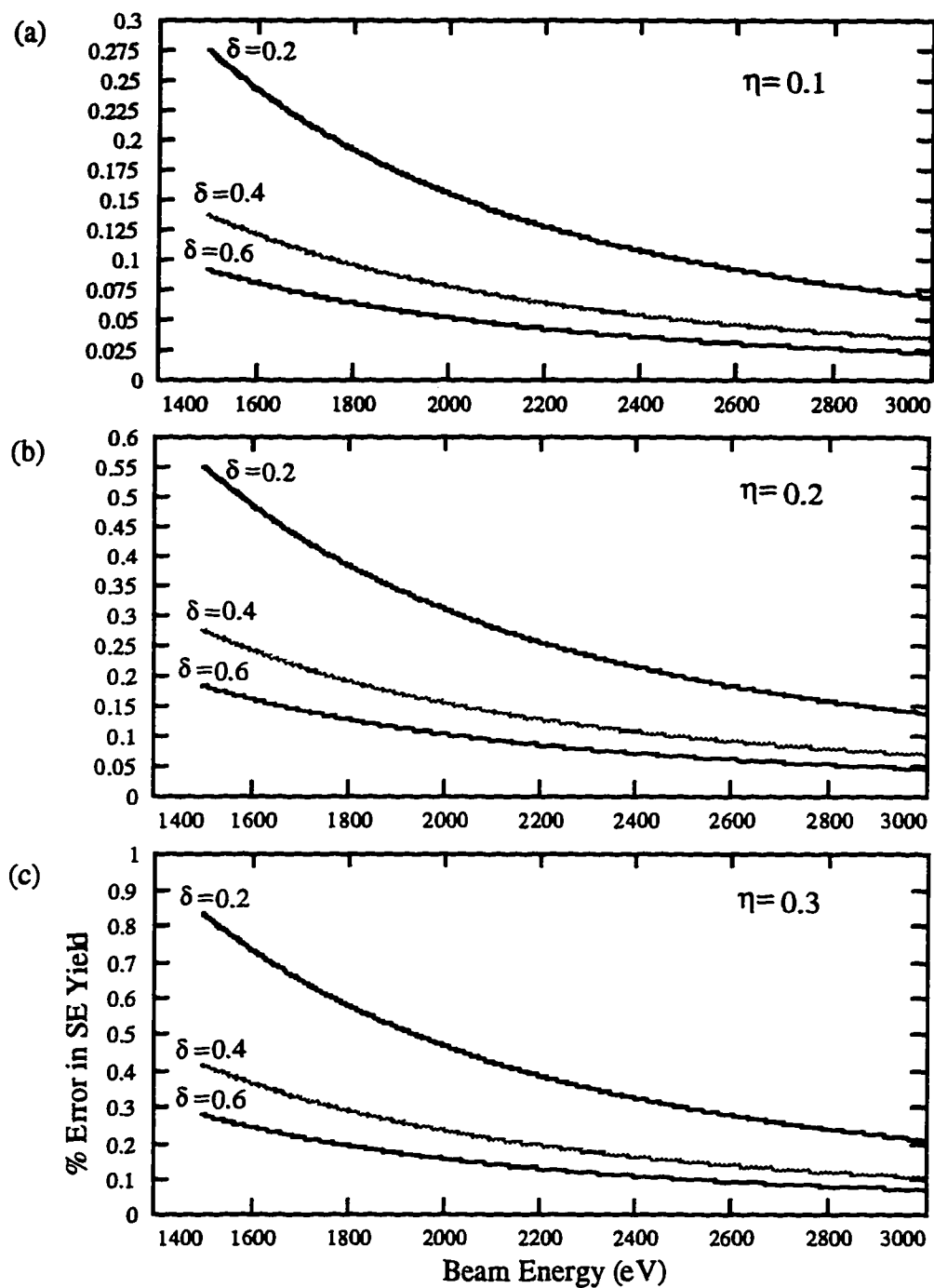


FIG. A-3. Percent error in δ due to non-normal exit angles of BSE's as a function of beam energy (1500 eV to 3000 eV) and BSE yield [(a) $\eta = 0.1$, (b) $\eta = 0.2$, and (c) $\eta = 0.3$].

This time, an expression is found⁴⁵ for the SE spectrum $I^{se}(E)$, depicted schematically in

Fig. 2-5:

$$I^{se}(E) = \frac{k}{E_b} \frac{E}{(E + \phi)^4}$$

for some proportionality constant, k , and the work function of the sample material, ϕ .

Substituting, we obtain

$$I_{true}^{se}(\Phi) = \frac{k\pi \cdot I(0)}{E_b} \left[\frac{-1}{2(E + \phi)^2} + \frac{\phi}{3(E + \phi)^3} \right]_0^{e\Phi} \quad (A15)$$

Next, after Eqn. (A10), we can write the measured SE current, $I_{meas}^{se}(\Phi)$, due to SE's at and below a given energy $e\Phi$ —i.e., the current due to SE's held on the sample with the sample biased to some positive Φ , *which includes those SE's with energies above Φ , but whose exit angles do not allow them to escape*:

$$\begin{aligned} I_{meas}^{se}(\Phi) &= 2\pi \cdot I(0) \int_0^{50\text{eV}} \int_0^{\pi/2} I^{se}(E) \cos \alpha \Theta(e\Phi - E \cos \alpha) \sin \alpha \, d\alpha \, dE \\ &= 2\pi \cdot I(0) \int_0^{e\Phi/\cos \alpha} \int_0^{\pi/2} I^{se}(E) \cos \alpha \sin \alpha \, d\alpha \, dE \\ &= \frac{2\pi k \cdot I(0)}{E_b} \int_0^{e\Phi/\cos \alpha} \int_0^{\pi/2} \frac{E}{(E + \phi)^4} \cos \alpha \sin \alpha \, d\alpha \, dE \end{aligned}$$

where this time we have used the Θ -function to modify the limits of integration over E .

Performing the integration over energy and evaluating at the given limits, one is lead to

$$I_{meas}^{se}(\Phi) = \frac{2\pi k \cdot I(0)}{E_b} \int_0^{\pi/2} \left[\frac{-\cos^3 \alpha}{2(\phi \cos \alpha + e\Phi)^2} + \frac{\phi \cos^4 \alpha}{3(\phi \cos \alpha + e\Phi)^3} + \frac{\cos \alpha}{6\phi^2} \right] \sin \alpha \, d\alpha$$

which has the solution

$$I_{meas}^{se}(\Phi) = \frac{2\pi k \cdot I(0)}{E_b} \left\{ \frac{(e\Phi)^2}{2\phi^4} \ln\left(\frac{\phi}{e\Phi} + 1\right) - \frac{(e\Phi)^3}{2\phi^3(e\Phi + \phi)^2} - \frac{2\phi^2(e\Phi)^2}{3\phi^2(e\Phi + \phi)^2} \right\} \quad (A16)$$

From Eqs. (A15) and (A16), then, we have

$$\frac{I_{\text{meas}}^{\text{se}}(\Phi)}{I_{\text{true}}^{\text{se}}(\Phi)} = \frac{2\left\{\frac{(e\Phi)^2}{2\phi^4} \ln\left(\frac{\phi}{e\Phi} + 1\right) - \frac{(e\Phi)^3}{2\phi^3(e\Phi + \phi)^2} - \frac{2\phi^2(e\Phi)^2}{3\phi^2(e\Phi + \phi)^2}\right\}}{\left[\frac{-1}{2(E + \phi)^2} + \frac{\phi}{3(E + \phi)^3}\right]_0^{e\Phi}}$$

Let $G(\Phi)$ denote the right-hand side, then we have

$$I_{\text{meas}}^{\text{se}}(\Phi) = G \cdot I_{\text{true}}^{\text{se}}(\Phi)$$

and we calculate the relative error in $\delta(E_s)$ as follows:

$$\begin{aligned} \delta(E_s)_{\text{meas}} &= \frac{I_{\text{meas}}^{\text{se}}(\Phi)}{I_b} = \frac{G \cdot I_{\text{true}}^{\text{se}}(\Phi)}{I_b} = G \cdot \delta(E_s)_{\text{true}} \\ \Rightarrow \boxed{\frac{\Delta\delta(E)}{\delta(E)} &= \frac{\delta(E)_{\text{meas}} - \delta(E)_{\text{true}}}{\delta(E)_{\text{true}}} = G(E) - 1} \end{aligned} \quad (\text{A17})$$

Results are plotted in Fig. A-4 and reveal just what one would expect, given the SE energy distribution depicted in Fig. 2-5. For small sample potentials ($\Phi \leq \sim 10$ V) the effect of non-normal exit angles on integrated current measurements (and therefore $\delta(E_s)$ determinations) is enormous—inflating them by as much as 120%—since the majority of SE's possess energies below ~ 10 eV. For $\Phi > 15$ V, however, the effect has dropped to less than 5%, and continues to drop as Φ is increased, since fewer and fewer SE's reside at these higher energies. It is noted that Eqn. (A17) and Fig. A-4 *do not* represent a worst-case scenario, but rather a realistic and detailed calculation of the error introduced into $\delta(E_s)$ determinations as a result of non-normal exit angles, and may therefore be used to correct $\delta(E_s)$ values obtained from raw data (integrated current measurements).

A.3 Expected RD Signal Magnitudes

We wish to do an order-of-magnitude calculation for the currents the rotatable detector must be able to measure. Assume a beam current of $10 \mu\text{A}$, an SE yield of $\delta = 0.3$, and a BSE yield of $\eta = 0.2$. Then we have a total current leaving the sample (at 0 V bias) of $I_{\text{se}} + I_{\text{bse}} = .3(10 \mu\text{A}) + .2(10 \mu\text{A}) = 5 \mu\text{A}$. This $5 \mu\text{A}$ of current is spread over 2π

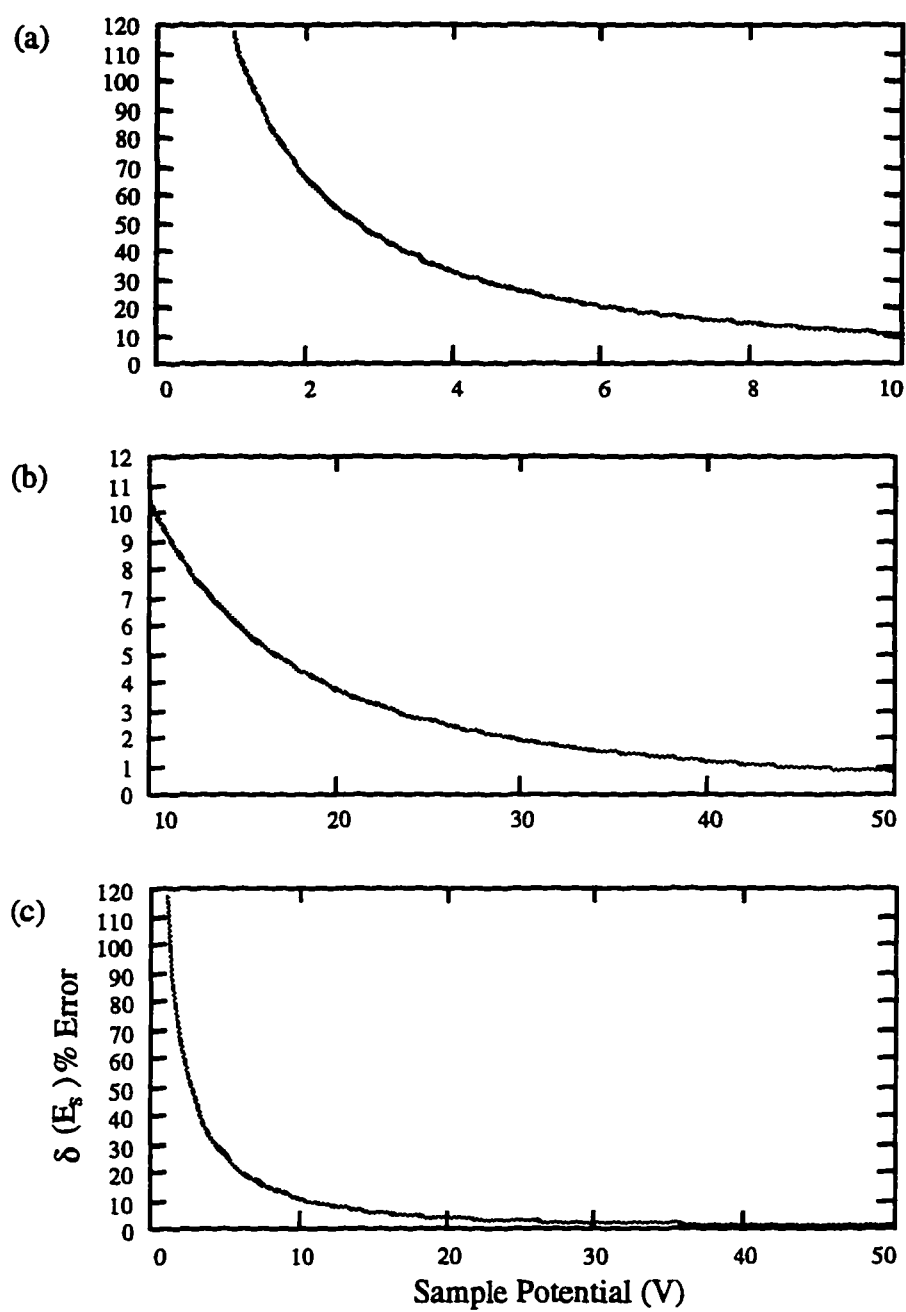


FIG. A-4. Percent error in $\delta(E_s)$ as function of sample potential Φ , for Φ ranging from (a) 0 V to 10 V, (b) 10 V to 50 V, and (c) 0 V to 50 V.

steradians, and the field-of-view of the RD is $\sim 10^{-3}$ sr, meaning that on the average we would expect the signal reaching the detector to be

$$I_{\text{det}} = \frac{10^{-3} \text{ sr}}{2\pi} \cdot (5 \mu\text{A}) = 8 \times 10^{-10} \text{ A}$$

—a signal that is detectable with the apparatus described in this thesis. More specifically, we can calculate the expected RD signal as a function of scattering angle, α (for the beam current, δ , and η given above):

$$I_{\text{det}}(\alpha') = I(\alpha' = 0) \cos \alpha' d\Omega = I(0) \cos \alpha' d\Omega$$

We can solve for $I(0)$, since we have already calculated the current leaving the sample:

$$I_{\text{tot}}^{\text{sc}} + I_{\text{tot}}^{\text{bse}} = \int_{\text{half-sphere}} I_{\text{det}}(\alpha') d\Omega = 2\pi \int_0^{\pi/2} I(0) \cos \alpha \sin \alpha d\alpha = 5 \mu\text{A}$$

$$\Rightarrow I(0) = \frac{5 \times 10^{-6}}{\pi}$$

Which then gives

$$I_{\text{det}}(\alpha') = \frac{5 \times 10^{-6}}{\pi} \cdot \cos \alpha' d\Omega$$

$$= \frac{5 \times 10^{-6}}{\pi} \cdot \cos \alpha' (10^{-3} \text{ sr})$$

(A18)

Equation (A18) is plotted in Fig. A-5, illustrating expected typical RD currents as a function of α . The figure suggests measurable RD currents even below $\alpha = 80^\circ$.

A.4 Electrical Resistance of Teflon

An order-of-magnitude calculation for the Teflon sleeve is accomplished via simple application of Ohm's law, $V = IR$. For a FC potential of -50 V, and a measured leakage current of 10^{-12} A, we have

$$R = \frac{V}{I} = \frac{50 \text{ volts}}{10^{-12} \text{ amps}} = 5 \times 10^{13} \Omega$$

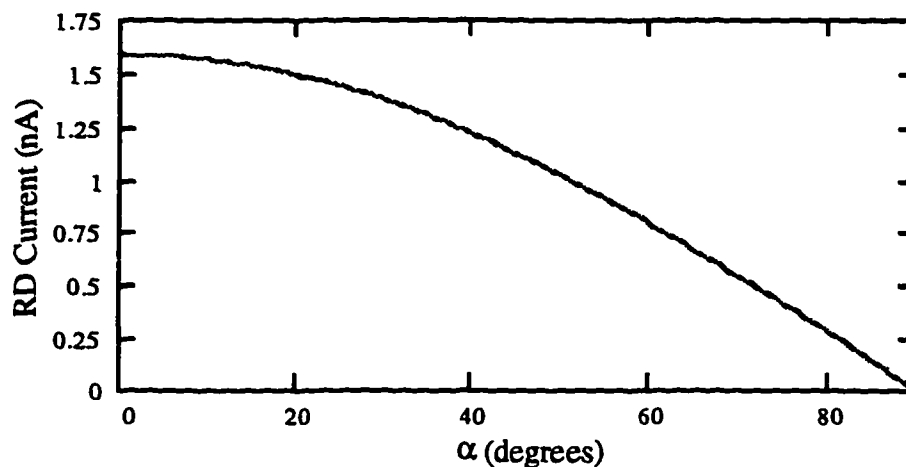


FIG. A-5. Expected RD signal as a function of scattering angle ($I_b = 10 \mu\text{A}$, $\delta = 0.3$, $\eta = 0.2$).

A.5 Effect of an Incident Electron Beam on the Temperature of an Aluminum Sample

Since δ and η are likely functions of temperature, it is reasonable to check the temperature increase of the sample due to the energy being deposited by the incident electron beam. Two basic calculations are of relevance: the equilibrium temperature, T_{eq} , and the time required to reach T_{eq} . For the first, we use the relation $E_{in} = E_{out}$, where E_{in} is the energy deposited by the electron beam, and E_{out} is due entirely to radiative energy loss. We then have

$$E_{in} = \sigma(T_{eq}^4 - T_i^4)A\epsilon$$

for the Stefan-Boltzmann constant σ , the radiative surface area, A , and the emissivity of the radiating body, ϵ . We assume an incident beam current of $\sim 10 \mu\text{A}$ and thus calculate E_{in} to be $\sim .03 \text{ Js}^{-1}$. Since the sample and sample block are in good thermal contact, we assume E_{in} is absorbed by the entire sample holder; then $A = 36.7 \text{ cm}^2$, and $\epsilon = 0.3$ (the emissivity for oxidized Al). Taking the initial temperature to be $T_i = 294 \text{ K}$ (21°C) and solving for T_{eq} then gives an equilibrium temperature of $\sim 299 \text{ K}$, which translates to a rise of $\sim 5^\circ$.

We now wish to calculate the length of time required to raise the temperature of the sample and sample holder by 5° C. Using the relation $Q = mc\Delta T$ —for the heat Q required to raise a specimen of mass m and specific heat c by a temperature ΔT —together with the relation $P = Q/\Delta t$ (for the power, P), and assuming *no* radiative heat loss, we find a lower bound to the time Δt required to effect a 5° temperature rise of the Al sample and sample holder to be ~2 hours.

APPENDIX B

Scattering Angle as a Function of
Detector Position

The geometry described in Chapter 4 dictates that the scattering angle, α , vary nonlinearly with detector position, ϕ . For the two different detector arms, the specific relationships are

$$\text{For the } 45^\circ \text{ arm: } \phi_{45} = 2 \cos^{-1} \left[1 - 4 \sin^2 \frac{\alpha}{2} \right]$$

$$\text{For the } 59^\circ \text{ arm: } \phi_{59} = 2 \cos^{-1} \left[1.08 - 5.49 \sin^2 \frac{\alpha}{2} \right]$$

A conversion table derived from these equations is given below, and the relations are presented graphically in Fig. B-1.

TABLE B.1. Scattering angle α as a function of detector position.

α	ϕ_{45}	ϕ_{59}	α	ϕ_{45}	ϕ_{59}
0	0	—	48	70	80
3	4	—	51	75	86
6	9	—	54	80	93
9	13	—	57	85	100
12	17	—	60	90	107
15	21	9	63	95	115
18	26	19	66	101	123
21	30	26	69	106	133
24	34	33	72	112	145
27	39	39	75	119	163
30	43	45	78	126	—
33	47	50	81	133	—
36	52	56	84	142	—
39	56	62	87	154	—
42	61	68	90	180	—
45	66	74			

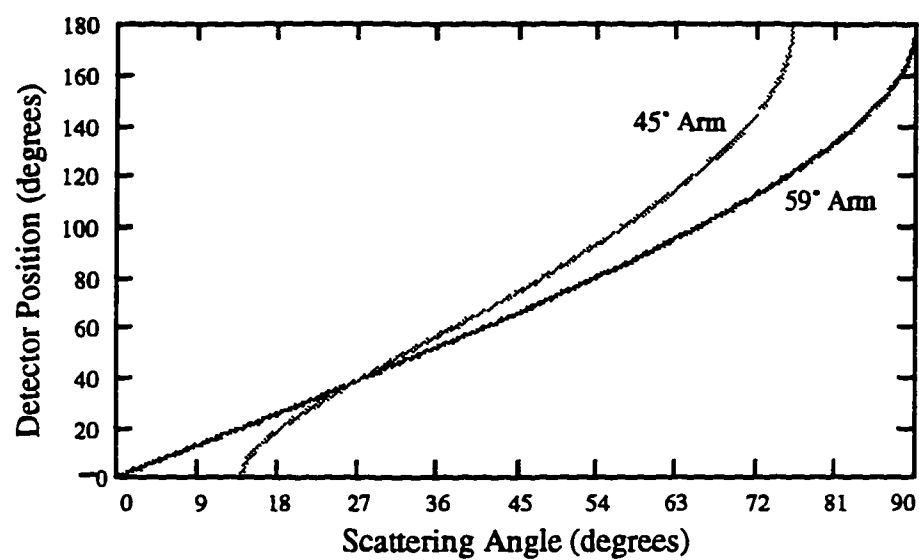


FIG. B-1. Scattering angle intercepted by the rotatable detector as a function of detector position.